

INSTITUTE OF PAPER SCIENCE AND TECHNOLOGY
Atlanta, Georgia

ANNUAL RESEARCH REVIEW

March 7, 2000

PAPER PHYSICS

John Waterhouse, PAC Liaison
Paper Physics, End-Use & Converting Unit

Doeung Choi, PAC Chairman
Hercules, Incorporated

David Knox, Vice-PAC Chairman
Westvaco Corporation

Pierre Brodeur, Ph.D.
Sensors, Measurement & Control Unit

Ross MacHattie, RAC Liaison
Honeywell-Measurex

Kari Ebeling, Alternate RAC Liaison
UPM-Kymene

February 12, 2000


TO: MEMBERS OF THE PAPER PHYSICS PROJECT ADVISORY COMMITTEE

Attached for your review are the Status Reports for the projects to be discussed at the Paper Physics Project Advisory Committee meeting. The Program Review is scheduled for Tuesday, March 7, 2000, at 8:00 a.m. - 5:00 p.m. and the PAC Committee Meeting will be held on Wednesday, March 8, 2000 from 8:00 a.m. to 12:00 p.m.

Please note that the meeting is being held at the Institute of Paper Science and Technology.

We look forward to seeing you at this time.

Sincerely,

A handwritten signature in black ink, appearing to read "John Waterhouse", with a long horizontal flourish extending to the right.

John Waterhouse
Senior Research Fellow/Unit Leader,
Paper Physics, End-Use and Converting Unit

And

A handwritten signature in black ink, appearing to read "Pierre Brodeur", written in a cursive style.

Pierre Brodeur, Ph.D.
Associate Professor/Unit Leader,
Sensors, Measurement and Control Unit

/djh
Attachment

**PAPER PHYSICS PROJECT ADVISORY COMMITTEE
PROGRAM REVIEW AGENDA
March 7, 2000**

Seminar Room

8:00 a.m. – 8:20 a.m.	Opening Remarks and Antitrust Statement	John Waterhouse & Doeung Choi
8:20 a.m. – 8:40 a.m.	Welcome from the Vice President of Research	Gary Baum

Ultrasonics

8:40 a.m. – 9:20 a.m.	Project F008 Fundamentals of Acoustic Radiation Pressure	Pierre Brodeur
9:20 a.m. – 10:00 a.m.	Project F007 On-line Measurement of Paper Properties	Maclin Hall
10:00 a.m. – 10:10 a.m.	Break	
10:10 a.m. – 10:50 a.m.	Project F031 Non-contact Ultrasonic Stiffness Measurements	John Waterhouse Chuck Habeger

Dimensional Stability

10:50 a.m. – 11:30 a.m.	Project F020 Fundamentals of Dimensional Stability	Doug Coffin
11:30 a.m. – 12:00 p.m.	Lunch	
12:00 p.m. – 12:40 p.m.	Project F026 Fundamentals of Accelerated Creep	Chuck Habeger

Fiber, Bonding & Structure

12:40 p.m. – 1:20 p.m.	Project F023 Fundamentals of Micromechanics of Fiber Networks	Martin Ostoja – Starzewski
1:20 p.m. – 1:35 p.m.	Break	
1:35 p.m. – 2:15 p.m.	Project F024 Improving the Refining of Chemical Pulps	John Waterhouse
2:15 p.m. – 2:55 p.m.	Project F025 Fundamentals of Interfiber Bonding	Hiroki Nanko
2:55 p.m. – 3:35 p.m.	Project F044 Liquid/Substrate Interactions	Wayne Robbins
3:35 p.m. – 3:45 p.m.	Break	

**Research Updates and New Project
Proposals**

3:45 p.m. – 4:00 p.m.	Fuzzy Front End	Anthony Colasurdo
4:00 p.m. – 4:30 p.m.	New Proposals For Year 2001	
4:30 p.m. – 5:00 p.m.	“Investigation of Shrinkage and Stiffness Profiles Developed During Drying”	Doug Coffin (STFI Sabbatical)

**PAPER PHYSICS ADVISORY COMMITTEE
COMMITTEE REVIEW**

March 8, 2000

Seminar Room

8:00 a.m. – 8:15 a.m.

- Opening Remarks and Antitrust Statement
- Next Meeting Date: Fall PAC (Tentative dates October 24 & 25, 2000)
- Project Evaluations

8:15 a.m. – 11:15 a.m.

- Project Reviews
 - Project F008 Acoustic Radiation
 - Project F007 On-line Measurements
 - Project F031 Non-contact Laser Ultrasonic Stiffness Measurements

 - Project F020 Dimensional Stability
 - Project F026 Accelerated Creep

 - Project F023 Micromechanics
 - Project F024 Refining
 - Project F025 Bonding
 - Project F044 Liquid Substrates

11:15 a.m. – 11:30 p.m.

Break

11:30 a.m. – 12:00 p.m.

“Project Management Portfolio/Research Lines”: David Orloff,
Assistant Vice President Research – IPST

TABLE OF CONTENTS

		Page
Project F008	Fundamentals of Acoustic Radiation Pressure	1
Project F007	On-line Measurement of Paper Properties	35
Project F031	Non-contact Ultrasonic Stiffness Measurements	62
Project F020	Fundamentals of Dimensional Stability	80
Project F026	Fundamentals of Accelerated Creep	89
Project F023	Micromechanics of Fiber Networks	111
Project F024	Fundamentals of Refining and Fiber Properties	137
Project F025	Fundamentals of Bonding	165
Project F044	Liquid/Substrate Interactions	193

FUNDAMENTALS OF ACOUSTIC RADIATION PRESSURE

STATUS REPORT

FOR

PROJECT F008

**Pierre Brodeur
Joseph Gerhardstein
Feler Bose
Jimmy Jong
Dolon Silimon
Mee Choi**

**Institute of Paper Science and Technology
500 10th Street, N. W.
Atlanta, Georgia 30318**

DUES-FUNDED PROJECT SUMMARY

Project Title: **FUNDAMENTALS OF ACOUSTIC RADIATION PRESSURE**
Project Code: **FARPE**
Project Number: **F008**
PAC: **Paper Physics**

Project Staff

Principal Investigator: **Pierre Brodeur**
Research Support Staff: **Joe Gerhardstein**
Jimmy Jong
Feler Bose
Dolon Silimon
Mee Choi

PAC Subcommittee **Thomas Rodencal**

FY 99-00 Budget: **\$141,000**
Allocated as Matching Funds: **100%**

Time Allocation:
Principal Investigator: **60%**
Research Support Staff: **75%**

Supporting Research:

Special Students: **None**
External (Where Matching Is Used): **Project 4190 (State of Georgia TIP³ program - 245k)**
Project 4183 (DOE-Agenda 2020 Program - 150k)

RESEARCH LINE/ROADMAP: #13: Reduce and/or control contaminants in recycled-fiber pulp using breakthrough technologies to allow complete interchange of recycled pulp with virgin pulp of similar fiber make at economical cost.

PROJECT OBJECTIVE: To perform a mill demonstration of ultrasonic whitewater clarification (AST clarification).

PROJECT BACKGROUND: *A laboratory demonstration of ultrasonic whitewater clarification was successfully completed during FY98-99. An economic analysis was performed and results are very promising. FY99-00 funding from IPST, the State of Georgia (TIP³) and DOE (Agenda 2020 – Recycling Task Group) was combined to develop a 100-gpm pilot-scale clarifier and perform a series of mill trials to begin in May 2000 at the SP Newsprint mill in Dublin, GA. Upon successful completion of trials in September 2000, the technology will be ready for commercialization.*

MILESTONES:

- Complete design and construction of pilot-scale system: April 2000
- Complete trials at SP Newsprint: August 2000
- Begin commercialization process: September 2000

DELIVERABLES: *Demonstration and economic feasibility study of ultrasonic whitewater clarification in a mill environment.*

STATUS OF GOALS FOR FY 99-00:

- Develop a 100-gpm pilot-scale AST system for whitewater clarification
- Perform whitewater clarification trials in a mill environment
- Secure an industrial partner for commercialization

SCHEDULE:

Task Descriptions	1999 Apr - Jun	1999 July - Sept	1999 Oct - Dec	2000 Jan - Mar	2000 Apr - Jun
1. Preliminary Economic Analysis	-----	-----X			
2. Freq. Analysis			-----	-----X	
3. Dissolved Air Exp.		-----	-----	-----X	
4. Design Ultrasonic Equipment		-----	-----	---X	
5. Build Ultrasonic Equipment				-----	---X
6. Design Clarifier		-----	-----	-----X	
7. Build Clarifier				-----	---X
8. Assemble and Test Clarifier					-----X
9. Begin Mill Trials					-----
10. Search for Industrial Partner			-----	-----	-----X

SUMMARY OF RESULTS:

Following three years of research and development on various aspects of a novel separation technology using acoustic principles, a dual chemical flocculation/ultrasonic method to clarify a whitewater stream was investigated in the laboratory. The method first considers the use of flocculants to create larger size particles or flocs. Then, an ultrasonic field normal to the flow direction of the whitewater stream is applied to the flocs in such a way as to obtain two output streams: a clarified water stream and a stream of concentrated flocs.

An in-line ultrasonic separation system was used to demonstrate the clarification concept. Different flocculants were tested and experiments at different flow rates, ultrasonic frequencies, and acoustic intensity levels were made. Best results were obtained using the neutral flocculant system PEO/PFR. Test conditions were

determined to achieve a clean stream with less than 100 ppm of solids. Also, clarification efficiency close to 80% of the maximum possible clarification efficiency in the experimental setup was obtained.

An economic analysis was performed on a theoretical 22,750 L-per-minute (6000 gpm) ultrasonic whitewater clarifier. It was compared to a conventional dissolved air flotation (DAF) unit of the same size. The ultrasonic clarifier is estimated to cost 66% less than the DAF to purchase and install and will cost 35% less to operate.

SUMMARY OF KEY CONCLUSIONS:

- *Successful laboratory demonstration of whitewater clarification using IPST's acoustic separation technology*
- *Favorable preliminary economic analysis of ultrasonic whitewater clarification*

INTRODUCTION

This report presents an overview of the progress accomplished in Projects F008, 4183, and 4190 during the past year. Funding for the last two projects comes from the State of Georgia and the Department of Energy, respectively. It was determined in February 1999 that whitewater clarification would be the first commercial implementation of IPST's acoustic separation technology (AST), which has been under investigation since 1996. In order to optimize resources, all three projects were merged into a single project last year to support the development of a pilot-scale ultrasonic clarifier, perform laboratory experiments related to the clarifier performance, and proceed with a mill demonstration and economic analysis of whitewater clarification.

First, background information on previous work is reported in Section 1. Section 2 provides a description of the experimental setup used to demonstrate the separation of fibers. Section 3 discusses the theoretical/modeling effort on fibers interacting with an ultrasonic wave field. Section 4 provides a brief review of research accomplishments in whitewater applications. Section 4 also delves into the economic analysis of the acoustic separation technology.

1. BACKGROUND

Since its inception in 1991, IPST's Project F008 has focused on the fundamental effects of acoustic radiation pressure on fiber suspensions. This led to an investigation of potential applications in the pulp and paper industry. In essence, when water-suspended wood pulp fibers interact with an ultrasonic wave field, they are subjected to an acoustic force which results in fiber migration [Brodeur, 1991; Brodeur, 1989; Garceau et al., 1989; Dion et al., 1988]. There is also an acoustic torque, which can reorient fibers. Both acoustic force and torque are nonlinear effects. These effects are very desirable because they enable the noncontact mechanical manipulation of flowing fibers. Although several studies have shown that fluid-suspended particles can agglomerate when subjected to traveling or standing ultrasonic wave fields, very little is known in the context of prolate spheroids (cigar-shaped particles) or cylindrical particles. An understanding of acoustic manipulation of fibers at large flow rates is of primary importance.

Early experimental observations in a small-scale flow loop confirmed that the acoustic force could potentially be used to separate/fractionate fibers based on fiber width [Brodeur, 1994]. Consequently, an in-flow divider blade was installed in such a way as to separate highly deflected fibers (coarse fibers) from weakly deflected or undeflected fibers (slender fibers and/or fines). This would lead to at least two output streams: a coarse fiber-enriched stream and a coarse fiber-depleted stream. Literature/patent searches did not reveal evidence of past work

in this area. A patent application was filed by IPST in 1996 and was granted in September 1998.

In a particular series of experiments, rayon fibers of constant width/variable length and constant length/variable width were tested as a function of acoustic intensity and flow rate at 0.05% consistency [Ma, 1995]. Rayon fibers were used as they best simulate wood pulp fibers. Separation efficiency was indirectly determined by measuring the cleanliness efficiency of the weakly deflected fiber output stream, i.e., by analyzing the percentage of fibers remaining in the “clean stream.”

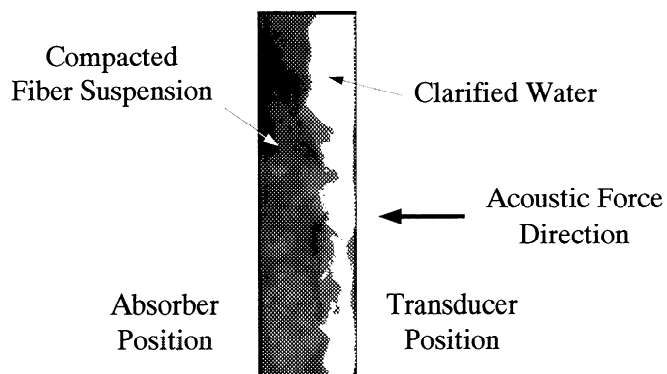


Figure 1-1. Pulp thickening effect [2 cm (horizontal) x 10 cm (vertical)].

Another series of observations was obtained using softwood fibers under zero-flow conditions to study the compactibility of fiber suspensions. Figure 1-1 shows a compacted fiber suspension for an initial pulp consistency of 1% (*white indicates water and black indicates fiber*). The acoustic intensity was 0.3 W/cm^2 . One can easily see a pulp thickening effect. A new test method, acoustic wet fiber compactibility, has been proposed to control the refining process and predict the apparent density of paper [Brodeur and Runge, 1996].

2. ULTRASONIC SEPARATION APPARATUS

The separation apparatus currently used for experiments is shown schematically in Figures 2-1 and 2-2.

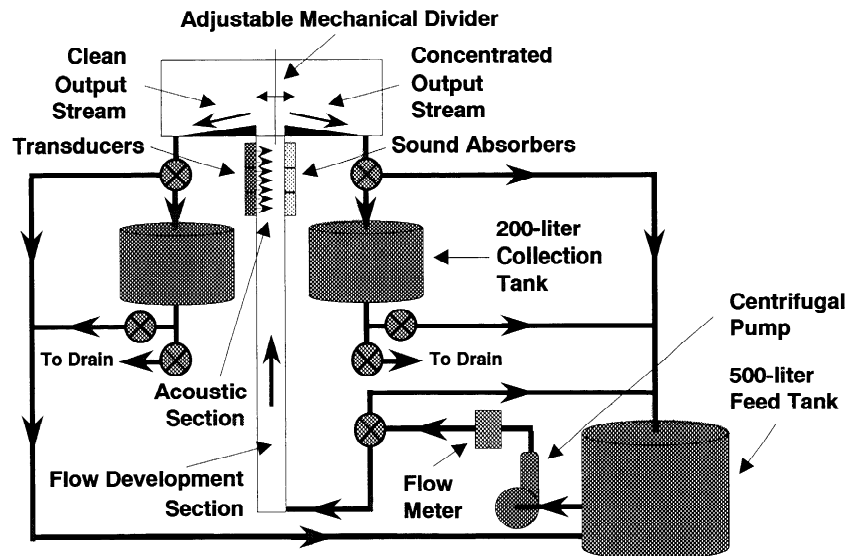


Figure 2-1. Schematic diagram of the flow system for clarification experiments.

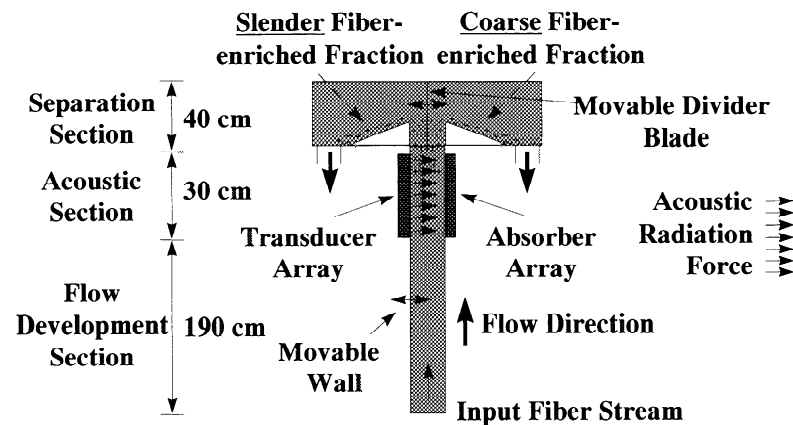


Figure 2-2. Schematic diagram of the laboratory prototype AST system (*drawing not to scale*). Separation using a traveling wave field (unidirectional) is shown.

Briefly, the flow cell consists of a 1.9-meter flow development section, an acoustic section containing three 5 x 10-cm piezoelectric transducers above it, and is topped by an atmospheric pressure mechanical separation system. The flow cell is rectangular in cross section, with one dimension fixed at 5 cm, and the other variable from 5 to 15 cm (in 5-cm steps). A 450-L/min (maximum) variable speed centrifugal pump is used to produce flows in the cell with

Reynolds numbers between 400 and 140,000. A 500-liter stock tank is used to feed the pump, and a pair of 200-liter stock tanks are on the output of the flow cell (one on each side). The cell is typically run in a closed-loop mode, where the stock flows from the 500-liter tank, through the pump, into the flow cell where it is acoustically processed, then out into one of the 200-liter tanks and back to the 500-liter tank (it can also be run in batch mode where the sample is collected only in the 200-liter tanks). Samples are usually taken from the 200-liter tanks while the cell is running in closed-loop mode. A mechanical flow straightener was added to the 1.9-meter flow development section to solve some problems with nonuniform flow when using the maximum wall spacing of 15 cm.

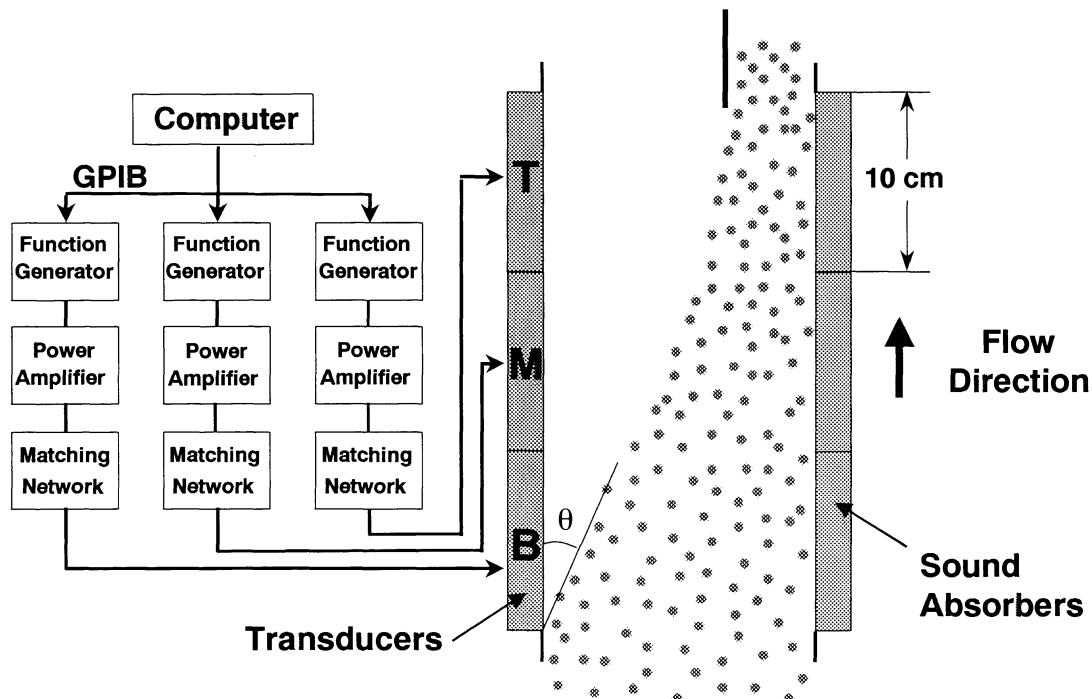


Figure 2-3. Schematic diagram of computer-controlled electrical/acoustical system and close-up of clarification process. T, M, and B refer to Top, Middle, and Bottom ultrasonic transducers, respectively. Flocs are deflected toward the absorbers by an angle θ as they move upward and interact with the ultrasonic field.

Figure 2-3 shows the electrical setup for the acoustic cell. Three separate channels are used, one for each transducer, to provide flexibility in how the system is run. A computer controls three function generators via a GPIB network. These function generators can be phase locked so that the waves are synchronized. The output from the function generators is fed into three power amplifiers, which boost the signal strength to the amplitude necessary to drive the transducers. Various amplifiers with powers up to 1500 watts and bandwidths from 20 kHz to 10 MHz are used. As the output from the power amplifiers is at 50 ohms and the transducers have a much larger input

impedance, a set of matching networks is used to perform the transition. Inline power meters are positioned between the matching networks and transducers to provide closed-loop control of the power going to the transducers.

A picture of the transducers is shown in Figure 2-4. Transducers of three different frequencies are currently used in the flow cell: 1.5 MHz, 150 kHz, and 60 kHz. All are 5 x 10 cm in shape and are easily interchangeable. The transducers are designed to handle temperatures up to 100°C.

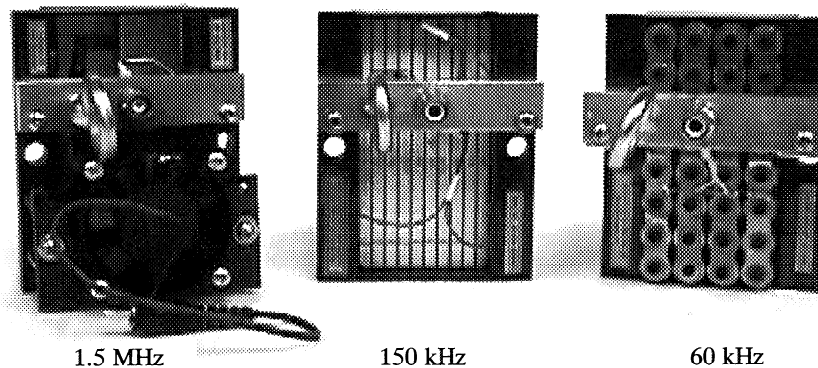


Figure 2-4. Transducers used in flow cell, 1.5 MHz (left), 150 kHz (center) and 60 kHz (right).

Heating in the transducers and matching networks is caused by inefficient power conversion. In order to determine where electrical power is being lost, an oscilloscope with high frequency current and voltage probes is used to measure power along the electrical path from the wall outlet to the transducer as shown in Figure 2-5. Measurements are done between the wall outlet and the power amplifier (amount of power the amplifier consumes), between the power amplifier and the matching network (amount of power output by the amplifier), and between the matching network and the transducer (power delivered to the transducer).

Electrical-to-acoustic efficiency of the transducers is measured using an energy balance method, as shown in Figure 2-6. An oversized absorber is hung underwater from a balance. The transducer to be evaluated is rigidly supported above the absorber. When power is applied to the transducer, the radiation pressure is transmitted to the absorber and read on the balance. A calibration factor of 6.8 g per watt of acoustic power is used. An optional anti-streaming membrane can be inserted between the transducer and absorber to eliminate streaming effects.

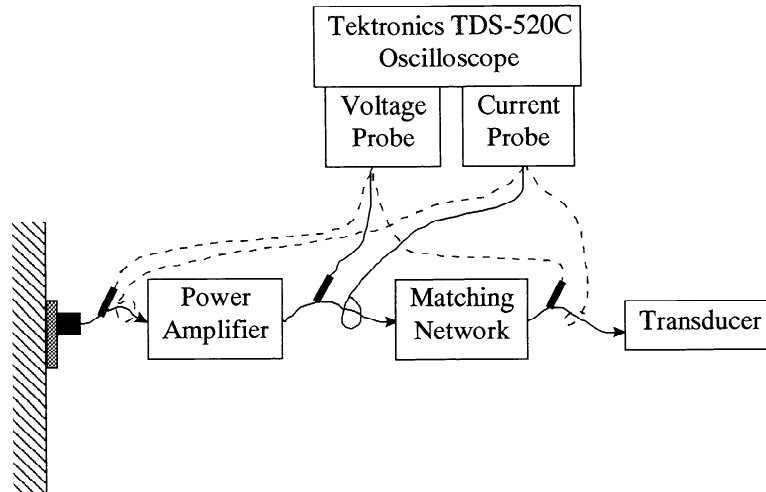
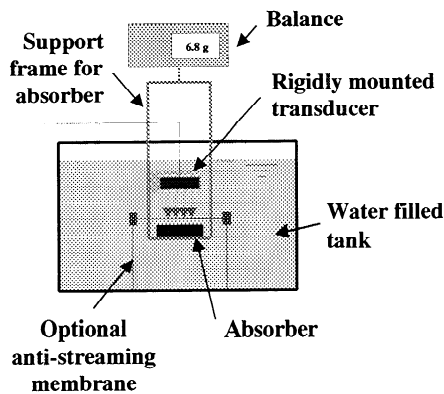
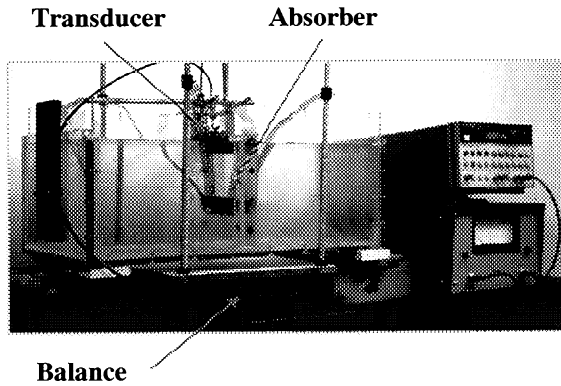


Figure 2-5. Measurement of electrical power usage from wall to transducer using new oscilloscope and high frequency probes. Oscilloscope is shown measuring power between Power Amplifier and Matching Network.



(a) Conceptual schematic showing transducer, absorber, balance, and water tank



(b) Picture of actual setup

Figure 2-6. Energy balance method for determining transducer efficiency.

3. THEORETICAL/MODELING RESEARCH PROGRAM

The acoustic field in the medium can be described by the following parameters: pressure p (local disturbance of the medium), density ρ , and velocity v of the fluid particles. The acoustic field carries the energy density E_o in the propagation path. The time-averaged total energy density \bar{E}_o can be written by $\rho_{max}^2 / 2\rho_o c^2$ where ρ_{max} is the maximum value of the pressure for one cycle, ρ_o is the density of the medium under the equilibrium, and c is the sound velocity in the medium.

We consider the transducer as the source of the sound wave. However, in the real situation, the ultrasonic beam radiated by the extended source should be considered equivalent to a large number of point sources. Therefore, unlike the exponential decay of the intensity, we would see the peaks and dips in the pressure for a distance from the transducer due to diffraction. It was reported by Beissner [1987] that a field distribution of the focused beam from a piston is not the same as a plane wave. We have not taken this into consideration; instead, we have treated the source simply as a traveling wave. Any discrepancy between the experimental and theoretical results may come from this simplified assumption.

Acoustic Radiation Pressure

The acoustic radiation pressure (ARP) is the time average of the pressure acting on an object in a sound field. In a linear approximation, the force is periodic and when averaged over time, it sums to zero. The radiation pressure comes from using higher order terms. The radiation force becomes significant only when the amplitude is high enough. Using hydrodynamics, the acoustic radiation pressure is equal to the time average momentum flux across the surface of the object. The equation of state accompanying the hydrodynamic equation has the form

$$p' = \rho c^2 + \frac{1}{2} \left(\frac{\partial}{\partial \rho} c^2 \right) \rho'^2 \quad (3-1)$$

where p' and ρ' are the second order variations of the pressure and density respectively, and c is the sound velocity.

ARP Acting on a Single Particle

Various theoretical results of the force acting on an object of a particular geometry are available. Forces acting on a sphere, a disk, and a cylinder are given by King [1934] (sphere), King [1935] (disk), Awatani [1953 and 1955] (cylinder), Zhuk [1986] (cylinder), and Hasegawa [1988] (cylinder). All derivations above are done by treating the medium as ideal. As a first approximation, a wood pulp fiber can be considered as a rigid cylinder.

A review of the different derivations for the acoustic force applied to rigid and elastic cylinders was undertaken. Derivations by Awatani [1955] and Zhuk [1986] (infinitely long rigid cylinder in traveling wave field with axis perpendicular to the sound field) and Hasegawa et al. [1988] (infinitely long elastic cylinder in traveling wave field with axis perpendicular to the sound field, including internal reflections and scattering) are compared in Figure 3-1.

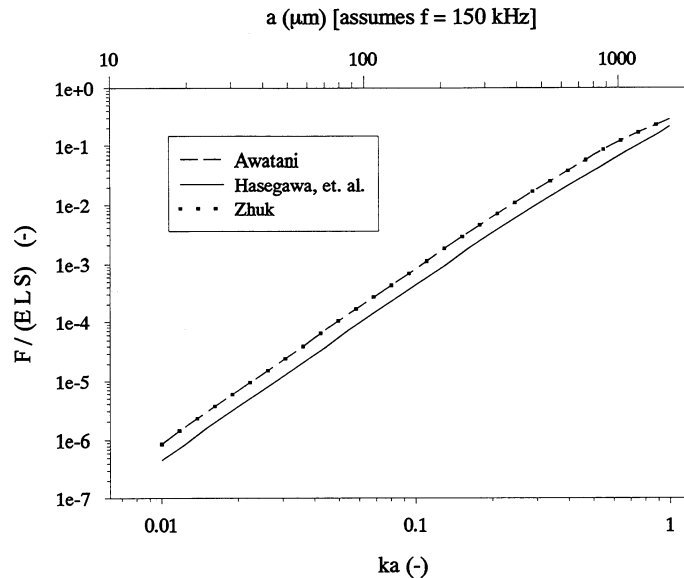


Figure 3-1. Plot of dimensionless acoustic radiation force vs. ka (also dimensionless) for the case of a traveling wave field as obtained using equations from Awatani [1955], Hasegawa [1969] and Zhuk [1986]. Upper axis is cylinder radius, a , in mm for a 150-kHz acoustic wave in water. Awatani and Zhuk give nearly identical results, hence the overlap.

In Figure 3-1, the dimensionless force (force per unit length L , per unit surface area S , and per unit acoustic energy density E) is plotted as a function of the parameter ka where k is the wave number and a is the cylinder radius. Assuming water as the suspending medium with a density of 1000 kg/m^3 and 150 kHz as the wave frequency, k becomes 628 m^{-1} . It can be seen that in the range of ka of interest to us ($ka = 0.01$ to 0.1), the derivations agree very well with each other. Also, increasing ka will cause an increase in the dimensionless force. Increasing ka one order of magnitude (say from 0.01 to 0.1) will cause an increase in the dimensionless force of approximately 2.5 orders of magnitude. This could also be interpreted as: an increase of one order of magnitude in ka will reduce the acoustic energy density (E) and, therefore, electrical power, by approximately 2.5 orders of magnitude. Hence, it appears that working in a ka range of 0.01 is not as efficient as working closer to a ka of 1 . The value of ka can be increased in two ways: an increase in the cylinder radius (a), or an increase in the acoustic wave frequency (increase in k). As the fiber dimensions are already determined (a), it would be preferable to increase the transducer frequency (k).

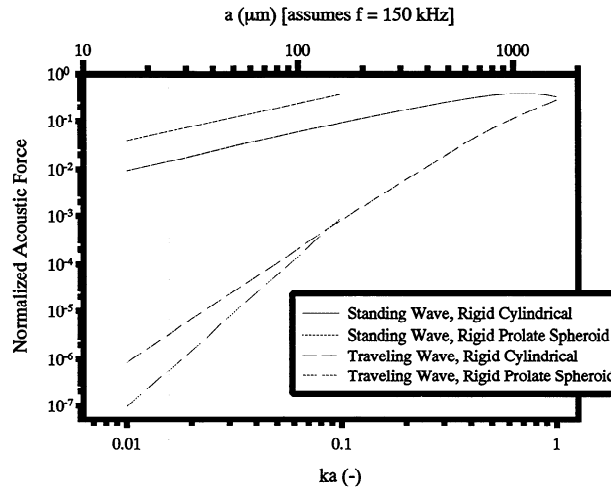


Figure 3-2. Comparison between acoustic radiation force for traveling and standing wave field for both a rigid sphere and a rigid cylinder, from Awatani [1955]. The acoustic force for a standing wave field is significantly larger in both cases.

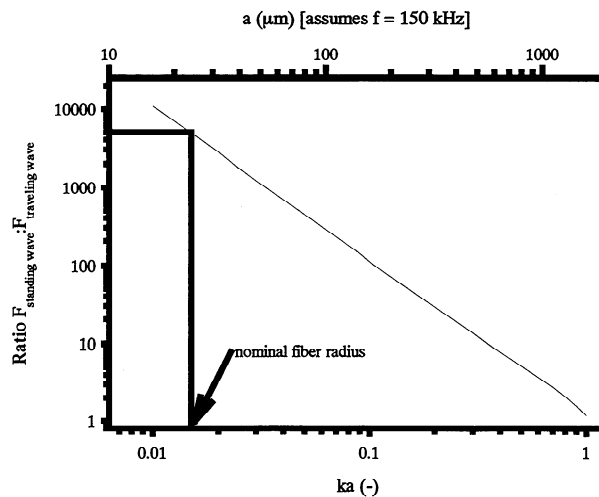


Figure 3-3. Ratio of Standing Wave acoustic force to Traveling Wave acoustic force, based on Awatani [1955]. For a fiber with a 25- μm radius at 150 kHz, the ratio is approximately 5000:1.

Figure 3-2 shows a comparison between the forces of a traveling wave and a standing wave field for both a rigid sphere and a rigid cylinder, as derived by Awatani [1955]. For a nominal fiber of 25- μm radius in water exposed to a 150-kHz sound field ($ka = 0.0157$), a standing wave will produce a force approximately 5000 times greater than the traveling wave. Figure 3-3 plots the ratio between the standing wave force and the traveling wave force. As ka approaches 1, the traveling wave and standing wave forces converge. For low

values of ka , the standing wave will produce a significantly stronger force than the traveling wave.

ARP Acting on an Acoustic Absorber

The acoustic radiation pressure acting on an absorbing object can also be used to deduce the total acoustic power. When an ultrasonic beam travels through a liquid medium and an absorbing material intercepts the entire beam, the Langevin radiation pressure can be used to evaluate the total acoustic power [Rooney and Nyborg, 1972]. The experimental setup for total power measurements was previously described in Section 2 and the apparatus was shown in Figure 2-6.

From the relationship

$$F = \frac{W}{c} \quad (3-2)$$

where F is the force acting on the absorber (it can be divided by the gravitational constant g to get an equivalent mass), W is the acoustic power, and c is the sound velocity through the medium. As the power goes up, we will expect the force measured to go up proportionally. We, therefore, determine the acoustic pressure from the force F . The acoustic radiation pressure can also be related to the energy density in a perfect absorbing medium [Hamilton and Blackstock, 1998]. The force acting on an absorber in terms of the energy density of the sound wave, i.e., E_o , is

$$F = 2E_o \quad (3-3)$$

This can be utilized for measuring the acoustic field intensity. The absorber generally spans the entire cross section of the field, and, therefore, the radiation force acting on the absorber is independent of the absorber dimensions.

Measurement of Local ARP and Total Power Associated with ARP

A hydrophone is used to measure the local acoustic radiation pressure. To measure the total power, we set up an imaginary plane parallel to the transducer. We then divide this plane into small segments (i.e., a grid) and measure the local pressure in each of the small segments. The total power associated with ARP (W) is then obtained by

$$W = \sum_{i=1}^N \frac{P_{rms}^2}{\rho_o c} dA_i \quad (3-4)$$

where P_{rms} is the RMS value of the reading of the pressure, dA is the area of a small segment, and the total number of segments is N . The upper bound of the total power associated with ARP is limited to the electric power. We expect a linear relationship between the total acoustic power and the electric power within a reasonable range. However, at high electrical powers, nonlinear effects such as cavitation and acoustic streaming may occur.

Acoustic Streaming

It has been conjectured that there are other phenomena along with the acoustic radiation pressure such as acoustic streaming (the flow motion of the fluid due to gradual absorption of the sound field), cavitation (bubble activity in a high intensity sound field), and the interrelationships of all of the above.

Calculation of Acoustic Streaming Based on Nyborg [1965]

Theory of acoustic streaming is based on hydrodynamic equations for viscous compressible fluid. We only consider the motion from a traveling wave in an unbounded medium here. When an ultrasound beam travels in any bounded medium, the presence of the boundaries may affect the streaming. Nyborg [1965] gives a comprehensive literature survey on acoustic streaming. Streaming is reported to occur due to the attenuated effect of the wave as it travels through the medium. His calculation was based on the approximation of the hydrodynamic equations up to the second order and did not consider nonlinear propagation.

The first-order velocity of the traveling wave, u_1 , is written as

$$u_1 = u_{d0} e^{-(\alpha + ik)x} \quad (3-5)$$

where u_{d0} is the unattenuated acoustic velocity, α is the attenuation coefficient and k is the wave number. The time-averaged force per unit volume responsible for the flow is written as

$$F_x = \alpha \rho u_{d0}^2 e^{-2\alpha x} \quad (3-6)$$

and can be rewritten using the power W ,

$$F_x = \frac{2\alpha W}{\pi d^2 c} \quad (3-7)$$

where d is the dimension of the transducer. The velocity u_2 for one dimensional axial streaming at position x is given by

$$u_2 = -\frac{\Delta W}{4\pi\mu cd} \quad (3-8)$$

$$\Delta W = 2\alpha W(x)dx \quad (3-9)$$

where ΔW is the energy lost in the acoustic wave while travelling a distance dx . The flow direction inside the acoustic beam will be in the positive direction. Conservation of mass requires that there be a flow in the negative direction outside of the acoustic beam. We can obtain the distance from the acoustic beam at which the flow changes direction from positive to negative. This depends on the ratio of the radius of the source and that of the bounding medium.

Calculation of Acoustic Streaming Based on Eckart [1948]

According to Eckart [1948], three types of streaming are known. The first type is streaming in a viscous boundary layer near obstacles, and the second type is streaming outside the boundary. Both of these have vortex structures. The third type of streaming occurs in a free, nonuniform sound field where the streaming scale is larger than the acoustic wavelength. Eckart [1948] obtained a stationary solution for a long acoustic beam with a radius of r . The typical streaming velocity is

$$U = \frac{b}{4\eta c} v_o^2 (kr)^2 \quad (3-10)$$

where $b = 4/3 \eta + \eta'$ (where η is the shear viscosity and η' is the bulk viscosity), k is the wave number, and v_o is the acoustic velocity. This equation shows that the flow motion arises due to both types of viscosity (shear and bulk).

Cavitation

No systematic theories have been developed describing what effect cavitation bubbles have on solid objects under ultrasonics since it would be a very complicated interaction involving three-phase media. The bubbles are known to be created when the acoustic pressure amplitude is high enough (so that the time varying amplitude creates pockets of negative pressure) to break the tensile strength of the liquid. Under this condition, the bubbles grow due to the surrounding dissolved gas. This behavior yields interesting phenomena, such as sonoluminescence, cavitation erosion, chemical reactions, etc., [Apfel, 1989; Neppiras, 1980]. The effect of cavitation on the acoustic radiation pressure is not well understood. We currently rely on experimental observations of the phenomena. Usually the sound intensity decreases when the acoustic energy is used to create bubbles in a cavitation zone. Therefore, we would expect to

observe Eckart-type fluid motion. Some interesting results by Prosperetti [1984] show that the insertion of air bubbles into the medium under ultrasonics can significantly increase the streaming effect. The exact mechanism of this phenomenon is not well understood. Analytical results on cavitation bubbles are currently limited to the study of a single bubble, while in a realistic situation, many bubbles are found in each stream.

Total Acoustic Force

The total force acting on any object in an acoustic field is the sum of the force due to ARP, streaming, and cavitation bubbles. At this time, the force due only to ARP and streaming is considered on two different objects (i.e., cavitation is neglected).

Total Force Acting on an Absorber

If we assume that the sum of the energy density of the sound field and the flow kinetic energy is constant, the average force acting on an absorber can be written as

$$F = F_I + F_s = \frac{W}{c} \quad (3-11)$$

where F_I is the force due to the acoustic radiation pressure, F_s is the force due to the streaming, and W is the equivalent power of the sound energy. We do not include the energy which may be lost due to the formation of cavitation bubbles. Our result from the balance experiment (Section 2) shows discrepancies at different frequencies, as we vary the intensity of the power. The reason is probably due to cavitation bubble losses in the medium.

Total Force Acting on a Fiber Mat

The force acting on a porous medium under ultrasonics would be very hard to calculate since the frequency dependence of scattered sound waves can generally depend on the internal structures of the porous medium. Also, since the shapes are random, a closed-form solution to the acoustic radiation force is difficult to obtain. We can treat the fiber mat as an absorbing object and consider the force acting on the surface. We can use Eq. 3-11 to get the upper bounds of the force. Based on observations, the total force acting on the fiber mat is larger than this estimate, possibly due to the strong water motion which is intensified due to the bubble activities. A speculation would be that when the bubbles collapse, they induce fluid motion which is similar to Eckart [1984] type streaming. This water motion can even be comprised of layers of turbulent jets. For a simplified picture, if the flow velocity is v_f , the additional force acting on the surface of the mat will be

$$F_{add} = \frac{1}{2} C_d v_f^2 \rho A \quad (3-12)$$

where C_d is the drag coefficient for the surface of the mat and A is the area of the porous medium.

4. APPLICATION TO WHITEWATER CLARIFICATION

Work performed in collaboration with Prof. Yulin Deng and Dr. Zegui Yan from IPST.

In mills optimizing raw material usage and closing up water systems due to environmental regulations, efficient removal techniques are needed to remove accumulating solid suspensions. As a novel approach to solids removal, an in-line dual chemical flocculation/ultrasonic method to clarify a whitewater stream was investigated. The method first considers the use of flocculants to create larger size particles or flocs. Then, an ultrasonic field normal to the flow direction of the whitewater stream is applied to the flocs in such a way as to obtain two output streams: a clarified water stream and a stream of concentrated flocs. A laboratory in-line ultrasonic separation system was used to demonstrate the clarification concept. Different flocculants were tested and experiments at different flow rates, ultrasonic frequencies, and acoustic intensity levels were made. Best results were obtained using the neutral flocculant system PEO/PFR. Test conditions were determined to achieve a clean stream with less than 100 ppm of solids. Also, clarification efficiency close to 80% of the maximum possible clarification efficiency in the experimental setup was obtained. An economic analysis was performed on a theoretical 22,750 L-per-minute (6000 gpm) ultrasonic whitewater clarifier. It was compared to a conventional dissolved air flotation (DAF) unit of the same size. The ultrasonic clarifier is estimated to cost 66% less than the DAF to purchase and install and will cost 35% less to operate.

Experimental Approach

The experimental methodology was two-fold. First, an optimization study of flocculants suitable for clarification experiments was undertaken. Then, a series of clarification experiments was performed using an experimental in-line ultrasonic separation system.

Flocculant Optimization Study

Whitewater is the filtrate from the forming fabrics of paper machines. Since the chemistry of whitewater is not well documented and varies from mill to mill, three whitewater samples and different flocculants were considered in the study.

Table I briefly describes whitewater samples. As seen in Table II, flocculants included an anionic polyacrylamide (APAM), two cationic polyacrylamides with different charge densities (CPAM1 and CPAM2), and a dual flocculant of poly(ethylene oxide) (PEO) with a water-soluble phenolic formaldehyde resin (PFR). These flocculants are widely used as flocculation and retention aids in the paper industry. Charge density was determined by colloidal titration.

Table I Whitewater samples used in the study

Whitewater Sample	Description	Particle size distribution (%<75 μm)	Consistency (%)	Colloid Titration (meq/L)
W1	From 24% OCC and 76% unbleached kraft softwood	97%	0.054	-0.42
W2	From 100% OCC	78%	0.072	-0.30
W3	From 100% ONP (Cloudy whitewater)	72%	0.036	-0.28

Table II Flocculants used in the study

Symbol	Flocculant	Chemical Composition	Charge Density (meq/g)	Supplier
APAM	Percol 172	Anionic PAM	-0.315	Allied Colloids
CPAM1	Percol 175	Cationic PAM	1.0	Allied Colloids
CPAM2	7523	Cationic PAM	0.163	Nalco
PEO	PEO*	Poly(ethylene oxide)	0	Aldrich

*One part of PEO is used with two parts of phenolic formaldehyde resin (PFR, from Borden Chemicals) in flocculation.

Particle size distribution was analyzed using a Malvern System 2600 Laser Particle Sizer. This apparatus was also used to evaluate flocculation efficiency. Since the solids in whitewater are mostly fines and fillers with particle size less than 75 μm , the flocculation efficiency could be evaluated from the amount of particles less than 75 μm in the whitewater before and after flocculation. The number 75 μm was chosen based on the fact that fines can go through a 200-mesh screen which has holes of 75 μm . A typical flocculation test was as follows: a specific amount of flocculant solution was added to 600 mL of whitewater with mechanical stirring at 500 rpm for 10 seconds. The solution was then added to the particle analyzer sample cell, gently stirred, and recirculated at a velocity of 0.6 m/s; finally, the particle size distribution was analyzed as a function of circulation time.

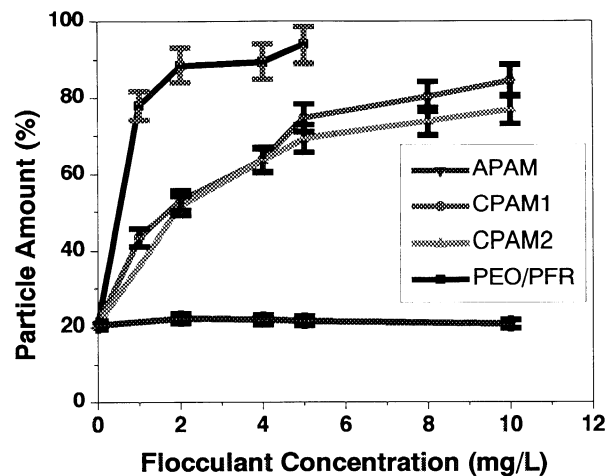


Figure 4-1. Amount of particles (%) greater than 75 μm in whitewater W3 as a function of flocculant dosage for the flocculants listed in Table II. The circulation time is one minute in the particle sizer.

Figure 4-1 shows the amount of particles larger than 75 μm for different flocculants using whitewater W3. One observes that the anionic polymer APAM is not effective for whitewater flocculation, while cationic polymers CPAM1 and CPAM2, and neutral dual flocculants PEO/PFR are all very effective. It is known that solid suspensions in whitewater are mainly anionic charged. The electric repulsion between the solid suspensions and the anionic APAM will reduce the adsorption ability of this flocculant, thus preventing satisfactory flocculation. On the other hand, the adsorption of cationic CPAM1 and CPAM2 is facilitated by electrostatic attraction, thus increasing the flocculation efficiency. However, the high cationic demand of the whitewater makes CPAM1 and CPAM2 inefficient at low dosages (< 10 mg/L). The mechanism of PEO/PFR flocculation is different from that of cationic flocculation. A complex reaction between PEO and PFR is involved in the flocculation [Lindstrom, 1984]. Because PEO is a nonionic polymer, the anionic nature of the suspensions does not affect the flocculation efficiency of PEO/PFR. This flocculant system also shows the best flocculation efficiency at low dosages (2 mg/L PEO:4 mg/L PFR).

The stability of the flocculates formed by the different flocculants (except APAM) is shown in Fig. 4-2 for whitewater W3. It is observed that the flocs formed by CPAM1 and PEO/PFR slowly break up as a function of time while the flocs formed by CPAM2 cannot resist the shear force and quickly break up. The flocculation of different whitewaters using the PEO/PFR system was studied and results are shown in Fig. 4-3. No obvious effect of whitewater on the flocculation was observed.

Results from the flocculant optimization study led to the conclusion that the PEO/PFR system should perform well during clarification experiments at relatively low dosages. This flocculant system was utilized in all clarification experiments.

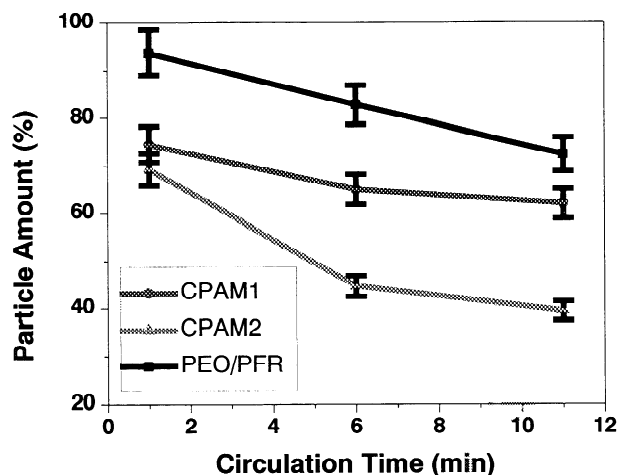


Figure 4-2. Amount of particles (%) greater than 75 μm as a function of circulation time for whitewater W3. The flocculant dosage and circulation velocity are 5 mg/L and 0.6 m/s, respectively. Circulation was done in the particle sizer.

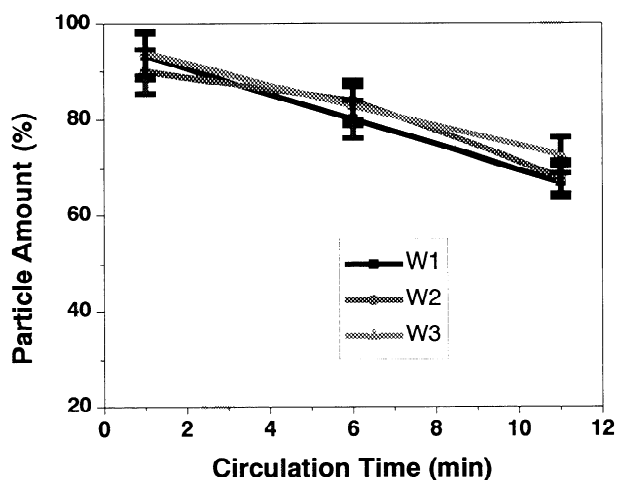


Figure 4-3. Amount of particles (%) greater than 75 μm as a function of circulation time in the particle sizer for whitenwaters W1, W2, and W3 (see Table I) using the PEO/PFR flocculant system. The dosage is 5 mg/L:10 mg/L.

Feasibility Study

Preliminary clarification experiments were conducted at the 5-cm transducer-absorber separation distance. Deflection of flocculated whitewater was easily observed. However, the relatively small separation distance did not facilitate satisfactory sampling of clean and concentrated streams. For this reason, it was decided to increase the separation distance to 15 cm. Also, the mechanical divider was set constant at the middle (50:50) position.

Table III summarizes the experimental design for the demonstration of whitewater clarification. All experiments involved varying the acoustic intensity (acoustic power per unit transducer area) at constant transducer frequency and constant flow velocity. Three transducer frequencies were investigated: 60 kHz, 150 kHz, and 1.5 MHz. The flow velocity was varied between 0.1 and 0.4 m/s in increments of 0.1 m/s. This velocity range corresponds to flow rates of 45 to 180 L/min and Reynolds numbers of approximately 7500 to 30,000 at room temperature (turbulent flow regime conditions). Equipment limitations did not allow testing at acoustic intensities higher than 3 W/cm² when using 1.5 MHz transducers. The PEO/PFR flocculant dosage was generally set to 5 mg/L:10 mg/L. Additional runs at 1.5 MHz were performed at 2 mg/L:4 mg/L to investigate using the minimum dosage of flocculants.

Table III Experimental Design

Transducer Frequency	PEO/PFR Dosage	Flow Velocity (m/s)	Acoustic Intensity (W/cm ²)					
			0	1	2	3	6	10
60 kHz	5 mg/L:10 mg/L	0.1	X	X	X	X		
150 kHz	5 mg/L:10 mg/L	0.1	X	X	X	X	X	X
		0.2	X	X	X	X	X	X
		0.3	X	X	X	X	X	X
		0.4	X	X	X	X	X	X
1.5 MHz	5 mg/L:10 mg/L	0.1	X	X	X	X		
		0.2	X	X	X	X		
		0.3	X	X	X	X		
		0.4	X	X	X	X		
1.5 MHz	2 mg/L:4 mg/L	0.1	X	X	X	X		
		0.2	X	X	X	X		

A typical run involved approximately 180 liters of fresh whitewater in the feed tank. PFR was first added to the whitewater. Once the flow velocity and acoustic intensity were adjusted according to the experimental design, PEO was added, thus triggering flocculation. It is important to mention that the need to

recirculate flocculated whitewater (batch mode operation) necessitated the use of flocculants at a higher dosage than would be required under a constant supply of fresh whitewater to compensate for the rapid (and otherwise desirable) degradation of flocculants.

An analog camera connected to a SVHS video recorder was used to record the deflection of flocculated whitewater in the acoustic section. A fiber optic backlight was used to create uniform lighting conditions. Analysis of the video recordings consisted of determining the initial deflection angle θ as depicted in Fig. 2-3. Three seconds of video (at 30 frames/sec) were digitized and averaged together frame by frame. After the operator identified the initial deflection line, the computer calculated the angle. Five successive three-second segments were analyzed for each recording. Average and standard deviation were then computed. As a first approximation, the initial deflection angle θ can be related to the flow velocity U and the floc migration velocity v (normal to the flow velocity) using the following equation:

$$\tan \theta = \frac{v}{U} \quad (4-1)$$

One should note that velocity gradients across the flow cell are neglected here. Assuming that v is constant at constant acoustic intensity, Eq. 4-1 can be rearranged as

$$\frac{1}{\tan \theta} = \left(\frac{1}{v}\right)U \quad (4-2)$$

where $1/v$ is the slope of the linear relationship between $1/\tan \theta$ and U . Eq. 4-2 can be used to determine v .

Simultaneous sampling of clean and concentrated streams was achieved using 10-liter buckets. Only 500 mL of whitewater was kept for consistency measurements (TAPPI Test Method T 240) and the leftover liquid was put back in the feed tank to minimize depletion of whitewater for subsequent runs. The flocculation effect degraded after a certain number of runs (can be seen visually), and additional flocculants were added or the whitewater was simply replaced with fresh whitewater.

Finally, equations describing the clean stream solids removal efficiency and clarification efficiency as a function of the divider blade position and feed and clean stream consistencies were derived (see Appendix A):

$$\% \text{ Clean Stream Removal Eff.} = 100\% \left(1 - \frac{C_{\text{clean}}}{C_{\text{feed}}} \right) \quad (4-3)$$

$$\% \text{ Clarification Eff.} = 100\% \left(\frac{\ell_t}{\ell} \right) \left[\frac{C_{\text{feed}} - C_{\text{clean}}}{C_{\text{feed}} \left(1 - \frac{C_{\text{feed}}}{100\%} \right)} \right] \quad (4-4)$$

where C_{feed} and C_{clean} are the percent consistencies of the input feed stream and output clean stream respectively, and ℓ and ℓ_t are the transducer-absorber separation distance and position of the divider blade from the transducer side, respectively. In order to achieve 100% clarification in Eq. 4-4, all solids must be completely separated from the water, and the divider blade position must be such that only solids are in the concentrated output stream and only water is in the clean output stream.

Results and Discussion

Several clarification experiments were conducted using whitewater and the flocculant system PEO/PFR. In general, it was found that experiments performed using the 60-kHz transducers were not satisfactory. This may be attributed to a lower threshold for cavitation at this frequency when compared to observations at 150 kHz and 1.5 MHz [Jong, 1999]. For a given amount of acoustic power coming from the 60-kHz transducer, a larger percentage of power is put into cavitation at this frequency than at higher frequencies, and, hence, less power is available to deflect the fibers. Therefore, results obtained at 60 kHz are not reported.

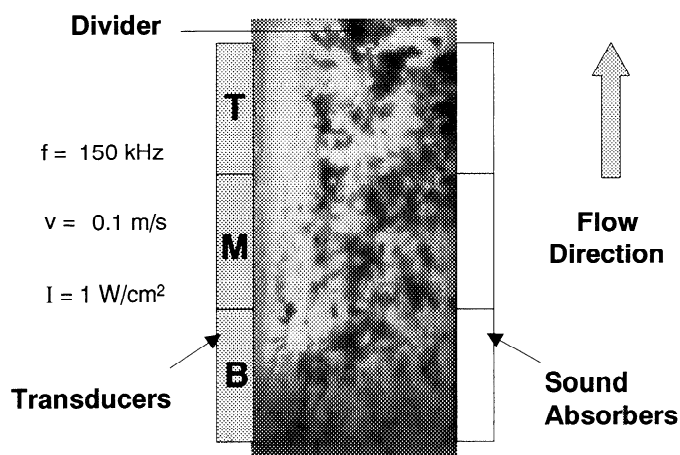


Figure 4-4. Whitewater clarification using three 150-kHz transducers. The PEO/PFR level is 5 mg/L:10 mg/L.

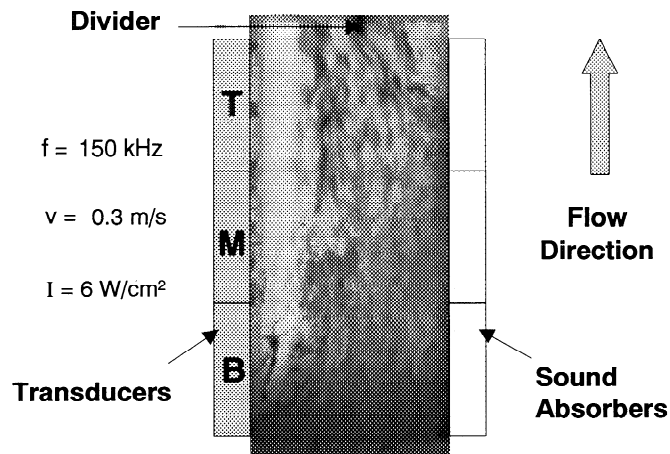


Figure 4-5. Whitewater clarification using three transducers operating at 150 kHz. The PEO/PFR level is 5 mg/L:10 mg/L.

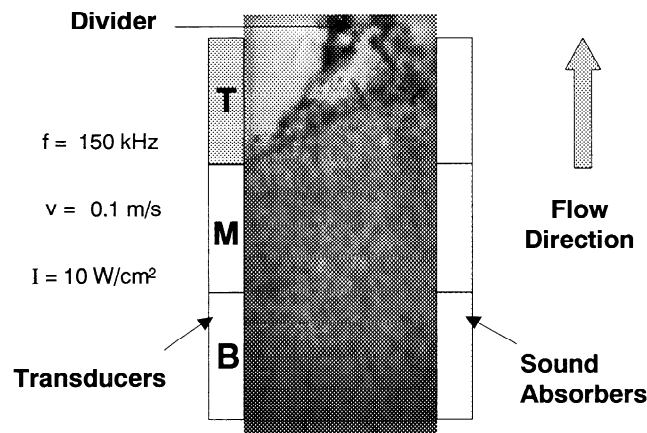


Figure 4-6. Observation of clarification using only the top transducer. The transducer frequency is 150 kHz. The PEO/PFR level is 5 mg/L:10 mg/L.

Selected frames from the video recordings of the clarification effect at 150 kHz are shown in Figs. 4-4 to 4-6. In these figures, flocculated whitewater (dark area) is deflected toward the right (absorbers); white areas represent clarified water. Comparison of Figs. 4-4 and 4-5 shows that a 0.1 m/s flow velocity and a 1 W/cm² acoustic intensity produce a similar deflection effect as a flow velocity of 0.3 m/s and an acoustic intensity of 6 W/cm². While these observations are qualitative and subject to experimental error, they indicate that a more intense ultrasonic field is generally required to counterbalance a larger flow velocity. In both cases, deflection of flocs occurs very early in the acoustic section (bottom

transducer position). Although not clearly visible in Figs. 4-4 and 4-5, the deflection effect past the initial stage is somewhat mitigated by the presence of undesirable back flows at the walls (edge effects). Possible causes include non-uniformity of the ultrasonic field, undesirable reflections of the ultrasonic field in the acoustic section, and the rectangular cross section of the flow cell. Neither a detailed analysis of the back flows nor any attempt to eliminate them was made. Figure 4-6, which involves the excitation of the top transducer only, is interesting because it indicates that an intensity of 10 W/cm^2 at 0.1 m/s produces a significantly larger deflection than seen in Fig. 4-4. However, the intensity level is such that the absorber is not very efficient in preventing reflection of the ultrasonic field transmitted through the whitewater. The end result is an apparent mirror deflection effect located in between transducers and absorbers. Optimization of this effect by substituting the absorber by a reflective surface (or a transducer) might provide an alternative approach to the clarification process by collecting flocs from the center of the acoustic section.

Just as excessive cavitation appears to be detrimental to the deflection effect at low frequency (60 kHz), the reduced level of cavitation at 1.5 MHz appears to be counter-productive as well. Because the ratio of the density of air bubbles to water is much smaller than the ratio of the density of flocs to water, air bubbles are easier to manipulate using the ultrasonic field than flocs are. It is possible that cavitation bubbles forming on the surface of the flocs significantly enhance their deflection. Hence, the proper balance between the amount of acoustic power going into bubble formation and the amount available for deflection may lead to optimal deflection of the flocs. At 1.5 MHz, the balance is tipped away from bubble formation, preventing efficient deflection of the flocs. One can hypothesize that the cavitation level at 150 kHz is such that the number and/or size of air bubbles offers a superior set of conditions for floc deflection. Whether or not 150 kHz is an optimized frequency for whitewater clarification remains to be determined through observations at other frequencies between 60 kHz and 1.5 MHz.

The initial deflection angle for all test conditions at 150 kHz and 1.5 MHz was determined according to the method previously described. In agreement with Eq. 4-2, results expressed as $1/\tan \theta$ versus U are presented in Figs. 4-7 and 4-8. Even though some results appear problematic (see below), an overall inspection supports linear trends. At constant acoustic intensity, $1/\tan \theta$ linearly increases when the flow velocity increases. Also, at constant flow velocity, $1/\tan \theta$ decreases when the acoustic intensity increases. Overlapping of the 150 kHz measurements at 3, 6, and 10 W/cm^2 (Fig. 4-7) suggests that there is a plateau for the acoustic intensity. In other words, too much intensity does not improve floc deflection and can be considered as wasted energy. Results gathered at 1.5 MHz (Fig. 4-8) also show linear trends. Since measurements above 3 W/cm^2 are not available, the existence of a plateau at/or above 3 W/cm^2 cannot be

confirmed at 1.5 MHz. Difficulties in getting better quality results can be explained by variations in the flow velocity ($\pm 10\%$), the presence of secondary flows (especially at 150 kHz), degradation of the flocculant during experiments, and variations in flocculation efficiency between experiments.

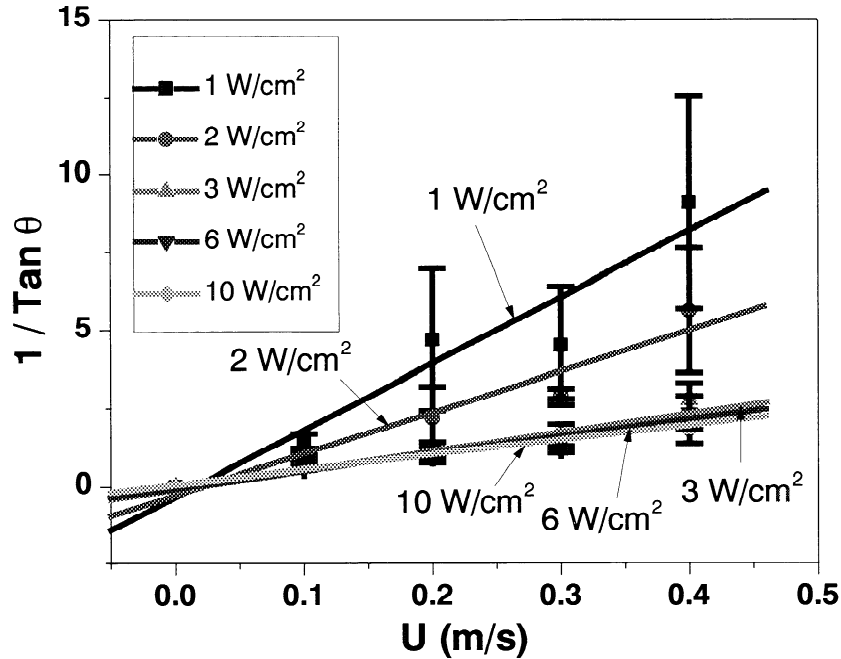


Figure 4-7. Plot of $1/\tan \theta$ vs. U for different acoustic intensity levels at 150 kHz. Linear curve fitting from 0 to 0.4 m/s was used to determine the floc migration velocity v per acoustic intensity level. Results are presented in Fig. 4-9.

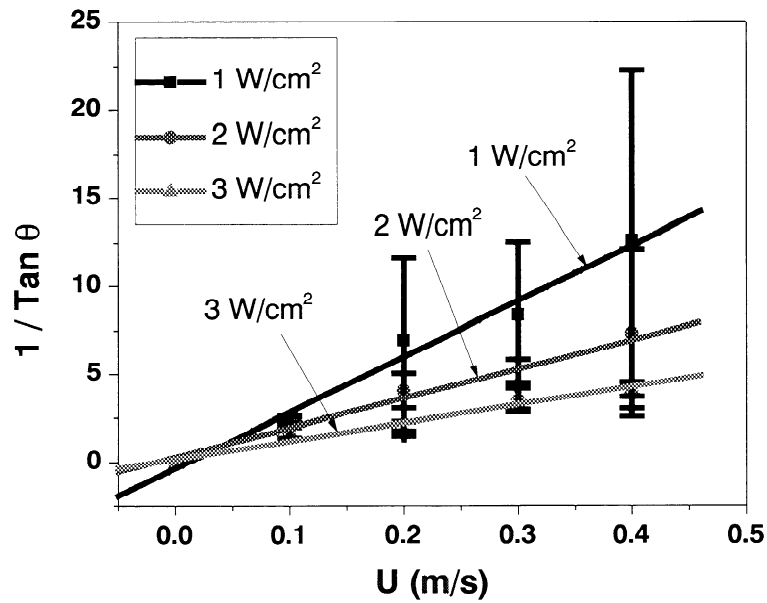


Figure 4-8. Plot of $1/\tan \theta$ vs. U for different acoustic intensity levels at 1.5 MHz. Linear curve fitting from 0 to 0.4 m/s was used to determine the floc migration velocity v per acoustic intensity level. Results are presented in Fig. 4-9.

Linear curve fitting applied to the results shown in Figs. 4-7 and 4-8 was used to determine the floc migration velocity as a function of acoustic intensity. Results are reported in Fig. 4-9. Since a strong linear relationship ($R^2 = 0.997$) is observed at 1.5 MHz, it is likely that there is a linear relationship as well at 150 kHz even though data points are more scattered. Larger velocities at 150 kHz confirm that energy is more efficiently used at this frequency in the initial stage of deflection.

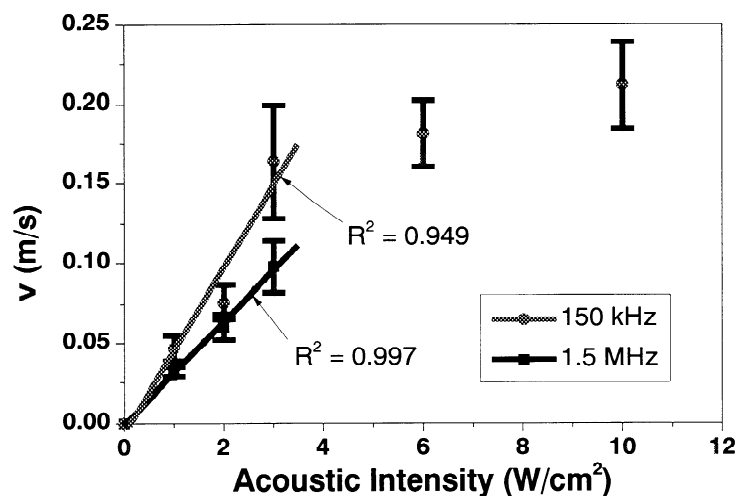


Figure 4-9. Graph of the floc migration velocity versus acoustic intensity for measurements obtained at 150 kHz and 1.5 MHz. Linear curve fitting between 0 and 3 W/cm² was used to relate v and I : slope at 150 kHz: $0.052 \pm 0.008 \left(\frac{m \text{ cm}^2}{s \text{ W}} \right)$; slope at 1.5 MHz: $0.032 \pm 0.001 \left(\frac{m \text{ cm}^2}{s \text{ W}} \right)$.

Economic Assessment

A preliminary economic assessment of the clarification method was conducted. Chemical costs for PEO and PFR are approximately \$5/kg (\$5k/ton) and \$1/kg (\$1k/ton), respectively. This means that the cost associated with using these chemicals at the 5 mg/L:10 mg/L and 2 mg/L:4 mg/L dosages are \$0.035/1000 L (\$0.133/1000 gal) and \$0.014/1000 L (\$0.053/1000 gal.), respectively. Since the need to maintain flocculation for several cycles would not apply for continuous in-line treatment in a mill environment, the use of a lower dosage level is expected, and, hence, anticipated chemical costs should be lower than the above figures.

Initial deflection angle measurements presented in Figs. 4-7 and 4-8 were used to predict the operating cost of a hypothetical whitewater ultrasonic clarification system aimed at increasing the feed stream consistency by a factor of 10. The basis for comparison is a 22,750 L-per-min (6000 gpm) commercial DAF system. Table IV shows capital (including installation cost in the mill) and operation costs for the DAF system and ultrasonic clarifier. It is assumed that the ultrasonic clarifier operates under the following conditions: frequency of 150 kHz, flow velocity of 0.3 m/s, and acoustic intensity of 3 W/cm². Also, the PEO/PFR flocculant dosage is 2 mg/L:4 mg/L. For this scenario, a unit-annualized cost of \$0.025/1000 L (\$0.094/1000 gal) is estimated for the ultrasonic clarifier (including chemical costs). Further reductions in capital and operating costs are expected in the future due to improved efficiency and lower part costs, as well as expected lower chemical demand. Installed capital is based upon 1999 part costs and includes installation.

Table IV Estimated cost for a 22,750 L-per-min (6000 gpm) hypothetical ultrasonic clarification system and commercial dissolved air system

Item	Ultrasonic Clarifier(\$k)	DAF System(\$k)
Capital and Installation Cost	352	1073
<i>Annual Energy Cost for Ultrasonic Equipment</i>	<i>45</i>	<i>0</i>
<i>Annual Energy Cost for Pumping</i>	<i>8</i>	<i>103</i>
<i>Annual Chemical Cost</i>	<i>168</i>	<i>250</i>
Total Annual Operating Cost	221	353

Other Benefits of Ultrasonic Clarification

In addition to the installation and operating cost reductions with the ultrasonic technology, there are several other advantages over a conventional DAF. First, the ultrasonic clarifier will be much smaller in footprint. A 22,750 L-per-min clarifier will require less than 5 square meters (55 square feet) of floor space, compared to the several hundred square meters (several thousand square feet) for a DAF of the same size. Second, because the ultrasonic clarifier is a closed system, no special environmental equipment will need to be installed in conjunction with the clarifier to control emissions because there will be no open surface for emissions to escape. This will become a more important issue as mills proceed to close up their water supplies and contaminants trapped in the water system buildup and look for escape routes.

CONCLUSIONS

This study has reviewed the progress made on development of acoustic separation technology including the large-scale experimental setup and fundamental understanding of the technology. To provide a practical perspective, the findings of a laboratory feasibility study using chemical flocculation in combination with an ultrasonic wave field to clarify whitewater were reported. In a preliminary set of experiments, different flocculants were tested and the neutral flocculant system PEO/PFR was determined to be the most effective for clarification experiments. The PEO/PFR system required the lowest dosages and produced the largest and most stable flocs of the flocculants tested. PEO/PFR was also found to be equally effective on all three whitewater samples tested.

A series of cloudy whitewater clarification runs was then undertaken. Experiments were performed at three different frequencies (60 kHz, 150 kHz and 1.5 MHz) for different flow velocities and acoustic intensities. A video camera was used to record the deflection of flocs and the initial deflection angle was measured. It was found that 150 kHz produces larger deflections than 60 kHz or 1.5 MHz. This was thought to be due to optimal energy split between the ultrasonic field and production of cavitation bubbles.

A trend of increasing deflection angle with increasing acoustic intensity was seen at 150 kHz, up to an intensity of 3 W/cm². Beyond this, an increase in intensity did not yield significantly higher deflection angles. Increasing flow velocity at constant acoustic intensity reduced the deflection angle. This was observed at both 150 kHz and 1.5 MHz. This is due to lower dwell times in the ultrasonic field as the flow velocity increases.

In addition to video deflection angle measurements, the consistency of the clean and concentrated output streams was measured and the clean stream solids removal efficiency and clarification efficiency were computed. Clarification efficiency was largest at 1.5 MHz, reaching nearly 40% (the maximum achievable was 50% due to the 50:50 divider blade position – no attempt was made to optimize the divider blade position). Lower flow velocities (longer dwell time in the ultrasonic field) improved the clarification efficiency at both 1.5 MHz and 150 kHz. Acoustic intensity did not significantly affect the clarification efficiency at 1.5 MHz, but an optimum of 3 W/cm² was found for 150 kHz.

An economic analysis was performed on a theoretical 22,750 L-per-minute (6000 gpm) ultrasonic whitewater clarifier. It was compared to a conventional dissolved air flotation (DAF) unit of the same size. The ultrasonic clarifier is estimated to cost 66% less than the DAF to purchase and install and will cost 35% less to operate (considering both chemical and electrical costs).

Various improvements can be made to further optimize the clarification technology. The geometry of the flow cell can be redesigned to minimize secondary flows and to optimize clarification efficiency at 150 kHz. While 150 kHz produced the largest deflection angles, and 1.5 MHz achieved the highest clarification efficiencies, other frequencies need to be evaluated to see if further advances can be made. With respect to clarification efficiency, no attempt was made to optimize the divider blade position. Instead, experiments were only performed with the divider blade at the 50:50 position, limiting the maximum clarification efficiency to 50%. Because the laboratory separation system works in a closed-loop mode, the flocculant concentration needed to be higher than would be necessary in a continuous system to compensate for degrading of the flocs as they made multiple passes through the pump. Also, work is ongoing to better understand the interaction between cavitation bubbles and the ultrasonic field, which may lead to optimization of energy transfer from the transducer to the flocs.

ACKNOWLEDGEMENTS

The authors would like to thank Member Companies of the Institute of Paper Science and Technology for their continuous support since 1991, and the State of Georgia Traditional Industries Program for Pulp and Paper (TIP³) for its financial support since 1997. Additional support was provided by the U.S. Department of Energy since 1997 (Award No. DE-FC07-97ID-13553) and Beloit Corporation. Support by DOE does not constitute an endorsement of the views expressed in this paper.

We are very appreciative of Mr. James Ramp from SP Newsprint Company in Dublin, GA for mentoring the project and graciously supplying whitewater for laboratory trials. Also, we are very thankful to Mr. David Grimes and Dr. Jack Milliken from Beloit Corporation for their technical guidance and assistance in the economic analysis of the technology.

REFERENCES

- Apfel, R.E., "Sonic Effervescence: A Tutorial on Acoustic Cavitation," *Journal of Acoustic Society of America*, 101 (1997).
- Awatani, J., "Radiation Pressure on a Cylinder," *Journal of the Acoustic Society of Japan*, 9 (1953).
- Awatani, J., "Study on Acoustic Radiation Pressure (IV) (Radiation Pressure on a Cylinder)," *Memo. Inst. Sci. Ind. Research Osaka Univ.* 12:95-102 (1955).
- Beissner, K., "Radiation Force Calculations," *Acoustica*, 62 (1987).
- Brodeur, P.H., "Acoustic Separation in a Laminar Flow," *Proc. IEEE Ultrasonics Symp.*, Cannes, France, Vol. 3:1359-1362 (1994).

- Brodeur, P.H., Dion, J.L., Garceau, J.J., Pelletier, G., and Massicotte, D., "Fiber Characterization in a Stationary Ultrasonic Field," *IEEE Trans. Ultrason. Ferroelec. Freq. Control.* 36:549-553 (1989).
- Brodeur, P.H., "Method and Apparatus for Acoustic Fiber Fractionation", U.S. Patent #5,803,270 (Sept. 8, 1998).
- Brodeur, P.H., "Motion of Fluid Suspended Fibers in a Standing Wave Field," *Ultrasonics* 29:302-307 (1991).
- Brodeur, P.H. and Runge, T.M., "Compactibility of a Wet Fiber Mat Using Acoustic Radiation Pressure," *J. Pulp & Paper Sci.* 22(8):J278-J282 (1996).
- Dion, J.L., Brodeur, P., Garceau, J.J., and Chen, R., "Caractérisation des fibres par un nouveau procédé acousto-optique: nouveaux résultats," *J. Pulp & Paper Sci.* 14:J125-J128 (1988).
- Eckart, C., "Vortices and Streams by Sound Waves", *Physical Review*, 48 (1948).
- Garceau, J.J., Dion, J.L., Brodeur, P., and Luo, H., "Acousto-optical Fiber Characterization," *Tappi J.* 72:171-173 (1989).
- Hamilton and Blackstock, "Nonlinear acoustics," Academic Press (1998).
- Hasegawa, T. and Yosioka, K., "Acoustic Radiation Force on a Solid Elastic Sphere," *The Journal of the Acoustic Society of America*, 46(5) (1969).
- Hasegawa, T., Saka, K., Inoue, N., and Matsuzawa, K., "Acoustic Radiation Force Experienced by a Solid Cylinder in a Plane Progressive Field," *Journal of the Acoustic Society of America* 83(5):1770-1775 (1988).
- Jong, J.H., Choi, M.H., Gerhardstein, J.P., and Brodeur, P.H., "Acoustic Separation of Moving Fibers in a Pulp Flow", *Proc. 1999 TAPPI Pulping Conf. Orlando, FL.*, TAPPI Press (1999).
- King, L.V., "On the Acoustic Pressure on Spheres," *Proceedings of the Royal Society of London*, 147A (1934).
- King, L.V., "On the Acoustic Pressure on Circular Disks," *Proceedings of the Royal Society of London*, 153A (1935).
- Lindstrom, T. and Glad-Nordmark, G., "Network Flocculation and Fractionation of Latex Particles by Means of a Polyethyleneoxide-Phenolic Formaldehyde Resin Complex", *J. Colloid Interface Sci.*, 97(1):62-67 (1984).
- Ma, K.V. "Acoustic Separation of Fibers," M.S. Research Report, IPST (1995).
- McGovern, J. N., "How to Use Oak-Containing Kraft Pulps for Offset Printing Papers," *Pulp and Paper*, December: 58-61 (1977).
- Neppiras, "Acoustic Cavitation," *Phys. Rep.*, 61, 159-251 (1980).
- Nyborg, W. L., *Physical Acoustics*, Vol. II B, p265-331 (1965).
- Prosperetti, "Bubble Phenomena in Sound Field," *Ultrasonics*, 70 (1994).
- Rooney, J.A., and Nyborg, W.L., "Acoustic Radiation Pressure in a Traveling Plane Wave," *American Journal of Physics*, 40 (1972).
- Yosioka, K. and Kawasima, Y., "Acoustic Radiation Pressure on a Compressible Sphere," *Acoustica*, 5 (1955).
- Zhuk, A.P., "Radiation Force Acting on a Cylindrical Particle in a Sound Field," *Soviet Appl. Mech.* 22(7):689-693 (1986).

Appendix A – Clarification Efficiency

In order to achieve 100% clarification efficiency, both the divider blade position and the clean stream solids removal efficiency should be optimized, i.e.,

$$\% \text{ Clarification Eff.} = (\text{Optimal Divider Position}) (\% \text{ Clean Stream Removal Eff.}) \quad (\text{A1})$$

Referring to Fig. A1, the clean stream consistency is optimized when it goes to zero. Hence, the clean stream solids removal efficiency is given by,

$$\% \text{ Clean Stream Removal Eff.} = 100\% \left(1 - \frac{C_{\text{clean}}}{C_{\text{feed}}} \right) \quad (\text{A2})$$

where C_{clean} is the % clean stream consistency and C_{feed} is the % feed stream consistency.

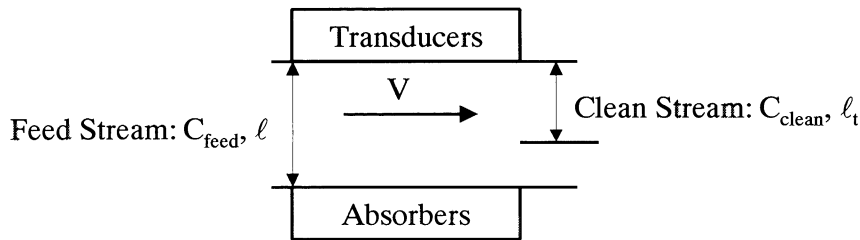


Fig. A1. Geometry of flow cell. C_{feed} and C_{clean} are the feed and clean stream consistencies, respectively. λ is the separation distance between the transducers and absorbers and λ_t is the distance between the transducers and the divider blade.

The divider position is optimized when it reaches the position furthest from the transducer that is theoretically possible. Referring to Fig. A2, if the water and suspended particles (flocs) are 100% separated, with pure water on the top of the cell and only flocs on the bottom, the water forms a layer λ_{water} thick, and the flocs form a layer $\lambda - \lambda_{\text{water}}$ thick.

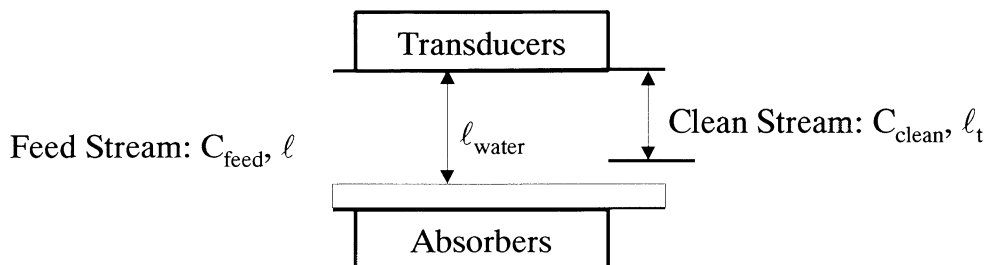


Fig. A2. Flocs on bottom of flow cell are completely separated from water on top of flow cell. Thickness of the water layer in this case = λ_{water} .

Hence, optimal divider position is achieved when $\lambda_t = \lambda_{\text{water}}$, which can be written mathematically as:

$$\text{Optimal Divider Position} = \left(\frac{\ell_i}{\ell_{\text{water}}} \right) \quad (\text{A3})$$

The thickness of the water layer for 100% separation is simply the percent water in the feed stream $[(100\% - C_{\text{feed}})/100\%]$ multiplied by the cell width (ℓ):

$$\ell_{\text{water}} = \ell \left(1 - \frac{C_{\text{feed}}}{100\%} \right) \quad (\text{A4})$$

Hence combining Eqs. A3 and A4 yields

$$\text{Optimal Divider Position} = \frac{\ell_i}{\ell \left(1 - \frac{C_{\text{feed}}}{100\%} \right)} \quad (\text{A5})$$

Substituting Eqs. A2 and A5 into Eq. A1 then gives the clarification efficiency:

$$\% \text{ Clarification Eff.} = 100\% \left(\frac{\ell_i}{\ell} \right) \left[\frac{C_{\text{feed}} - C_{\text{clean}}}{C_{\text{feed}} \left(1 - \frac{C_{\text{feed}}}{100\%} \right)} \right] \quad (\text{A6})$$

In order to illustrate Eq. A6 and the hypothetical performance of an acoustic clarifier, one can consider a whitewater stream entering the flow cell at 0.03% consistency. If the clean stream consistency is 0.001%, and the divider blade is placed at 97% of the way across the flow cell ($\lambda_v \lambda = 0.97$), the efficiency of the clarification process is then

$$\% \text{ Clarification Eff.} = 100\% (0.97) \left[\frac{0.03\% - 0.001\%}{0.03\% \left(1 - \frac{0.001\%}{100\%} \right)} \right] = 94\%$$

This is comparable to a typical DAF system.

ON-LINE MEASUREMENT OF PAPER PROPERTIES

STATUS REPORT

FOR

PROJECT F007

**Mac Hall
Ted Jackson
Andy Brown**

**Institute of Paper Science and Technology
500 10th Street, N. W.
Atlanta, Georgia 30318**

DUES-FUNDED PROJECT SUMMARY

Project Title: ON-LINE MEASUREMENT OF PAPER PROPERTIES
Project Code: OLIN
Project Number: F007
PAC: PAPER PHYSICS

Project Staff

Principal Investigator: Mac Hall
Co-Investigators: Ted Jackson and Andy Brown

PAC Subcommittee Thomas Rodencal, Georgia-Pacific

FY 99-00 Budget: \$56,000
Allocated as Matching Funds: 100%

Supporting Research:

External (Where Matching Is Used):
Project 3942 (FY Funds \$98,800 from DOE as part of Cooperative Agreement DE-FC02-95CE41156 with DOE, ABB Industrial Systems Inc., Herty Foundation, and Georgia-Pacific Cedar Springs Mill).

RESEARCH LINE/ROADMAP:

10. Energy Performance
 - Reduce energy consumption.
12. Sensors and Process Control
 - Develop on-line ultrasonic sensors to measure paper stiffness.
 - Develop algorithms/models relating material and manufacturing variables to process and product.

PROJECT OBJECTIVE:

Verify on-machine ultrasonic sensor measurements and determine sensitivity of ZD ultrasonic measurements to papermaking process variables, e.g., refining, wet pressing, wet straining, and calendering.

PROJECT BACKGROUND:

Last Spring, the in-plane and ZD sensors had been installed on a linerboard machine and were undergoing check out in preparation for extended bump-test trials.

DELIVERABLES:

1. Verification of on-machine sensor measurements.
2. Relationships between on-machine ultrasonic measurements, mill grade specifications, and papermaking process variables.

GOALS and SCHEDULE FOR FY 99-00:

FY99-00	Jan-Mar	Apr-Jun	Jul-Sep	Oct-Dec
1. Combine ZD data with ABB data processing and display system	-----	-----	-----*	
2. Verify on-machine sensors: (1) In-plane; (2) ZD	-----1	-----2		
3. Determine correlation of ultrasonic measurements with mill grade specifications	-----	-----	-----	-----*
4. On-machine measurement / process relationships		-----	-----	-----*

STATUS OF GOALS FOR FY 99-00:

1. Combine ZD data with ABB data processing and display system -- This goal was cancelled when DOE/Agenda 2020 reduced previously approved project funding.
2. Verify on-machine sensors -- Demonstrated successful operation of sensors for extended runs scanning linerboard being produced at speed up to 1800 ft/min.
3. Determine correlation of ultrasonic measurements with mill grade specifications -- Completed bump-test runs involving 25 successive reels of 69# and 55# linerboard. Compared measurements of end-of-reel strips with on-machine data.
4. On-machine measurement / process relationships -- Compared on-machine data with process variables selected from mill PI system.

SUMMARY OF RESULTS:

The On-Machine ZD sensor system works:

ZD measurements are sensitive to:

- ◆ Refining
- ◆ Calendering

ZD measurements correlate with:

- ◆ Z-Direction Tensile (plybond)
- ◆ Burst (Mullen)

The In-Plane sensor has operated continuously for extended periods of time. A paper by Bradley Pankonin and Doug Jimmerson entitled, "Mill Experiences with On-Line Ultrasound Based Stiffness Measurements" summarizes the in-plane sensor measurement performance and test results. This paper was presented at the TAPPI Engineering / Process and Product Quality Conference held in Anaheim, California, September 12-16, 1999. The paper may be found in the Conference Proceedings, pages 919-928.

SUMMARY OF KEY CONCLUSIONS:

- ◆ Successfully demonstrated the ZD (out-of-plane) stiffness technology on a commercial paper machine.
- ◆ Correlation of ZD measurements with ZDT (Z-Direction Tensile) and Plybond show potential value to mill. Production that does not meet the Plybond specification must be reprocess. Significant savings may be obtained by acceptable first quality.
- ◆ Display of ZD data to operator both as time trend of scan average and as contour map of scan-by-scan cross-web profiles would provide early warning of process upsets. Constant visibility of product status would assist operator in maintaining stable and efficient process operation.

DISCUSSION:***Review***

The variations of the elastic stiffnesses of paper with refining, fiber orientation, wet pressing pressure, wet straining (draws), drying restraints, and calendering have been studied and reported (Baum et al., 1984; Habeger and Baum, 1986). These studies have demonstrated that elastic stiffnesses are sensitive to changes in furnish and to changes in various process parameters. This project has been focused on paper stiffness measurements using ultrasonics and the relationships of ZD and in-plane stiffnesses to on-machine process parameters. It supplements the Cooperative Agreement project to develop and demonstrate sensors and instrumentation for on-machine ultrasonic measurements in both the in-plane and thickness directions.

The instrumentation has the potential of providing:

- 1) Improved First Quality
 - a) Quicker Grade Changes
 - b) Less Culls due to CD "Strength" Variations
 - c) Less Downgraded Tonnage during the Run
- 2) Fiber Savings
 - a) Reduce Fiber Usage while maintaining "Strength" Targets
 - b) Use Cheaper Fiber Sources while Maintaining "Strength" Targets
 - c) Reduce Ring Crush Variability Creating Opportunity to Operate at Lower Ring Crush Targets
- 3) Energy Savings
 - a) Minimize Refiner Loads while Maintaining "Strength" Targets
 - b) Reduce Total Steam Requirements Though Better Drainage and Less Fiber to Dry
- 4) Increased Production
 - a) Increase Machine Speed while Maintaining "Strength" Targets

A 1000-ton/day machine producing 350,000 tons/year uses approximately 4.725 trillion Btu/year. For each 1% of production that is substandard and reprocessed at 13.5 million Btu/ton, the 1000-ton/day machine wastes 47.25 billion Btu/year. Assuming this technology may limit substandard production to 2%, the energy saving would be 94.5 billion Btu/year or \$378,000 (@ \$4/million Btu) annually for the 1000-ton/day machine.

Further energy savings should result from optimum utilization of refining and drying (Lantz and Chase, 1988). Refining requires approximately 200 kWh/ton or 2.1 million Btu/ton (1 kWh = 10,500 Btu). For a 1000-ton/day machine, the annual energy usage for refining is approximately 70.0 million kWh or 735 billion Btu. Assuming the optimization of refining could reduce the energy required by 10%, this would be equivalent to savings of 73.5 billion Btu or \$294,000 annually.

By decreasing refining, drainage is improved, requiring less steam for drying the web. The steam required for drying is equivalent to approximately 8 million Btu/ton, or 2.8 trillion Btu/year for a 1000-ton/day machine. If the moisture of the paper entering the dryer were reduced by 1.0%, the dryer steam required would be reduced by about 3%. This would save an additional 84 billion Btu/year or \$336,000 annually.

Summary for a 1000-ton/day paper machine:

Annual Energy Use = 4.725 trillion Btu = \$18,900,000 @ \$4/million Btu

Reprocessing savings:

* Electricity	38.5 billion Btu		
* Steam	56.0 billion Btu		
	Total reprocessing savings	94.5 billion Btu	= \$378,000

Refining savings:

* Electricity	73.5 billion Btu	= \$294,000
---------------	------------------	-------------

Drying savings:

* Steam	84.0 billion Btu	= \$336,000
---------	------------------	-------------

Total potential savings for 1000-ton/day machine:

* Electricity	112.0 billion Btu	= \$448,000
* Steam	140.0 billion Btu	= \$560,000
	@ \$4/million Btu	= \$1,008,000
Total potential savings/year	252 billion Btu/year	= 5.3%

Status of On-machine Demonstration

The Institute has had a Cooperative Agreement with the U.S. Department of Energy's Office of Industrial Technologies (DOE-OIT) for a project to develop and demonstrate on-line ultrasonic sensors. The project includes systems with the ability to make both in-plane and out-of-plane (ZD) ultrasonic measurements.

IPST is prime contractor with cost-share participation by ABB Industrial Systems Inc., Columbus, Ohio, the Herty Foundation, Savannah, Georgia, and the Georgia-Pacific Mill in Cedar Springs, Georgia. We are at the end of a 5-year development and testing program.

An AccuRay® 1190™ System with a Smart Platform™ 1200 has been installed at the Cedar Springs Mill on their paper machine #1. The sensor carriage of the scanner contains state-of-the-art basis weight, moisture, temperature, and caliper sensors. The sensor carriage also accommodates the installation of in-plane and ZD ultrasonic sensors. ABB has built and installed the in-plane sensor.

IPST has designed and built a ZD ultrasonic sensor using transducers mounted in fluid-filled wheels. The wheel mounting modules have been designed so that the wheels can be steered during scanning. The ZD system was first install on PM#1 at the Cedar Springs Mill during outage July 28, 1998. Access to the sensor carriage on the scanner to correct problems has been limited primarily to the one-shift-a-month outage of PM#1 for maintenance.

A number of changes have been made to the ZD system since it was first installed in the mill: an air conditioner was added to the E-Box; cooling air was directed at the wheels; the wheels were overhauled with new bearings, seals and connectors; silicone rubber tires were substituted for polyurethane tires; the fluid in the tires was changed to a special fluid for high temperature ultrasonic coupling; two co-ax cables and two air hoses were installed in both the top and the bottom auxiliary flex tracks of the scanner for communication with the ZD modules; the solenoid air valves were replaced; and the modules were rewired. The positioning of the In-Plane and the ZD sensors in the carriage was changed so that the center of gravity is closer to the center of support in the scanner frame. The ZD system was first operated continuously for 24 hour around the clock collecting data in March 1999.

Detailed plans were prepared for both step tests and end-of-reel testing to determine relationships between in-plane stiffness measurements, sheet properties and process variables for PM #1. The following step tests were conducted: 69 lb/1000 ft² linerboard, May 17, 1999; and

55 lb/1000 ft² (USP 120) linerboard, June 9, 1999. The process variables manipulated, the sources of data collected, and the tests performed on collected samples are outlined below.

Process Variables Manipulated:

1. Machine Speed
2. Rush/Drag
3. Number of Calender Stack Nips
4. % Top Stock Coverage
5. Basis Weight
6. % Moisture
7. Base Refiner Load
8. Broke Flow
9. DLK Flow

Sources of Data

1. Recorded Notes
2. ABB 1190 Profiles (600 to 60 data boxes):
Basis Weight/Conditioned Weight; % Moisture; Caliper; Temperature;
Longitudinal Velocity Squared; & Shear Velocity Squared
3. ZD Sensor Profiles (600 to 60 data boxes):
ZD Transit Time; Energy of ZD Pulse at Receiver
4. Mill PI System time-based Process Data
5. Mill PI System Profile data (60 data boxes)
6. Mill RMS (Roll Management System) Data
7. GP QC test data (30 point profiles on CD strips)
8. IPST Lab test data (60 point profiles on CD strips)

Tests Performed on Collected CD Strip Samples at GP:

1. CD Ring Crush
2. Plybond (69#)
3. Mullen, felt side & wire side
4. STFI
5. Basis Weight
6. % Moisture
7. Caliper
8. MD Tensile
9. MD & CD Tear

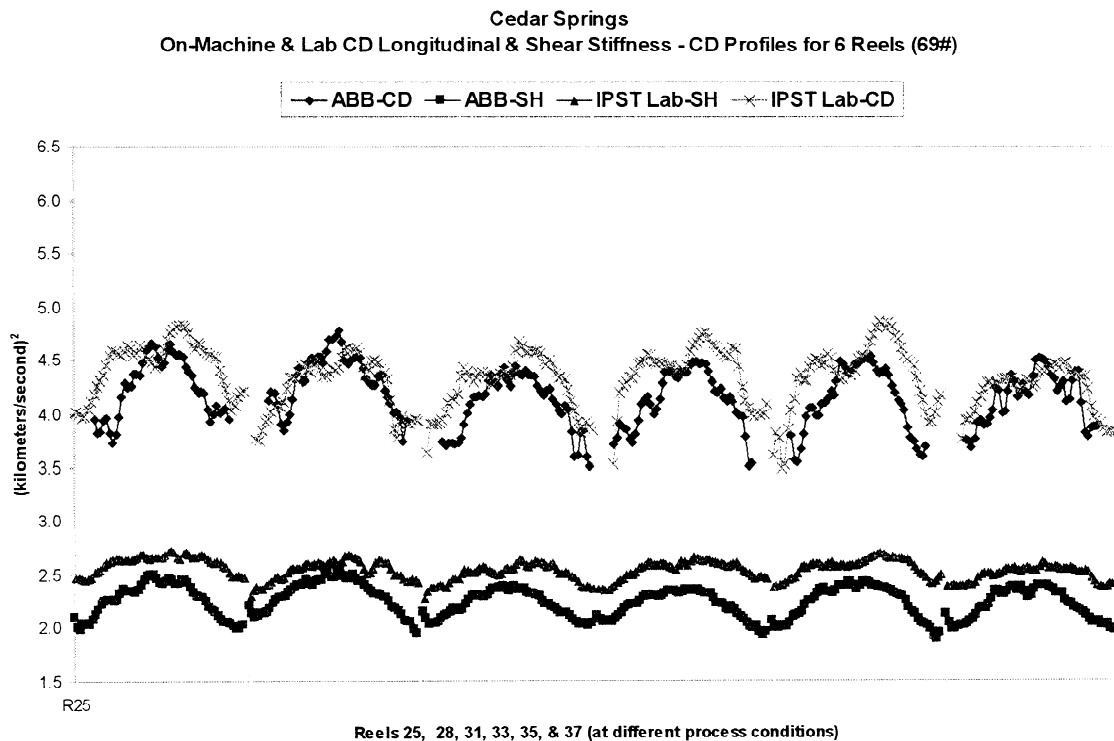
A similar set of off-line measurements was performed at IPST. In addition to the CD strips collected for testing at the mill, two CD strips were collected for IPST for each test reel.

The data transferred to Excel spreadsheets could be plotted and/or analyzed using FactNet 4.5 software. The time stamps for the data from the ABB, GP, and IPST systems needed to be as close as possible. Care was taken to match samples with the profiles and data to obtain spatial alignment between collected data and actual strips to the extent feasible.

Results

In-Plane Ultrasonic Measurements

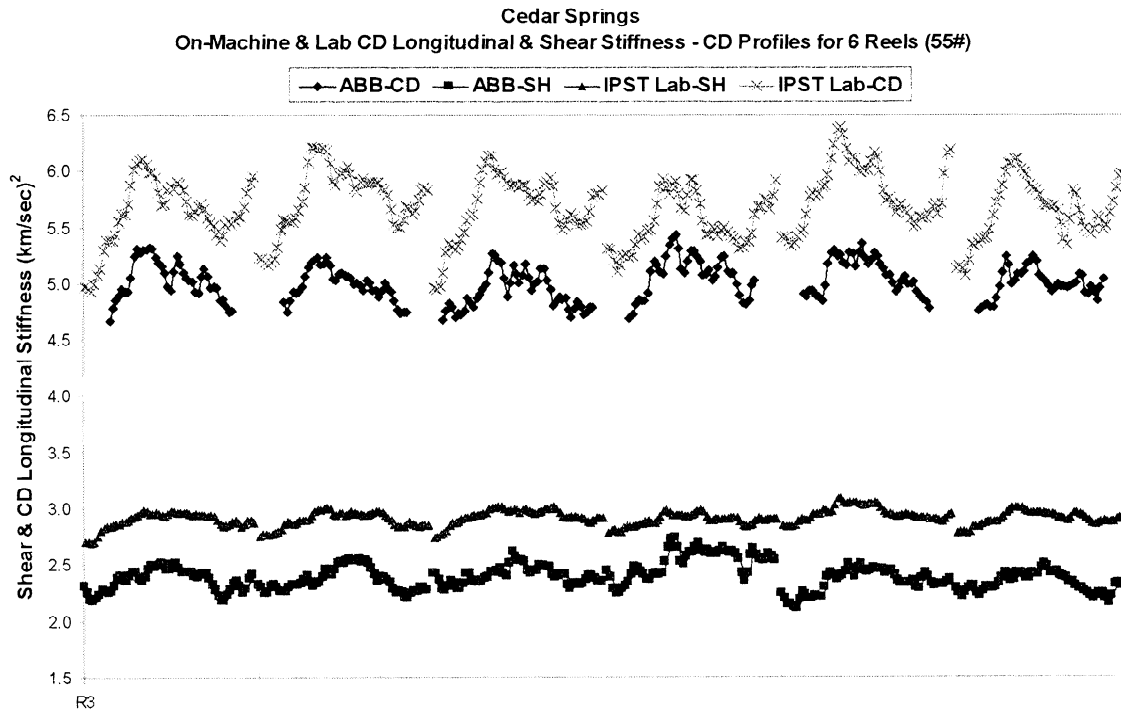
A description and discussion of the in-plane system may be found in the attached copy of a paper by Bradley Pankonin and Doug Jimmerson entitled, "Mill Experiences with On-Line Ultrasound Based Stiffness Measurements." This paper was presented at the TAPPI Engineering / Process & Product Quality Conference in September 1999. Some additional observations are presented here.



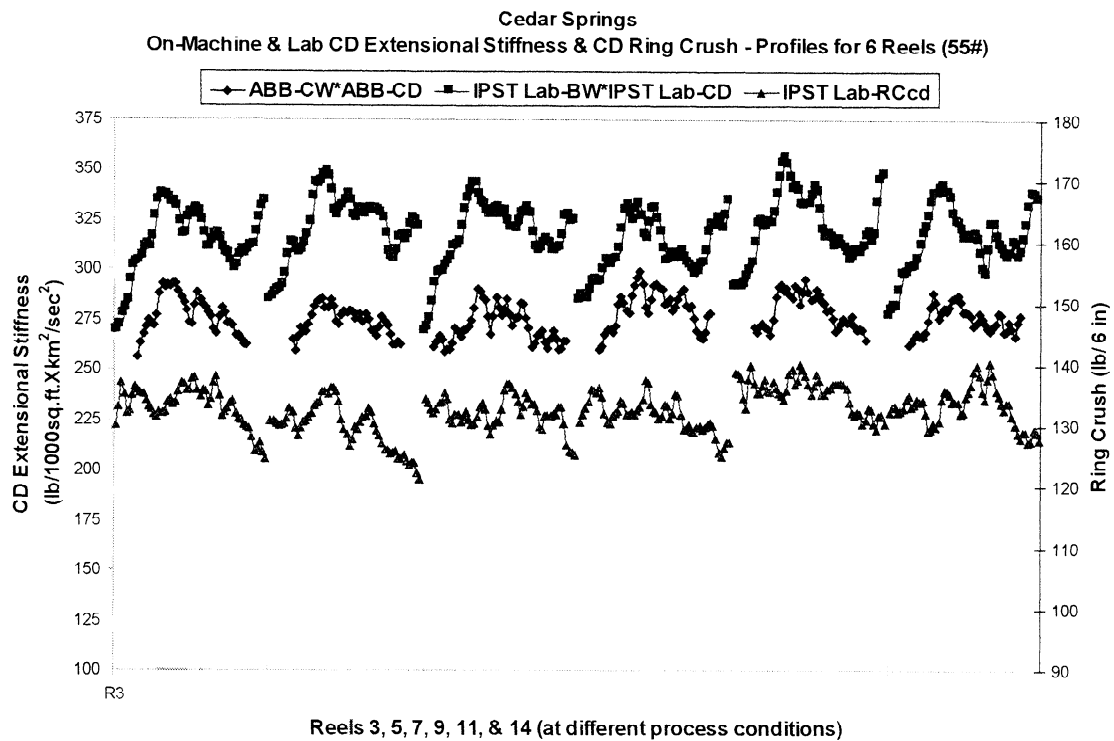
The plot above compares the ABB on-machine in-plane data with the data recorded at IPST on end-of-reel strips with the laboratory "robot" instrument. The data from six reels of 69# produced at different process conditions are plotted side by side. The upper two sets are for the CD Longitudinal Stiffness and the lower two sets are a comparison of the Shear Stiffness. One may note that changes across the profile of each sample are greater than any apparent change due to process changes.

Of particular note is the observation that the "degree of frown" in the on-machine data profile is greater than that found for the laboratory data. This is particularly apparent in the lower two sets of Shear Stiffness data. Similar observations of differences in the "degree of frown" between on-

machine and laboratory measurements have been reported (Reed and Brown, 1999). It appears that this is a real physical property change rather than an instrumental effect.



The plot above is similar to the previous plot except that it is for the data from six reels of 55# produced at different process conditions and plotted side by side. The scale is the same so that one can see that the CD Longitudinal Stiffnesses for the 55# are greater than for the 69# samples. The Shear Stiffnesses are also somewhat greater for the 55#. Again the changes across the profile of each sample are greater than any apparent change due to process changes.

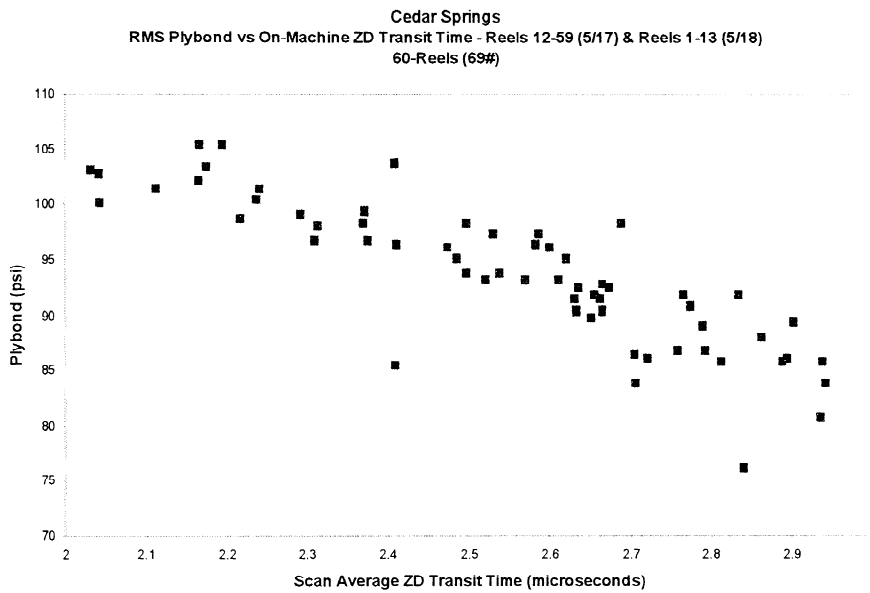


The above plot compares the CD Extensional Stiffness calculated from the ABB on-machine in-plane data, the CD Extensional Stiffness determined at IPST on end-of-reel strips, and the Ring Crush determined at IPST. Again the data from six reels of 55# produced at different process conditions are plotted side by side. In view of the uncertainty in the spatial alignment between the on-machine data and the sampled CD strips, the similarity in CD profile of the data is reasonable. One may again note that changes across the profile of each sample are greater than any apparent change due to process changes for both the CD extensional stiffness and for Ring Crush. Similar results were observed for CD STFI measurements.

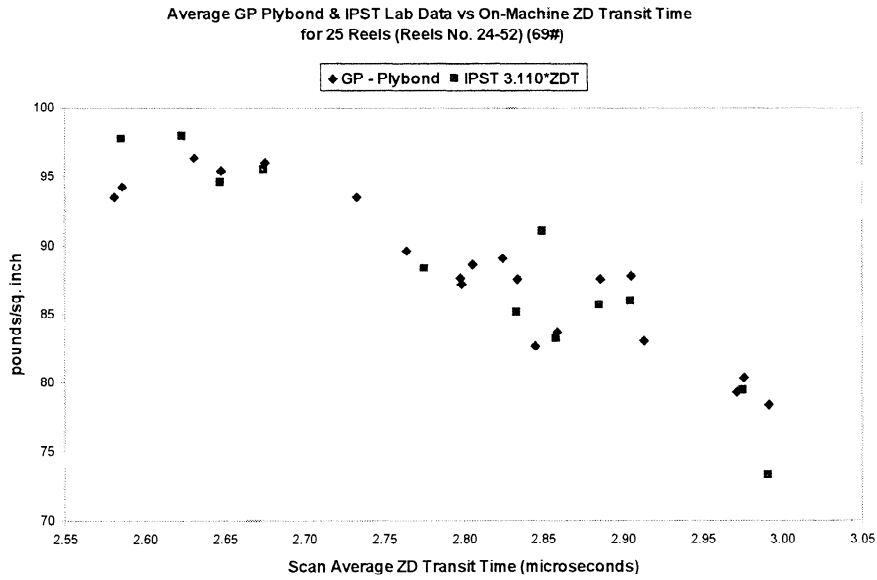
ZD (Out-of-Plane) Ultrasonic Measurements

The ZD system has a stand-alone E-box separate from the ABB 1190 system. However, a position tachometer is used to provide scan position for the ZD system. The distance between scan limits is divided into 600 data boxes similar to the ABB 1190 system. It takes slightly more than one minute to scan across the 256-inch wide web. A data box has a width slightly less than one-half inch. With a sampling rate of 20 per second, approximately 2 measurements will be averaged in each data box. A computer connected to the E-box can display the ZD Transit Time or Receiver Energy as a color contour plot and trend plot. The transit time profile is also a "frown" -- larger transit time in the center than at the edges of the web.

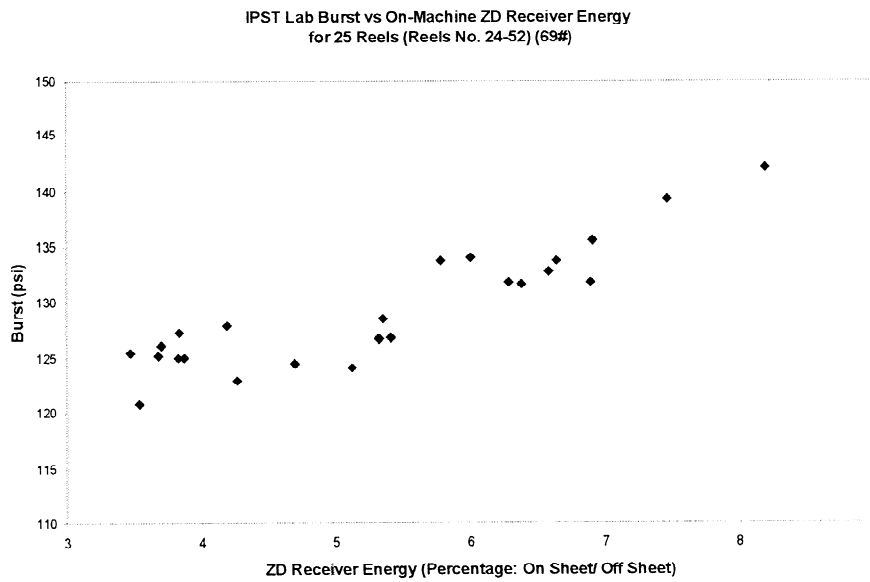
For determination of relationships of the ZD measurement with process parameters or paper properties, scan averages are used. The average for the scan completed nearest to the minute data from the mill's PI system and the reel turn-up time from the RMS (Roll Management System) is used. Below some observations are presented: the correlation of ZD Transit Time with Plybond and Z-direction Tensile; the correlation of ZD Receiver Energy with Burst; and the sensitivity of ZD ultrasonic measurements to refining and calendering.



Above is a plot of the plybond measurements entered into the mill's RMS (Roll Management System) for 60 successive 69# reels versus the Scan Average ZD Transit Time recorded near the recorded turn-up time.

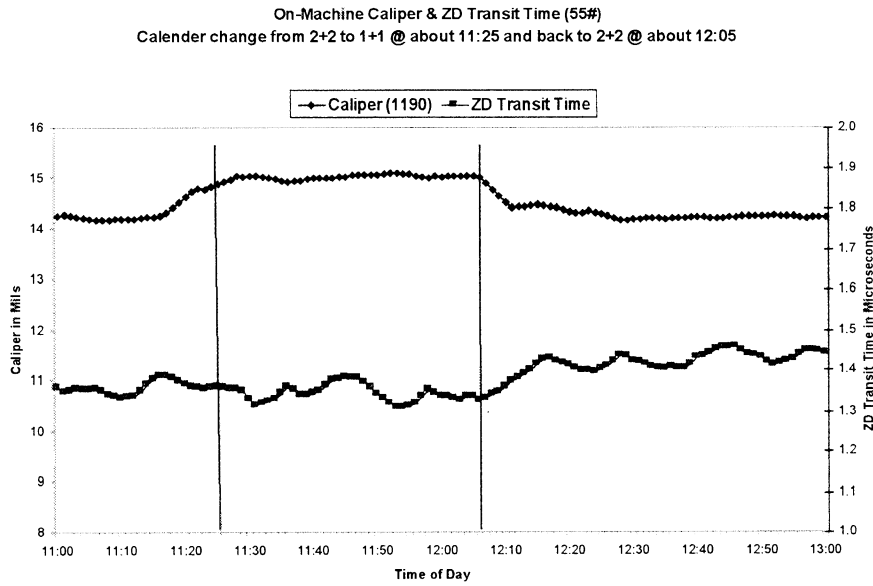


Georgia-Pacific determines plybond by the procedure that uses a circular sample mounted in a Mullen tester. Comparisons with the ZDT (Z-direction Tensile or internal bond strength) method have shown these procedures provide measurements that differ by a factor of approximately three. The above plot shows plybond data measured by G-P for 20 of the 25 reels from the 69# test. Also shown are 3.11 x ZDT measurements by IPST for 12 of the 25 reels. These are plotted versus the Scan Average ZD Transit Time at reel turn-up. The correlation is apparent and has an R squared greater than 0.8.

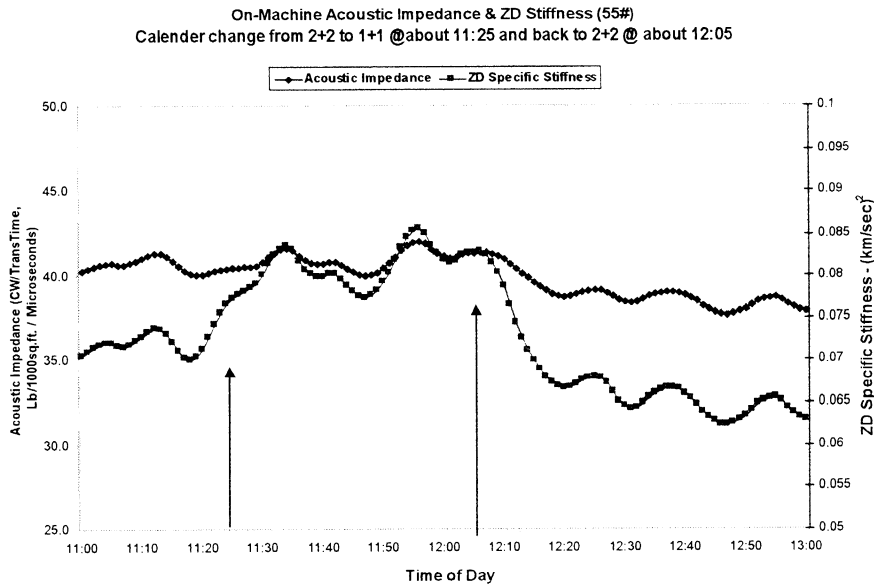


The above shows Burst measured in the IPST lab for the reel sampled from the 69# test versus the scan average Receiver Energy at the time of reel turn-up. This suggests that the on-machine determination of ultrasonic energy received through the web may provide an indication of Burst or Mullen.

The sensitivity of ZD ultrasonic measurements to calendering is present in the following two plots.

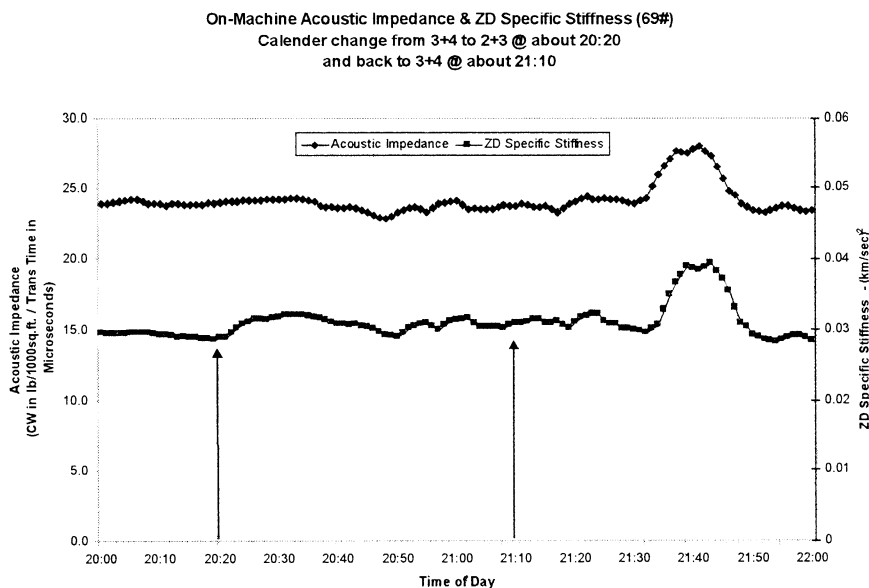


The scan average data was smoothed by a moving average of 5. This plot shows the caliper and ZD transit time versus the time of day for the two hours that included the calendar change from 2+2 nips to 1+1 and back during the 55# test. The increase in Caliper is apparent, but no associated change is visible in the ZD Transit Time.

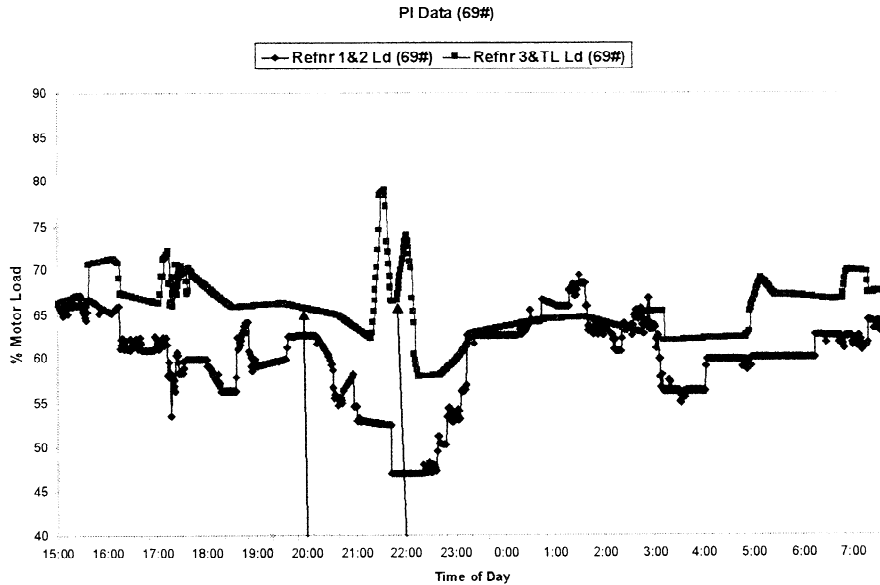


The acoustic impedance is determined by dividing basis weight by ZD transit time. The ZD stiffness is determined by squaring the ZD velocity, i.e., the caliper divided by the ZD transit

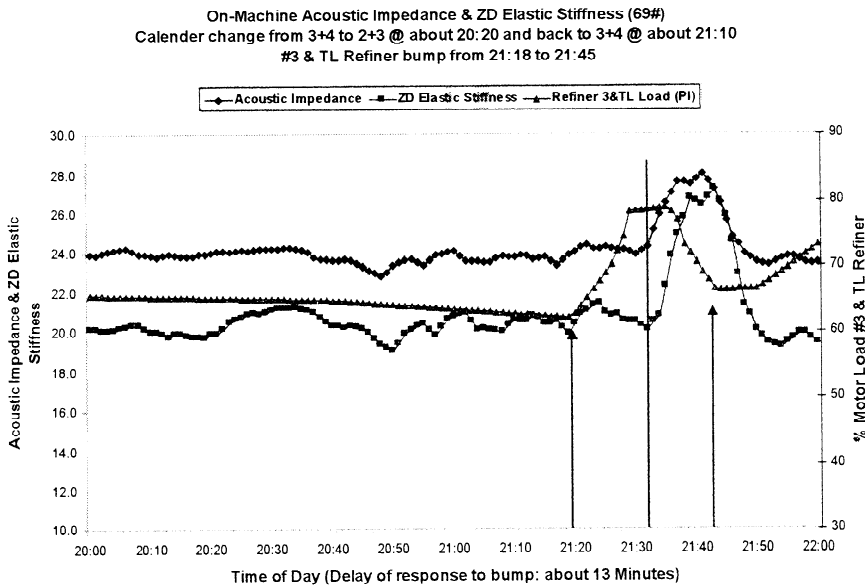
time. Since the basis weight and ZD transit time did not change with calendaring, there is no change in acoustic impedance. However, there is a significance change in the ZD velocity and ZD stiffness



The two hours that included the calender change from 3+4 nips to 2+3 and back during the 69# test was also examined. The above plot shows only a slight change in ZD stiffness with calendaring. This may be expected since the change in total nips from 7 to 5 for the 69# test is a much smaller change than the 4 to 2 for the 55# test. The bump in the acoustic impedance and in the ZD stiffness at 21:40 was noted and examined by reviewing various process parameters recorded by the mill' PI system. Selected refiner motor load data is plotted below versus time of day.



The two hours (20:00 to 22:00) are marked. A sharp bump in the #3 & TL refiner motor load is noted just before 22:00. The #3 & TL refiner motor load for the two-hour period is added to the previous plot and shown below.



The acoustic impedance and the ZD stiffness show a sensitive response to the bump in the #3 & TL refiner motor load with a delay of approximately 13 minutes.

RECOMMENDATIONS FOR FUTURE WORK:

- Integrate the ZD measurements with the ABB 1190 system to provide real-time display to the machine operators scan-average trends of ZD Transit Time, Receiver Energy, and "ZD bond".
- Determine changes in ZD data trend plots with grade and process changes and upsets.
- Determine the benefits of ZD data trend plots for operator use in monitoring and controlling the process conditions and product properties.

REFERENCES

Baum, G.A., Brennan, D.C., and Habeger, C.C., "Orthotropic Elastic Constants of Paper," *Tappi J.* 64 (8):97(1981).

Baum, G.A., Pers, K., Shepard, D.R., and Ave'Lallemant, T.R., "Wet Straining of Paper," *Tappi J.* 67 (5):100(1984).

Habeger, C.C., and Baum, G.A., "On-line Measurement of Paper Mechanical Properties," *Tappi J.* 69 (6): 106(1986).

Lantz, K.G., and Chase, L.M., "On-line Measurement and Control of Strength Properties," *Tappi J.* 71 (2): 75(1988).

Reed, W.M., and Brown, T., "Online Strength sensor Improves Linerboard for MacMillan Bloedel," *Pulp & Paper* 73 (3): 61(Mar 1999).

MILL EXPERIENCES WITH ON-LINE ULTRASOUND BASED STIFFNESS MEASUREMENTS

Bradley M Pankonin
Senior Staff Scientist
ABB Industrial Systems Inc
Columbus, OH 43202

Doug Jimmerson
Process Engineer
Georgia Pacific Corporation
Cedar Springs, GA 31732

ABSTRACT

ABB has developed an on-line Ultrasonic Specific Stiffness Sensor. The sensor has been installed on a paper machine producing Linerboard in the range of 40-90-lbs/1000 sq.-ft. and the measurement has operated reliably for 6 months. This report summarizes the on-line measurement performance and emphasizes field test results.

Many of the relationships expected between paper stiffness, process parameters, and paper 'strength' are confirmed. The impact of process upsets and grade changes on stiffness properties are tracked. For example, increasing the rush-drag ratio is shown to increase both the on-line CD Specific Stiffness and the QC laboratory CD Ring Crush and Ring crush indexes. These and other results provide the basis for improved product quality and reduced production costs.

INTRODUCTION

Traditional on-line measurements are of parameters used by papermakers because they imply the actual properties of interest. For example, few paper users really care about the papers' weight. What is important is its color, its smoothness, its opacity, its strength, stiffness, feel, volume etc.; that is those properties, which determine the performance of the paper in use.

The mechanical attributes of the sheet (strength, stiffness, etc.) are very important to the manufactures of heavy paperboard and paper. While 'strength' can never be measured directly on-line (strength tests are by their nature destructive), elastic stiffnesses can be. Strength can be inferred through correlation relationships. On-line measures of sheet stiffness characteristics are limited, but perceived as valuable. The potential value of an on-line stiffness sensor could easily offset its cost in reducing waste from off-specification product. Other potentials exist by the reduction of weight while maintaining the same load carrying capacity.

Both Honeywell-Measurex (H-Mx.) (1) and Lorentzen & Wettre (L & W) (2) have recently reported solutions to measure the mechanical characteristics of paper at the time of manufacture. The former system physically deforms the sheet by known amount and effectively measures the load to do so. Elastic stiffness coefficients result from the application of Hooks' Law (system is non-acoustic). The system can be mounted on a scanner and hence can generate important profile information. Major error inducing effects are preset as a result caliper and web tension and carefully accounted for. The L & W system is acoustic based, however, at present can only be implemented as a single point measurement. The need for an acoustic based measurement system that is capable of being installed on a scanner has been addressed by ABB in the current work.

MEASUREMENT PRINCIPLE

Physical Acoustics

The sensor is designed to measure the propagation velocity of ultrasound waves in the paper web. These velocities are used to calculate "elastic stiffness" coefficients.

The velocity of ultrasound is related to the elastic stiffness and the density of the material it is traveling in. Extensional stiffness can be derived from the velocity of longitudinal ultrasound waves and shear stiffness can be derived from the velocity of transverse ultrasound waves. For paper, considered as an orthotropic material, the stiffness coefficients for cross machine direction extension, C_{cmd} , and shear, G_{cmd} , are:

$$C_{cmd} = \rho \cdot V_{l,cmd}^2$$

$$G_{md} = G_{cmd} = \rho \cdot V_{s,md}^2 = \rho \cdot V_{s,cmd}^2$$

Mass specific stiffnesses are obtained by dividing the stiffness by the density, ρ .

$$C_{cmd}/\rho = V_{l,cmd}^2$$

$$G_{md}/\rho = G_{cmd}/\rho = V_{s,md}^2 = V_{s,cmd}^2$$

The measurement system described here reports specific stiffnesses, which are compensated for by the process moisture and temperature at the time of the velocity determination.

Conditioned Stiffness

The elastic stiffness coefficients, and hence the ultrasonic velocities, of paper depend on moisture and temperature (4). Paper behaves like a polymer to plastisizers (water) and temperature. Increasing moisture content lowers the elastic stiffness coefficients and hence the ultrasonic propagation velocities. Increasing temperature lowers the elastic stiffness coefficients.

$$C_{cmd} = C_{cmd,0} \cdot [\beta_{M,C} \cdot (M - M_0) + \beta_{T,C} \cdot (T - T_0)] + C_{cmd,T,M}$$

$$G_{cmd} = G_{cmd,0} \cdot [\beta_{M,G} \cdot (M - M_0) + \beta_{T,G} \cdot (T - T_0)] + G_{cmd,T,M}$$

The measurement system reports **conditioned** elastic stiffness coefficients (TAPPI: 50% R.H., 23°C). The moisture content and temperature of the paper are obtained from the other sensors in the measurement platform.

Sensor Description

A digital photograph of the measurement system is shown in Figure 1. The basics of the measurement involve two sets of three ultrasonic transducers (3) mounted in a cylinder, which rolls on the moving paper web. One set is for the shear measurement and the other for the longitudinal measurement. Each sensor set consists of one transmitter and two receivers. In the figure the transmitter is located on the left side of the measurement cylinder and the two receivers are on the right. When the three transducers in a measurement set come into contact with the sheet the transmitter fires a short burst of 60-kHz ultrasound into the sheet. The ultrasound travels in the plane of the sheet and is picked up first by the near receiver (73 mm path length) and then latter by the far (115 mm path length). The time difference between the signal arrival times at the two receivers divided into the path length difference for the two signal paths determines the appropriate ultrasound velocity. The entire measurement takes place inside of a 200 μ sec time window. Post processing of the received signals takes place in less than 2 msec., and is performed in a digital signal processor (DSP). The square of the velocity determined is the specific acoustic stiffness for the appropriate mode, shear or longitudinal. Both measurements are cross-machine direction.

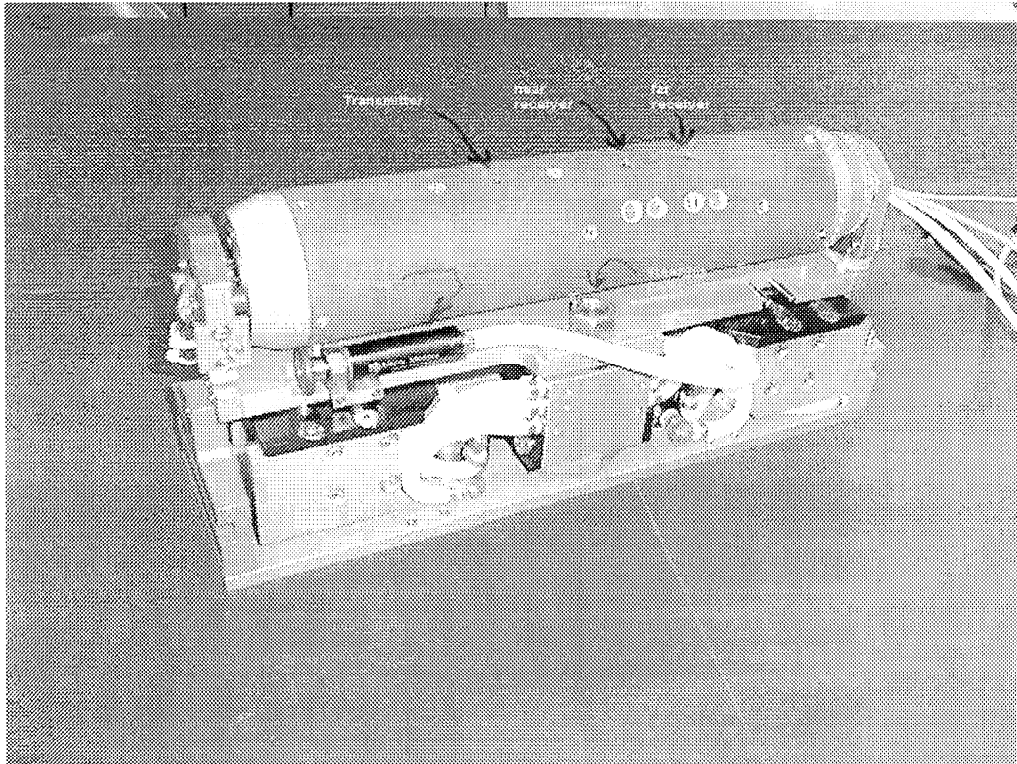


Figure 1. Measurement cylinder showing ultrasonic transmitter and two receivers for shear. Longitudinal transducers are located on the opposite side of the cylinder, 180 degrees from the longitudinal transducers. Air driven spin-up assist motor and cylinder steering gumball is also identified.

Sheet control in the measurement system is accomplished with a pair of small backing rollers. The rollers are on the opposite side of the sheet from the measurement cylinder. These *backside* rollers create a small wrap of the sheet over the measurement cylinder, Figure 2. This wrap insures that the transducers are in full contact with the sheet for the duration of the measurement. The rollers and the measurement cylinder do not pinch the sheet.

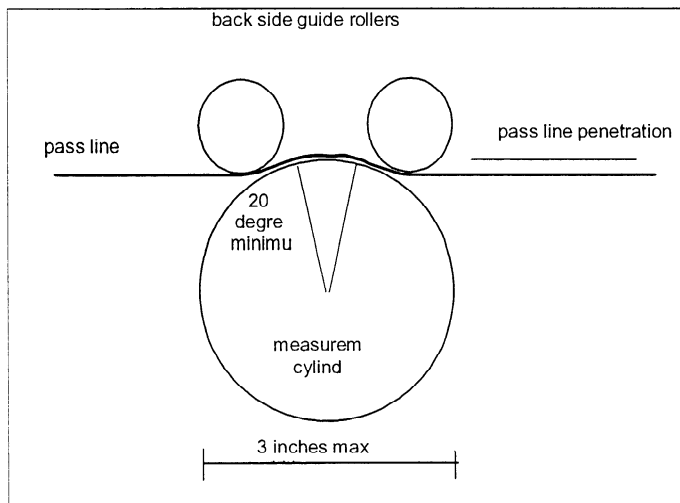


Figure 2. Sheet control configuration, showing the *backside* rollers creating a 20-degree sheet wrap over the measurement cylinder.

One important feature of the current measurement system is that the cylinder steers across the process as the scanner scans (Figure 3). This has two direct effects. The first is that there is no slippage between the measurement cylinder and the process, minimizing any possible marring of the sheet. The second benefit is that the signal strength during scanning is greatly enhanced. A small amount of slippage between the transducers and the sheet can easily reduce the signal strength by a factor of 100 (kinetic coupling of acoustic energy into the sheet vs. static).

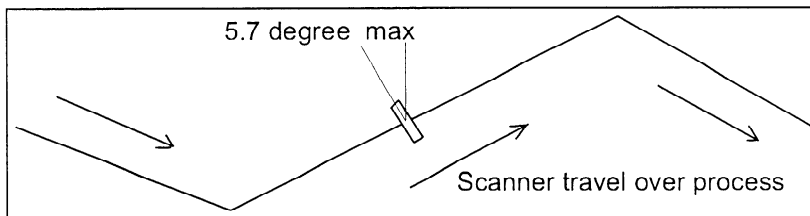


Figure 3. Depiction of sensor path over the process during scanning.

The measurement data rate depends on the process speed. The measurements of shear and longitudinal stiffnesses take place once each per revolution of the cylinder. The measurement cylinder has a circumference of approximately 9 inches. Therefore, at a process speed of 1800 fpm the data rate is about 40Hz.

ON-LINE RESULTS

Moisture and Temperature

Moisture has a profound influence on the stiffness of paper and therefore is addressed first. This interaction is effectively explained as the typical effect of a plasticizer (in this case water) on paper (cellulose).

Stiffness Value	$B_M(\% / \%)^3$	$B_T(\% / C)^3$
Shear(time of flight method)	5.6	0.45
Md (resonance method)	4.7	0.38

Md (resonance method)	4.1	0.33
Cd (resonance method)	5.9	0.49

Table 1. Moisture and Temperature compensation gains used in the current sensor system.

The following operators trend display page, Figure 4., shows the effect of moisture on the shear and the longitudinal specific stiffness of 55# Linerboard. The trend is for one hour and the data is scan averages of shear and longitudinal specific stiffnesses and percent moisture. The process temperature was approximately constant at 78C. At times before the ruler line indicator β_M was set at 0 (no moisture compensation) and at times after the ruler β_M was set at 5.2 for both shear and longitudinal stiffnesses.

When moisture compensation is off, the specific stiffness is the as measured value on the process including the influence of moisture. It is clear that as moisture increases the shear and longitudinal stiffnesses decrease. Wet paper gets soggy and limp. When β_M is set to 5.2 the influence of process moisture is effectively removed, suggesting that the lab measured stiffnesses of the paper over this time period would show only stiffness changes that were reel and not just the result of variable process moisture.

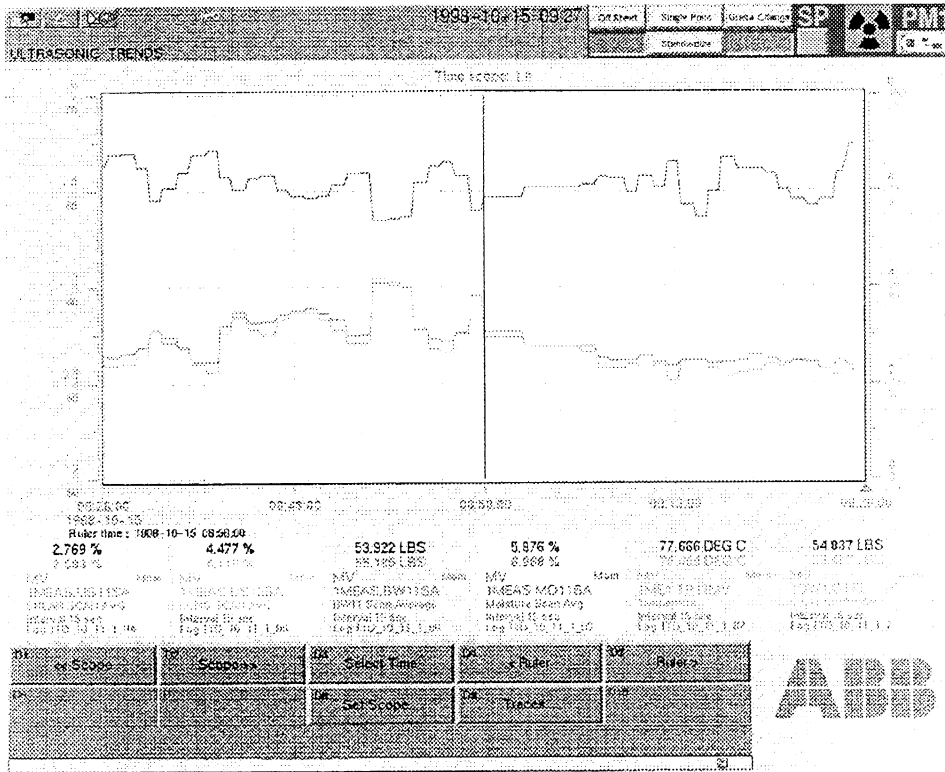


Figure 4. Trend displays showing scan averages for percent moisture, and shear stiffness, and extensional stiffness. The vertical ruler line indicates when moisture and temperature compensation was turned on. Basis weight, Sheet temperature, and the Basis weight controller set point have been hidden from the display for clarity.

Drying Restraint

Paper dried under restraint (i.e. not allowed to shrink) has a higher stiffness than paper that is allowed to shrink during drying. In addition, paper that is stretched slightly (<5% ΔL/L) while still wet (> ~20%M) will also have a higher stiffness than paper that is not stretched. Typical scanner profiles for shear and longitudinal specific

stiffnesses are presented in Figure 5. Both profiles exhibit a profound frowned shape. These shapes are attributed to the nonlinear shrinkage of the paper web in the cross machine direction during drying.

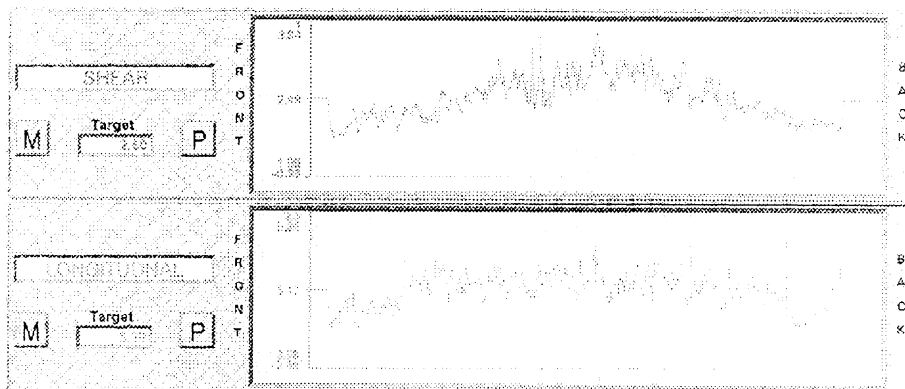


Figure 5. Profile displays showing shear and longitudinal specific stiffnesses.

On the centerline of the paper machine the web is restrained in both the machine direction and in the cross machine direction. On the edges of the machine it is only restrained in the machine direction and it shrinks in the cross machine direction. The frowned profile shapes are the direct result of the drying restraint conditions that exist on the paper machine. Sheet shrinkage at the edges results in a lower stiffness at the edges.

On-Line vs. Off-Line Profiles

As discussed previously paper machine profiles are frowned. These on-line profile shapes can be verified off-line. Profile verification is presented in Figure 6.

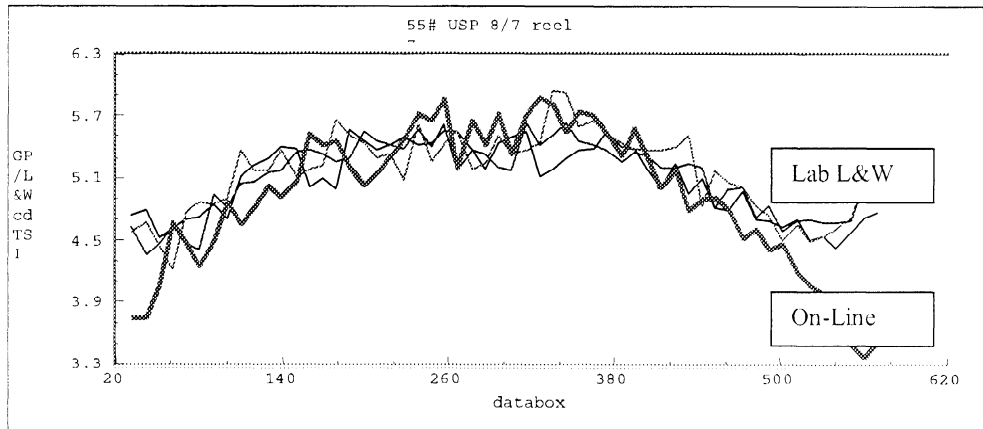


Figure 6. Comparison of off-line measured cross machine direction extensional stiffness with on-line measurement for 55-lb. Linerboard. Offline data was acquired using a L&W TSO tester under standard TAPPI test conditions. On-line data is a composite of 5-minutes of scanner data just prior to reel turn-up.

The 'Lab L&W' data set was collected on samples taken at reel turn-up. Three samples were acquired from the reel at the end of the paper machine, one each from three successive wraps. The samples were 12 inches in the MD by 258 inches in CD. Roughly 60 equally spaced CD TSI measurements were conducted on each sample. The 60 TSI measurements were then mapped back to the 600 data box profile from the Smart Platform. The on-line data was logged in the Smart Platform during five minutes prior to the reel turn-up and mapped to 60 data points.

Good correspondence is observed between the on-line and off-line profiles with the exception of the region above data box 500. The disparity between of the on-line and off-line profiles has not been explained yet and maybe due to the existence of dried in stresses on the machine, which relax by the time the lab tests are conducted.

Jet-to-Wire Ratio

One of the process parameters used to control 'strength' on the paper machine is the rush or drag of the jet relative to the wire. In general, the Mullen grades are manufactured with a rush-drag set point of 'zero' and high performance ring crush grades with positive rush-drag set point. The main effect is to increase the distribution of fibers in the cross-machine direction in the high performance grade.

The following Operators trend display page, Figure 7, shows Speed Trends (Machine Speed, Reel Speed, Wire Speed, Base sheet rush-drag, and Top sheet rush-drag). The time period is for one day.

During about a four period beginning about 5:00PM on the 15th the paper machine was running out of stock and the machine speed had to be cut back from about 1500 fpm to 1400 fpm. Rush-drag on the top and base sheets were not changed during this period, consequently, the rush-drag ratio or the ratio of rush-drag to wire speed did change. Table 2.

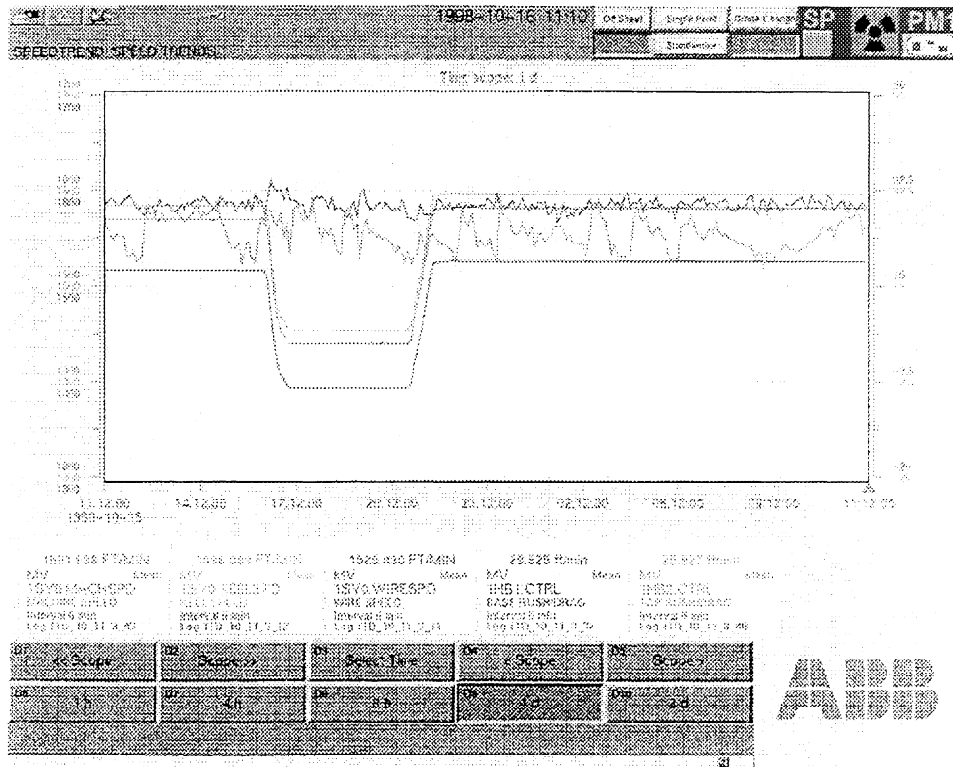


Figure 7. Operators QCS display page showing machine speed, reel speed, wire speed, base rush/drag, and top rush/drag.

Time period	Rush-drag / wire speed (%)
11:00 to 17:00	2.0
17:00 to 21:00	2.2
21:00 to 11:00	2.0

Table 2. Rush/drag ratio expressed as a percent of wire speed the three time periods of interest in Figure 7.

The corresponding ultrasonic stiffness trends from the QCS system (Shear Stiffness, CD Longitudinal Stiffness, and Basis weight) follow in Figure 8., along with line plots for the QC lab test data for Ring Crush and Ring Crush Index, Figures 9 and 10. Machine speed can be used as the point of reference into the trends.

It is evident from the CD Longitudinal Stiffness trend that there is a step increase going into the reduced speed time period beginning at 5:00PM on the 15th. The stiffness then decreases at the end of the period, however, not to its original value but some intermediate value and after another five hours to its original value. The Shear Stiffness did just the opposite, it decreased, then increased part way, and finally back to its original value. The QC Lab value for the CD Ring Crush and the Index experienced increases during the slow down period and persisted for about five hours afterwards. Basis weight was constant over the one-day period except for what appear to have been short term upsets. It is not clear at this time what the exact correlation relationships are between Stiffnesses and strength properties like Ring Crush and Ring Crush Index and this is also part of the on-going activity at the mill. Once the relationships are clearly defined it is presumed that fiber could have been reduced during the roughly ten-hour period and the target 'strength' could have been meet.

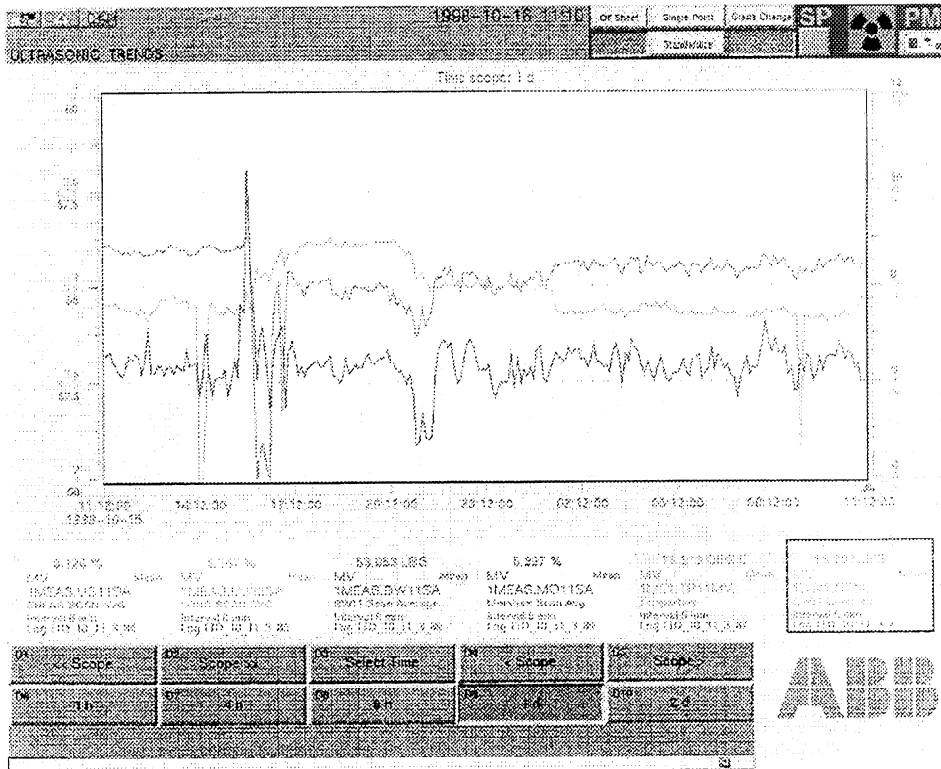


Figure 8. . Operators QCS display page showing Shear Specific Stiffness, Longitudinal Specific Stiffness, and Moisture. Basis weight, Sheet temperature, and the Basis weight controller set point have been hidden from the display for clarity.

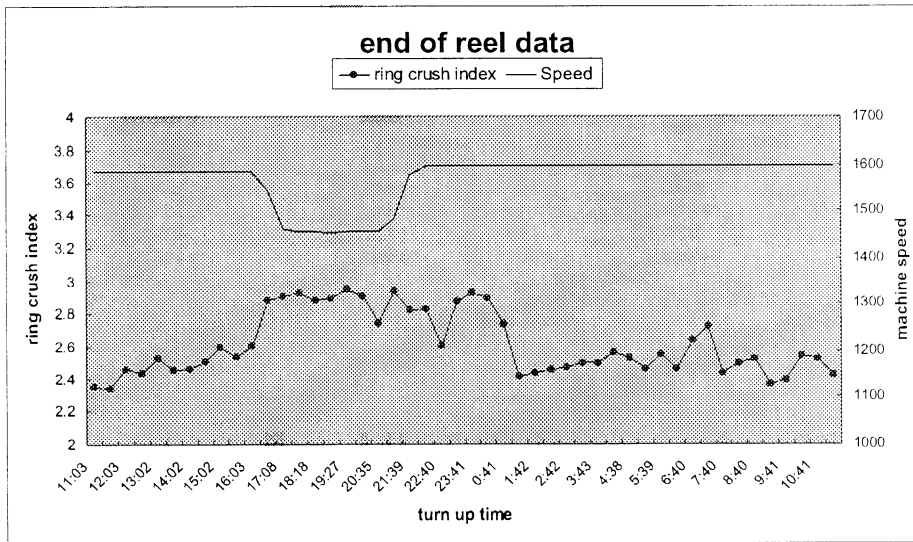


Figure 9. Roll Management data for Ring Crush Index for the same time period as shown in Figures 7 and 8.

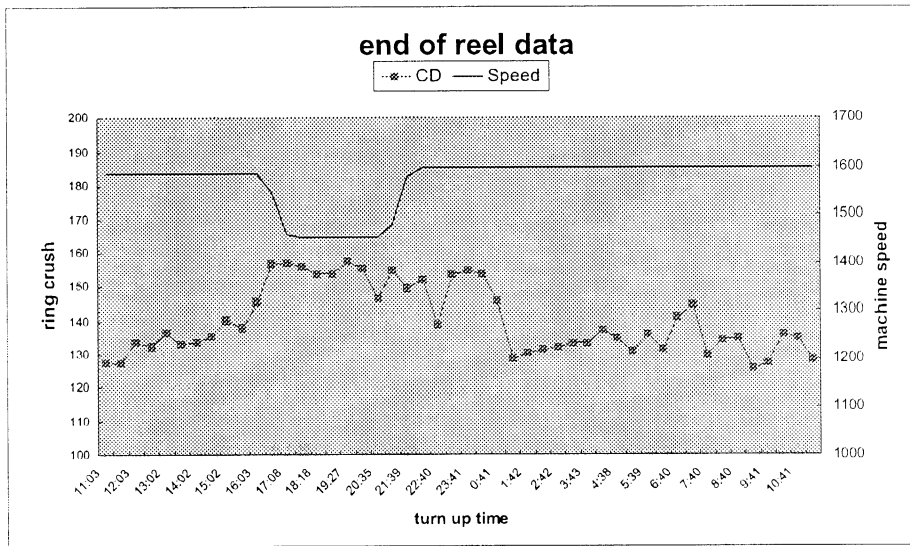


Figure 10. Roll Management data for Ring Crush Index for the same time period as shown in Figures 7 and 8.

SUMMARY

ABB has developed a new on-line Ultrasonic Specific Stiffness Sensor. The sensor has been successfully installed on a paper machine producing Linerboard in the range of 40-90-lbs/1000 sq.-ft. and the measurement has operated reliably. This report described briefly the sensor and measurement physics and summarized the on-line measurement performance.

Many of the relationships expected between paper stiffness, process parameters, and paper strength are confirmed. The impact of process upsets and grade changes on stiffness properties are tracked. Increasing the rush-drag ratio is

shown to increase both the on-line CD Specific Stiffness and the QC laboratory CD Ring Crush and Ring crush indexes. These and other results can provide the basis for improved product quality and reduced production costs.

REFERENCES

1. Kopin, B., *On-line measurement of strength and elastic properties of a running paper web*, TAPPI Journal: Vol. 82 No. 5 May 1999
2. Reed, W. M. and Brown, T., *Online Strength Sensor Improves Linerboard for MacMillan Bloedel*, Pulp and Paper: March 1999
3. Williams, P. and Pankonin, B. M., U. S. Patent 5,479,825 (Jan. 2, 1996)
4. Berger, B.J., Habeger, C.C., Pankonin, B.M., *The Influence of Moisture and Temperature on the Ultrasonic Viscoelastic Properties of Cellulose*, Journal of Pulp and Paper Science: Vol. 15 No. 5 Sept 1989

ACKNOWLEDGEMENT

The authors wish to gratefully acknowledge Maclin Hall, Theodore Jackson, and Andy Brown all of The Institute of Paper Science and Technology for their continued assistance and support of this project work.

NON-CONTACT ULTRASONIC STIFFNESS MEASUREMENTS

STATUS REPORT

FOR

PROJECT F031

**John Waterhouse
Chuck Habeger
Emmanuel Lafond
Jimmy Jong
Joseph Gerhardstein**

**Institute of Paper Science and Technology
500 10th Street, N. W.
Atlanta, Georgia 30318**

DUES-FUNDED PROJECT SUMMARY

Project Title: Fundamentals of Accelerated Creep
Project Number: F031
PAC: Paper Physics

Project Staff

Principal Investigator: John Waterhouse, Chuck Habeger
Research Support Staff: Emmanuel Lafond, Jimmy Jong, Joe Gerhardstein,

FY 99-00 Budget: \$82,000
Allocated as Matching Funds: \$82,000

Time Allocation:

Principal Investigator 1: 5%,
Principal Investigator 2: 10%
Research Support Staff: 20%, 10%, 5%

Supporting Research:
 Ph.D. Students

RESEARCH LINE/ROADMAP: Line #11, 12

PROJECT OBJECTIVES: Design and construct an automated laboratory laser-ultrasonic stiffness instrument

PROJECT BACKGROUND: This is a matching project for a DOE on-line laser ultrasonic contract. The goals of the two projects are complementary. We plan to use fundamental advances from the DOE work to configure a laboratory tester. Innovations in signal analyses, optical and electronic design, interferometry, and laser technology will be dual applications.

DELIVERABLES: *Techniques for laser ultrasonic signal detection and analysis on paper. An automated apparatus to do routine laboratory testing.*

SCHEDULE:

Task Descriptions (example)	1999 Apr - Jun	1999 July - Sept	1999 Oct - Dec	2000 Jan - Mar	2000 Apr-Jun
1. signal analysis methods	-----	-----	-----	-----	
2. Instrument design				-----	-----

DISCUSSION:**Ao Signal Analysis****Introduction:**

In contrast to contact ultrasonic testing, laser ultrasonics is most efficient at exciting and detecting Ao wave motions in paper webs. In fact, before the advent of laser ultrasonics [1], high frequency Ao waves had not been detected in paper. As we will demonstrate, analyses of this mode provide determinations of elastic parameters which are of practical importance and which have hitherto gone unmeasured. Bending stiffness (or its close cousin flexural stiffness) is the elastic parameter that determines the structure rigidity of paper structures and sheets. Laser ultrasonics will provide the first nondestructive measure of this important paper property. Furthermore, traditional bending stiffness measurements on lightweight papers are fraught with experimental difficulties. Laser ultrasonics flexural stiffnesses will be the first reliable, repeatable measures for lightweight papers. Out-of-plane shear rigidity is the other elastic parameter that will be gleaned from Ao dispersion curves. This parameter is also determined by contact ultrasonics. However, contact values cannot be trusted on sheets with basis weights below about 200 g/m^2 . Laser ultrasonics shear rigidities will be valid down to at least 60 g/m^2 . Thus, especially for lightweight papers, Ao analysis of laser ultrasonic signal opens the door for the determination of a new set of paper elastic parameters.

There are different modes of harmonic plane wave propagation in plates, and laser ultrasonic testing is best for those with large out-of-plane motions. In the low frequency regime, where for practical reasons paper operation is limited, there are three distinct modes of interest. One of these is a nondispersive, transverse shear mode that propagates with velocity squared equal to the in-plane shear modulus divided by the density. It generates no out-of-plane motion, and it is a poor candidate for laser ultrasonic analysis. The So mode is also basically an in-plane motion. At low frequencies, it is nondispersive, and its velocity squared is the planar stiffness divided by the density. It has been detected with laser ultrasonics, and specific planar stiffnesses can be determined by time of flight methods. The lion's share of the laser ultrasonic signal in paper sheets is concentrated in Ao motion. At low frequencies, this is principally a bending action with much out-of-plane motion. It propagates dispersively: phase velocity depends on frequency. Pulses of finite width will widen as they propagate since the different frequency components travel at different velocities. At low frequency, in the limit of pure bending motion, phase velocity increases with frequency: velocity squared equals the angular frequency times the ratio of planar bending stiffness to basis weight. At higher frequencies, the Ao transcends into a surface wave. Its velocity squared plateaus at about 90% of the out-of-plane shear stiffness divided by the density. Away from the excitation point, Ao displacements, generated from short laser blasts, become long pulses with their high frequency components arriving first. For paper-like materials with uncertain calipers, it appears from this cursory discussion that bending stiffness divided by basis weight and

out-of-plane shear rigidity (shear stiffness times caliper for uniform plates) divided by basis weight are the elastic parameters most likely to be measured from an Ao analysis.

Paper Elastic Parameters from Ao Dispersion Curves:

Newton's second law dictates that mechanical disturbances in an infinite, elastic material must obey wave equations. The harmonic solutions to these are plane waves. In every direction of propagation, there are two independent plane wave solutions. In an elastically anisotropic medium, one of these, the quasi-longitudinal mode, will have particle displacement more-or-less parallel to the direction of propagation, whereas the other (the quasi-transverse) will have particle displacement more-or-less perpendicular to propagation. The velocity of the longitudinal mode depends more-or-less on a normal mass-specific stiffness, and will generally be greater than that of the transverse mode, whose velocity depends more-or-less on a mass-specific shear stiffness. The bulk waves are nondispersive, but their velocities do depend on the direction of propagation.

Harmonic disturbances in an anisotropic plate must meet the stress free boundary conditions at the surfaces. With the exception of the transverse shear wave, none of the bulk waves qualify. However, there are combinations of quasi-longitudinal and quasi-transverse waves that do meet the boundary conditions [2]. These combinations are called plate waves. The Ao mode is a particular plate wave for which the in-plane motion is anti-symmetric about the center plane and the out-of-plane motion is pronounced. The angles of propagation of bulk waves that combine to meet the surface boundary conditions change with frequency. Therefore, the Ao phase velocity along the plate is also a function of frequency. The dispersion relation (plate phase velocity graphed versus frequency) is a complicated function of the density and the four elastic parameters in the plane of propagation [2]. For a homogeneous material, it can be mathematically determined from the roots of a 4x4 determinate whose elements are functions of the sheet density and thickness and of the four independent elastic constants in the plane of propagation. As a demonstration, Figure 1 displays two theoretical Ao dispersion curves for plates with elastic properties typical of paper. The elastic parameters used to construct the theoretical dispersion curves for one of these were taken from contact ultrasonic measurements on an 80 g/m² machine-made copy paper tested in the CD, whereas the other came from measurements on a 210 g/m² bleached kraft handsheet. Notice that the curve representing the heavier sheet has a greater low-frequency slope and asymptotes to a surface wave at a lower frequency.

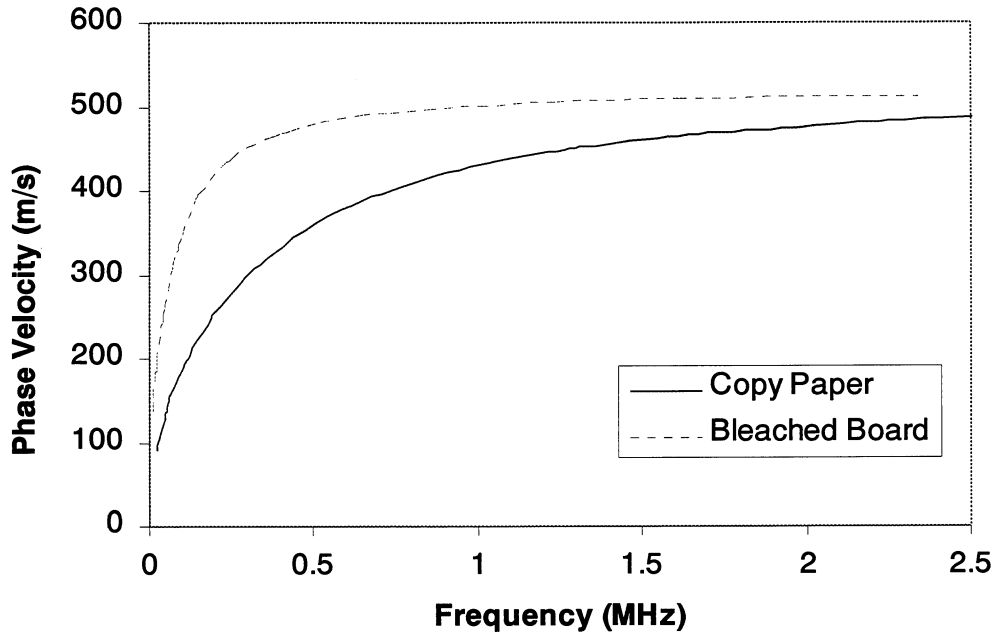


Figure 1
Typical Ao Dispersion Curves for Lightweight Paper and a Paperboard

Our goal is to experimentally construct dispersion curves from broadband laser ultrasonic experiments; however, there are some fundamental paper limitations. Paper has a microstructure with elements on the order of 0.05 mm in diameter. This microstructure attenuates coherent mechanical disturbances through Rayleigh scattering. This attenuation increases rapidly as frequency increases, and the wavelength approaches the scale of the heterogeneity. When the scale is around 0.01 times the wavelength, attenuation becomes excessive. Transverse bulk waves in paper have a velocity of about 2 mm/ μ sec, and above about 1 MHz plate waves don't propagate well. Through active adaptation, laser ultrasonic interferometers block out low frequencies vibrations. This is a great benefit (especially for on-line application) as it makes them insensitive to mechanical vibrations. However, it also limits resolution of the dispersion curves at low frequency. As you will see directly, the net result of all these frequency restrictions is that it is practical to expect to decode Ao disturbances in paper in the frequency range of 40 to 400 KHz. Notice, from Figure 1, that this gives us most of the upward swing of the Ao dispersion curve and that we get close to the surface wave asymptote for thicker papers.

A dispersion relation gives phase velocity versus frequency as a function of density, caliper, and four bulk elastic constants in the plane of propagation, e.g. C_{11} , C_{33} , C_{13} , and C_{55} . A straightforward method of deducing elastic properties from an Ao dispersion curve would begin by measuring caliper and basis weight and calculating density. Then, an optimization routine would be utilized to find the combination of C_{ij} 's that give a best fit to the dispersion curve. These C_{ij} 's would become the laser ultrasonic

estimates of stiffnesses. The approach has shortcomings. First, because of paper's inhomogeneous character, rough surface, and high out-of-plane compressibility, paper caliper is a poorly defined parameter. It is best to describe paper in terms of mass specific properties rather parameters, which do not require a thickness definition. Secondly, the Ao dispersion relationship is not equally sensitive to all four of the elastic stiffness coefficients. As we will soon show, it is almost totally defined by parameters in the region of practical application.

In the attached appendix and later in the text, we argue that, without input of basis weight or thickness, two elastic parameters can robustly be decoded from the Ao dispersion curve. They are the flexural stiffness divided by the basis weight (D/BW) and the shear rigidity divided by the basis weight (SR/BW). In the appendix, we derived a gross simplification for the Ao dispersion curve:

$$c^4 + \omega^2 (D/SR) c^2 - \omega^2 (D/BW) = 0 \quad (1)$$

We will demonstrate that it is highly accurate for paper in the range of experimental practicality. In Eqn. (1), c represents the frequency-dependent phase velocity, and ω is the angular frequency. The flexural stiffness of a plate is the bending moment per unit width divided by the inverse of the radius of curvature in bending. The shear stiffness is the ratio of shear load per unit width to the out-of-plane shear deflection angle. These are elastic properties of the plate that directly relate applied load to deflection. By simply fitting the experimental Ao dispersion curve to the quadratic equation above, we can find D/BW and SR/BW [(D/BW)/(D/SR)]. Then we can multiply the basis weight, a well-defined quantity even for paper, by parameters taken from the Ao dispersion curve and directly determine the elastic parameters that define plate bending and shear compliances. If the plate is homogeneous, isotropic, and smooth, the flexural stiffness and shear rigidities can be written in terms of engineering elastic constants and thickness (t) as $D = Et^3/12(1-\nu^2)$ and $SR = 5Gt/6$.

Next we want to compare the Ao dispersion curves as estimated by Eqn. (1) with the full-blown solutions of the 4x4 determinate as demonstrated in Figure 1. In doing this, we find it convenient to plot the dispersion curve in a different manner. Notice from Part A of the Appendix that a pure bending mode plane wave will have a phase velocity that decreases as the square root of the frequency. The value of $c/f^{1/2}$ is $(2\pi)^{1/2}(D/BW)^{1/4}$ independent of frequency. Therefore, to accentuate the deviation from pure bending motion, we plot the dispersion curve as $c/f^{1/2}$ against f . This is done in Figure 2 and 3 respectively for the copy paper and the bleached board parameters used in Figure 1. Notice particularly that the detailed dispersion curves deviate from the horizontal pure bending lines (also drawn) but intersect with them at zero frequency. Also plotted are the simplified dispersion curves from Part B and Part C of the Appendix. These are solutions to flexural wave equations with first order corrections for shear deformation. The Part C development has a more sophisticated analysis of the shear stress distribution through the sheet. In the end, the difference is that Part B uses Eqn. (1) with $SR = Gt$, whereas Part C amends SR to $5Gt/6$. Notice that the Part C development makes almost a perfect fit up to about 500 KHz. Since Ao paper propagation has very little energy above about 400 KHz,

it is fair in most cases to employ the simple quadratic of Eqn. (1) as a huge simplification of the rigorous dispersion equation. Very thick paperboards will show discrepancies at lower frequencies, and use of Eqn. 1 should be looked at more critically.

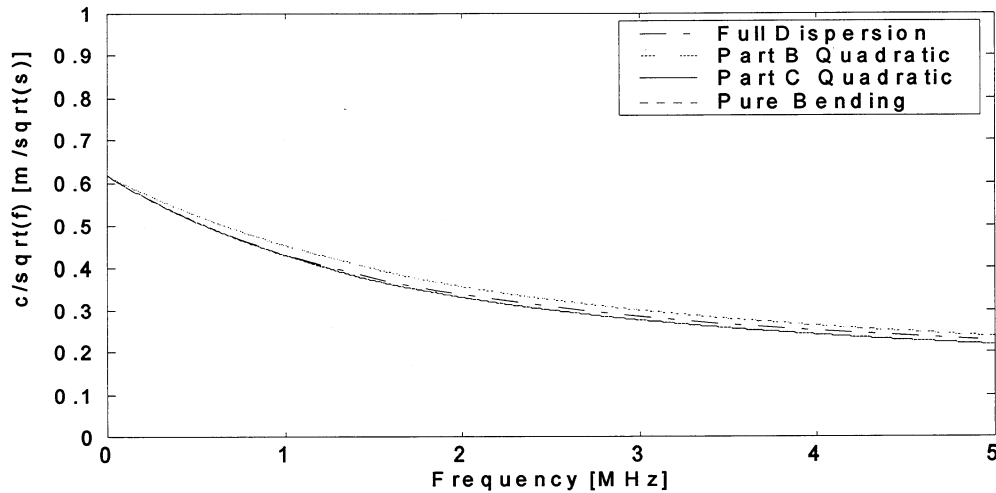


Figure 2
A $c/f^{1/2}$ Dispersion Curve for a Lightweight Paper
Compared with Bending and Bending Plus Shear Approximations

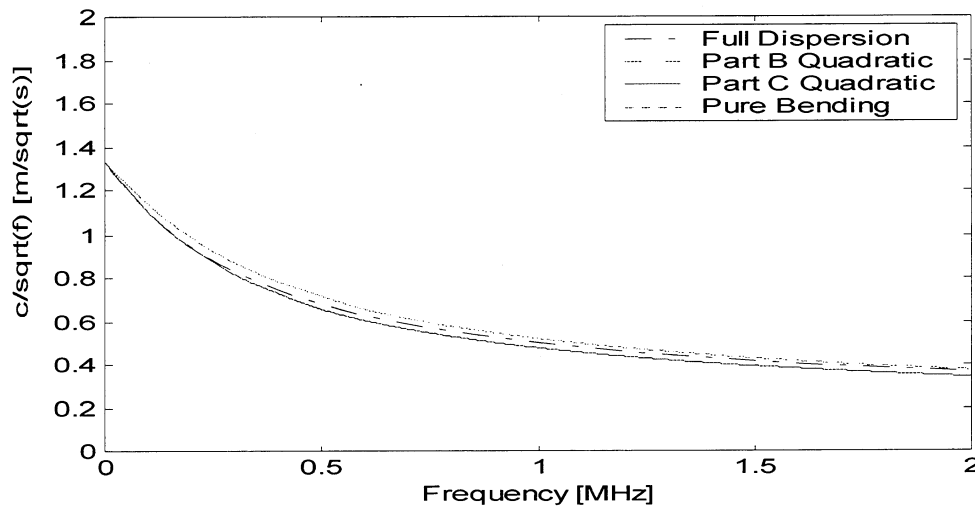


Figure 3
A $c/f^{1/2}$ Dispersion Curve for a Bleached Paperboard
Compared with Bending and Bending Plus Shear Approximations

According to Eqn. (1), the dispersion equation deviates from pure bending because the shear rigidity is finite. At shorter wavelengths (higher frequencies), both shear and bending deformations contribute to plate compliance. Notice that, in the

frequency range of experimental laser ultrasonics, out-of-plane shear deformation has significant effect on the dispersion curve. These shear influences should be evident in phase velocity measurements, and laser ultrasonic analysis should be capable of determining out-of-plane shear rigidity as well as flexural stiffness.

Phase Unwrapping:

For examples of typical Ao disturbances as detected by laser ultrasonic equipment on a lightweight paper, please inspect Figure 4. The graph at the top-left is the signal obtained on an 80 g/m^2 machine-made copy paper tested in the cross-machine direction with 1 cm separation between the excitation and the detection points. The separation was 2 cm for the top right curve. The time-of-arrival is clearly greater at the longer separation, but simple time-of-flight analyses are not proper. The Ao mode propagates dispersively, and the signals spread out over wide time-bands with high frequency components arriving first. Notice the curves are flat in the beginning. This is because the signals have been artificially time-windowed to cut out the So signals that are complete before the high frequency portions of the Ao mode arrive. Figure 5 displays similar curves for the 210 g/m^2 bleached kraft paperboard handsheet taken at 0.5 and 1 cm transducer separations. Notice that the low frequency portions of the signals propagate much faster in the stiffer board. The board wavelengths are longer, and the signals are much less time-dispersed.

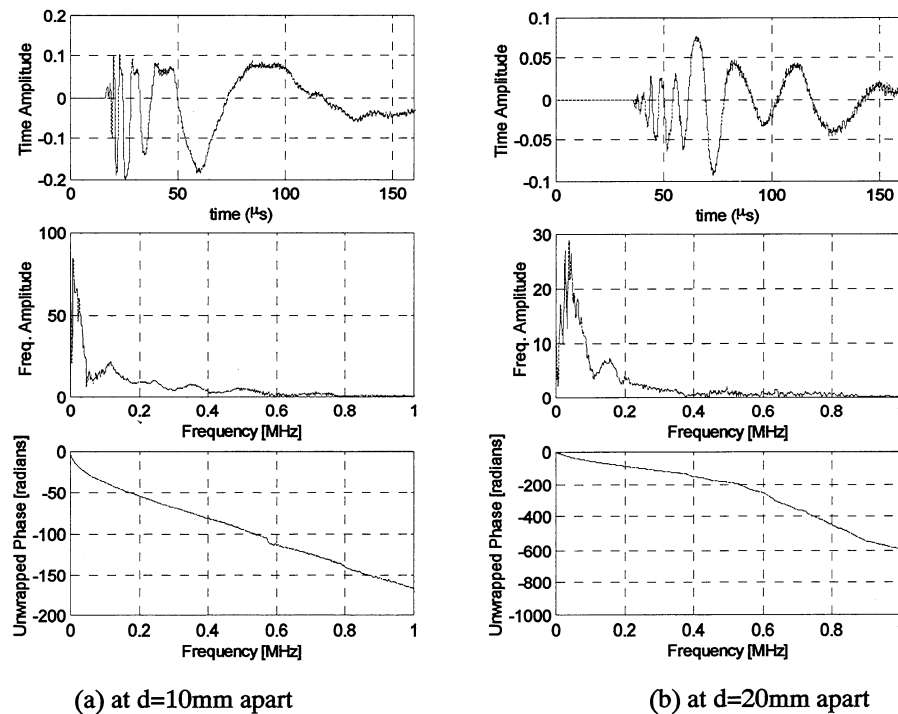


Figure 4
Time and Frequency Domain Laser Ultrasonic Signals
Propagating in the Cross Direction on a Lightweight Paper

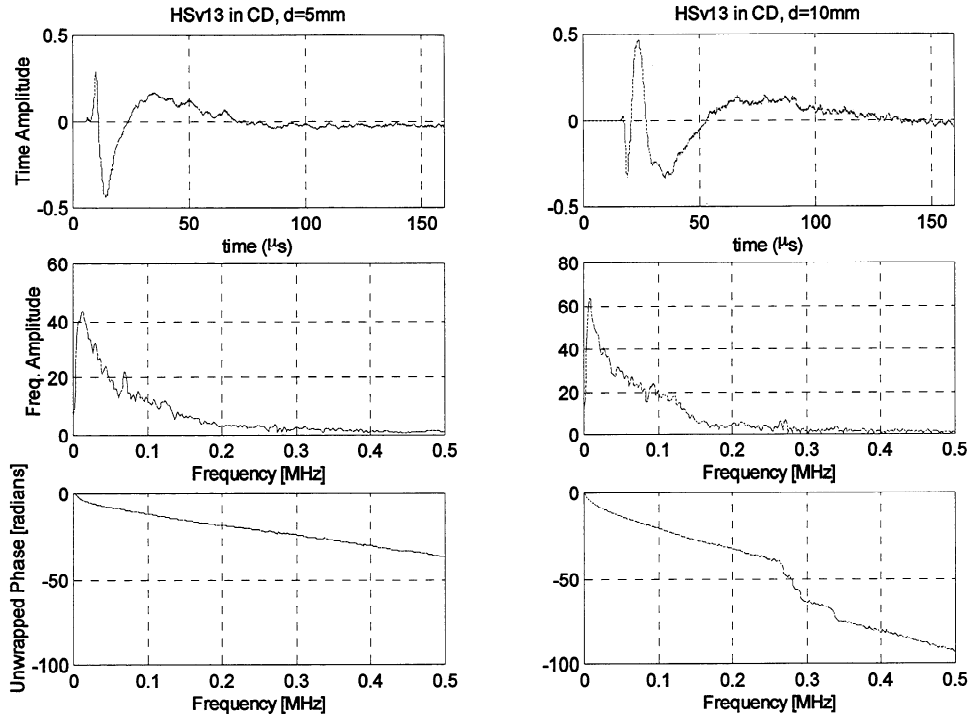


Figure 5
Time and Frequency Domain Laser Ultrasonic Signals
Propagating in a Bleached Paperboard Handsheet

In order to realize frequency-dependent phase velocity measurements, we need to do Fourier analyses of the two laser ultrasonic signals. The amplitude and phase components of the Fourier transform are plotted in the lower parts of Figures 4 and 5. In order to make the phase versus frequency plots continuous, we performed a preliminary unwrapping of the phase information. From the magnitude of the amplitude signals and regularity of the phase signals, notice that (except for the bleached board at 1 cm) the signal strengths are adequate up to at 500 KHz.

Now, we want to calculate the frequency-dependent phase velocities from the phase plots. The phase velocity at a given frequency is $\Delta d(\omega/\Delta\phi)$, where Δd is the difference in separations (1 cm for copy paper and 0.5 cm for bleached board) between the two signals and $\Delta\phi$ is the difference in phase. We cannot naively take the phase differences at the two distances because they are unknown to multiples of 2π . We must “unwrap” (add the correct multiple of 2π) properly so as not to get anomalously high or low results. At low frequency, the phase velocity of the A_0 mode approaches zero. For a given spacing difference, actual phase differences decrease rapidly with frequency. Below some frequency, which depends on spacing difference, $\Delta\phi$ will be less than 2π , and unwrapping will be trivial. For unwrapping to be unambiguous, it is important to have low frequency components in the signal. Of course, the unwrapping could be

simplified by decreasing Δd , but this would reduce the resolution in the phase velocity determinations. The value of Δd must be chosen as a compromise between resolution and surety of unwrapping. The inclusion of low frequency components in the signals will make this tradeoff less painful.

We demonstrate our unwrapping technique using the data of Figure 4 and 5 as examples. First, we draw the $c/f^{1/2}$ dispersion curves from the Fourier transform phase data. We do this with all reasonable unwrappings (integral 2π additions to the raw differences between phases). Look to Figure 6 and 7. Now, which of these are the correct experimental dispersion curves? The issue is clearer for the bleached board experiment, so we discuss it first. In reference to Eqn. (1) and Figures 2 and 3, remember that the $c/f^{1/2}$ dispersion curves at low frequency approach a finite zero-frequency limit almost linearly from below. Those dispersion curves which are “overwrapped” (too many extra 2π 's added) have $c/f^{1/2}$ values which approach zero at low frequency. Examples of overwrapping are easily identified in Figure 7. Here, the -2π and -4π unwrapping actually begin to fall off in the good signal range as frequency decreases. They can be disqualified. When “underwrapping” takes place, the values of $c/f^{1/2}$ shoot off towards positive infinity as frequency decreases, and then at very low frequencies flip to negative infinity. These can also be ruled out. The $+2\pi$ unwrapping is clearly doing this. All that's left is the -0π unwrapping, and, as it should, it approaches a finite limit at zero frequency. It is obviously the right curve. Notice that highest curve that didn't run away at low frequency was the proper choice. It is a bit harder to make a decision for the copy paper (Figure 6). To insure a totally obvious selection, it would have been better to select a lesser separation difference. The -6π is the highest curve that doesn't run away at low frequency. It has an always increasing trend as frequency drops, whereas the -8π unwrapping is flat then trails off at the lowest energy containing frequencies. The -6π unwrapping is the right dispersion curve. This unwrapping by process of elimination will work fine as long as we maintain low frequency components in our A_0 signals and as long as we do not let separation differences get too large. We are pushing the limit in the copy paper demonstration, but we easily could have reduced the far separation.

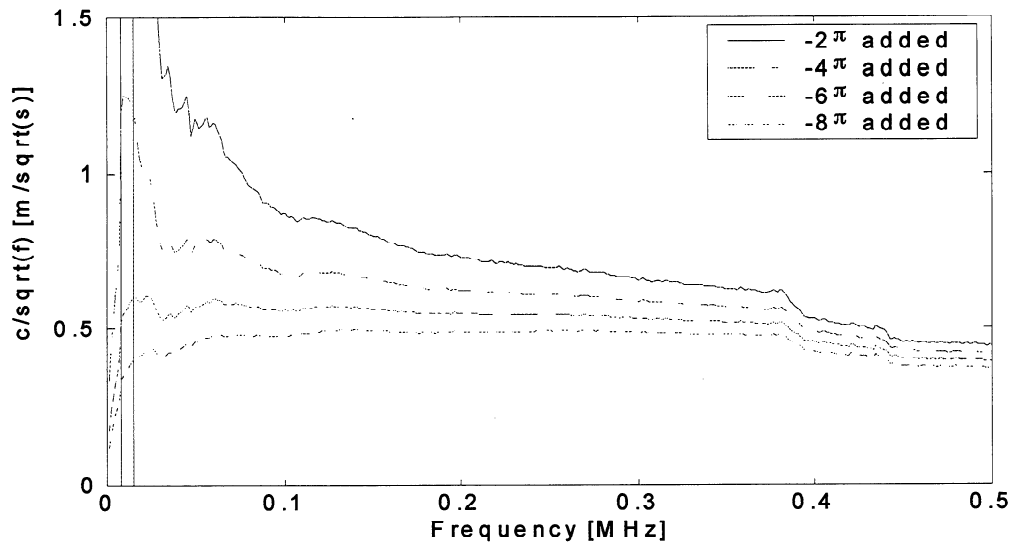


Figure 6
Experimental Lightweight Paper $c/f^{1/2}$ Dispersion Curves
Assuming Different Unwrappings

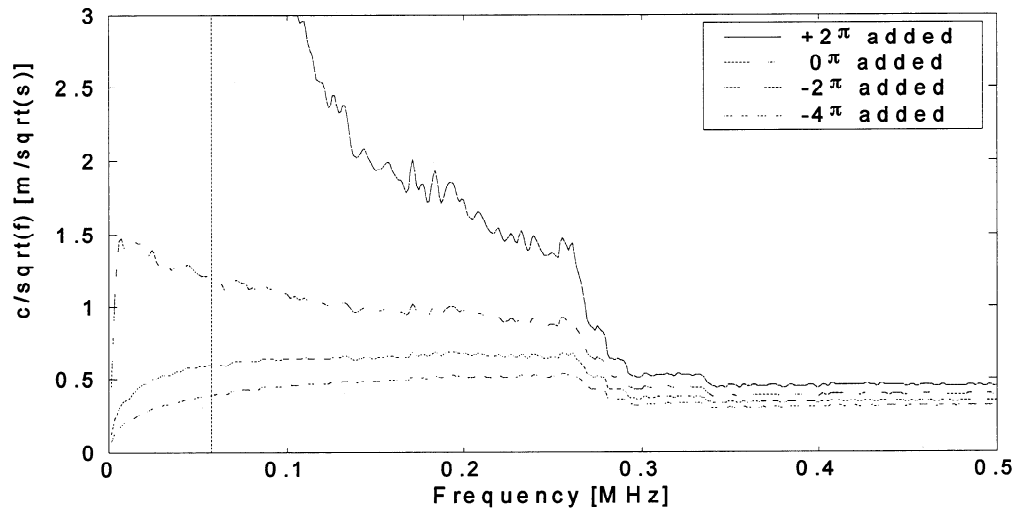


Figure 7
Experimental Bleached Paperboard $c/f^{1/2}$ Dispersion Curves
Assuming Different Unwrappings

Comparisons of Laser Ultrasonics and Contact Ultrasonics:

Now that we have successfully unwrapped the copy paper and bleached board experimental dispersion curves, we need to make flexural stiffness and shear rigidity determinations. The laser ultrasonic values of D and SR will be determined from least-squared fits of the quadratic equations of Eqn. (1) to the experimental dispersion curves

and the basis weight. Figures 8 (copy paper) and Figure 9 (bleached board) are blowups of the $c/f^{1/2}$ dispersion curves over frequency range in which Fourier amplitudes are large. The solid lines are the best-fit quadratic curves. The extracted elastic stiffnesses are copy paper $SR = 1.96 \times 10^4$ Nt/m and $D = 2.47 \times 10^{-4}$ Ntm and bleached board $SR = 5.01 \times 10^4$ Nt/m and $D = 1.59 \times 10^{-2}$ Ntm.

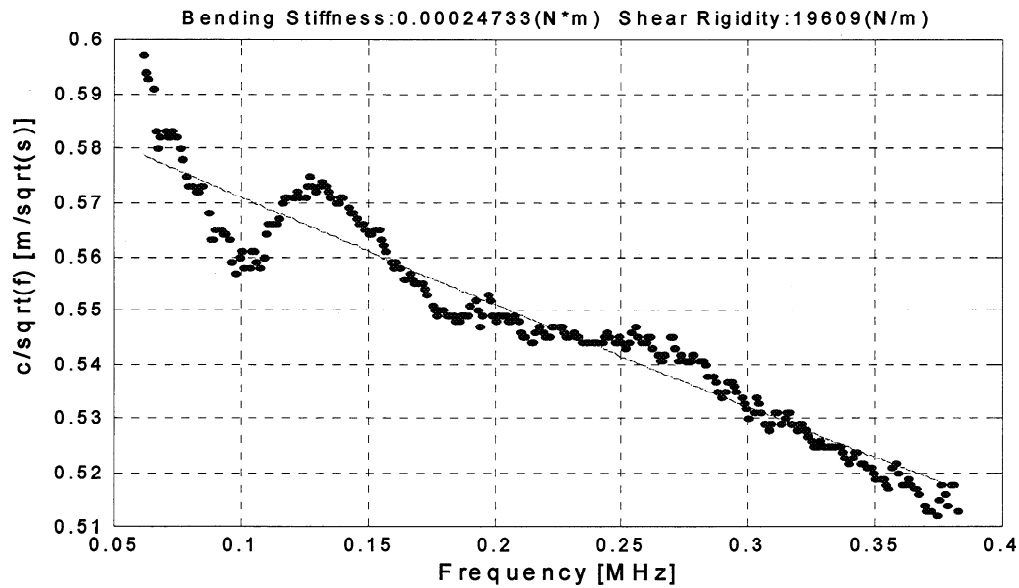


Figure 8

A Least-Squared Fit of an Eqn. (1) Dispersion Curve to Experimental Lightweight Paper Phase Velocities

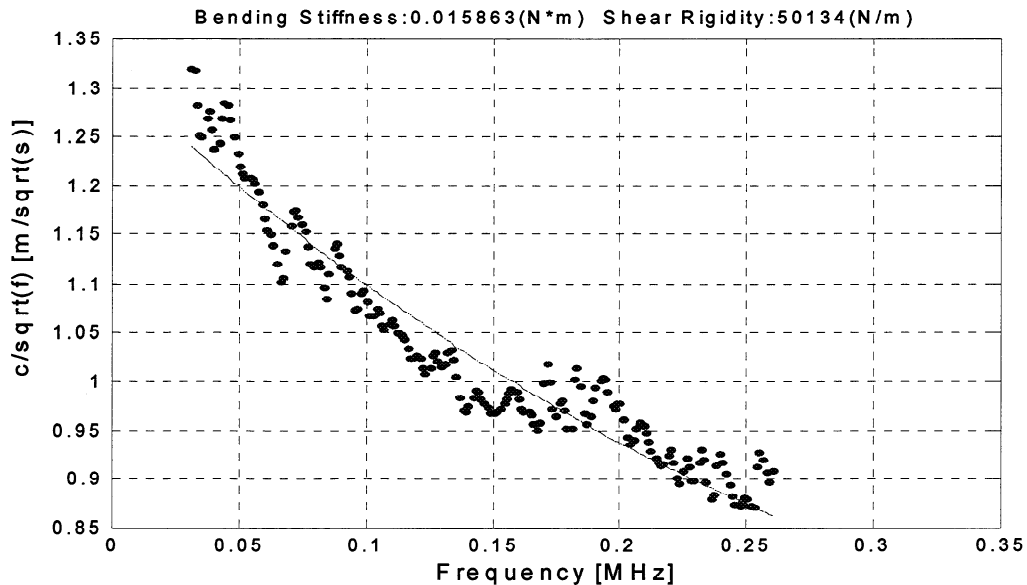


Figure 9

A Least-Squared Fit of an Eqn. (1) Dispersion Curve to Experimental Bleached Paperboard Phase Velocities

These parameters can also be calculated from contact ultrasonic measurements.

The out-of-plane shear velocity is measured with contact shear transducer by dividing the caliper, t , by an ultrasonic pulse delay time, ΔT . To get a shear rigidity one has to square the velocity multiply by the density and by the caliper $[SR = (5/6) (t/ \Delta T)^2 (BW/t) t]$. As has been discussed ad infinitum, caliper is a very tricky number. Contact ultrasonic shear rigidities depend on caliper squared. Laser ultrasonic stiffness calculations require no caliper determinations. Also, contact measurements are made with the sheet compressed at 50 KPa between platens, whereas laser results are for free sheets. This undoubtedly will have an influence on comparisons. Finally, because of the interference of multiple reflections with the once-through signal, out-of-plane times-of-flight are very suspect on samples as thin as copy paper. The shear stiffnesses, calculated from contact ultrasonics times-of-flight and soft platen caliper, are copy paper $SR = 1.88 \times 10^4$ Nt/m and bleached board paper $SR = 5.10 \times 10^4$ Nt/m. This embarrassingly close agreement of the shear rigidities between the two experimental techniques is surely fortuitous.

Values of flexural stiffness can be estimated from contact in-plane ultrasonics and a caliper measurements ($D = (\Delta d/ \Delta T)^2 (BW/t) t^3/12$), where Δd is the difference in in-plane transducer separations and ΔT is the time-of-flight for longitudinal waves. Again, the calculation depends on caliper squared. This time, however, the paper is not under load during contact testing, and values on thin paper are not of special concern. On the other hand, the contact calculation assumes homogenous stiffness properties through the sheet, and inside to outside stiffness variability can have big effects on sheet flexural stiffness. Analyses of the A_0 dispersion curves provide the only true ultrasonic bending stiffness measures. The contact results are, for copy paper, $D = 2.87 \times 10^{-4}$ Ntm and, for bleached board, $D = 1.61 \times 10^{-2}$ Ntm. This time, there is a 10% difference in copy paper numbers, but nonetheless the comparison is better than we rightly should expect.

Summary:

We contend that we have demonstrated the following points. (1) For purposes of laser ultrasonic analysis of paper, the god-awful 4×4 determinate A_0 dispersion equation can be reduced to a simple equation that is quadratic in phase velocity. (2) As long as one maintains good low frequency response and separation differences are not too great, A_0 phase velocities can be unambiguously unwrapped. (3) Flexural stiffness and out-of-plane shear rigidity can both be sensitively determined for experimental A_0 dispersion curves of papers. (4) A preliminary comparison of stiffnesses taken from laser ultrasonic and from contact ultrasonic measurements went remarkably well.

References:

- 1 Johnson, M., Ph.D. Thesis Georgia Institute of Technology (1996)
- 2 Habeger, C., Mann, R., and Baum, G., Ultrasonics 17, 57-62 (1979)

Appendix

First Order Ao waves in Inhomogeneous Plates

A) Warm-up: Zero Order Ao waves in Inhomogeneous Plates

Consider a thin plate that is homogeneous in-the-plane, but can vary arbitrarily in mass density and elastic stiffness in the out-of-plane direction. Assume that this plate can deform only by simple bending: Plane sections through the plate remain plane after deformation. Derive the dispersion equation ($c(\omega)$) for out-of-plane wave propagation as a function of the plate's basis weight (BW) and the flexural stiffness per unit width (D). Above, c represents the frequency dependent phase velocity of plane wave solutions to the governing wave equation, and ω represents the angular frequency.

First establish the neutral plane of the plate and set up a coordinate system such that the neutral plane is at $z = 0$ in the unstressed state. Consider plane waves ($z_b(x,t)$) propagating in the x -direction (along the plane of the plate, perpendicular to the z -direction). A cross-section of the plate perpendicular to the x -axis maintains a shear force per unit width ($V(x,t)$) (For this development V is taken as positive, if it is in the positive z -direction on a face whose outward normal is along the positive x -axis) and a moment per unit width $M(x,t)$. Applying N2L (Newton's second law) to an infinitesimal section of length, dx , and unit width gives Eqn. (A1).

$$\partial V/\partial x = BW \partial^2 z_b/\partial t^2 \quad (A1)$$

Next, doing a moment balance on this infinitesimal section and ignoring rotational inertia yields Eqn. (A2).

$$\partial M/\partial x = -V \quad (A2)$$

From basic bending analysis, we know that the maintenance of the plane section assumption causes M to equal D divided by the radius of curvature of the neutral axis. For small deformations ($\partial z_b/\partial x \ll 1$), the inverse of the radius of curvature is $\partial^2 z/\partial x^2$. Thus we have

$$M \approx D \partial^2 z_b/\partial x^2 \quad (A3)$$

Substituting M from Eqn. (A3) into Eqn. (A2), then substituting V from Eqn. (A2) into Eqn. (A1) gives us the wave equation for zeroth order out-of-plane plate waves:

$$BW \partial^2 z_b/\partial t^2 \approx -D \partial^4 z_b/\partial x^4 \quad (A4)$$

Traveling wave solutions ($z_b(x,t) = e^{i(kx-\omega t)}$) fulfill this wave equation only if

$$BW \omega^2 = D k^4 \quad (A5)$$

The phase velocity c is ω/k ; therefore, the dispersion equation ($c(\omega)$) under these simplifications is

$$c^2 = \omega(D/BW)^{1/2} \quad (A6)$$

The wave length, λ , is $2\pi/k$, thus wavelength as a function of angular frequency is:

$$\lambda = 2\pi(D/BW\omega^2)^{1/4} \quad (A7)$$

If the assumptions of this development are appropriate, a plot of phase velocity squared divided by frequency (f) versus frequency would produce a straight horizontal line of height $2\pi(D/BW)^{1/2}$. The ratio of a plate's flexural stiffness to basis weight could thereby be determined from an experimental dispersion curve.

B) A Dispersion Equation Including Out-Of-Plane Shear Deformations

When a beam or plate is secured at one end and vertically loaded at the other, the out-of-plane bending deformation depends of the cube of the length, whereas the out-of-plane shear deformation depends on length to the first power. Thus, shear deformations can be ignored in long beams, but not in short beams. Likewise, shear deformations can be disregarded in Ao plane waves when the wavelength is long, but must be considered as the wavelength decreases. From Eqn. (A7), note that the wavelength of a simple bending plane wave decreases with frequency. At high frequencies, the wavelength could become short enough that shear deformations will be of the order of bending deformations, and Eqn. (A6) would need to be modified.

Now, we assume that the total out-of-plane deformation arising from out-of-plane loads is the sum of bending and shear deformation: $z(x,t) = z_b(x,t) + z_s(x,t)$. As a first approximation, we assume that uniform shear stress prevails through sheet. If this were the case, a vertical load would deform in shear a section in the x-z plane such that the angle between the neutral axis and the x-axis goes from zero to ϕ everywhere. Assuming linear elasticity,

$$\phi = V/SR \quad (A8)$$

where SR represent the shear rigidity which for a homogeneous plate equals Gt (the shear modulus in the x-z plane times the thickness). The tangent of the angle ϕ equals the slope of neutral axis as deformed by shearing. If deformations are small, $\tan\phi \approx \phi$, and the shear deformation can be expressed in terms of the out-of-plane loading as

$$\partial z_s / \partial x = V/SR \quad (A10)$$

Now, N2L becomes $\partial V/\partial x = BW \partial^2 z/\partial t^2$, or

$$\partial V/\partial x = BW (\partial^2 z_b/\partial t^2 + \partial^2 z_s/\partial t^2) \quad (A11)$$

From Eqn. (A10), $\partial V/\partial x$ must also be

$$\partial V/\partial x = SR \partial^2 z_s/\partial x^2 \quad (A12)$$

and finally from Eqn. (A2) and Eqn. (A3), $\partial V/\partial x$ must in addition be

$$\partial V/\partial x = -D \partial^4 z_b/\partial x^4 \quad (A13)$$

We look for plane wave solutions ($z_b(x,t) = z_{ob} e^{i(kx-\omega t)}$, $z_s(x,t) = z_{os} e^{i(kx-\omega t)}$, and $V(x,t) = V_o e^{i(kx-\omega t)}$) that satisfy Eqns. (A11), (A12), and (A13). Eqns. (A11), (A12), and (A13) now become Eqns. (A14), (A15), and (A16).

$$ikV_o = -\omega^2 BW (z_{ob} + z_{os}) \quad (A14)$$

$$ikV_o = -D k^4 z_{ob} \quad (A15)$$

$$ikV_o = -SR k^2 z_{os} \quad (A16)$$

Solving for z_{ob} from Eqn. (A15) and z_{os} from Eqn (A16), then inserting into Eqn. (A14) shows that plane wave solutions are acceptable only if

$$1 = \omega^2 BW [1/(D k^4) + 1/(SR k^2)] \quad (A17)$$

Again, the phase velocity is ω/k . This time, phase velocity squared can be written in a quadratic equation in terms of ω^2 , D , and SR .

$$c^4 + \omega^2 (D/SR) c^2 - \omega^2 (D/BW) = 0 \quad (A18)$$

Solving Eqn. (A18) for c^2 (taking the positive root) gives

$$c^2 = 1/2 (-\omega^2 (D/SR) + [\omega^4 (D/SR)^2 + 4\omega^2 (D/BW)]^{1/2}) \quad (A19)$$

Doing a Taylor series expansion of the square root term establishes that, in the limit as frequency becomes small, Eqn. (A19) can be approximated as

$$c^2/\omega = (D/BW)^{1/2} - 1/2 \omega (D/SR) + 1/8 \omega^2 (D^{3/2} BW^{1/2}/SR^2) \quad (A20)$$

C) A Better Dispersion Equation Including Out-Of-Plane Shear Deformations

In developing Part (B), we assumed that the shear stress and strain were uniform through the thickness of the web. This is clearly not the case. The surfaces of plate are free, and zero shear stress boundary conditions must apply there. The shear stresses and strains are concentrated near the center. In actuality, the out-of-plane stress distribution is complicated. However, it is often approximated to first order assuming the normal stresses as calculated without shear deformations are unchanged when shear deformations are included. Below, we follow the Timoshenko approach (Timoshenko, S., and Woinowsky-Krieger, S., *Theory of Plates and Shells*, Engineering Societies Monographs 2nd Edition The Maple Press Co. York, PA (1950) p 165-170) to obtain a dispersion equation that includes to first order the non-uniform shear distribution.

Timoshenko's Eqn. (j) for the angle of deflection includes shear deformations. Under our nomenclature and sign convention, it is

$$\phi = \partial z / \partial x + 6V / 5SR \quad (A21)$$

Notice that instead of G in the last term of Eqn. (A21), Timoshenko has a term containing the Young's modulus and Poisson ratio. He reached this point through an earlier utilization of a relationship between G and E and ν that applies for isotropic materials. Paper, however, is very anisotropic. Therefore, we backed-up and reworked the equation to its proper form if isotropy were not assumed. That is, Eqn. (j) was achieved by assuming $G = E / 2(1 + \nu)$, and we inverted this relation to get Eqn. (A21).

In our notation, with spatial variation only in the x -direction, Timoshenko's Eqn (i) is

$$M = D \partial \phi / \partial x \quad (A22)$$

Substituting Eqn. (A22) into Eqn. (A21) gives our version of (j).

$$M = D \partial^2 z / \partial x^2 + (6D / 5SR) \partial V / \partial x \quad (A23)$$

Now, using the force balance of Eqn. (A2) to get rid on V in Eqn. (A23), we derive Eqn. (A24).

$$M + (6D / 5SR) \partial^2 M / \partial x^2 = D \partial^2 z / \partial x^2 \quad (A24)$$

Newton 2nd law (Eqns (A1,A2)) in terms of M remains

$$\partial^2 M / \partial x^2 = -BW \partial^2 z / \partial t^2 \quad (A25)$$

For a proper plane harmonic wave solutions, Eqns. (A24) and (A25) must be satisfied with $z(x,t) = z_0 e^{i(kx - \omega t)}$ and $M(x,t) = M_0 e^{i(kx - \omega t)}$. This gives us two equations involving M_0 and z_0 .

$$M_o - 6Dk^2M_o/5SR = -k^2Dz_o \quad (A26)$$

and

$$k^2M_o = -BW \omega^2 z_o \quad (A27)$$

These two equations will have a non-trivial solution only if

$$c^4 + (6/5)(D/SR)c^2\omega^2 - (D/BW) \omega^2 = 0 \quad (A28)$$

where, as before, the phase velocity, c , is ω/k . This is the dispersion equation accounting for a first order shear stress distribution. Notice that it differs only slightly (the 6/5 multiplier in the second term) from Eqn. (A18), the Part B dispersion equation. Since both developments employ the same average shear stress, V/t , it may seem strange that they predict different shear deformations. Physically, this is because the uneven distribution gives a slightly higher strain energy, and thereby a slightly greater deformation.

Solving Eqn. (A26) for c^2 gives the new quadratic relation.

$$c^2 = 1/2 (-\omega^2 (6D/5SR) + [\omega^4 (6D/5SR)^2 + 4\omega^2 (D/BW)]^{1/2}) \quad (A29)$$

The second order in frequency approximation of Eqn. (A29) analogous to the Part B Eqn. (A20) is

$$c^2/\omega = (D/BW)^{1/2} - 3/5 \omega (D/SR) + 3/20 \omega^2 (D^{3/2} BW^{1/2}/SR^2) \quad (A30)$$

At high frequency the full dispersion equation (derived with no assumption about deformations) of the A_o mode asymptotes to a constant velocity. Notice that Eqn. (A28) does the same. Ignoring the first term in Eqn. (A28) gives

$$c^2 \approx (5/6)(SR/BW) \quad (A31)$$

There is another way to look at this result. The Timoshenko analysis is effectively saying that, because of uneven shear stress distributions, the shear rigidity for a rectangular section is really $(5/6)Gt$ rather than Gt . Therefore, Eqn. (A19) and its friends are acceptable as long it was understood that the relationship between shear rigidity and shear modulus is $SR = (5/6)Gt$.

FUNDAMENTALS OF DIMENSIONAL STABILITY

STATUS REPORT

FOR

PROJECT F020

**Douglas Coffin
Barry Hojjatie
Kennisha Collins**

**Institute of Paper Science and Technology
500 10th Street, N. W.
Atlanta, Georgia 30318**

DUES-FUNDED PROJECT SUMMARY

Project Title: DIMENSIONAL STABILITY
Project Code: DIMSTAB
Project Number: F020
PAC: PAPER PHYSICS PAC

Project Staff

Principal Investigator: Douglas W. Coffin
Co-Investigators:
Research Support Staff: Barry Hojjatie, Kennisha Collins

PAC Subcommittee

FY 99-00 Budget: \$92,112
Allocated as Matching Funds: 0%

Time Allocation:

Principal Investigator: 1%
Co-Investigators: 0%
Research Support Staff: 60%

Supporting Research:

Special Students: None
External (Where Matching Is Used): None

RESEARCH LINE/ROADMAP: 11 Convertibility and End-Use Performance

Improve the ratio of product performance to cost for pulp and paper products 25% by developing: models, algorithms and functional samples of fibrous structures and coatings, which describe and demonstrate, improved convertibility and end-use performance.

PROJECT OBJECTIVE: Reduce the amount of paper rejected because of cockle through improved efficiency in identifying the causes of cockle and/or use of corrective measures to prevent cockle. To develop a science-based understanding of the dimensional stability of paper and paperboard, especially the phenomenon of cockle, and to apply these fundamental results to practical industrial problems.

PROJECT BACKGROUND: This project was initiated in July of 1994. The scope of work for this project is to gain an understanding of cockle in paper and to develop the knowledge and tools required to eliminate its occurrence. Cockle is a manifestation of the dimensional instability of paper due to local variations in the physical state of the paper coupled with a change in moisture content. The phenomenon of cockle is directly related to the mechanical, hygroexpansive, and physical properties of paper. These properties will be a result of the constituent materials and the papermaking process used to produce the sheet. With an understanding of how cockle occurs, steps can be taken to eliminate it by modifying the constituent materials or papermaking process.

Since cockle is inherently a complex problem and is influenced by many different factors, the advances made in this research program will benefit the scientific understanding in all areas of dimensional stability.

MILESTONES:

With the initial joint work with project F02102, we now have improved equipment for conducting cockle studies as a result of drying. More involved emphasis should be placed on this aspect.

We can modify formation by chemical and/or mechanical means and study the effect of formation on cockle.

DELIVERABLES:

Literature review of cockle: F020 Report 2, 1996

Fundamental Mechanism of Cockle and review of buckling: F020 Report 1, 2, 3

Analysis of hygrobuckling: (*Int. J. Nonlinear Mechanics* 40(6) 1999.)

Method to quantify cockle: (Shadow Moiré equipment, IPST)

Report on factors affecting cockle: (Report at end of Project)

Strategies to eliminate cockle: (Report at end of Project)

STATUS OF GOALS FOR FY 99-00:

Conduct handsheet study to determine the effect of papermaking parameters on cockle that develops after initially flat and dry sheets are exposed to high humidity. (6-30-00). In progress.

Conduct handsheet study to better characterize the effect of papermaking parameters on cockle that develops during drying. (6-30-00) In progress.

Conduct joint cockle study with project F02102 (3-20-00) in progress.

Summarize results and prepare final project report. (6-30-00). Not started.

(Due to absence of PI, work on project delayed more than expected. New schedule shown below.)

SCHEDULE:

Task Descriptions (example)	1999 Apr - Jun	1999 July - Sept	1999 Oct - Dec	2000 Jan - Mar	2000 Apr- Jun	2000 Jul- Sept	2000 Oct- Dec	2000 Apr- Mar
1. cockle during drying	-----	-----	-----	-----	-----	-----X		
2. cockle in converting	-----	-----			-----	-----	-----X	
4. joint work with F02102			-----	-----X		-----	-----	-----X
5. Analysis of results							-----	-----
6. Final report								-----

SUMMARY OF RESULTS:

This year we focused on cockle studies with handsheets. After the Spring PAC meeting of 1999, we started investigating the effect of the amount of chemical additives and degree of mixing on the formation index of handsheets. Then we tried to evaluate the degree of cockle as a function of the formation. It took an excessive amount of time to get the formation measurements. By the time enough data was collected the PI had gone to STFI as a guest researcher and this slowed down progress even more. After the Fall PAC meeting, it was determined that we needed to re-establish our methods of making sheets using a systematic procedure. Currently we are in the progress of doing this. By the Spring PAC 2000 meeting, results should be available.

During the summer of 1999, the opportunity was made available through a member company to evaluate cockle that develops in the copy process for a variety of handsheets. We developed a method using a copy machine and the shadow Moiré System to measure cockle directly after 2-sided copying. This should provide a means of evaluating the propensity of a sheet to cockle during copying.

During the fall of 1999, we upgraded the Shadow Moiré system to increase the ease and speed of analyzing the data. This has resulted in tremendous timesavings.

During the fall of 1999, we began a joint venture with project F02102 (Papermaking PAC, Dryer Efficiency). This provided a means of investigating cockle that develops during drying of paper, with control of the drying conditions. Preliminary results of this study are given below.

SUMMARY OF KEY CONCLUSIONS:

- Can modify formation by chemical and/or mechanical means
- Partial drying under restraint and elevated temperatures leads to more cockle than freely-air-dried sheets.
- Nonuniformities in drying lead to worse cockle.

DISCUSSION:**Upgrading of the Shadow Moiré System**

During the fall, we upgraded our shadow Moiré system, which is used to measure topography. A more efficient and time saving unit replaced the old Moiré System Model PS-911. The new system, Moiré Model PS 88, like the older model is a non-contact test that is capable of detecting and characterizing surface topography. The basic hardware of the system (e.g., camera, light source, and sample holder) that provides a cockle measurement with a resolution of 0.2 mils is the same as the old system. A new frame grabber, and modification in the system set-up, data acquisition system, and data presentation has resulted in a significantly faster cockle measurement. For instance, with the previous version only a maximum of 6 measurement could be made and analyzed in one hour (e.g., 10 minutes per sample). However, with the new system at least 12 measurement can be made and analyzed in one hour (less than 5 minutes per sample).

Basic System Setup for the new Model PS-88 has taken the three-step process in PS-911 and combined them into one. In the initial workspace, the sample is loaded, phase image captured, fringe analyzed, and data file created all at one level. The unit now has the capability to specify sample dimensions and displacement units.

Data Acquisition with Model PS-88 has also been improved. Now four images are combined instead of the original three providing improved fringe patterns for analysis.

The upgraded system currently has four options for graphical display of the displacement data: 3D Surface Chart, 3D Contour Chart, Diagonal Plot and Chord Plot. In addition calculation of curl and twist parameters can be completed.

Handsheet Study

Much of the time between March 1999, and July 1999 was spent quantifying the effect of chemical additives on formation. Formation was determined as the coefficient of variation in grammage of the sheet as determined by the IPST formation tester. British handsheets were made from either hardwood or softwood pulps. The chemicals used were Polyethylene Oxide (PEO) and Phenolic Formaldehyde Resin (PFR). Equal portions of each were added to the slurry. Figure 1 provides an example of how the formation index increased as the amount of chemical additives was increased (1, 2, and 3, ml of each PEO and PFR). For the results shown in the figure, the slurry was not mixed after the chemicals were added. For the case of adding chemicals and then mixing the slurry, the formation was worse than a sheet with no chemical additives, but the formation index was not very sensitive to increased amounts of chemicals. We also affected formation by allowing the pulp slurry to settle on the forming wire before draining the water and increasing the consistency of the slurry.

Starting in July, we were to begin our handsheet study of cockle during drying and converting using Noble and Wood sheets. At this time, the PI left for a 1 year-stay at STFI. Well, we learned that it is difficult to manage this project from across the ocean. Things did not progress as planned. Since the Fall, we have refocused the study and

started anew. We modified the formation with mechanical means and dried sheets either under full restraint or no restraint. The flatness of the sheets has been analyzed. At present the formation of the sheets has not been measured for correlation to the sheet flatness.

For standard sheets with good formation we looked at the differences in cockle with and without drying restraint. The topography was filtered to remove curl. The sheets dried under restraint had a standard deviation in filtered height of 1 mil. The sheets dried under no restraint had a standard deviation in the height of about 5 mils. This gives us a scale to use when we now look at effect of formation. We expect that even with poor formation the sheets dried under full restraint should be fairly flat. Under partial restraint, the poor formation sheets should produce more cockle. These tests are currently being conducted. For the sheets dried under full restraint, we will expose them to a cycle of high humidity and measure the change in sheet flatness. We hope to see the effect of formation on cockle that occurs during, for example, converting or printing.

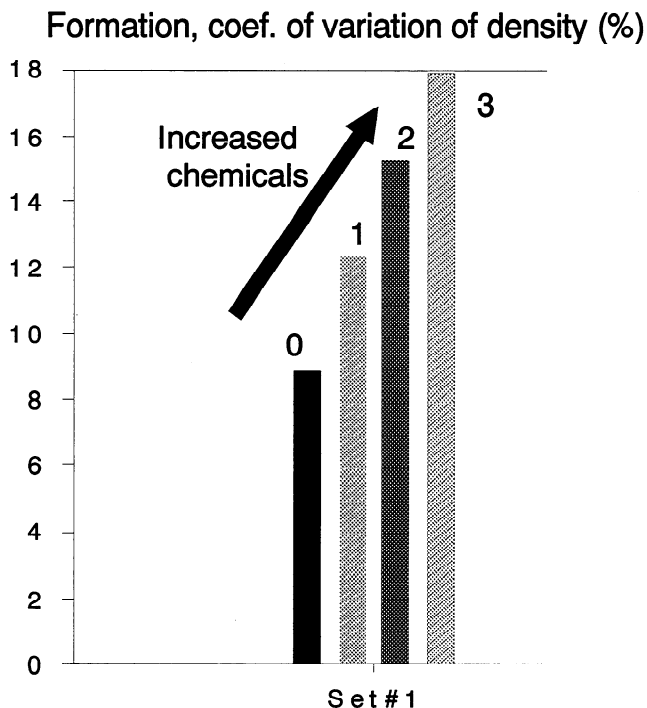


Figure 1. Formation index versus amount of chemical additives

Joint work with F02102

One of the reasons given for the use of temperature graduation in the dryer section (i.e., use of low temperatures in the first dryer section) is that heating/drying the sheet too quickly can increase the likelihood/severity of cockle. Another problem associated with high initial dryer temperatures is increased surface deposits. Since deposits can easily be non-uniform, they are expected to contribute to cockle due to the associated non-uniformity of heat flux to the sheet.

An existing dryer simulator was upgraded to have two heated surface options, a uniform cast iron platen and a cast iron platen having a pattern of epoxy-filled depressions to simulate non-uniform surface deposits. The simulator offers control over surface temperature, dwell time, and restraint pressure; the sheet can be lightly pressed against the hot surface with samples of real dryer fabrics (which apply somewhat non-uniform pressure to the sheet).

The objective of the trial was to quantify the effect of surface temperature on cockle and to investigate the effect of heat flux non-uniformity on cockle. Samples were cut (5"x5" squares) from existing Formette sheets made for project F02102. The 70 gsm sheets were 75% BHWK and 25% BSWK with appropriate additives to simulate a copy paper furnish and a freeness of 450 CSF. The sheets had an MD/CD Tensile strength ratio of about 2.0. The initial solids level is about 45% after pressing.

Figure 2 provides results from initial tests using this set-up. The sheets were removed from the dryer at different moisture ratio levels and allowed to freely shrink. The figure shows the standard deviation of the sheet height, after filtering to remove curl and warp, versus the moisture ratio at the point of removal from the dryer. Values represent the average of 5 samples. Results from uniform heating at two different drying temperatures are shown along with the case when nonuniform drying is imposed with the special platen. The results show the sheet is flattest if it is completely dried in the platen, agreeing with our earlier findings that cockle is minimized with drying restraint. Interestingly, intermediate drying gave worse cockle than the case of a freely air-dried sheet. Most likely, the drying under elevated temperatures sets up larger nonuniformities in the sheet, so that when the sheet is removed from the dryer cockle worsens. As one might expect the nonuniform drying had the largest cockle.

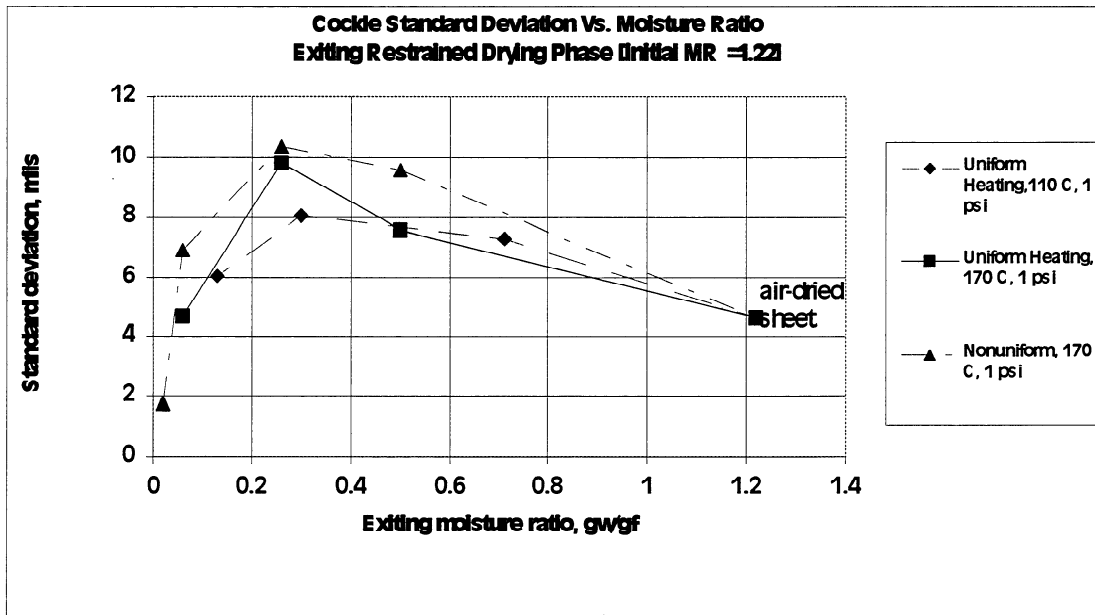


Figure 2. Cockle severity versus exiting moisture content for uniform and nonuniform drying.

Evaluating Cockle that Develops During Copying

A member company provided us with samples of 7 different sheets to see if we could distinguish differences in cockle that developed during copying. It was suspected that cockle that develops in the sheet leads to image deletions. Only a few sheets of each type were provided and the following discussion is given to show that the developed methods could be used for future evaluations.

The sheets were stored at TAPPI standard conditions. Moisture contents were obtained for the samples. Two-inch by 2-inch regions on each sheet were marked.

The shadow Moiré system was placed beside an Océ copy machine, and shadow Moiré fringes were recorded before and after two-sided copying. As a reference, the initial topography of the marked region was obtained. The sheet was sent through the copier for two-sided copying, but with no image. Twenty-five to 30 seconds after copying, the topography of same marked region was measured.

Table 1 provides a summary of the topography before and after the copying. The table provides the standard deviation of the height, and the volume per unit area (average of absolute value of the height). The reference plane for the height is the best fit plane through the topography (average height equals zero.) The data is filtered to remove curl from the measurements.

Table 1. Summary of the Results for the 50% RH (2ndRun)

Sheet #	Moisture Content (%)	St. Dev. Height (mils)			Volume per Area (mils)		
		Before	After	Rank	Before	After	Rank
1	5.7	1.2	1.7	4	0.9	1.1	5
2	6.0	0.3	0.5	7	0.2	0.3	7
3	5.6	0.4	1.6	5	0.3	1.2	4
4	5.9	0.8	2.3	3	0.6	1.8	3
5	5.8	0.6	2.6	1	0.5	2.1	1
6	5.6	0.6	2.6	2	0.5	2.0	2
7	5.7	0.3	0.9	6	0.2	0.7	6

The after-copying data provided in the table was used to rank the sheets for degree of cockle. A rank of 1 corresponds to the most cockle and a rank of 7 has the least cockle. The data shows that after going through the copier, sheet 5 had the worst cockle followed closely by sheets 6 and 4. Sheets 1 and 3 were in the middle range, and sheets 2 and 7 had the least cockle. Sheet 1 had the most severe cockle before the copying process.

From the results presented here, it appears that we can use this method to evaluate copy-induced cockle. The sheets showed different amounts of cockle. Sheet 2 appears to develop the least cockle during copying.

Based on the initial tests the proposed test procedure we developed is as follows:

1. condition samples at Tappi Standard Conditions (preconditioning is debatable)
2. Mark sheets with a predetermined area, say 2X2 inch (possibly larger)
3. measure moisture content of sheets
4. Run copier to warm-up.
5. Image first sheet.
6. Place sheets in copier feed tray as last sheet of a stack of 50.
7. Run sheets through copier (one or two sided to be prescribed)
8. With-in 30 seconds measure topography.
9. Repeat for all sheets alternating between sheet types.

Then the images can be used to rank the sheets for cockle after copying.

FUNDAMENTALS OF ACCELERATED CREEP

STATUS REPORT

FOR

PROJECT F026

**Charles Habeger
Douglas Coffin
Barry Hojjatie
Kennisha Collins**

**Institute of Paper Science and Technology
500 10th Street, N. W.
Atlanta, Georgia 30318**

DUES-FUNDED PROJECT SUMMARY

Project Title:	Fundamentals of Accelerated Creep
Project Code:	CREEP
Project Number:	F026
PAC:	Paper Physics

Project Staff

Principal Investigator:	Chuck Habeger and Doug Coffin
Research Support Staff:	Kennisha Collins, Barry Hojjatie

FY 99-00 Budget:	\$108,000
Allocated as Matching Funds:	0

Time Allocation:

Principal Investigator 1:	25%
Principal Investigator 2:	20%
Research Support Staff:	20%, 20%

Supporting Research:

Ph.D. Students	Adisak Vorakunpinij, Chris Dreher
-----------------------	--

RESEARCH LINE/ROADMAP: Line #10 – Reduced net energy consumption per ton by 30% compared to “97” levels.

PROJECT OBJECTIVES: Establish that sorption-induced stress gradients and intensification of creep at high load are the root cause of accelerated creep, sorption-induced physical aging, and loss tangent transient phenomena. Determine the influence of mechanical conditioning on the behavior of paper under sustained load. Develop methods to measure residual stresses in paper.

PROJECT BACKGROUND: Established experimental and theoretical basis for the sorption-induced stress gradient explanation of accelerated creep and physical aging.

DELIVERABLES: *Published papers that convincingly argue that our mechanism is the explanation for accelerated creep, sorption-induced physical aging, loss tangent transients. Assessment of work hardening for manufacturing creep resistant papers.*

SCHEDULE:

Task Descriptions (example)	1999 Apr - Jun	1999 July - Sept	1999 Oct - Dec	2000 Jan - Mar	2000 Apr-Jun
1. tensile work hardening			-----	---X	
2. ac publications	-----	-----	-----X		
3. loss tangent transients			-----	-----X	
4. fiber ac	-----	-----	-----	-----X	
5. comp-tensile work hardening				-----	-----
6. X-ray doping experiments				-----	-----
7. ORNL X-ray work					-----

SUMMARY OF RESULTS: Three papers (the fundamentals of accelerated creep, the effects of recycling on accelerated creep, and the influence of pulp blends and multi-ply sheet structure on accelerated creep) submitted for publication. Developed a formal explanation for the transient loss tangent phenomenon using the same sorption-induced stress concentration approach (publication in preparation). Our accelerated creep work demonstrated that residual stresses play a major, unappreciated role in paper creep: therefore, we initiated a joint project with Oak Ridge National Laboratory to use X-ray analysis to determine residual stresses in paper. Demonstrated that work hardening by accelerated creep reduces accelerated creep and is resistant to mechanical relaxation.

A. Accelerated Creep Work Hardening*Introduction:*

Cyclic moisture greatly accelerates creep and failure in many hydrophilic materials. Corrugated boxes and other paper products, which must perform in cyclic humidity environments, suffer greatly as a result. Paper structures, as a consequence, are either over designed to deal with uncontrolled humidity, or they fail prematurely. In conjunction with our fundamental work on accelerated creep, we are beginning to explore strategies for increasing resistance to creep and to accelerated creep. Creep is greatly influenced by moisture; therefore, an established approach is to chemically treat or coat the paper so that it sorbs less moisture. This is effective, but it also can be expensive. As an alternative, we are entertaining the possibility of enacting manufacturing procedures that do not reduce sorption, but do produce papers that are less prone to creep and accelerated creep.

Our purpose here is to show that we can make papers that are very rigid in tensile creep. Boxes, however, fail in compression. It could be that our papers also have enhanced compression performance, or it could be that an analogous treatment would generate papers with superior compression properties. We don't know because we are not yet equipped to do the compression testing or treatment. We do demonstrate that tensile work hardening can produce papers with long-lasting tolerance to cyclic humidity tensile loading. We do not speculate as to how the requisite work hardening could be achieved in a commercial setting. We merely present a potential opportunity. Before

practical application is considered, the parameters necessary for augmenting performance in compression must be established. We begin below by exploring in the tensile mode.

We would be remiss if, before beginning, we did not remind you that papermakers have a love-hate relationship with water. The softening of paper by moisture is much regretted in the field. On the other hand, it is important in conversion. A paperboard, that is more resistant to creep, will be less compliant in combined board manufacture and in box building. If we do devise a way to make more rigid board, we will promptly need to also consider its influence on converting.

Work Hardening:

It is well known that the compliance of many materials to long-time load exposures can be reduced by work hardening. Creep is a decreasing rate phenomenon. Soon after load application creep rates are large, but they fall off more-or-less linearly with the logarithm of time. Materials that have been crept for awhile creep more slowly at the same load and are "work hardened". Upon release of the load the material is allowed to "relax", and some of its newfound creep resistance may be lost, but in many cases a permanent decreases in creep rigidity are achieved.

The first question is: How does simple work hardening affect accelerated creep? If a sample is maintained at load then subject to an accelerated creep experiment, will it fair better? If there is improvement, will the benefit persist after the load is released and sample relaxes for a period of time? To answer these questions, we made experiments. Five commercial 180 g/m² linerboard samples were conditioned to 80% RH in our humidity-controlled tensile creep apparatus. At time zero, a tensile load in the cross-machine equal to 25% of the 50% RH tensile strength was applied to three of the samples. The creep strain of all five samples was monitored and plotted as a function of time in Figure 1. After 3 hours, the same load was applied to the other two samples. After six hours the chamber humidity was cycled back-and-forth, at one hour intervals between 30 and 80% RH. You can see the obvious influence of load sustenance on creep. The first-loaded samples get some of their creep out-of-the-way before load was applied to last two samples, and during the second three-hour period they experienced much less creep than the newly-loaded specimens. However, when humidity cycling begins, notice that all samples undergo accelerated creep with equal virulence.

Figure 2 documents the results of a similar experiment. After the first three-hour load exposure, weights were removed and all samples were left hanging freely overnight. Then, an identical accelerated creep experiment was performed on all samples. The load was applied for three hours before humidity cycling commenced. Notice that the creep work hardening survived the relaxation process. Upon inception of the second load dose, the treated samples exhibited less creep than the first-loaded ones. Of course, all samples equally displayed accelerated creep. In summary, tensile work hardening improves tensile creep rigidity, but has no influence in the accelerated creep regime.

Well, regular work hardening doesn't reduce accelerated creep. But, accelerated creep is also a decreasing rate phenomenon. Maybe it takes accelerated creep to fix accelerated creep. What if we did the work hardening treatment under cyclic humidity condition? Would the sample be more rigid upon second exposure? Figure 3 presents the results of a double accelerated creep experiment. Three of the samples were loaded at the 25% of 50% RH tensile strength from the beginning. The other two were not. After a 10 cycle accelerated creep exposure, the weights were hung from the other two samples, and a standard accelerated creep test was conducted on all five specimens. Notice that, not only are the work hardened papers much less creep compliant, but they also are much more stable under cyclic humidity conditions. These are not surprising results. The treated samples are merely continuing creep at their normal reduced rate during the second cycling.

Now, we need to know if accelerated creep work hardening relaxes away when the load is removed. The test documented by Figure 4 contrasts the performance of three-cycle-treated samples and non-work hardened samples. Even after overnight relaxation at 80% RH, the second accelerated creep appears to continue on from where it left off. It is much less prone to creep and accelerated creep. We record the results of a similar experiment with a five-day relaxation as Figure 5. The effects of work hardening persist.

Strength Measurements:

We can't yet look at the effect of tensile work hardening on compression creep, but we can determine the influence on tensile load-elongation properties and on compressive strength. We did STFI short-span compression strength testing on the five samples subjected to the work hardening of Figure 1. The average compressive strength is 3320 N/m with a standard deviation of 180 N/m. The comparable numbers for untreated samples are 3579 and 250 N/m. So, tensile work hardening may cause a small decrease in compressive strength. The effects on tensile properties are more pronounced. We made tensile load-elongation tests on the samples of Figure 2. Tensile strength was unchanged, but extensional stiffness increased by 27%, stretch dropped by 48%, and TEA decreased 53%. In the direction of application, accelerated creep work hardening produces a significant stiffer, more creep resistant, but more brittle paper.

Comments:

From the limited work presented here, it appears that a good part of accelerated creep is irreversible. Sequential wetting and drying under load reduces accelerated creep. Actually, cyclic humidity without loading does some good (compare the two first accelerated creep actions in Figure 3.). Since by-far the largest increment of accelerated creep comes in the first humidity cycle, it appears that even a single extra dry-to-wet-to-dry under load treatment could be beneficial to paper creep performance. If work hardening translates to compression and if there is an increase in compressive strength, it may be worth while to consider schemes that subject paper to accelerated creep before

end use application. Even assuming positive outcomes on these contingencies, we are not yet ready to speculate on methods. It is not clear what levels of load, humidity cycle magnitude, and cycle duration will be necessary to harden a paper. Remember this a creep process, and conditioning may require too much time for on-papermachine or during-conversion moisture cycling to be effective. It may be that load-during-storage approaches are necessary. The room temperature 30 to 80 % RH cycling of this demonstration is gentle. Perhaps more extreme moisture cycling could be potent over shorter times, we just don't know.

B. X-ray Residual Stress Analysis

Introduction:

We believe that accelerated creep happens because cyclic sorption sets up cyclic residual stresses. We believe that sorption-induced deaging is a result of residual stresses that we claim are built up during sorption, and that physical aging comes as these residual stress relax over time. We believe that a type of work hardening occurs because an applied load removes residual stresses, and we believe that sorption-induced residual stresses are the source of the loss tangent transient phenomenon. According to our modeling, residual stresses have large influence on those parts of the material compliance that are nonlinear in their response to stress. For polymers these are the relatively long-time, high-temperature thermal transitions that require long-range polymer backbone motion. Thus, we are arguing that residual stresses have an unappreciated importance in the long time mechanical responses of paper. These claims need to be experimentally checked out. Does sorption truly set up significant stress gradients that relax away as the logarithm of time? Does load reduce residual stresses over time? Are freely dried sheets more compliant because their residual stresses are significantly greater than those in restrain-dried sheets are? Since these measurements have not been made, we can only speculate.

X-ray Diffraction and Residual Stresses in Paper:

The determination of internal stresses through X-ray diffraction methods is an established science [1]. Full strain tensors can be measured as functions of depth in samples with proper characteristics. Internal stress distributions are then calculated from the material stiffnesses. Proper characteristics means that material contains randomly oriented crystallites of about a micron or greater in diameter, that X-rays can penetrate the region of interest, and that the crystallites produce a sharp diffraction peak at high 2θ for X-ray source in use.

In one sense, paper is a good candidate for the X-ray approach. X-rays penetrate sheets easily. Materials that are opaque to X-rays require implementation of the more complex neutron diffraction technique. On the other hand, the X-ray diffraction peaks of crystalline cellulose are broad, overlapping, and at low 2θ for common X-ray sources. One can also question whether they meet the random orientation stipulation.

Realizing that paper was not ideal for the X-ray diffraction approach, we nonetheless decided to investigate its potential. There is at Oak Ridge National Laboratory the equipment, software, and expertise for making state-of-the-art stress determination by X-ray diffraction. They are anxious to serve industry and academia, and there are abundant opportunities for free collaboration on joint projects. Therefore, we arranged some preliminary testing. Last Fall, Chuck Habeger, John Waterhouse, and Adisak Vorakunpinij from IPST took paper samples to Tom Watkins of ORNL for analyses. We found, as might have been foretold, that cellulose peaks are too broad and at too low of a 2θ for decent strain determinations. At the same time, we learned that many other polymers also do not have proper diffraction peaks. Nonetheless, X-ray successful internal stress analyses have been carried out on polymers doped with metals particles [2-6]. The crystalline metal particles must have a proper diffraction peak, be randomly oriented, and be mechanically integrated into the structure so that they carry some of the load. In order to realize sharp diffraction peaks, the crystallites must be at least about a micron in diameter.

Future Plans:

We intend to experiment with various doping techniques. We will use the IPST X-ray diffractometer to assess the peak quality. We settle on best candidates. Next, we will go to Oak Ridge and see if strains can be detected in the dopants. If this looks promising, we will negotiate a larger project with ORNL. We will make sheets at best conditions and dope with the right particles to optimum levels. We will return to Oak Ridge and place samples in loading jigs to calibrate the relations between dopant strains and overall sheet strains. We will devise techniques for making residual stress measurements in papers with dopants. Next, we will develop an experimental regime to subject doped sheets with different papermaking and sorption histories to X-ray residual stress measurements. Finally, if all goes well, we assess the influence of residual stresses on paper mechanical properties.

We plan to take advantage of resident IPST expertise in identifying and executing the doping strategies. Hiroki Nanko and Derek Page have already suggested possible approaches. John Waterhouse will contribute on papermaking issues and David Rothbard will advise and make X-ray measurements.

Judging from the doped polymer literature, we will need to achieve a 10 to 15% by weight dopant load into a millimeter thick sample to get, at the same time, sufficiently strong peaks and stress profile resolution through the sample. Initial ideas that need further critical review include: lumen loading with metal particles; lumen loading with titanium dioxide; soaking sheets with a Kymene metal particle solution; using sheets subjected to osmium tetroxide vapor deposition; and precipitating crystal structures in the cell wall. A successful approach must not only provide suitable X-ray diffraction peaks, but it must also supply particles that carry load and that doesn't interfere with papermaking or sorption processes.

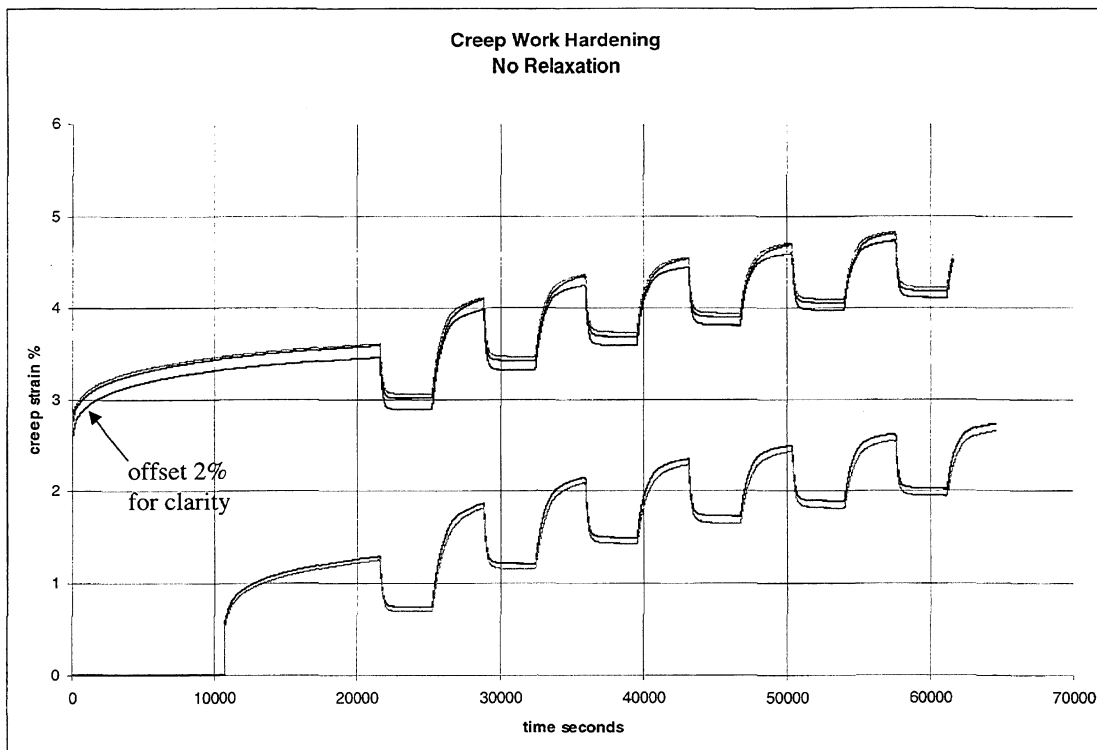


Figure 1

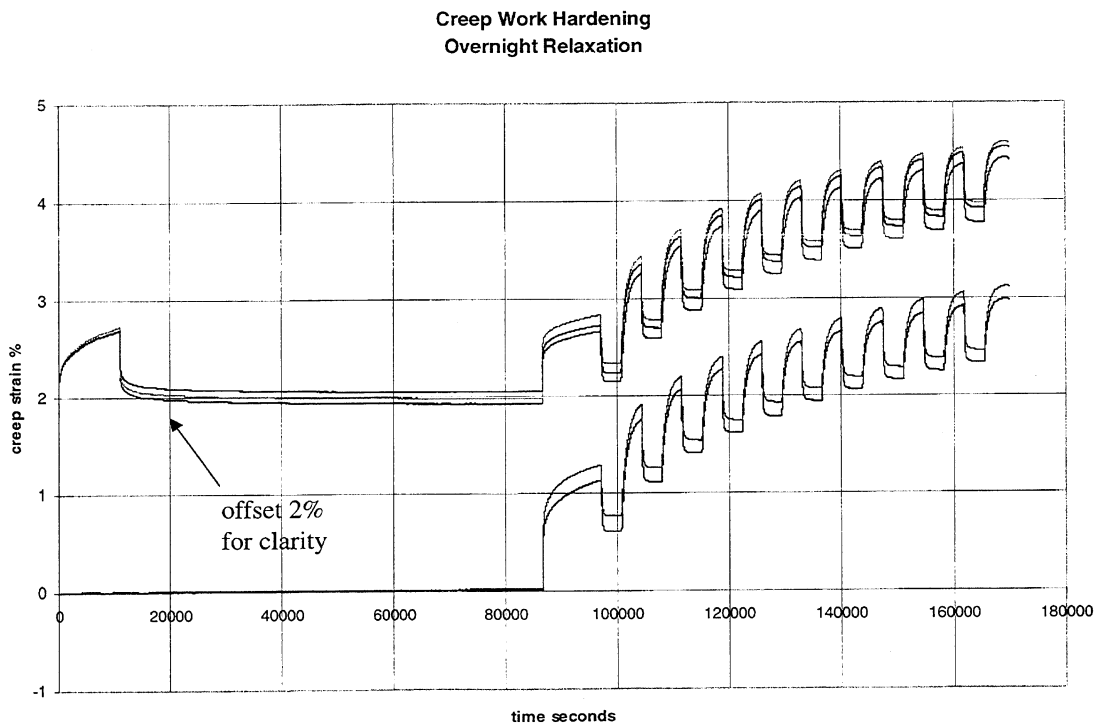


Figure 2

Accelerated Creep Work Hardening
No relaxation

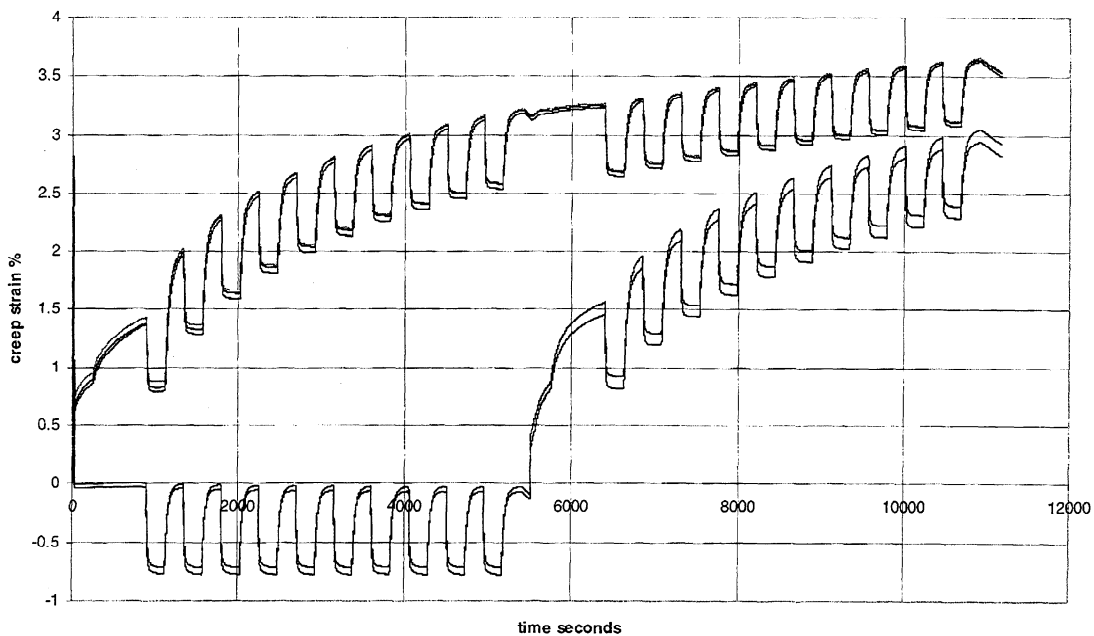


Figure 3

Accelerated Creep Work Hardening
Overnight Relaxation

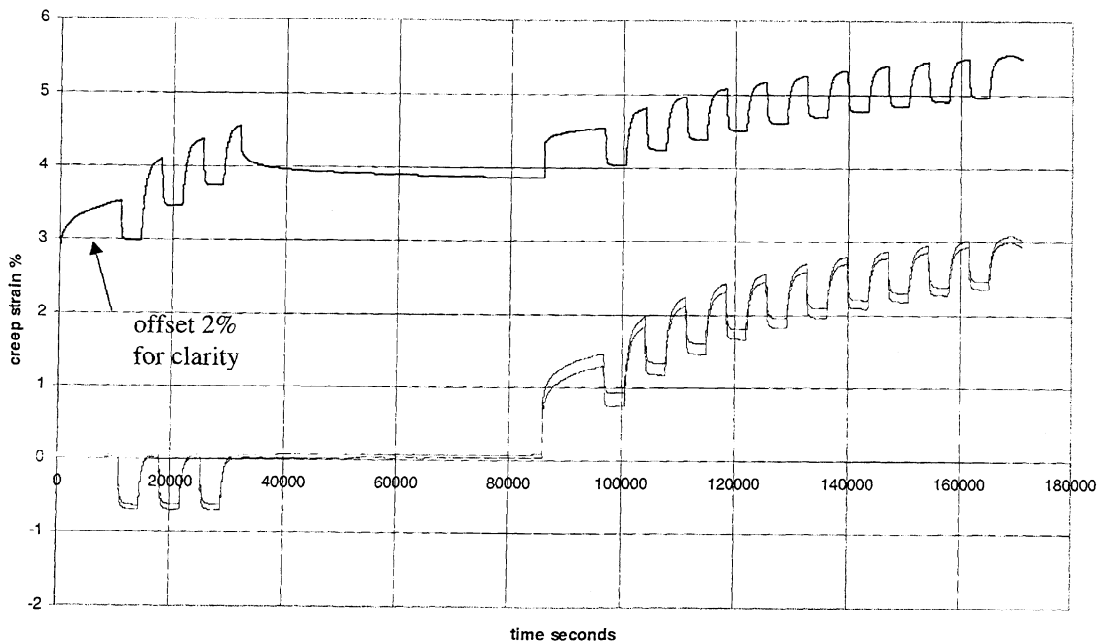


Figure 4

Accelerated Creep Work Hardening
Five Day Relaxation

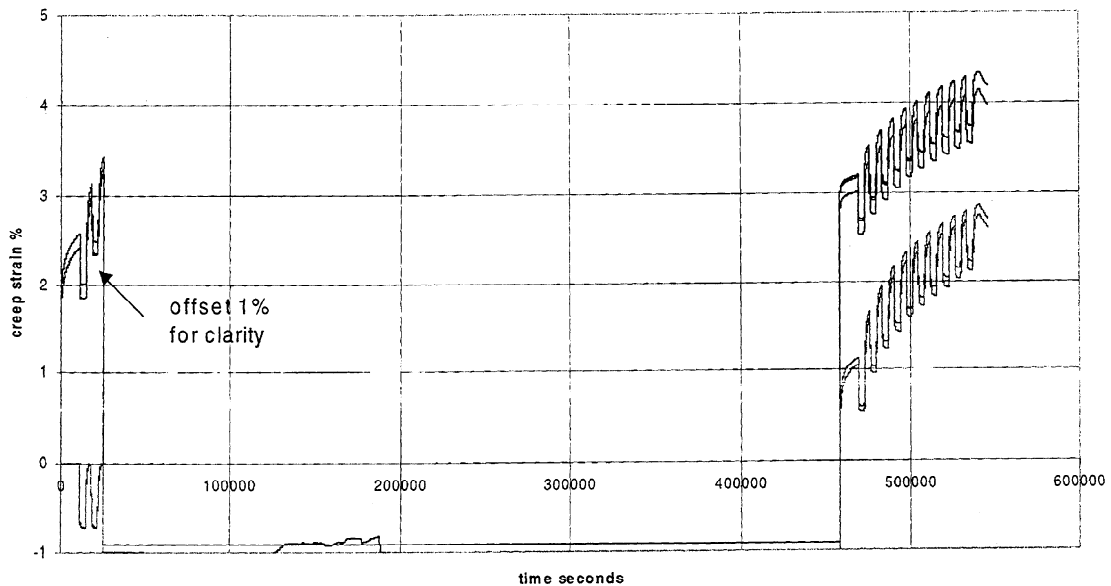


Figure 5

References:

1. Noyan, I. and Cohen, J., Residual Stress: Measurement by Diffraction and Interpretation; Springer-Verlag (1987)
2. Barrett, C., and Predecki, P., Polym. Engr. & Sci 16(9), p. 602 (1976)
3. Predecki, P., and Barrett, C., J. Composite Mater. 13, p. 61 (1979)
4. Barrett, C., and Predecki, P., Polym. Composites 1(1) p. 2 (1980)
5. Fenn, R., Jones, A., and Wells, G., J. Composite Mater. 27(14), p. 1338 (1993)
6. Prinz, B. and Schnack, E., J. Composite Mater. 31(9), p. 852 (1997)

C: Mechanics of Sorption-Induced Loss Tangent Transients

Douglas W. Coffin and Charles C. Habeger

Institute of Paper Science and Technology
500 10th Street N. W., Atlanta, GA30318

ABSTRACT

We demonstrate mathematically that hygroexpansive materials displaying nonlinear viscoelastic behaviors can have larger loss tangents during and immediately after moisture changes than they do at equilibrium. Our analyses reveal that these sorption-induced transients can be a direct result of the stress gradients created by moisture changes. Further calculations show that artificial transients can also arise from improper data analyses. Together, these observations support the contention that loss tangent transients are real but that much of the large transient excursions reported during sorption are artifacts of the test methods.

BACKGROUND

It is frequently claimed that loss tangents, as determined by small-strain sinusoidal loading experiments, are larger during sorption and immediately after sorption than they would have been at the same equilibrium moisture content. Obvious moisture-induced artifacts that could account for at least part of the anomalous effects are rarely acknowledged, much less considered. Nevertheless, loss tangent excesses are consistently observed long after sorption is complete and the measurement artifacts have ceased to be operative.

In 1965, Kubat and Lindbergson [1,2] conducted torsion pendulum, loss tangent from amplitude changes of a freely oscillating torsion pendulum. Cellophane and paper sheets were investigated in changing moisture and ammonia atmospheres [2]. They registered large (factor of 2 and more) damping transients upon absorption and desorption. They encountered a disconcertingly large, unexplained longitudinal load influence on loss tangent and torsional stiffness [1] that gives the reader concerns in interpreting their transient results. For the strip geometries employed, the stiffness parameter governing the oscillation dynamics of a homogeneous sheet is $G_{23}bd^3/3L$, where G_{23} is the complex, in-plane shear modulus, b is the sheet width, and d is the sheet thickness. Irrespective of loss processes, the amplitude of the freely oscillating torsion pendulum will change during sorption as $G_{23}bd^3/3L$ changes. Neglecting this effect, they took the loss tangent as being directly proportional to the log decrement of the oscillation amplitude. They also did not consider temperature changes due to sorption and through-sheet stiffness distribution effects. Nevertheless, the loss tangents maintained their depressions long after the sorption events were complete and after these criticisms had relevance. De Ruvo et al. [3] report similar results from what appears to be torsion pendulum experiments on single wood fibers.

Commercial dynamic mechanical thermal analyzers (DMTA's) are intended to measure the dynamic stiffnesses and loss coefficients of polymers under slowly changing temperature conditions. Nonetheless, they have been used to monitor sorption transient effects. Stiffness coefficients are reported directly from unspecified, internal calculations, which assume that dimensional changes, stiffness changes, and stiffness redistribution within a cycle are negligible. When the instrument is confronted with a rapidly sorbing material, the meanings of the standard outputs (especially the loss coefficients) are unclear. As the frequency increases, less material change occurs during each measurement cycle and artifacts from material inconstancy decrease. Padanyi [4] used a DMTA manufactured by Polymer Laboratories to study kraft linerboard samples in bending. Large transient increases in loss tangent and decreases in bending stiffness were detected. The influences of heat of sorption, moment of inertia changes due to swelling, and through-sheet stiffness gradients were not considered. The drastic decreases of the transients observed as the frequency increased are consistent with a measurement artifact explanation; however, transient persistence long after sorption argues for the legitimacy of the effect.

Salmen and Fellers [5] performed dynamic tensile modulus measurements on paper and Nylon 6,6 fibers during sorption on a Perkin Elmer DMA7e. They report absorption and desorption loss tangent transients that decrease as frequency goes from 0.2 to 11 Hz. In paper, they saw an absorption-induced undershoot in the real part of the modulus, which one might attribute to the heat of sorption. They argue that their loss tangent transient observations are a consequence of the non-loop-closure artifact caused by hygroexpansion occurring in one cycle. Tensile DMTA loss and modulus transients are also reported by Jackson and Parker [6] and Denis and Parker [7] in wood fibers and in kraft papers. Berger [8] made cyclic stiffness measurements on paper in an Instron tensile instrument during sorption. Even after making a correction for the non-loop-closure effect, loss transients remained.

Berger and Habeger [9] investigated the influence of changing RH on in-plane ultrasonic stiffnesses. Ultrasonic stiffnesses are measured at such high frequencies (about 80 KHz) that material changes during a test cycle are inconsequential. They found that, after proper corrections were made for temperature changes caused by sorption, the real part of the stiffness was the same during sorption as it was at the same equilibrium moisture content. A small absorption overshoot in the loss tangent was detected, but this was ascribed to the absorption-induced temperature rise.

Possibly the cleanest experiments which demonstrate that paper is more compliant after moisture changes are the creep tests of Padanyi [10]. He clearly shows that, even after moisture equilibrium is reached, creep rates decrease as the time lapse between moisture change and load application increases. These creep experiments have a much longer time frame than dynamic stiffness tests, and they exhibit a larger, longer-lasting effect. Padanyi's findings further sway us towards the opinion that paper, as well as other swelling polymers, are more compliant in long-time experiments after a sorption event.

From the past work, we draw the conclusion that there are true moisture-transient loss tangent effects that become less prominent as the time frame of the experiment is decreased. A good portion of the large during-sorption low-frequency excursions may well be a result of measurement artifacts. However, the general observations at low frequency of compliance excesses after sorption are hard evidence for a real phenomenon.

We submit that the mechano-sorptive effects, which include accelerated creep, Padanyi's sorption-induced physical aging observations, and transients in the dynamic mechanical properties, can be explained in terms of nonlinear mechanics. We previously showed that accelerated creep and physical aging can be manifestations of sorption-induced stress gradients and nonlinear creep compliance [11]. The purpose of this article is to demonstrate that nonlinear viscoelastic behaviors of hygroexpansive materials, of which paper is an example, can also account for sorption-induced loss tangent transients.

In our accelerated creep paper [11], we argued that sorption creates substantial stress gradients in hygroexpansive materials. This can happen either as a result of the moisture gradients established during sorption or because the material responds heterogeneously to moisture. Especially for long-time responses (such as creep) which require long-range polymer backbone motions, compliance increases more than linearly with load. Thus, when stress gradients are established, the extra compliance in regions of high stress results in a more overall compliant material. After sorption, these residual stresses decay through viscoelastic relaxation, and the material slowly returns to its stiffer equilibrium state. Here, we demonstrate that this action can also cause loss tangent transients. We intend only to convince the reader that the process is plausible in general. We are not attempting to quantitatively reproduce complex actions. Because it is mathematically expeditious, we employ overly simple constitutive equations and handle only the case in which the stress gradients are generated by heterogeneous hygroexpansion. We insist, however, that the same processes prevail regardless of the complexity of the constitutive behavior and of the mechanism for generation of sorption-induced stress gradients.

ANALYTICAL DEVELOPMENT

Consider a hygroexpansive and viscoelastic material. Assume the total strain is the sum of linear-elastic, power-law-viscous, and linear-hygroexpansive strains. That is the strain rate, $\partial \varepsilon / \partial t$, at any point in the material can be written as

$$\frac{\partial \varepsilon}{\partial t} = \frac{\partial(\sigma / E)}{\partial t} + \lambda \sigma^n + \frac{\partial(\beta \Delta m)}{\partial t} \quad (1)$$

where E is the elastic modulus, λ and the odd integer (n) are material properties related to the viscosity, b is the hygroexpansion, Δm is the change in moisture, and σ is the stress.

In general, the mechanical properties and the stress and strain can be functions of position in the material and time. We consider only the case of uni-axial loading under

conditions of uniform strain. Therefore, the strain is a function of time only, while the stress can be a function of position and time.

To further simplify the formulation, we choose a symmetric-three-ply sheet. Each outer ply has one half the thickness of the middle ply. We assume that all properties of the plies are equal except the hygroexpansion. Furthermore, we require the moisture to be evenly distributed at all times. Under these assumptions, the deformation of the laminate is governed by Eqs (2-5).

$$\frac{d\varepsilon}{dt} = \frac{1}{E} \frac{\partial \sigma_1}{\partial t} + \lambda \sigma_1^n + \beta_1 \frac{\partial m}{\partial t} \quad (2)$$

$$\frac{d\varepsilon}{dt} = \frac{1}{E} \frac{\partial \sigma_2}{\partial t} + \lambda \sigma_2^n + \beta_2 \frac{\partial m}{\partial t} \quad (3)$$

$$\sigma_1 + \sigma_2 = 2\sigma_{avg} \quad (4)$$

$$\varepsilon(0) = \frac{\sigma_{avg}(0)}{E}, \quad \sigma_1(0) = \sigma_{avg}(0), \quad \sigma_2(0) = \sigma_{avg}(0) \quad (5)$$

Above, the subscript 1 denotes the outer plies, the subscript 2 denotes the inner ply, and, σ_{avg} is the applied force at any time divided by the total cross sectional area of the sheet.

Next we subject the laminate to constant load and a small sinusoidal test load at a constant moisture content ($m(t)=\text{constant}$):

$$\sigma_{avg}(t) = \sigma_0 + \Delta\sigma \sin(\omega t) \quad (6)$$

For this case, Eqs. (2-5) yield

$$\begin{aligned} \varepsilon(t) = & \frac{\sigma_0}{E} + C + \lambda \sigma_0^n \left[1 + F_1\left(\frac{\Delta\sigma}{\sigma_0}\right) \right] t \\ & + \frac{\Delta\sigma}{E} \sin(\omega t) - \frac{n\lambda \sigma_0^{n-1} \Delta\sigma}{\omega} \cos(\omega t) \left[1 + F_2\left(\frac{\Delta\sigma}{\sigma_0}, t\right) \right] \end{aligned} \quad (7)$$

where

$$F_1\left(\frac{\Delta\sigma}{\sigma_0}\right) = \sum_{j=1}^{(n-1)/2} \frac{n!}{2^{4j} (n-2j)! j!} \left(\frac{\Delta\sigma}{\sigma_0}\right)^{2j},$$

$$F_2\left(\frac{\Delta\sigma}{\sigma_0}, t\right) = \sum_{j=2}^{(n-1)/2} \frac{(n-1)!}{(n-j)! j!} \left(\frac{\Delta\sigma}{\sigma_0}\right)^{j-1} \begin{cases} \sum_{k=0}^{(j-1)/2} \frac{(j-1-2k)!}{j!} \left[\frac{2^k ((j-1)/2)!}{((j-1-2k)/2)!} \right]^2 \sin^{j-1-2k}(\omega t) & \text{if } j \text{ is odd} \\ \sum_{k=1}^{j/2} \frac{j!}{(j-1)!} \left[\frac{((j/2)-k)!}{2^k (j/2)!} \right]^2 \sin^{j+1-2k}(\omega t) & \text{if } j \text{ is even} \end{cases}$$

and

$$C = \frac{n\lambda \sigma_0^{n-1} \Delta\sigma}{\omega} \left[1 + F_2\left(\frac{\Delta\sigma}{\sigma_0}, 0\right) \right]$$

The first two terms in Eq. (7), $\sigma_0/E + C$, are integration constants added to insure that the initial strain is the instantaneous elastic response, σ_0/E . The third term is the

overall creep response. It is a linear function of time and a nonlinear function of load. The term, $F_1(\Delta\sigma/\sigma_0)$, represents the increase in the creep rate due to the sinusoidal load. For $n=1$, the material behavior is linear, $F_1(\Delta\sigma/\sigma_0)=0$, and the cyclic load creates no excess creep. When $n>1$, cyclic loading leads to excess creep above the creep created by the mean load, σ_0 . We argue that this type of excess creep is the source of accelerated creep [1].

The fourth and fifth terms of Eq. (7), which represent the dynamic response, provide the main concern of this article. The fourth term is the elastic part of sinusoidal response, which is in-phase with the stress. The fifth term is the out-of-phase, viscous response. Notice that the elastic response is at the same frequency as the cyclic stress, whereas the viscous term includes harmonic terms through $F_2(\Delta\sigma/\sigma_0, t)$. Like $F_1(\Delta\sigma/\sigma_0)$, $F_2(\Delta\sigma/\sigma_0, t)$ is a direct consequence of material nonlinearity.

For the case in which the amplitude of the cyclic load is small compared to the amplitude of the applied force, the higher order terms are negligible, $F_2(\Delta\sigma/\sigma_0, t) \approx 0$, and Eq. (7) becomes

$$\varepsilon_{dyn}(t) = \frac{\Delta\sigma}{E \cos(\delta)} \sin(\omega t - \delta) \quad (8)$$

where

$$\tan(\delta) = \frac{n\lambda\sigma_0^{n-1}E}{\omega} \quad (9)$$

From Eq. (9), we see that the magnitude of the loss tangent increases with both the magnitude of the applied constant load and the exponent n . In our opinion, this dependence of loss tangent upon load is the source of moisture-induced loss tangent transients.

σ_1

Now let moisture vary with time. Since the hygroexpansions of the inner and outer plies are not equal, a sorption-induced stress will be created in each ply. These hygroexpansive stresses are equal in magnitude (σ_1) but opposite in sign, and they add to the stress in Eq. (6). If σ_1 is much greater than σ_0 and $\Delta\sigma$, this extra stress elevates the loss tangent of each ply. If σ_1 is less than σ_0 , the nonlinear character of the viscous term will result in a greater increase in loss in the high stress ply than there is decrease in loss in the low stress ply. In either case, the net loss tangent remains elevated as long as the hygroexpansive stresses are present. For the case where $\sigma_0=0$, the loss tangent obeys Eq. (9) with σ_1 substituted for σ_0 :

$$\tan(\delta) = \frac{n\lambda\sigma_1^{n-1}E}{\omega} \quad (10)$$

When the viscous response is nonlinear, notice that an extra loss term that depends on the hygroexpansive stresses arises due to sinusoidal loading.

It would be tedious to analytically solve Eq. (2) for this case of variable moisture. Therefore, we calculated the strain and stress in each layer through simultaneous numerical integration of Eqs. (2-5). The loss tangent was defined from the extra energy dissipated in a test cycle due to application of the sinusoidal load as

$$\tan(\delta) = \frac{E}{\pi\sigma_0^2} \int_0^{2\pi/\omega} \sigma(t) \frac{d(\varepsilon - \varepsilon_{(\Delta\sigma - 0)})}{dt} dt \quad (11)$$

where $\varepsilon_{(\Delta\sigma - 0)}$ is the strain response without the cyclic load. For the case in which $\sigma_0=0$, the numerical results of Eq. (11) were equivalent to the analytic expression when the numerical values for σ_I were substituted into Eq. (10).

NUMERICAL RESULTS

The simple constitutive equation proposed in Eq. (1) leads to an analytic expression for the transient loss tangent; however, it is not a realistic model for polymers. It evokes the basic transient mechanism, but it misses important response characteristics. First of all, with no applied or hygroexpansive load, loss tangents from Eq. (1) approach zero as $\Delta\sigma$ approaches zero. Real polymers experience thermal transitions, and for small sinusoidal excitations loss tangent is finite and independent of load. Long-time, high-temperature transitions require long-range polymer backbone motions. They are stress activated and have a nonlinear dependence on load. On the other hand, the short time, low-temperature transitions are side-chain motions that are insensitive to overall load. A representative polymer constitutive equation would have a finite low-load loss tangent that generally decreased with frequency and was more dependent on load at low frequency. To capture these basic features, we modified Eq. (1). (Describe (at least qualitatively) modification here! Define ω_0 .) This model produces the loss tangent versus frequency and load behavior exhibited in Figure 1. Note that loss tangent has a finite low-load limit and a nonlinear dependence on load that is pronounced at low frequency. Therefore, loss tangent decays rapidly as a function of frequency only at high loads.

The three-ply laminate made from the simulated material was numerically subjected to the moisture change shown in Figure 2, and a small amplitude sinusoidal load. The stress in ply 1 (also plotted in Figure 2) was normalized to the purely elastic hygroexpansion stress that would be generated by the same moisture change. Notice that even after moisture equilibrium is essentially reached, $\omega_0 t = 15$, residual stresses persist in the sheet. Over longer times the residual stresses relax away, and the loss tangent approaches its equilibrium value.

For $\sigma_0 = 0$, Figure 3 provides the transient response of the loss tangent for three different testing frequencies. As the frequency increases, the magnitudes of the transients decrease. As long as the amplitude is small and high-order, nonlinear effects are negligible, the transient loss tangent is not a function of the amplitude of the forcing function.

In the simulation, strains, which are not directly attributable to the sinusoidal loading, are removed through the use of Eq. (11) as the loss tangent determination. Unfortunately, in physical testing the sinusoidal strain component is not so easily separated from the hygroexpansive strain. If these extra strains are not removed, the cyclic stress-strain loops will not close, and the loss tangent determination becomes ambiguous. As the frequency of the forcing function increases the magnitude of this hygroexpansion artifact is reduced. As the amplitude of the forcing function is increased, the relative effect of open loops diminishes and the artifact is also reduced. Figures 4 and 5 document these artifacts through the presentation of loss tangent versus time curves in which the loss tangent was naively calculated without removing the hygroexpansive strain. The testing frequency is ω_0 in Figure 4 and $10 \omega_0$ in Figure 5. The figures demonstrate that large, low-frequency loss tangent artifacts can occur during moisture changes. When sorption is complete, the artifact disappears, whereas the stress gradient induced transient remains. Notice that the magnitude of the artifact decreased as either the amplitude or the frequency increased.

DISCUSSION

We have shown that nonlinear viscoelastic and hygroexpansive materials (such as paper) exhibit transients in the loss tangent. For our case study, transient stresses were created during sorption and desorption due to the mismatch in hygroexpansion of the plies. Stresses would also be created if moisture gradients existed during the moisture change, or if the mechanical properties of the plies exhibited different dependence on moisture content [11]. No matter how the transient stresses are created, they influence the resulting deformation because the material possesses nonlinear properties.

Conducting DMA tests in a changing humidity environment is a difficult task. One must account for transient temperatures due to the sorption process. At low frequencies, extra strains occurring during a given cycle introduce artifacts. Dimensional changes in the cross section introduce even more artifacts. These artifacts account for part of the transients and explain to some degree the great disparity of results reported in the literature. Whereas, Salmén and Fellers [5] maintain that this behavior is all an artifact of the test method, we propose that part of the observed transient's effect is real. Of course, as we have shown improper analysis of the raw data introduces large artifacts, but only until the sorption is complete.

We selected a constitutive equation that has a known polymer characteristic: non-linearity in compliance preferentially for low frequency and long-time processes. Therefore, the trends shown in Figure 2 agree with the experimental observation [4,5,9] that increasing frequency reduces the magnitude of transient loss tangent. From our perspective, both the non-loop-closure artifact and the stress-gradient-driven transient lose influence at high frequency. This is consistent with the reported non-existence of loss tangent transients' [9] in ultrasonic testing.

ACKNOWLEDGEMENTS

The financial support of the Institute of Paper Science and Technology and its member companies is greatly appreciated.

REFERENCES

1. KUBAT, J. and LINDBERGSON, B., *J. Appl. Polymer Sci.* 9: 2651-2654 (1965)
2. KUBAT, J. and LINDBERGSON, B., *Svensk Papperstidn.* 68(21): 743-751 (1965)
3. DE RUVO, A., LUNDBERG, R., MARTIN-LOF, and SOREMARK, C., 785-810 (1976)
4. PADANYI, Z. V., *Proceedings of the 1991 International Paper Physics Conference, Kona Hawaii*, 397-411 (1991)
5. SALMEN, L. and FELLERS, C., *Nordic Pulp and Paper Research Journal* (3): 186-191 (1996)
6. JACKSON, T., and PARKER, I., *Proceeding of the 3rd International Moisture and Creep Effects on Paper, Board and Containers Rotorua New Zealand*, 53-67 (1997)
7. DENIS, E. S., and PARKER, I. H., "Creep and Dynamic Testing of Eucalypt Paper and Fibers in Changing RH," *Proc. 1995 International Paper Physics Conference*, 143-147 (1995)
8. BERGER, B. J. Doctoral Thesis The Institute of Paper Chemistry (1988)
9. BERGER, B. J., and HABEGER, C. C., *J. of Pulp and Paper Sci.*, 15(5) J160-J165 (1989)
10. PADANYI, Z. V., in Vol. 1 *Products of Papermaking Transactions of the Tenth Fundamental Research Symposium*, (Baker C. F. ed.) Oxford, 521-45 (1993)
11. HABEGER, C. C. and D. W. COFFIN, *JPPS* to appear April 2000.

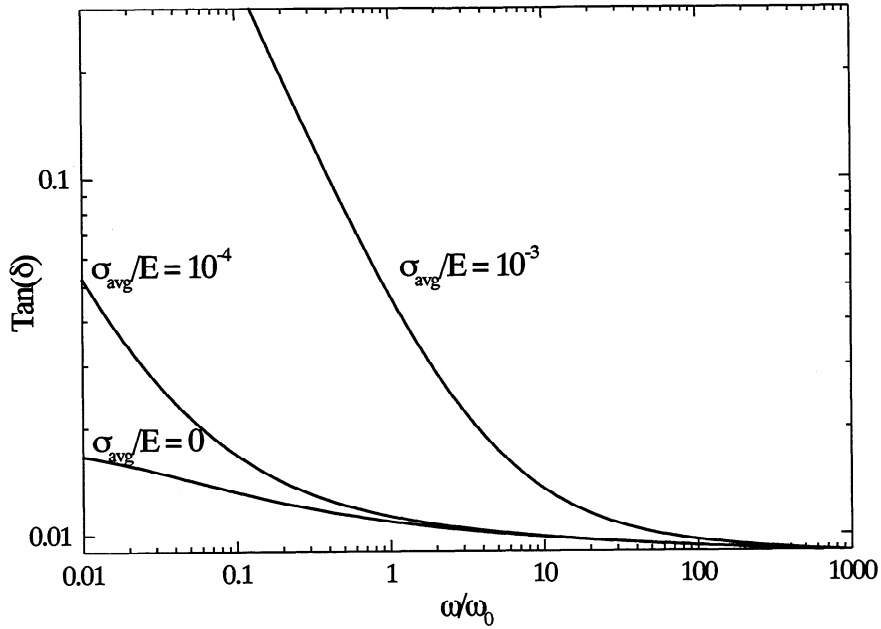


Figure 1. Loss tangent versus frequency for several magnitudes of load.

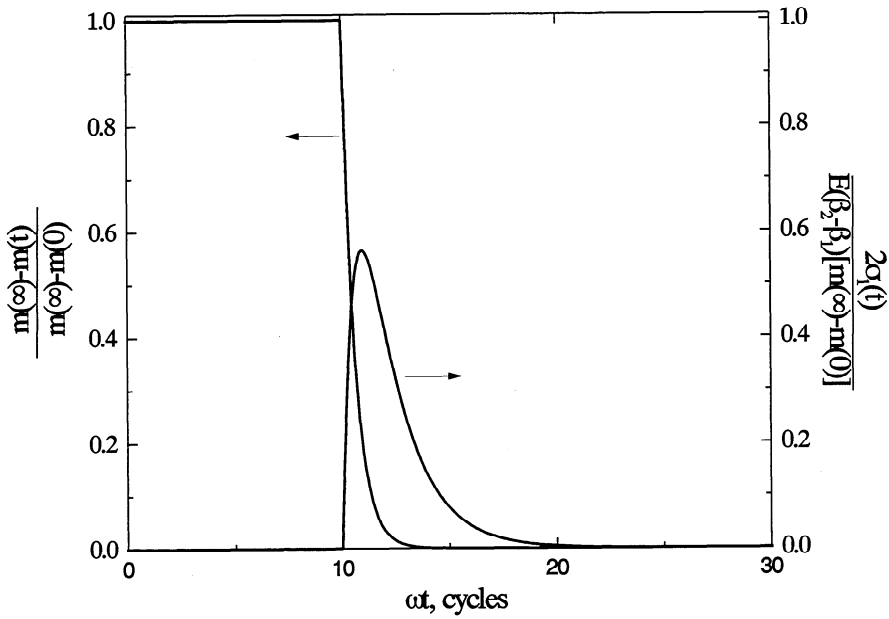


Figure 2. Moisture change and resulting stress in ply-1.

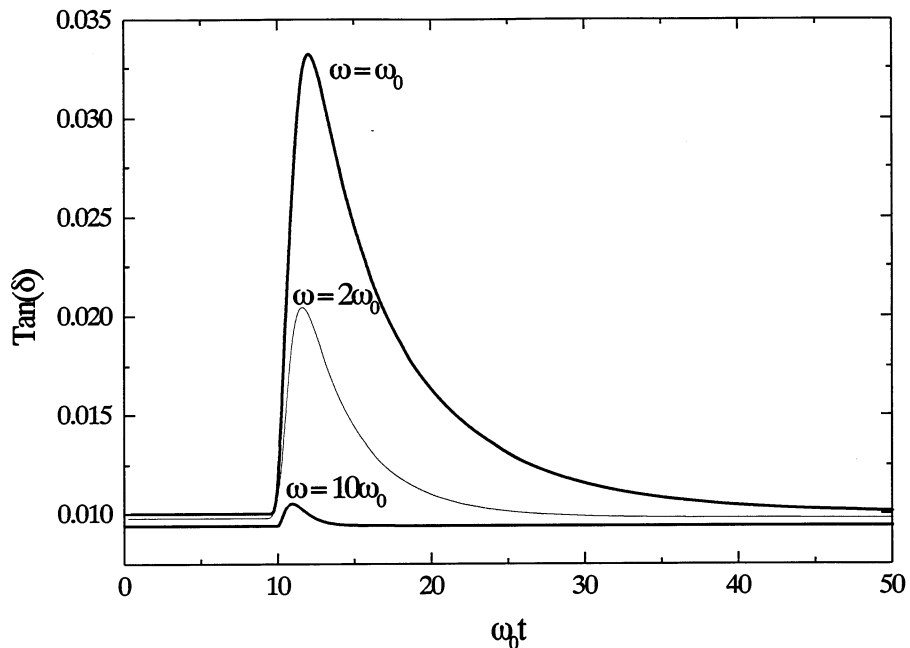


Figure 3. Moisture-induced transients for 2 frequencies of cyclic load.

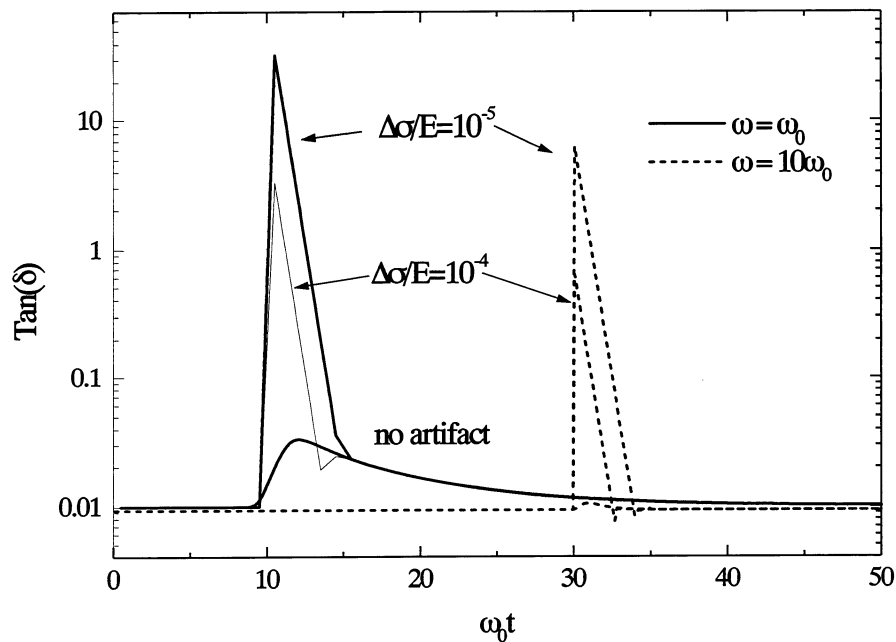


Figure 4. Artifacts in transient loss tangent due to hygroexpansion.

D. Accelerated Creep in Fibers

Introduction:

We initiated this work because it is predictive test of our accelerated creep model [1]. It is widely reported and accepted that fibrous structure experience much more accelerated creep than their single fiber components. With the exception of Kevlar fibers, in general fiber creep is not much enhanced by cyclic humidity. We believe that this is consequence of the testing regime rather than a manifestation of an inherent difference in response. For moisture gradient driven accelerated creep to be operative, the sorption time of sample and cycle time of the humidity must be of the same order of magnitude [1]. Accelerated creep is usually measured in environmental chambers that have cycle times of about an hour. The sheet samples under test usually have sorption times of about 15 minutes. So, there is an adequate match between sorption time and humidity cycle time. Single fibers, on the other hand, sorb much more rapidly. They generally complete sorption in less than a minute. We believe that the stress gradients set up by sorption can drive accelerated creep in fibers. These stress gradients are formed when moisture gradients exist across the sample. If the sample sorbs rapidly compared to transition time of chamber or to the humidity cycle time, small stress gradients will be established for small portions of testing time, and the creep will be little accelerated. To support this contention, we point out that Kevlar, the only fiber suffering large accelerated creep, also undergoes abnormally slow sorption. Its sorption times (tens of minutes) are much closer to those at which the chambers are operated.

To test this hypothesis, we decided to conduct accelerated creep tests on Nylon 6,6 fibers. We chose Nylon 6,6 because there already is some literature reporting a lack of accelerated creep, and we figured that this conclusion was due to a cycle-sorption mismatch. To vary sorption time, we procured fibers of different diameters. The deniers ranged from 6 to 40 (30 to 200 microns in diameter). Hopefully, we will discern a difference in degree in the influence of cyclic moisture depending on fiber size and cycle.

The fiber creep tester used for this work is the one supplied by Dave Dillard of Virginia Tech. It well documented in the literature [2], and we described earlier in conjunction with our Kevlar fiber experiments. We are able to dead-weight load single fibers in small chamber and record elongation with an L.V.D.T. The humidity is cycled by switching an input duct between dry and wet air sources.

From our perspective, there are two stipulations that must be met before moisture-gradient-driven accelerated creep is possible: (1) the material must creep more under cyclic load than at a constant average load; and (2) there has be a reasonable match between cycle times and sorption times in the experiment. We first demonstrated that Nylon 6,6 met the first requirement. There is a considerable increase in creep that is attributed directly to cycling. It is at least as large as we observed in cellophane and paper. Nylon 6,6 should show accelerated creep if the times match.

We have been working to make comparison between accelerated creep in Nylon 6,6 fibers of different diameters; however, we have been plagued with experimental difficulties. It is clear that the large Nylon 6,6 fibers do experience accelerated creep. Sorption times do increase with fiber diameter, and they become more in to accord with chamber cycle times. It seems that the accelerated creep increases with diameter. But, to confidently compare the action of different fibers, we must obtain reproducible results. We have had difficulties maintaining the humidity limits in our cycling from day-to-day. We have reduced this problem by working at lower top-end humidities. Upon occasion, we have observed very different creep rates for the same nominal conditions. We suspect movement in the epoxy bond between fiber and fixture as well as issues with fiber kinks. We recently have adapted our procedures to take great care with the joints, use the longest possible fibers, and to pre-stress before testing. We are starting to get more repeatable results, and we hope to have data that we can present confidently at the PAC presentation in March.

MICROMECHANICS OF FIBER NETWORKS

STATUS REPORT

FOR

PROJECT F023

**Martin Ostoja-Starzewski
Andrew N. Woods
Ted Jackson**

**Institute of Paper Science and Technology
500 10th Street, N. W.
Atlanta, Georgia 30318**

DUES-FUNDED PROJECT SUMMARY

Project Title: FUNDAMENTALS OF MICROMECHANICS OF FIBER NETWORKS
Project Code: MICRO
Project Number: F023
PAC: End-Use, Paper Physics and Converting

Project Staff

Principal Investigator: Martin Ostoja-Starzewski
Co-Investigators: none
Research Support Staff: Andrew Woods, Asst. Scientist (Sept. '98 - Oct. '99)
 Andrew Woods, Consultant (Nov. '99 – present)
 Ted Jackson
PAC Subcommittee A. Colasurdo, W. Hamad, E. Stewart

FY 99-00 Budget: \$96,133
Allocated as Matching Funds: 0%

Time Allocation:

Principal Investigator: 31%
Co-Investigators: 0%
Research Support Staff: 50% (Woods, Asst. Scientist)
 50% (Woods, Consultant)

Supporting Research:

Special Students: Jaime Castro (IPST), Mallie Clark (GT)
External (Where Matching Is Used): N/A

RESEARCH LINE/ROADMAP: Line #11 - Improve the ratio of product performance to cost for pulp and paper products 25% by developing: models, algorithms, and functional samples of fibrous structures and coatings which describe and demonstrate improved convertibility and end-use performance; breakthrough papermaking and coating processes which can produce innovative webs with greater uniformity than that achieved by current processes.

PROJECT OBJECTIVE:

To develop an understanding of the relation of the macroscopic (scales of centimeters to meters) to the microscopic (fiber and fibril scales) mechanical properties of paper. The main focus is on paper's stiffness, strength, and fracture in the MD-CD plane in terms of single fiber and fiber-fiber bond properties as well as formation.

PROJECT BACKGROUND:

Macroscopic and effective mechanical properties of paper in the end-use applications (e.g., converting operations) are a function of its microstructure. The project, therefore, focuses on a determination of qualitative and quantitative structure-property relations in paper physics and mechanics. The work was theoretical and experimental in nature.

On the theoretical side, the following analyses were conducted: (i) mechanics of a single fiber treated as a layer of helically-wound fibrils; (ii) computational mechanics programs of random fiber

networks which have been further developed (several versions in two or three dimensions, or with rigid versus flexible fiber-fiber bonds); (iii) modeling of the statistics and the spatial correlation structure of four elastic and strength properties measured in the conventional TAPPI tests.

On the experimental side, extensive tensile strength tests of elasticity and strength of paper have been carried out. These tests, involving specimens over a very wide range of sizes/scales (from 2mm to 2m), were carried out on conventional paper. It was found that the loading/boundary conditions, consistent with Saint-Venant's principle, have a significant influence on effective stiffnesses and failure properties. Different effects were established for the pure size effect under geometrically similar loading conditions. Special attention was paid to the statistics of the standard TAPPI 7"x1" test versus other specimen sizes.

MILESTONES:

1. 2-D and 3-D network models with rigid (or flexible fiber-fiber bonds) running on a supercomputer – **fall '99**.
2. Verification of the models – **in progress**.
3. Bending stiffness of paper versus network's compaction and thickness – **Sept. '99**.
4. Parametric studies of stiffness and strength using the 3-D network model – **spring, summer '99**.
5. Mechanics of a single fiber as a multilayer composite – elasticity, **fall '99**; visco-elasto-plasticity – **in progress**.
6. Effects of formation on propagation of stress waves in paper – 1-D wave motion - **fall '99**; flexural waves – **in progress**.
7. Statistics and correlation structure of elastic and strength properties of paper – two-point correlations - **summer '99**; multiscale correlations - **in progress**.

DELIVERABLES:

[Member companies may access these deliverables through the PI]

1. 2-D and 3-D network models of elasticity and strength (progressive damage phenomena) of fiber networks with rigid (or flexible fiber-fiber bonds) that run on a personal computer – successive versions in **'98 and '99**. These models rigorously account for a multitude of microscale interactions and formation (flocculation) structure.
2. Parametric studies of stiffness and strength using the 3-D network model – several cases examined in **spring, summer '99**.
3. Mechanics of a single fiber as an elastic, multilayer composite (explicit formulas) - **fall '99**.
4. Effects of formation on propagation of stress waves in paper (quantitative results for one-dimensional wave motion) - **fall '99**.
5. Statistics and correlation structure of elastic and strength properties of paper – two-point correlations examined in **'98 and '99**.

STATUS OF GOALS FOR FY 99-00:

Goal 1. *Extension, optimization, and acceleration of the computer models of random fiber networks to handle more fibers by one or two orders of magnitude than presently possible. Systems of tens of thousands (and perhaps more) of fiber-beams are envisaged.*

Status: In the fall of 1999, a decision was made to remove this goal from the PAC project and conduct it under the federal grants (NSF and USDA).

Goal 2. *Further verification of the fiber network model using laboratory experiments.*

Status: in progress.

Goal 3. *Investigation of optimal formation patterns for best mechanical properties of paper.*

Status: Given a recent award of a grant by USDA ("Towards Optimal Performance of Cellulose Fiber Networks"), this topic will no longer be studied under this PAC project. However, the following work has already been carried out:

Goal 3.1 *Development of a computational mechanics model of random fiber networks that is consistent with laws and concepts of mechanics.*

3.1.1 It allows an assessment of various effects:

- 2-D versus 3-D geometry*
- uniform versus random geometry*
- rigid versus flexible bonds*
- special orthotropy of paper*

3.1.2 Detailed modeling of the microstructure needs a number of microscale parameters: fiber length, width, thickness; fiber angular orientation; fiber flocculation; single fiber stiffness; single fiber strength; fiber-fiber bond flexibility and strength.

3.1.3 All the parameters are drawn either from the image analysis or from the spatial statistics.

Goal 3.2 *Investigation of inclusion of deformation in the Z direction in the model, when fibers lie flat in the plane of the sheet, even when the fibers' locations vary through the sheet.*

Goal 3.3 *Investigation of the difference between the deformation field from the computational mechanics approach and the affine displacement field as affected by formation. The uniform strain assumption is not expected to produce good paper strength predictions when network geometry is inhomogeneous, as it is with any but the mildest degree of flocculation.*

Goal 3.4 *The model has been applied to demonstrate, for the first time and quantitatively, the opposing effects of the in-plane paper stiffness and the paper Z-thickness on the paper bending stiffness. As a result, an optimal thickness of paper – for best bending stiffness - can be computed.*

Goal 4. *Investigation of the effect of strength additives on the overall strength of paper. Flexible bonds were found to have a predictable effect on the effective stiffness, and also to increase the ductility of overall network stress-strain response by allowing more microfailures to occur after the first failure and before the peak stress.*

Goal 5. *Inclusion of single fiber mechanics for input to computer models of random fiber networks, and further development of a model of a single fiber, treating it as a helically-wound*

multilayer composite. Mechanics of a single fiber as a multi-layer composite studied via a 3-D model. It provides a stepping-stone to studies of inelastic response, shrinkage, and swelling.

Goal 6. *Correlation of mass distribution and crack/damage patterns (a goal for the next year). Some experimental and data analysis work was carried out; other aspects of this topic are presently being researched by Jaime Castro, Ph.D. student, and will be reported once completed.*

Goal 7. *Biaxial tests and biaxial failure envelopes (a goal for the next two years). Status: In planning stage.*

Note: Given the available resources, this goal has, for this year, been replaced by a study of sensitivity of wave propagation in paper to its formation – listed above as Milestone 6 and Deliverable 4; see also Discussion below. Stress wave propagation in paper treated explicitly as a randomly inhomogeneous plate. Noteworthy are: (i) strong sensitivity to formation imperfections (i.e., random spatial fluctuations); (ii) different sensitivity to imperfection in mass density than imperfection in elastic moduli and paper thickness.

SCHEDULE:

Task Descriptions (example)	1999 Apr - Jun	1999 July - Sept	1999 Oct - Dec	2000 Jan - Mar	2000 Apr-Jun
1. Literature Survey	---	---	---	---	---
2. Verification of the fiber network model	---	---			
3. Optimal formation patterns	---	---			
4. Effect of strength additives	---	---			
5. Single fiber mechanics	---			---	---
6. Correlation of mass distribution and crack/damage patterns		---	---	---	---
7. Wave propagation	---	---	---	---	---
8. Write yearly report					---

SUMMARY OF RESULTS:

1. The fiber network model has been extended to accommodate several thousand fibers (all the interactions handled according to the laws of mechanics). This model (in both the 2-D and 3-D versions) allows computation of elasticity as well as strength/fracture (progressive damage phenomena) of fiber networks with rigid (or flexible fiber-fiber bonds) while accounting for the formation (flocculation) structure. The program runs on a personal computer or workstation.
2. Several aspects of (micro)mechanics of paper, using the above model, were examined: (i) the uniform strain assumption has been shown not to produce good paper strength predictions; (ii) an explanation of special elastic orthotropy of paper has been advanced; (iii) optimal paper thickness for highest bending stiffness was computed for a model problem; (iv) the flexible bonds have been demonstrated not only to lower the effective stiffness but also to increase the ductility of paper.
3. Mechanics of a single fiber as an elastic, multilayer composite has been investigated; explicit formulas are available.

4. A range of various dependencies of stiffness and strength properties on specimen size, aspect ratio, and loading/boundary conditions have been found.
5. Model of single fiber mechanics as a filament-wound multilayer composite has been developed.
6. Statistical, multi-scale correlation structure of stiffness and strength of paper – primarily due to the turbulence on wire - has been investigated. Quasi-isotropic random fields (i.e., random processes in the MD-CD plane) have been identified as the simplest model able to grasp this structure.
7. Effects of formation on propagation of stress waves in paper were studied. It was found that imperfection in mass density has different effects on stress waves than imperfection in elastic moduli or cross sectional area of paper. Depending on the wavelength, there is a tendency to diffuse the resonance frequency around that of a reference (idealized), homogeneous material.

SUMMARY OF KEY CONCLUSIONS:

1. The fiber network model offers a powerful tool to study several thousand fibers so as to determine all the internal stresses as well as the global response of low-basis-weight paper. As an example, optimal thickness of paper – for bending stiffness – has been computed. Verification of the model was conducted by experiments on handsheets.
2. The difference between the deformation field produced by the computational mechanics approach and a uniform strain field shown to be dependent on formation.
3. Stiffness and strength properties strongly depend on specimen size, aspect ratio, and loading/boundary conditions.
4. Fiber-fiber bonds' flexibility lowers the effective stiffness and increases the ductility of paper.
5. The statistical, multi-scale correlation structure of stiffness and strength of paper – primarily due to the turbulence on wire – may be modeled via quasi-isotropic random fields.
6. Mass density (respectively, elastic moduli and cross sectional area) imperfections of paper cause a diffusion of the resonance frequency around that of a reference homogeneous material at wavelengths that are larger (respectively, smaller) than the characteristic lengths of formation.

DISCUSSION:

1. Literature Survey

A. Significance, Results and Conclusions

An extensive literature survey has been conducted. It must be concluded that no prior work of the scope and nature intended by us for any of the topics has been carried out – neither in paper physics nor in the general context of applied and theoretical sciences and engineering. The relevant references are given separately in each respective topic area.

2. Verification of the Fiber Network Model

A. Significance

Over the past few decades, many attempts have been made to derive closed-form expressions for stiffness and strength of paper. These are, in essence, so-called effective medium models [1-9]. Each one of them is based on some type of assumption(s), such as the uniform strain field, which makes it impossible to realistically handle geometric heterogeneity (formation, streaks, ...), variable single fiber properties, variable fiber-fiber bond properties, etc.. This motivates a computational mechanics approach, in which all the fibers and bonds in a given volume of paper sheet are to be explicitly included, and interact according to the laws of mechanics.

B. Approach and Results

Thin paper (approximately 12 grams per square meter) made of Kozo fiber was used. This fiber is the bast fiber of Kozo tree (paper mulberry, *Broussonetia Kazinoki* Sieb.) which has been used for traditional Japanese paper making. They are fine fibers of 6 to 20mm long and 10 to 30 microns in diameter. The fibril angle of the fiber is nearly zero [10].

Two handsheets of such fibers were made. They displayed rather poor formation. Sheet #1 was retained for mechanical testing. The second handsheet was cut into 2mm wide strips, soaked, disintegrated, and resheeted – this resulted in Sheet #2. That handsheet had a much better formation, but, as expected, shorter fibers (see Table). Both sheets were cut into 7"x1" specimens and subjected to tensile strength tests. As can be seen from the Table, going from Sheet #1 to Sheet #2:

- modulus decreases, scatter decreases;
- maximum load does not change, no change of scatter;
- toughness as measured by strain increases, scatter decreases;
- TEA decreases, scatter decreases.

Number behind the comma indicates the coefficient of variation.

	Sheet #1	Sheet #2
mean fiber length (arithmetic)	1.01mm	1.24mm
mean fiber length (length weighted)	3.80mm	2.30mm
mean fiber length (weight weighted)	4.87mm	3.22mm
basis weight (g/m^2)	12.0	12.4
modulus (MPa), CV	11039.7, 0.18	855.3, 0.027
Max load (N/mm), CV	0.278, 0.15	0.277, 0.14
% strain, CV	1.197, 0.25	1.384, 0.15
TEA (J/m^2), CV	2.89, 0.55	2.22, 0.31

The fiber network model was run with two sets of parameters: (i) long fibers and bad formation, and (ii) shorter fibers and good formation. The stiffness displayed the same trend as in the experiments: a decrease in mean by some 20%, and a decrease in scatter by an order of magnitude. The inelastic response (max load, % strain, and TEA) also followed the same, or similar, trends as in the experiments. However, a precise numerical adjustment of the model requires knowledge of (i) fiber stiffness, and (ii) fiber segment strength relative to fiber-fiber bond strength, and (iii) all the microscale geometric parameters. This fine tuning is in progress.

C. Conclusions

- *Scientific Conclusions*

Good verification of the fiber network model.

- *Economics*

Good verification of the fiber network model.

- *Deliverables*

Good verification of the fiber network model.

E. References

1. Cox, H.L., The elasticity and strength of paper and other fibrous materials, *British J. Appl. Phys.* **3**, 72-79 (1952).

2. Ramasubramanian, M. K. and Perkins, R. W., Computer simulation of the uniaxial elastic-plastic behavior of paper, *ASME J. Eng. Mater. Tech.* **110**, 117-123 (1988).
3. Schulgasser, K. and Page, D. H., The influence of transverse fibre properties on the in-plane elastic behavior of paper, *Composites Sci. Tech.* **32**, 279-292 (1988).
4. Kärenlampi, P., Effect of distributions of fiber properties on tensile strength of paper: a closed-form theory, *J. Pulp Paper Sci.* **21(4)**, 138-143 (1995).
5. Kärenlampi, P., Tensile strength of paper: a simulation study, *J. Pulp Paper Sci.* **21(6)**, 209-214 (1995).
6. Lu, W. Carlsson, L. A., and Andersson, Y., Micro-model of paper. Part I: Bounds on elastic properties, *Tappi J.* **78(12)**, 155-164 (1995).
7. Lu, W. and Carlsson, L. A., Micro-model of paper. Part II: Statistical analysis of the paper structure, *Tappi J.* **79(1)**, 203-210 (1996).
8. Lu, W., Carlsson, L. A., and de Ruvo, A., Micro-model of paper. Part III: Mosaic model, *TAPPI J.* **79(2)**, 197-205 (1996).
9. Jayaraman, K. & Kortschot, M.T. (1998) Closed-form network models for the tensile strength of paper – a critical discussion, *Nordic Pulp Paper Res. J.* **13(3)**, 233-242.
10. Nanko, H., Kobayashi, Y., Harada, H. and Saiki, H., Cell wall structure of nonwoody plant fibers, *International Symposium on Wood and Pulping Chemistry (Japan)* **4**, 1-5 (1983).

3. Optimal Formation Patterns

Given a recent award of a grant by the USDA (“Towards Optimal Performance of Cellulose Fiber Networks”), this topic will no longer be studied under this PAC project. However, work on the following subjects has already been carried out.

Goal 3.1 Explanation of the special orthotropy of paper from the standpoint of mechanics of random fiber networks is consistent with laws and concepts of mechanics

A. Significance

The computational mechanics model of fiber networks developed earlier under this PAC project allows a quantitative assessment of various effects: 2-D versus 3-D geometry, uniform versus random geometry, rigid versus flexible bonds, etc. We have, therefore, employed it to examine the long standing dilemma of ‘special orthotropy’ of paper (Horio & Onogi, 1951; Campbell, 1961). These authors made experimental observations that Young’s modulus at an arbitrary angle in the plane of a sheet, E_θ , is dependent only on Young’s moduli in the principal material directions

$$1/E_\theta = \cos^2 \theta / E_1 + \sin^2 \theta / E_2 \quad (3.1.1)$$

which is equivalent, according to the second author, to

$$1/G_{12} = (1 + \nu_{12})/E_1 + (1 + \nu_{21})/E_2 \quad (3.1.2)$$

The above relations are obviously different from the relation derived from proper transformation of coordinates:

$$1/E_\theta = \cos^4 \theta / E_1 + (2\nu_{12}/E_1 + 1/G_{12}) \cos^2 \theta \sin^2 \theta + \sin^4 \theta / E_2 \quad (3.1.3)$$

Henceforth, we shall express this special orthotropy behavior in terms of the in-plane compliances:

$$S_{1111} + S_{2222} - 2 \cdot S_{1122} - S_{1212} = 0 \quad (3.1.4)$$

In (3.1.4), S_{ijkl} are the components of the in-plane compliance tensor.

Schulgasser (1981) tried to explain (3.1.2) using the Cox model (Cox, 1952). This model provides an analytical derivation of the in-plane compliance of a mat of infinitely long fibers, laid in a plane according to probability density function

$$f(\theta) = \frac{1}{\pi} (1 + a_1 \cos 2\theta + a_2 \cos 4\theta + \dots + a_n \cos 2n\theta) \quad (3.1.5)$$

In (3.1.5), θ is the angle a fiber makes with respect to the MD-axis and it must be between zero and π . The Cox model involves an assumption that all the fibers carry axial forces only, which necessarily implies that they interact via frictionless pivots. This, combined with the fact that they are infinite, results in the entire fiber network deforming by a uniform strain. The Cox model generally leads to good estimates of effective Young's moduli but underestimates the shear modulus, both for isotropic and orthotropic systems. Schulgasser (1981) showed that the Cox model results in (3.1.2) when (3.1.5) is used with

$$a_2 = \frac{(a_1)^2}{2} \quad (3.1.6)$$

or when a wrapped Cauchy distribution is used

$$f(\theta) = \frac{1}{2\pi} \left(\frac{1 - \rho^2}{1 + \rho^2 - 2\rho \cos \theta} \right) \quad (3.1.7)$$

where ρ is a constant between 0 and 1. Schulgasser & Page (1988) showed that a model of paper treated as a laminate composite could yield the special orthotropic relations as well, providing certain values of fiber moduli were used; this model, too, relied on the uniform strain assumption.

B. Approach

Our modeling of the mechanics of fiber networks is based on the following assumptions and steps (Stahl & Cramer, 1998; Stahl & Saliklis, 1997):

(i) Generate a system of finite-length straight fibers according to probability density functions controlling the spatial distribution of fibers and distribution of fiber orientations. The fibers are placed in three dimensions with possible non-zero angles to control out-of-plane orientation of the fiber axis and the "roll" of the fiber about its own axis.

(ii) Fibers may have different dimensions and mechanical properties, sampled from any prescribed statistical distribution.

(iii) Bonds are identified where the prismatic volumes of two fibers intersect. Bonds are rigid, but because fiber elements extend to the center of a bond, the end of the fiber element in what really is a bonded zone with finite dimension offers some simulation of bond flexibility.

(iv) Each fiber is a series of linear elastic, 3-D Timoshenko beam elements (shear deformation being permitted) between bonds.

(v) The network's effective stiffness tensor is established from a postulate of strain energy equivalence.

C. Results

Anisotropic networks were analyzed to evaluate special orthotropy. Two degrees of anisotropy were evaluated; some networks had a_1 equal to 0.5 with all other a_i 's equal to zero, and some had a_1 equal to 0.5 with a_2 equal to 0.05. Closeness of fit to the condition of special orthotropy is given by a nondimensional parameter we call the "Campbell number"

$$n_c = \frac{S_{1111} + S_{2222} - 2 \cdot S_{1122} - S_{1212}}{S_{1111} + S_{2222}} \quad (3.1.8)$$

Each point in Fig. 3.1.1 represents the mean value for five example networks. The variability is high enough that we cannot make significant conclusions regarding the trends as network thickness increases, but we can make qualitative observations regarding the effect of flocculation and fiber orientation. The data show that networks with little flocculation (low parameter b) can come closer to satisfying the Campbell relation than networks with tighter flocs (compare solid triangles and squares, or outlined triangles and squares). Also, networks with slightly less orientation (a_1 and a_2 nonzero) are closer to satisfying the Campbell relation than strongly oriented networks (compare solid and outlined shapes).

D. Conclusions

- *Scientific Conclusions*

An analysis which simulates the heterogeneous three-dimensional network of fibers in paper, avoiding several of the assumptions that made the Cox model attractive for its simplicity, can reproduce the conditions of special orthotropy.

It is not clear from the literature whether or not "special orthotropy" as proposed by Horio & Onogi, Campbell, and others, is common in paper. Thus, we considered the issue "under what conditions special orthotropy *could* occur." The Cox model, with its neglect of fiber bending stiffness, can only produce special orthotropy with a few specific fiber orientation distributions. On the other hand, closed-form solutions for the effective compliances of a *periodic* network can be used to show that such a network, if anisotropic, cannot satisfy the required conditions [Ostojic-Starzewski & Stahl, 1999]. Given the need to consider disordered networks, an analysis for random networks which may contain flocs and other inhomogeneities was used.

The random network analysis showed that under certain conditions, namely low degree of flocculation and weak fiber orientation, special orthotropy can be achieved. These results are dependent on taking into account the flexural and shear deformation of fibers as well as their axial deformation. The evaluation of parameter space was not comprehensive, so there likely are other means to achieve the same relation among the effective material properties. Various potentially important parameters – correlation of fiber stiffness with its orientation in MD-CD plane, fiber curl, ratio of fiber flexibility to bond flexibility, and ratio of fiber flexural stiffness to fiber axial stiffness - need to be evaluated in the future.

- *Economics*

New insight into a long-standing dilemma of paper physics.

- *Deliverables*

Computer program.

E. References

- Campbell, J.G. (1961), The in-plane elastic constants of paper, *Austral. J. Appl. Sci.* **12**, 356-357.
- Cox, H.L. (1952), The elasticity and strength of paper and other fibrous materials, *Brit. J. Appl. Phys.* **3**, 72-79.
- Horio, M. and Onogi, S. (1951), Dynamic measurements of physical properties of pulp and paper by audiofrequency sound, *J. Appl. Phys.* **22**, 971-977.
- Schulgasser, K. (1981), On the in-plane elastic constants of paper, *Fiber Sci. Tech.* **15**, 257-270.
- Schulgasser, K. and Page, D.H. (1988), The influence of transverse fibre properties on the in-plane elastic behaviour of paper, *Composite Sci. Tech.* **32**, 279-292.
- Stahl, D.C. and Cramer, S.M. (1998), A three-dimensional network model for a low density fibrous composite, *ASME J. Engng. Mat. Tech.* **120**(2), 126-130.
- Stahl, D.C. and Saliklis, E.P. (1997), A non-homogeneous network model for paper, *Mechanics of Cellulosic Materials*, ed. by Perkins, R. W., ASME AMD-221/MD-77, 19-25.

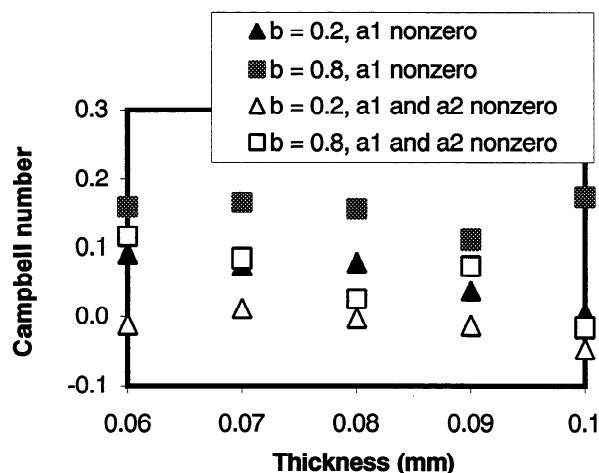


Fig. 3.1.1 Relation of Campbell number to sheet thickness t (RBA decreases as t increases), flocculation parameter b (flocs tighten as b increases), and fiber orientation function.

Goal 3.2 Assessment of the importance of 3-D versus 2-D deformations in fiber network models

A. Significance and Approach

The fiber network models have the capability to handle displacements and forces in three dimensions (3-D). This is obviously a computationally intensive procedure, and to allow analysis of larger networks, we can disable the out-of-plane degrees of freedom at each node. When this is done, the network geometry remains truly three-dimensional – but the translation and rotation at each node are constrained to be in the plane of the sheet. By far the most significant time consumption during the analysis is for assembly and factoring of the global stiffness matrix (along with associated tasks such as renumbering nodes to minimize storage requirements), and this is nominally the same with ordinary 2-D analysis and the pseudo 2-D approach resulting from elimination of out-of-plane deformations in a 3-D network. The same tasks become much more time consuming for a true 3-D model, which has twice as many degrees of freedom and more-or-less four times the storage requirements.

B. Results

As an example, identical sets of ten networks were analyzed both ways, and the effective in-plane elastic properties are shown in Fig. 3.2.1. Note that the properties have been normalized by comparison to predictions of the Cox analysis [1]. The sets of networks were identical in every way, so all of the differences in effective properties can be attributed to the different displacement restraints. The networks had rigid bonds. Fiber in-plane orientation was controlled by the Fourier series of Cox with constants a_1 equal to 0.3, a_2 equal to 0.5, and other constants equal to zero. Fiber out-of-plane orientation angles were all set to zero, so the out of plane deformations are only the result of bonded fibers having an offset through the sheet thickness. The significantly lower stiffnesses of the present model as compared to the Cox model can be attributed to short fibers and flocculation; the latter was mild. The difference in behavior resulting from the shift from 3-D to 2-D is subtle and predictable, provided that the fibers' out-of-plane orientations are minimal. Restraining the out-of-plane displacements adds stiffness to the network, so the effective elastic properties increase. For extremely low basis-weight papers, papers that are creped or given some other three-dimensional geometry, or other fibrous composites, the ability to model deformations in three dimensions may be critical.

C. Conclusions

- *Scientific Conclusions*

Including deformation in 3-D is not important when fibers lie flat in the plane of the sheet, even when the fibers' locations vary through the sheet. The 3-D deformation is expected to have a more significant effect – by increasing in-plane elastic moduli – when fibers' orientations themselves are more 3-D.

- *Economics*

Running the program in a 2-D (rather than 3-D) mode offers a saving of computer memory and the execution time by a factor of four or higher. As a result, much larger networks can be analyzed in the 2-D mode.

D. Reference

[1] Cox, H.L. (1952), The elasticity and strength of paper and other fibrous materials, *British J. Appl. Phys.* 3, 72-79.

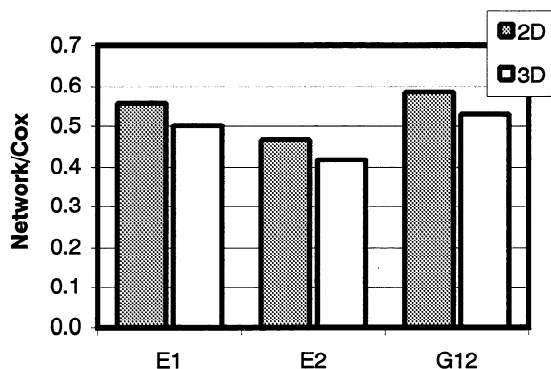


Fig. 3.2.1 In-plane effective elastic properties for 3-D and 2-D analyses, normalized by the formulas of Cox (1952); averages for ten specimens.

Goal 3.3 Assessment of the effect of formation on deformation field In paper

A. Significance

The computational mechanics model of fiber networks developed earlier under this PAC project allows a quantitative assessment of various effects: 2-D versus 3-D geometry, uniform versus random geometry, rigid versus flexible bonds, etc. We have, therefore, employed it to examine the effect of formation on the deformation field of paper.

B. Approach

Flocculation in the network is modeled through a two-step process. First, floc centers are generated in the volume – the number is controlled by a parameter n equal to the number of flocs per MD-CD square mm . Then, fibers are placed into the network, first by randomly assigning each fiber to a floc and then by locating each fiber with respect to the floc's center. The latter is done by placing the fiber's center a distance r from the floc's center according to the probability density function

$$f(r) = -\frac{b^2}{2}r + b \quad r > 0 \quad (3.3.1)$$

As b increases, fibers are clustered into tight flocs, and as b decreases they are scattered. This is apparent in Fig. 3.3.1. A fiber's in-plane orientation angle is controlled with (3.1.5), and the flocs are dilated in the MD direction according to

$$r_{MD} = r(1 + a_1)\cos\theta \quad r_{CD} = r\sin\theta \quad (3.3.2)$$

To evaluate the effect of disordered network geometry on displacement fields, a series of networks with three degrees of flocculation were analyzed. Example networks are shown in the left column of Fig. 3.3.1; they are $4mm$ square with $30mm$ of fiber length per square mm MD-CD area. The fibers are $0.05mm$ wide, and this combined with the total fiber length gives a coverage of 1.5. Using a typical value for fiber coarseness this is equivalent to approximately $8gram/m^2$ basis weight. The sheet thickness was $0.03mm$, and the resulting RBA varied from 0.56 to 0.66. There is no preferred direction in these networks – all coefficients in (3.1.5) are zero. The only parameter that was varied was the floc parameter, with the three values shown in Fig. 3.3.1.

C. Results

The networks were analyzed subject to a prescribed x -strain *on the boundaries*, and the figures in the right column of Fig. 3.3.1 show the difference between the resulting displacement of each node and what the displacements would be if the strain field *in the interior of the network* were uniform. If the displacement field were actually uniform, the figures would consist simply of dots; the lines represent deviation from uniformity. Two qualitative observations can be made: First, the deviation from uniform displacements is certainly apparent in all three networks, even the one with a low degree of flocculation. Second, there seems to be a combination of two main effects – groups of well connected fibers are held back or pulled along depending on whether their connections to the left or right edge are stiffer (apparent at the lower right and lower left of the middle figure); and there are swirls where the fibers on opposite sides of open areas are pulled more or less severely (apparent near the upper right corner of the top figure and also at several spots in the bottom figure). To quantitatively describe the non-uniformity in the displacement fields, we calculate the root-mean-square difference between each node's actual displacement and what it would be if displacements were uniform. The average *rms* displacement difference for sets of ten networks is 1.66 for floc parameter $b = 0.2$, 2.61 for $b = 1.6$, and 2.86 for $b = 2.4$. While

the absolute magnitudes of these numbers are not worth discussing, they clearly show a trend toward less uniformity in the displacement fields as the network geometry becomes less homogeneous.

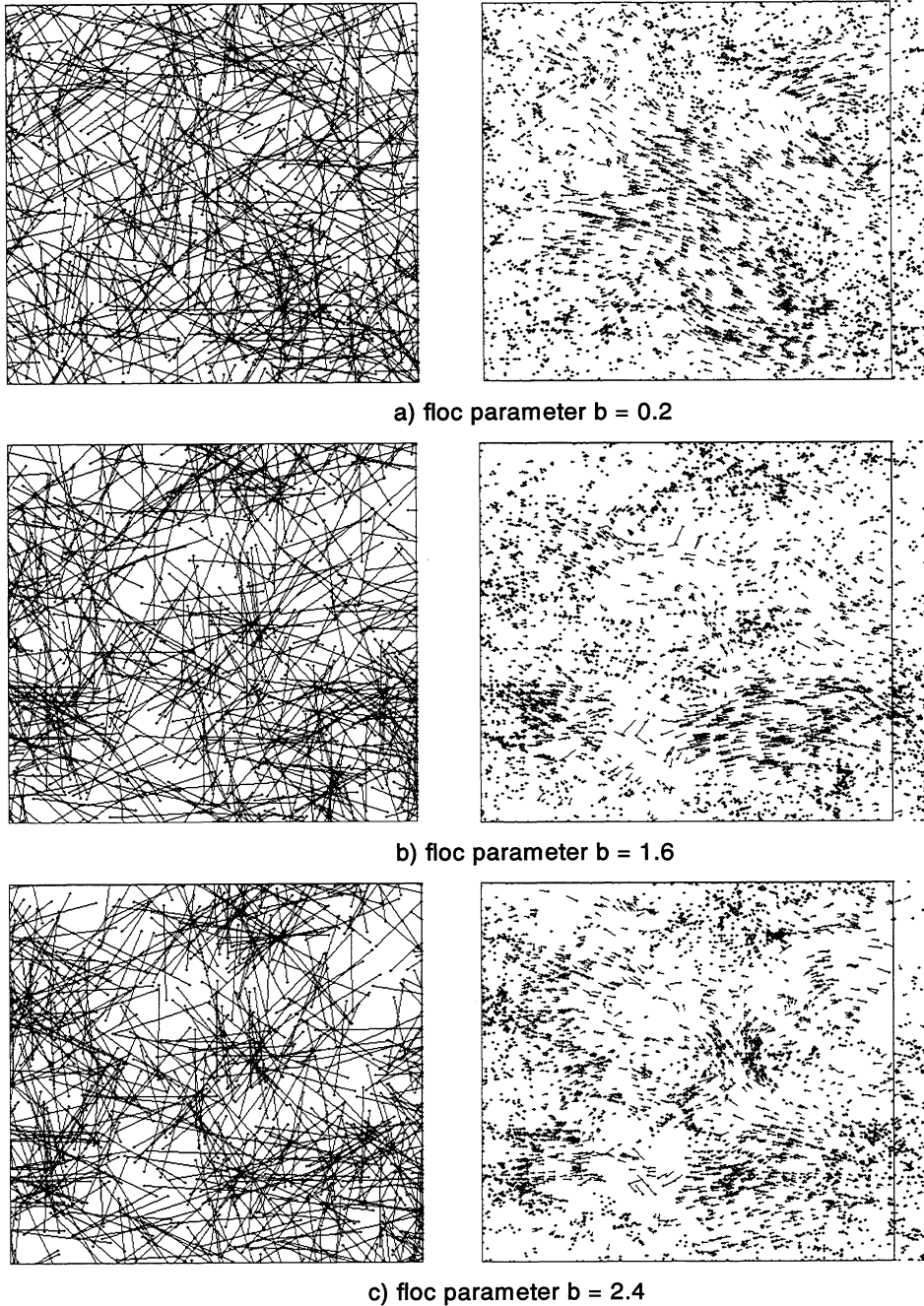


Figure 4. Undeformed network geometry (left) and comparison of node displacements to uniform displacement field (right)

Fig. 3.3.1 Undeformed network geometry (left) and comparison of node displacements to uniform displacement field (right), due to an extension in the x-direction.

D. Conclusions

- *Scientific Conclusions*

The difference between the deformation field from the computational mechanics approach and the affine displacement field is dependent on formation. The uniform strain assumption should not be expected to produce good paper strength predictions when network geometry is non-homogeneous, as it is with any but the mildest degree of flocculation.

- *Economics*

New insight into the mechanics of paper, which cannot be obtained with conventional models or through experiments.

- *Deliverables*

Computer program.

Goal 3.4 Determination of the optimal thickness of paper for highest bending stiffness

A. Significance

Bending stiffness of paper $C_b = EI$ is defined from the classical equation of strength of materials

$$M = C_b \frac{1}{\rho} \quad (3.4.1)$$

It is seen, intuitively, that E increases, while I decreases, with decreasing H . Thus, there must be an optimal thickness H_{opt} that maximizes $C_b = EI$.

B. Approach

The computational mechanics model of fiber networks developed earlier under this PAC project allows a quantitative assessment of the in-plane modulus E versus network's compaction and thickness H . The system under study is shown in Fig. 3.4.1.

C. Results

The resulting optimal stiffness in function of paper thickness is shown in Fig. 3.4.2. The fiber network's parameters are given in Fig. 3.4.3 – note that eight network compaction levels were investigated, so that we have eight values of RBA (relative bonded area).

D. Conclusions

- *Scientific Conclusions*

The optimal paper thickness giving the highest bending stiffness, with all the other parameters kept constant, can be determined.

- *Economics*

The optimal paper thickness giving the highest bending stiffness may be desired in a number of applications.

- *Deliverables*
Computer program for determination of effective flexural response.

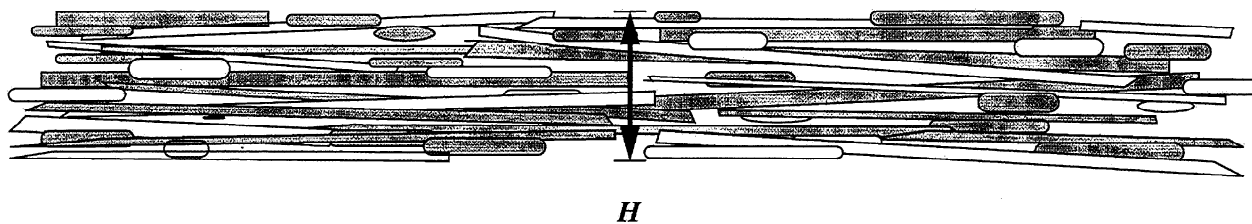


Fig. 3.4.1 A schematic of fiber networks' cross-section.

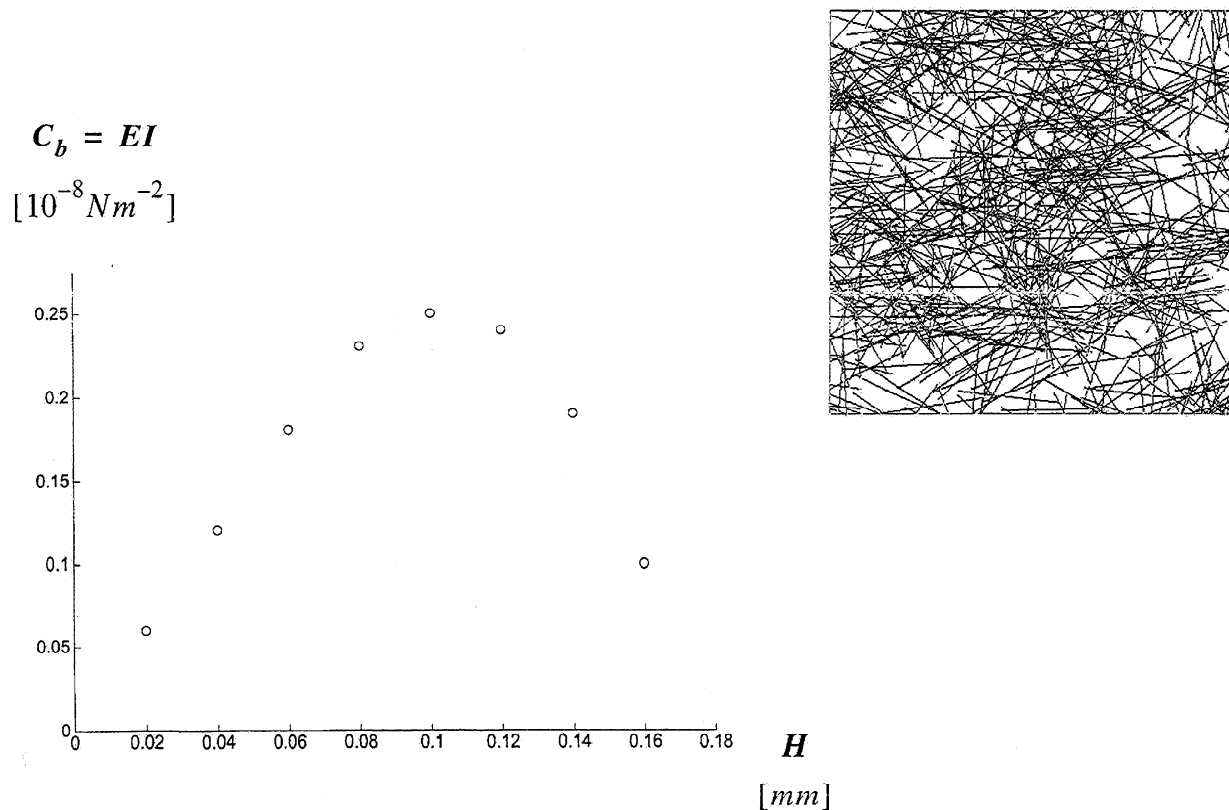


Fig. 3.4.2 Determination of the optimal bending stiffness of a fiber network whose MD-CD structure is fixed (as shown on the right) but compaction decreases as H increases. Effectively, $H_{opt} = 0.1$ is found.

4. Effect of Strength Additives

A. Significance

Bonds are idealized as prismatic members with a small but finite length between the centerlines of the bonded fibers. Bond geometric properties (area, torsion constant J , and area moments of inertia about two axes) are based on the plane parallelogram shape which would occur if fibers were beveled so their surfaces fit tightly together [Stahl and Cramer, 1998]. The shape is further idealized as an ellipse to facilitate shear stress calculations. While this bond idealization may not be realistic, it does give us the opportunity to control bond axial, flexural, and shear stiffness and to account for differing bond size caused by variations in fiber size or proximity.

B. Approach and Results

The model has the ability to include or neglect bond flexibility: When bonds are not flexible, each bond consists of a master node and two slave nodes [Ostoja-Starzewski *et al.*, 1999; Stahl and Cramer, 1998]. The slave nodes are on the fiber centerlines, and the master node is at the center of the fibers' idealized interface surface. Only the master node has degrees of freedom that affect the global stiffness matrix. When bonds are flexible, the master-slave mechanism is not applicable. Instead, each of what were previously described as "slave" nodes become regular nodes. A short beam element, representing the bond itself, joins these nodes. The bond element's orientation and cross-sectional dimensions are based on the bond idealization presented above. While an ordinary beam element may seem out of place acting as the bond, the element does include the capability for shear deformation, so its very short length makes shear and torsion the predominant modes of deformation. The effect of bond flexibility on network effective elastic properties was verified to be that reported by Raisanen *et al.* (1995), with subtle loss of network stiffness as bond flexibility increases. The more important effect of bond flexibility is seen when the network is subjected to progressive failure analysis, and the amount of force a given bond takes is proportional, along with geometry, to the bond stiffness. A simple drawback to the flexible bond model is that it requires twice as many degrees of freedom as the rigid bond model.

C. Conclusions

- *Scientific Conclusions*

Are listed above.

- *Economics*

Depending on the end-properties desired, it may be desirable to add flexibility to the fiber-fiber bonds. Various effects on elasticity and strength may be predicted with the computer model.

- *Deliverables*

Conclusions given above and the computer program.

D. References

- Ostoja-Starzewski, M., Quadrelli, M.B. and Stahl, D.C. (1999), Kinematics and stress transfer in quasi-planar random fiber networks," *Comptes Rend. Acad. Sci. Paris – IIb* **327**, 1223-1229.
- Raisanen, V. I., Alava, M. J., Nieminen, R. M., and Niskanen, K. J. (1995), Elastic-plastic random fibre networks, *1995 International Paper Physics Conference*, 109-112.
- Stahl, D.C. and Cramer, S.M. (1998), A three-dimensional network model for a low density fibrous composite, *ASME J. Eng. Mater. Tech.* **120**(2), 126-130.

5. Single Fiber Mechanics

A. Significance

It is a trivial statement that mechanics and physics of paper depends on the properties of a single fiber. Moreover, it is well known that the fiber-fiber bonding is a function of single fiber properties. Thus, several studies in the past were conducted of a single fiber from the standpoint of a fibril bundle [1, 2, 3, 4]. These studies, however, did not treat the cellulose fiber as a multilayer composite with each layer being made of a bundle of fibrils arranged in a helical geometry. The reason for this drawback, to the best of our understanding, has been the failure to fully treat the fibril-layer-fiber mechanical system at hand. For example, some studies dealt with a planar, rather than tubular, orthotropic composite. Others, considered the problem in the cylindrical geometry from the outset, but missed the ‘helically-wound orthotropy’ and thus lacked the dependence of the global fiber response on the fibril angle.

B. Approach and Results

We first determine the effective, chiral response of a single layer, taken as a transversely isotropic material having a given helix (fibril) angle θ (Fig. 5.1). This is expressed by a matrix relating the axial force F and the twisting moment M to the axial strain ε and the rotational strain β

$$\begin{bmatrix} F \\ M \end{bmatrix} = \begin{bmatrix} C_{11} & C_{12} \\ C_{21} & C_{22} \end{bmatrix} \begin{bmatrix} \varepsilon \\ \beta \end{bmatrix} \quad (5.1)$$

All the C_{ij} ‘s are functions of the elastic moduli of fibrils and matrix, their volume fractions, and θ . With the solution for a single layer, a system of n layers can next be treated – its response is again defined by an equation of the type (5.1). The fiber is taken as a system of n concentric, perfectly bonded cylinders, each of a different fibril angle. The explicit formulas are not given here for the sake of economy of space. The derivation proceeds as follows: each layer of fibrils is replaced with an orthotropic lamina, whose axes are wound helically to form a cylinder. Elastic parameters in the cylinder’s tangential plane are obtained under the ‘perfect bonding interlayer’ assumption. On the other hand, radial motion is solely due to the variation in the fibril angle under tensile load. The effect of Poisson’s ratio in this direction is neglected.

D. Conclusions

- *Scientific Conclusions*

A basis is made for inclusion of inelastic strains for investigation of fiber swelling and drying effects.

- *Economics and Deliverables*

Explicit formulas for single fiber’s elastic response.

C. References

- [1] Schniewind, A.P. and Barrett, J.D. (1969), Cell wall model with complete shear restraint, *Wood and Fiber* 1(3), 205-2114.
- [2] Cave, I.D. (1969), The anisotropic elasticity of the plant cell wall, *Wood Sci. Tech.* 2, 268-278.
- [3] Mark, R.E., Gillis, P.P., New models in cell-wall mechanics, *Wood and Fiber* 2, 79-95.
- [4] Cave, I.D. (1969), The longitudinal Young’s modulus of *Pinus Radiata*, *Wood Sci. Tech.* 3, 40-48.

[5] Spencer, A.J.M., Rogers, T.G., England, A.H. and Parker, D.F. (1984), Continuum Theory of the Mechanics of Fiber-Reinforced Composites, *CISM Courses and Lectures*, Udine, Italy.

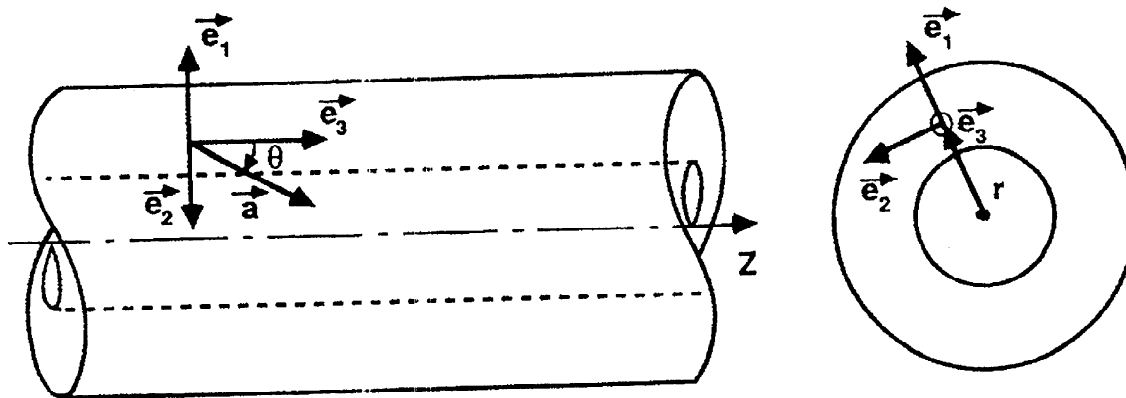


Fig. 5.1 Locally transversely isotropic cylindrical fiber: system of coordinates.

6. Correlation of Mass Distribution and Crack/Damage Patterns

A. Significance

Cracks propagating in paper are not straight, but rather, disordered lines of random character. While this randomness must be caused by the spatially nonuniform paper microstructure, no clear connection between the two has been established as yet. It is, therefore, important to find the missing link. The complexity of a crack (damage zone) in a fiber network, as a result of successive fiber and fiber-fiber bond failures – in accordance with the local redistribution of the stress field - is shown in Fig. 6.1. Evidently, there is an influence of formation on the geometry of the damage zone. This figure also demonstrates the power of our fiber network model and the need to embed this model in, say, a large-scale finite element model so as to include other length scales. A full study of this topic is presently being researched by Jaime Castro, Ph.D. student, and will be reported once completed.

It is a well-known fact that mechanical properties of paper display considerable statistical scatter. In the recent PAC reports we were asking the following questions:

Q1: What can the 7"x1" TAPPI test say about the web strength?

Q2: How does the tensile strength of paper depend on specimen size and loading conditions?

Q3: What is the statistical scatter and the cross-correlations of
 the elastic (Young's) modulus in *lbf/in*,
 the tensile breaking strength in *lbf/in*,
 the strain to failure in %,
 the tensile energy absorption in *lbf/in*.

Q4: What is the spatial correlation structure of these four properties?

In this PAC report we address Q4 by conducting extensive experiments for two specimen sizes: 1"x1" and 1"x10".

B. Approach

Spatial statistics is the language in which to express the spatial nonuniformity of mechanical properties of paper. Guidance in this respect is offered by the statistical fluid mechanics, especially once we recognize that it is the turbulence on the wire which is (probably) the main cause of the aforementioned nonuniformities. It follows that the paper web is a random field in MD,CD-plane, or, simply, a random process in the MD (DiMillo and Ostoja-Starzewski, 1998). The correlation structure of random fields is described by the correlation coefficient

$$\rho_{ij}(x_1, x_2) = \frac{\langle u_i(x_1)u_j(x_2) \rangle - \langle u_i(x_1) \rangle \langle u_j(x_2) \rangle}{\sigma_i(x_1)\sigma_j(x_2)} \quad (6.1)$$

its determination being based on experiments obtained on arrays of specimens of the type shown in Fig. 6.2. The notation above involves

$$\begin{bmatrix} u_1 \\ u_2 \\ u_3 \\ u_4 \end{bmatrix} \equiv \begin{bmatrix} E \\ \sigma_{\max} \\ \varepsilon_{\max} \\ TEA \end{bmatrix} \quad (6.2)$$

and $\langle u_i(x_1) \rangle$ for the mean and σ_i for the standard deviation of a the quantity i at a point x_1 .

If the random field is wide-sense stationary

$$\rho_{ij}(x_1, x_2) = \rho_{ij}(r) \quad (6.3)$$

with $r = |x_1 - x_2|$. It may then be isotropic,

$$\rho_{ij}(r) = \rho_{ij}(|r|) \quad (6.4)$$

which makes it an obvious candidate model for a handsheet. Possible fits include an exponential function

$$\rho_{ij}(|r|) = \exp(-A|r|^\alpha) \quad A > 0 \quad 0 < \alpha \leq 2 \quad (6.5)$$

or a power function

$$\rho_{ij}(|r|) = (1 + A|r|^\alpha)^{-1} \quad A > 0 \quad 0 < \alpha \leq 2 \quad (6.6)$$

These can be composed to grasp the multiscale nature of the paper web

$$\rho_{ij}(|r|) = \sum_{n=1}^N \exp(-A_n|r|^{\alpha_n}) \quad A > 0 \quad 0 < \alpha \leq 2 \quad (6.7)$$

and

$$\rho_{ij}(|r|) = \left[\prod_{n=1}^N (1 + A_n |r|^{\alpha_n}) \right]^{-1} \quad A > 0 \quad 0 < \alpha \leq 2 \quad (6.8)$$

Now, given the machine direction preference – such as higher stiffness and strength in MD vs. CD – it is preferable to use *quasi-isotropic* correlation functions (DiMillo and Ostoja-Starzewski, 1998), e.g., elliptic type.

Results

1. Paper exhibits a random multiscale structure (from millimeters up to thousands of kilometers) - statistical continuum models are needed to grasp spatial variability.
2. Anisotropic structure of paper requires quasi-isotropic random fields. An example of a correlation function in the MD and its spectral analysis is shown in Fig. 6.2.
3. Continuum random field description serves as the starting point of stochastic finite element models for multiscale mechanics of paper.
Details to be presented in a yearly report.

D. Conclusions

- *Scientific Conclusions*

Same as results above.

- *Economics*

Turbulence on the wire and, probably, fluctuations in the approach flow systems are the cause of multiscale statistical structure of paper (formation, streaks, etc.). Quantitative description of this structure is now offered.

- *Deliverables*

Function fits of statistical variability in paper.

Software for determination of function fits from measurements.

E. References

DiMillo, M. and Ostoja-Starzewski, M. (1998), Paper strength: Statistics and correlation structure, *Intl. J. Fract.* **90**, L33-L38.

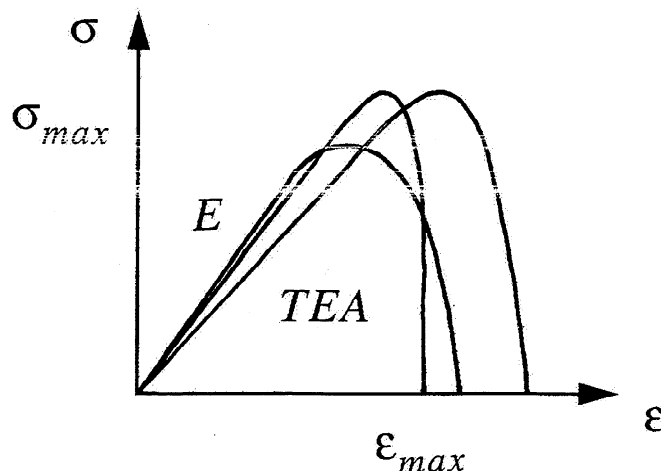


Fig. 6.1 Three stress-strain responses, showing scatter in the elastic modulus, the tensile breaking strength, the strain to failure, and the tensile energy absorption.

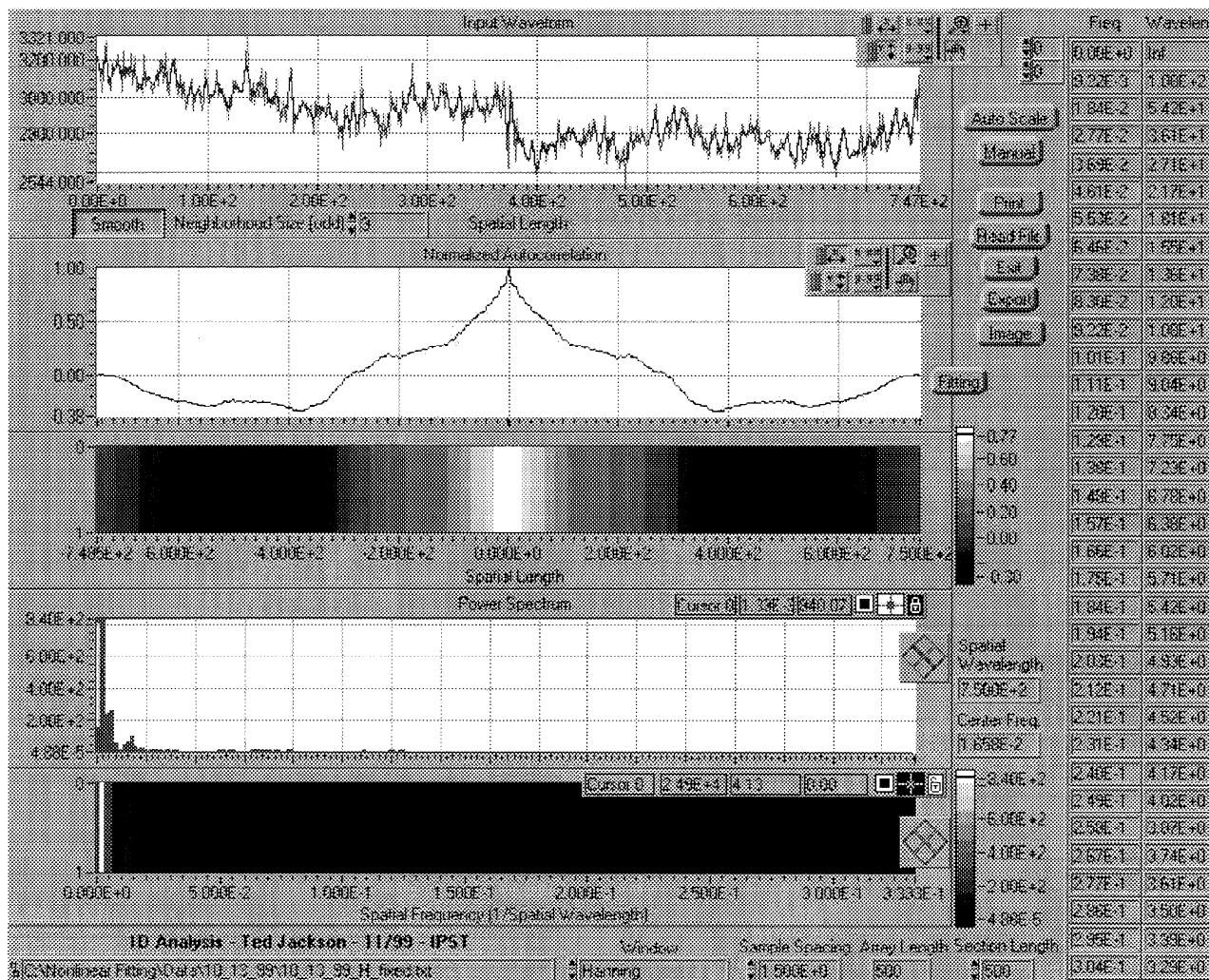


Fig. 6.2 Measurement of MD stiffness at 500 locations in the MD; the corresponding correlation function; the corresponding spectrum.

7. Wave Propagation Sensitivity to Paper Formation

A. Significance and Motivation

Paper of all kinds is well known to possess spatial inhomogeneities – commonly called formation - on a multitude of scales:

- fibril-bundle structure randomness of single fiber’s properties,
- fiber microstructure disorder of flocs’ geometry,
- streaks imperfection on scales of meters in MD and CD,
- imperfection on scales of meters in MD and CD.

Thus, there arises a need to understand these effects in:

- dynamic response of paper webs (flutter, runnability, ...),
- ultrasonic measurements.

B. Approach

In our study of this problem we recognize the interplay of three basic length scales (Fig. 7.1):

- the typical wavelength λ ,
- the typical size of inhomogeneity d ,
- the physical domain of size L .

Let us first consider the classical wave equation, which also serves as a basic model of longitudinal or transverse waves,

$$\frac{\partial^2 u}{\partial x^2} - \frac{1}{c^2} \frac{\partial^2 u}{\partial t^2} = 0 \quad (7.1)$$

By considering spatial fluctuations in mass density ρ , we obtain a (classical) stochastic Helmholtz equation [1-10]

$$\frac{\partial^2 u}{\partial x^2} + k_0^2 n^2(x)u = 0 \quad (7.2)$$

where $k = \omega/c = \omega\sqrt{\rho/E}$ is the wave number of a reference homogeneous (unperturbed) medium, and n is the refraction index; $n = 1$ in the homogeneous medium. In the above, and henceforth, u stands for the displacement in the frequency domain. We note that (7.2) grasps the spatial fluctuations in the mass density but not the fluctuations in elastic modulus or the cross section. As a result, the quite extensive range of techniques for waves in random media governed by (7.2) is not applicable, and the above formulation needs to be generalized to account for the space dependent mass density ρ , elastic modulus E , and cross-sectional area A . Thus, in place of (7.1), we have

$$\frac{\partial}{\partial x} [A(x)E(x) \frac{\partial}{\partial x} u] - \rho(x)A(x) \frac{\partial^2 u}{\partial t^2} = 0 \quad (7.3)$$

and, in the frequency space,

$$\frac{\partial}{\partial x} [A(x)E(x) \frac{\partial}{\partial x} u] + \rho(x)A(x)\omega^2 u = 0 \quad (7.4)$$

The spatial fluctuations in ρ , E , and A are modeled via random Fourier series

$$\begin{aligned} \rho(x) &= \rho_0 [1 + \varepsilon_\rho \sum_{n=1}^N a_\rho \cos ngx + b_\rho \sin ngx] \\ E(x) &= E_0 [1 + \varepsilon_E \sum_{n=1}^N a_E \cos ngx + b_E \sin ngx] \\ A(x) &= A_0 [1 + \varepsilon_A \sum_{n=1}^N a_A \cos ngx + b_A \sin ngx] \end{aligned} \quad (7.5)$$

ρ_0 , E_0 , and A_0 are the mean properties, while ε_ρ , ε_E , and ε_A are strengths of imperfections. With this model a wide range of correlation functions (R) of any random field (ρ , E , and/or A) may be investigated. For example, the band-limited white-noise model is extensively being used. For the random field of ρ it is written as (see Fig. 7.2)

$$R_\rho(r) = 2S_0 \frac{\sin \omega_c r}{r} \quad r = x - x' \quad S_\rho(\omega) = \begin{cases} S_0 & |\omega| < \omega_c \\ 0 & \text{else} \end{cases} \quad (7.6)$$

Note that the measurements and studies of previous section, such as those presented in Fig. 6.2, play a crucial role in finding the best fits to $R_\rho(r)$.

We study the imperfection sensitivity of a paper's elastodynamic response via spectral finite elements. The advantage of this approach is that all the three length scales mentioned at the beginning of this section are grasped at once, so that their relative effects can readily be assessed. First, we note that such an element for the longitudinal waves in a homogeneous rod (ρ , E , and $A = \text{const}$) is [11]

$$\begin{bmatrix} F_1 \\ F_2 \end{bmatrix} = \begin{bmatrix} k \cot k & -k \csc k \\ -k \csc k & k \cot k \end{bmatrix} \begin{bmatrix} u_1 \\ u_2 \end{bmatrix} \quad (7.7)$$

With respect to Fig. 7.3, '1' and '2' subscripts in the entries of both vectors denote quantities at the left and right ends of the rod, respectively. In Section C below we discuss the effect of spatial variability (i.e., random fluctuations) in ρ , E , and A on this spectral finite element.

Before we end this section, however, we give the model formulation for study of flexural waves in paper. Confining ourselves to a 1-D problem, in analogy to (7.3), we have

$$\begin{aligned} K(x)G(x)A(x) \frac{\partial}{\partial x} \left[\frac{\partial}{\partial x} w - \varphi \right] - \rho(x)A(x) \frac{\partial^2 w}{\partial t^2} &= 0 \\ E(x)I(x) \frac{\partial^2 \varphi}{\partial x^2} + K(x)G(x)A(x) \left[\frac{\partial}{\partial x} w - \varphi \right] - \rho(x)I(x) \frac{\partial^2 \varphi}{\partial t^2} &= 0 \end{aligned} \quad (7.8)$$

where w is the transverse displacement, and φ is the rotation. Here ρ , E , and A are the same as before, while I is the cross-sectional moment of inertia, and K is the shape factor. Evidently, with all of these being constant (homogeneous problem of the reference case), (7.8) reduces to well-known equations of the classical Timoshenko beam. The spatial fluctuations in ρ , E , A , I , and K are modeled via random Fourier series – recall (7.5). Finally, the spectral finite element in the reference case is

$$\begin{bmatrix} V_1 \\ V_2 \\ M_1 \\ M_2 \end{bmatrix} = \begin{bmatrix} k_{11} & k_{12} & k_{13} & k_{14} \\ k_{21} & k_{22} & k_{23} & k_{24} \\ k_{31} & k_{32} & k_{33} & k_{34} \\ k_{41} & k_{42} & k_{43} & k_{44} \end{bmatrix} \begin{bmatrix} w_1 \\ w_2 \\ \varphi_1 \\ \varphi_2 \end{bmatrix} \quad (7.9)$$

wherein the k_{ij} 's are not shown explicitly for the economy of space. As before, 1 and 2 in the entries of both vectors denote quantities at the left and right ends of the beam, respectively.

C. Results

The results we get by letting either ρ or E vary are very similar so we will discuss them together. First, we note that letting these two quantities vary produces a large effect with small to moderate g . By a large effect we mean a strong departure from the reference case at and around the resonant frequencies. The effects decrease with increasing g but, regardless of the value of g , the effects are most noticeable at higher frequencies. Variable density has practically no effect for $g = 100.0$ while there is a noticeable effect from variable modulus for the same g .

When A alone is allowed to vary, we see practically no effect for $g = 0.01$ or 0.1 , but there is a noticeable effect present for low to mid-range frequencies. However, this effect vanishes at higher frequencies. As g is increased to 10.0 , the effect is weaker for lower frequencies but is quite pronounced in the mid to high frequency range. Finally, when $g = 100.0$, the effect all but vanishes for low frequencies but is still noticeable for higher frequencies.

D. Conclusions

- *Scientific Conclusion*

- (i) Strong sensitivity of elastodynamic response to formation imperfections.
- (ii) Different effects of imperfection in mass density than imperfection in elastic moduli or cross sectional area. Depending on the wavelength, there is a tendency to diffuse the resonance frequency around that of the reference (idealized), homogeneous material.

- *Economics*

Formation imperfections have strong influence on elastodynamic response of paper. Depending on the application, it may, or may not, be desirable to keep a certain degree of spatial nonuniformity (inhomogeneity) in paper. For example, the propagation of steady-state flexural waves on the web – that are potentially destructive - would be hindered by the web's nonuniformity. On the other hand, the ultrasonic measurements work best on perfectly uniform sheets – their interpretation on nonuniform ones requires a careful consideration of the results presented here.

- *Deliverables*

- (i) Research results listed above.
- (ii) A method (computer programs) developed to assess sensitivity of acoustic and flexural waves to formation imperfections in mass density, elastic moduli, and cross sectional area.

E. References

- [1] Asch, M., Kohler, W., Papanicolau, G.C., Postel, M. & White, B. (1991), Frequency content of randomly scattered signals, *SIAM Review* **33**(4), 519-625.
- [2] Cash, J.R. & Wright, M.H. (1991), A deferred correction method for nonlinear two-point boundary value problems: Implementation and numerical evaluation, *SIAM J. Sci. Stat. Comput.*, **12**, 971-989.
- [3] Chernov, L.A. (1960), *Wave Propagation in a Random Medium*, McGraw-Hill, New York.
- [4] Frisch, U. (1968), Wave propagation in random media, in *Probabilistic Methods in Applied Mathematics 1* (A.T. Bharucha-Reid, ed.), 75-198, Academic Press.
- [5] Howe, M.S. (1971), Wave propagation in random media, *J. Fluid Mech.* **45**(4), 769-783.

- [6] Kharanen, V.Y. (1953), Sound propagation in a medium with random fluctuation of the refractive index, *Dokl. Acad. Nauk SSSR* **88**, 253.
- [7] Sobczyk, K. (1985), *Stochastic Wave Propagation*, Elsevier-Polish Sci. Publ.
- [8] Sobczyk, K. (1986), Stochastic waves: The existing results and new problems, *Probab. Eng. Mech.* **1**(3), 167-176.
- [9] Taniuti, T. & Nishihara, K. (1983), *Nonlinear Waves*, Plenum, London.
- [10] Uscinski, B.J. (1977), *The Elements of Wave Propagation in Random Media*, McGraw-Hill, New York.
- [11] Doyle, J.F. (1997), *Wave Propagation in Structures: Spectral Analysis Using Fast Discrete Fourier Transforms*, Springer-Verlag, Berlin.

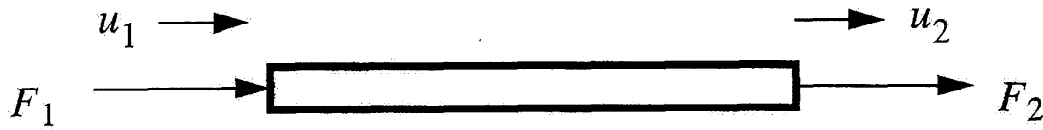


Fig. 7.1 Nodal loads and degrees of freedom of a rod element for longitudinal waves.

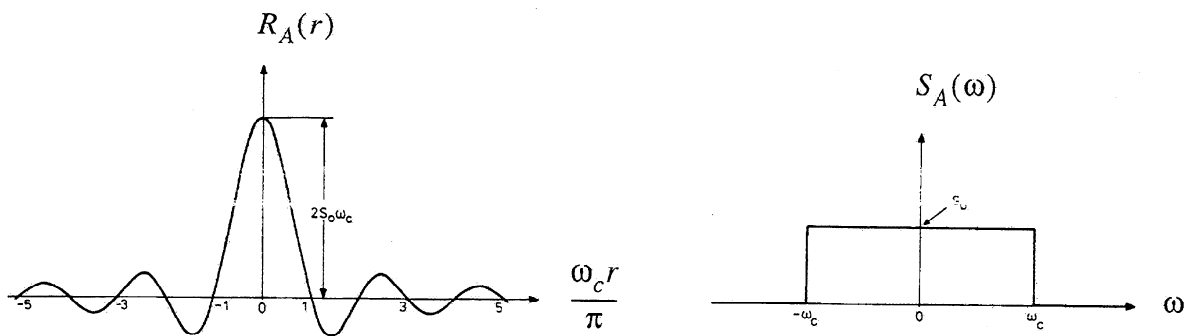


Fig. 7.2 Autocorrelation function and spectral density of the band-limited white-noise model.

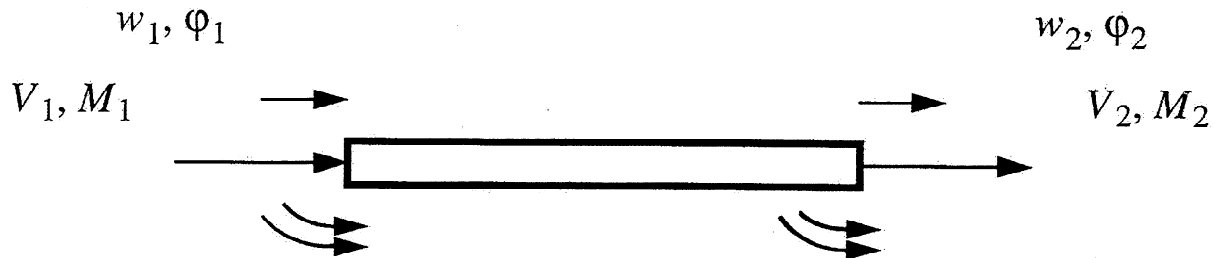


Fig. 7.3 Nodal loads and degrees of freedom of a beam element for flexural waves.

IMPROVING THE REFINING OF CHEMICAL PULPS

STATUS REPORT

FOR

PROJECT F024

**John Waterhouse
Hiroki Nanko
Miranda Bliss**

**Institute of Paper Science and Technology
500 10th Street, N. W.
Atlanta, Georgia 30318**

DUES FUNDED PROJECT SUMMARY

Project Title: Improving the Refining of Chemical Pulps
 Project Number: F024
 PAC: Paper Physics

Project Staff:

Principal Investigator: John F. Waterhouse
 Co-Investigator: Hiroki Nanko
 Research Support Staff: (Miranda Bliss) position vacant

FY 99-00 Budget: \$ 76,000

Allocated as Matching Funds: none

Time Allocation

Principal Investigator: 25%

Co-Investigator: 10%

Research Support Staff: 50%

Supporting Research

M.S. Students: None

Ph.D. Students: None

RESEARCH LINE/ROAD MAP:

10. Reduce net energy consumption per ton by 30% compared to '97' levels.

- reduce energy consumption

11. Convertibility and End-Use Performance

Improve the ratio of product performance to cost for pulp and paper products by 25% by developing:

- models, algorithms, and functional samples of fibrous structures and coatings, which describe and demonstrate improved convertibility and end-use performance, and breakthrough papermaking and coating processes which can produce innovative webs with greater uniformity than achieved by current processes

PROJECT OBJECTIVE:

Define and determine a pulp's refinability behavior, and determined how changes in fiber structure, produced by refining, are related to an improved balance between paper machine runnability, i.e., water removal and paper properties, i.e., strength.

PROJECT BACKGROUND

This project was initiated in October 1996. Its value to member companies includes: 1) improved utilization of raw materials, 2) increases in paper-machine productivity, 3) improved tools for pulp characterization, 4) enhanced control of refining process, and 5) energy reduction associated with refining and water removal.

The main project goal is to develop a pulp refinability index, i.e., its propensity to cut, fibrillate, produce fines, and to curl and microcompress, which can be applied to pulps produced by new pulping and bleaching processes, genetically modified pulps, as well as pulps produced by more conventional pulping and bleaching methods.

A concomitant goal is to produce and characterize specific changes in fiber structure and measure their impact on water removal and paper properties. The specific changes in fiber structure are: (1) fines production, (2) external changes in fiber structure, (3) internal changes in fiber structure, and (4) curl removal.

Ultimately, we would like to determine for both laboratory and production refiners the extent to which these changes are produced with selected furnishes and the means for controlling them.

MILESTONES:

See Gantt Chart below.

DELIVERABLES:

1. Methodology for determining a pulp's response to refining.
2. Tools for improved pulp characterization.
3. Strategies for reducing energy consumption and/or improving paper machine productivity.

STATUS OF GOALS FOR FY 99-00

1. Develop methods to produce specific changes in fiber structure by refining and the means for their characterization.
2. Determine the extent to which specific changes in fiber structure are produced in production refining systems as a function of C factor.
3. In conjunction with goals 1 and 2 measure wet and dry state properties as they might relate to machine runnability and paper performance.

SCHEDULE:

March 99 - March 00

TASK	April	May	June	July	Aug	Sept	Oct	Nov	Dec	Jan	Feb	March
Pulp character. Methods	←---	-----	-----	-----	-----	-----	-----	-----	-----	-----	-----	-----→
Int. Changes	}											
Ext. Changes	}←--	-----	-----	-----	-----	-----	-----	-----	-----	-----	-----	-----→
Fines Generation	}											
Fiber Length Reduction	}											
Prod. Refining Systems												
- samples & charact.	←	-----	-----	-----	-----	-----	-----	-----	-----	-----	-----	-----→
Reports & Presentations				R			P					R & P

SUMMARY OF RESULTS (March 99 - March 00)

- 1) Completed of joint project with Pulping & Bleaching Unit (Project F013), examining the impact of refining on different yield pulps and bleaching sequences.
- 2) Established a hypothesis and methods to determine a pulp's propensity to "cutting".
- 3) Examined cross sections of earlywood and latewood Fe-colloid stained PFI refined fibers at different kappa numbers using the transmission electron microscope.
- 4) Established a model as a basis for improving the (disk) refining process using the Invention Machine (Tech Optimizer) software.

SUMMARY OF KEY CONCLUSIONS

- Curl effects either need to be avoided or accounted for in comparing new pulping and bleaching techniques.
- The never-dried to dried zero-span, Znd/Zdried, is proposed as a measure of a fiber's propensity to cutting.
- The Znd/Zdried varies from 0.931 to 0.612 over the kappa number range of 110 to 10.7.
- Transmission electron microscopy of Fe-colloid stained fiber has shown significant differences in the refining of earlywood and latewood fibers at different kappa numbers.

INTRODUCTION

Refining or beating (terms used interchangeably) is defined as the changes in fiber structure necessary to maximize the papermaking potential of a pulp. Papermaking potential is concerned with achieving the right balance between important paper properties and machine runnability within specified economic restraints.

We have previously identified, from the review by Page (1), 9 changes in fiber structure produced by refining. In addition, we have chosen to examine more closely the contribution of the changes given below.

1. Internal changes in fiber structure
2. External changes in fiber structure
3. Fines production
4. Changes in fiber curl
5. Fiber length reduction

The major tasks identified at our Project Advisory Committee Meeting on March 26, 1997 were as follows:

- **Select and characterize pulp types to be used.**
- **Develop methods to produce specific refining actions.**
- **Measure wet and dry state properties as they might relate to machine runnability and paper performance.**

At our March 1999 PAC meeting the following tasks were proposed:

1. Test hypothesis that a fiber's propensity to "cutting" is in part controlled by its never-dried zero-span strength using an Escher Wyss (EW) or production refiner.
2. Establish method for producing controlled external changes in fiber structure and fines production.

Progress on the above tasks are discussed below.

Select and characterize pulp types to be used – Joint Project with Pulping and Bleaching Unit (Project F013)

Project F013 (PI's Tom McDonough and Charles Courchene) is ultimately concerned with improved pulping and chlorine-free bleaching strategies.

The pulps that were produced are identified in Table 1. The species is loblolly pine and the kappa number ranges from a high of 110 to a low of 10.7 for the unbleached pulps, which were delignified using either a conventional kraft cook or a kraft cook to kappa number 30 followed by oxygen delignification. The final pulp brightness for the CED and DED bleaching stages are also included in Table 1 together with viscosities determined after the E stage.

Table 1. Kappa Number and Brightness of Pulps Prepared by the CBSD

Material & Cook	Unbl. kappa no.	CED	R_∞	DED	R_∞
S.P. chips* ⇒ conventional kraft	110.1	-	-	-	-
S.P. chips ⇒ conventional kraft	28.1	22.8	84.0	26.6	75.9
S.P. chips ⇒ conventional kraft	17.1	11	86.9	12.5	84.7
kappa 30 ⇒ O oxygen	20.4	17.1	88.3	20.3	81.2
kappa 30 ⇒ O oxygen	15.7	-	88.6	17	83.1
kappa 30 ⇒ O oxygen	12.1	10.1	90.8	13	84.1
kappa 30 ⇒ O oxygen	10.7	9.8	89.9	11.9	85.8

*S.P. chips - refers to southern pine chips

Refining characteristics and paper properties for the above pulps were presented at the PAC Meeting in March 1999. The refining response of the above pulps was examined at one level, i.e., 3000 revs. in the PFI mill.

It was evident that the pulps delignified using the kraft-oxygen process were significantly curled when compared to the kraft pulps, the fiber of which were relatively straight. This finding complicates the interpretation of the results reported last March, particularly in deciding the relative merits of kraft versus kraft-oxygen delignification.

In a further investigation of the curl problem, the amount of curl developed in various mixer types is shown in Figure 1. The above kraft-oxygen pulps were produced in the Peg type mixer. It can also be seen that curl index tends to increase with increasing temperature.

One parameter that we consider important for refining, is the never-dried strength of the fiber. We hypothesize that the strength of the fibers in the never-dried wet state should be an indication of a fiber's propensity to cutting. One possible measure of never-dried fiber strength is never-dried zero-span strength. However, in order to mitigate the effects of curl mentioned above, I have chosen to examine the ratio of never-dried zero-span to dried zero-span strength. In

addition we have also looked at the ratio of rewetted zero-span strength to dried zero-span strength.

The variation of wet to dry zero-span ratio for the unrefined and refined kraft and kraft-oxygen pulps is shown in Figure 2. The ratio falls with decreasing kappa number especially below a kappa number of 20. There does not appear to be any large differences in the ratio between the two methods of delignification. However, it appears that PFI refining tends to reduce the ratio. This is more clearly shown in Figures 3 and 4 for the CED and DED bleach sequences. It should also be emphasized that the never-dried zero-span strength is lower than the re-wet zero-span strength. This may be due to cross-linking or hornification effects.

An examination of selected fibers by Dr. Hiroki Nanko using the transmission electron microscope (TEM) is given in Appendix 1 of this report.

Develop methods to produce specific refining actions

The type of refining action is central to the structural changes produced in the fiber. The C Factor analysis developed by Kerekes et al. (2-5) is one approach to defining refining action in terms of the number and severity of impacts a fiber receives in the refiner. Changes in fiber structure are given at two extremes, i.e., low severity with a high number of impacts produces "fibrillation", while the converse, high severity and a low number of impacts produces "cutting". What happens in between these extremes is largely unknown.

In the C-factor approach the specific energy of refining E is partitioned as follows:

$$E = N * I$$

where $N = C/F$ is the number of impacts and C and F are C factor and flow rate, respectively. The intensity of refining, $I = P/C$ where P is the net power used in refining. Therefore, the severity or intensity of refining decreases, and the number of impacts increases, as C-factor increases. Kerekes et al. (2-3) have derived equations for calculating C-factor for both disk and conical refiners. Kerekes in a private communication was kind enough to give me a copy of his Excel spreadsheet for this calculation.

In more recent work Croney, Ouellet, and Kerekes (4) have looked at how refining intensity influences tensile development, and examined various models, including C-factor, as a means to correlate the behavior of a variety of softwood and hardwood pulps. They concluded that C-factor analysis provided the best correlation and Figure 12 of their report illustrating this is reproduced in Figure 5.

In Figure 5 we note that the intensity is expressed as a specific intensity or energy of impact S , i.e., the energy impact per fiber is divided by the mass of the fiber, which is the product of coarseness time's fiber length. The interesting features of Figure 5 are that hardwoods are refined at a higher intensity than softwoods, and at very low intensities, strength may be either inadequately developed or highly developed levels of strength development can occur. The specific energy input is constant at 120 kWh/t. The authors provide no explanation for why this occurs. It is presumed that at high intensities fiber length is reduced and the treatment is more heterogeneous; however, these effects might be offset by fines production. No fiber strength or fiber length data are included in the paper. However, for the range of furnishes investigated, it is likely that there was significant variability in fiber strength.

Kerekes and Ouellet (5) have also reported their concerns about the homogeneity of Escher Wyss multipass refining, stating that in a production refining system where there is just one pass through the refine, only approximately half of the fibers are treated.

Iribarne and Schroeder (6) have made an interesting and extensive investigation of the relationship between fiber weak points and cutting to explain fiber quality differences in mill and laboratory cooked pulps.

Fiber weaknesses were induced by chemical means using a potassium superoxide and cellulase and PFI refining was used to investigate, in a limited sense, fiber "cutting". It was proposed that the PFI mill should reveal weak points along the fiber. The PFI mill has a lower intensity of impact $PFI \equiv SEL$ 0.5 Ws/m.

The mill pulps (southern pine bleachable grade kraft pulps) and their respective chips were obtained from two mills designated A and B. Acid chlorite pulp (holocellulose) and a lab kraft pulp were produced from the chips. Pulp properties are summarized in Table 1 below taken from Iribarne and Schroeder's paper (6).

The fibers from mill B were slightly longer and stronger than those from mill A, i.e., 2.73 mm vs. 2.41 mm.

Table 1. Selected Properties of Kraft Pulp and Holocellulose Fiber Samples ^(a,b)

Mill	Sample	κ ± 0.3 mL/g	μ ± 1 mPa·s	L_L ± 0.09 mm	C ± 0.03 mg/m	ρ_s ± 10 kg/m ³	WZS ± 7 kNm/kg
A	mill kraft (A0)	27.1	23	2.41	0.33	530	112
	lab. kraft (A1)	27.9	23	2.38	0.33	500	149
	holo. fibers (A3)	19.1	41	3.00	0.38	640	102
B	mill kraft (B0)	28.6	24	2.73	0.32	480	122
	lab. kraft (B1)	28.0	24	2.66	0.29	530	153
	holo. fibers (B3)	18.4	40	2.87	0.42	660	96

- (a) κ = kappa number, μ = CED viscosity, L_L = length-weighted average fiber length, C = fiber coarseness, ρ_s = apparent sheet density, WZS = wet zero-span tensile index. TAPPI Test Methods were used for κ , μ , ρ_s and WZS. L_L and C by Kajaani FS-100.
- (b) All precision limits are the standard deviation of two to six replicate determinations.

In our earlier work we found that for a kappa number of 17.1, the zero-span strength of our kraft pulp was 115 Nm/g, 140 Nm/g, and 128 Nm/g, for wet, dry, and rewet conditions, respectively. It is not clear whether the wet zero-span strengths given in Table 1 are for the never dry condition or rewet condition. It seems likely that the latter is the case.

The main conclusions of this study are: (1) that fiber "cutting" during PFI refining is greater for the long fiber fraction of the mill pulps due to damage incurred during the hot blow from the digester. (2) Kraft pulping chemistry preferentially weakens the short fibers. (3) All fiber lengths can be weakened by a combination of chemical and mechanical treatments. (4) Fatigue would affect fibers in proportion to their length while chemical attack would more likely occur in the short fibers.

Iribarne and Schroeder's proposed model to explain weak point formation on the short and long fiber fractions of the pulp is reproduced in Figure 6.

New Approaches to Refining Action

Other methods for producing changes in fiber structure are under consideration including ways to improve the disk refiner. With regards to the latter, Project **ROCIT** (re-evaluating our core industry technologies) has provided this author with the opportunity to learn and use a very powerful software package called Tech Optimizer ("Invention Machine"). One of the most important and critical steps in the use of this package is to model the process to be improved. Once this model has been established, then there are a number of systematic steps one can take to evaluate either incremental or radical changes to the current process.

One of the diagrams that has been developed to date is shown in Figure 7. A vital part of the refining process is the associated hydrodynamics and rheology. The flow is part laminar and part mixing. Recent studies of the effective viscosity μ_e of the refining process (7) suggest that the pulp suspension behaves as a shear thinning fluid, i.e., and its viscosity decreases as refining progresses.

It is possible that refining might be more effectively carried out in turbulent flow. This might ultimately lead to a more compact and energy efficient process. Gullichsen and Harkonen (8) have reported that the turbulent flow characteristics in the consistency range of 8 to 15% are basically the same as in the range 0 to 6%. They also found, as shown in Figure 8 that a significant refining effect occurs when softwood fibers at 10% consistency are exposed to turbulence for different time intervals up to 40 seconds. The refining action presumably is from fiber-fiber interaction as well as the flexing which is likely to occur.

The geometry of the cell in which the measurements were carried out is shown in Figure 9. The ribs are necessary to transfer shear stresses to the suspension, since without them slippage would occur. It is speculated that the addition of particulate matter, e.g., fillers, would significantly enhance refining action. There is a considerable body of knowledge concerned with the behavior of particulate or granular matter.

In summary, refining seeks to produce certain changes in fiber structure, which will enhance product properties. However, productivity can be adversely affected since refining generally impairs the water removal behavior of the furnish. Waterhouse (9) has recently commented on how water removal is affected by furnish, refining, and the other unit processes of papermaking.

The three major considerations associated with refining are properties, water removal, and energy. As refining action is changed by, say, decreasing specific edge load (SEL), then for a given energy input, strength will improve but the CSF will be lower. Furthermore, the intensity of treatment should match the characteristics of the furnish to be treated. Hurter (10) has examined the differences between mill and laboratory refining. She demonstrates, as have others, that the PFI mill does not do a good job of simulating mill refining, particularly as it applies to fiber "cutting" and refining energy considerations.

In the next section we present results relating to the specific tasks given at the March 1999 PAC:

1. Test hypothesis that a fiber's propensity to "cutting" is in part controlled by its never-dried zero-span strength using an Escher Wyss or production refiner.

2. Establish method for producing controlled external changes in fiber structure and fines production.

RESULTS AND DISCUSSION

Our initial plan was to take advantage of Weyerhaeuser's offer to use their Escher Wyss laboratory refiner. However, due to various circumstances, including the difficulties of processing and evaluating pulp samples between two distant laboratories, it was decided to further explore IPST's refining capabilities. Finally, we decided to conduct some preliminary refining experiments using IPST's 12-inch Sprout Waldron disk refiner as a step to more closely simulate production refining.

In order to prove or disprove the above hypothesis, it was decided to use a never-dried commercial bleached kraft southern pine pulp obtained from an IPST member company. Several methods of systematically reducing the strength of the fiber in the never-dried wet state were considered. These included enzyme treatment, bulk and vapor phase HCl treatment. An indication of how fiber strength is affected by such treatments is shown in Figure 10. Also shown in Figure 10 is the variation of zero-span strength with cellulose content. Thus any lignin or hemicelluloses present do not significantly contribute to the load-bearing capacity of the fiber. Ideally, fiber strength is invariant with yield if calculated on the basis of cellulose only; however, cellulose degradation processes can result in a significant reduction in fiber strength as shown by Gurnagul and Page (11).

Degradation processes can also be expected to reduce the never-dried wet fiber strength. As stated earlier I have chosen to use the ratio of never-dried to dry zero-span ratio as a measure of fiber degradation primarily to avoid the effects of fiber curl. We have found in our joint experiments with the Pulping and Bleaching Unit (Project F013) that this ratio can vary from 0.931 to 0.612, depending on the pulping and bleaching sequences employed.

Bulk acid hydrolysis was used to vary wet fiber strength and consisted of treating a bleached southern pine kraft pulp with 2.6 M HCl @ 2.5% at a temperature of 45°C for time intervals of up to 4 hours. The variation of dry zero-span strength and the ratio of wet to dry zero-span strength with treatment time is shown in Figures 11 and 12. The initial values are close to what we found with our model pulp study, but bulk hydrolysis, as expected, results in large losses in fiber strength., i.e., the ratio drops from an initial value of 0.73 to around 0.3 after 4 hours of treatment.

Following these results we decided to use a 30-minute interval for treating 1 kilogram of pulp for the Sprout Waldron disk refining experiments. This

treatment resulted in an average zero-span ratio of 0.394, which was lower than expected.

The Sprout Waldron refiner is equipped with a 7 HP motor and was estimated to have a rotational speed of 2600 rpm. The plate design (# 12716) consisted of 8 bars/segment with each plate having a total of 6 segments. Three plates were used on the stator and three identical plates were used on the rotor. The average bar angle was 10° . The specific edge load calculated was $SEL = 0.801$ Ws/m.

Using Kerekes's C-factor analysis the value of C was calculated to be 2.09×10^{10} impacts/sec. The number of impacts per fiber/pass $N = 412$ and the intensity of impact $I = 1.78 \times 10^{-7}$ J/impact giving a specific impact of 0.296 KJ/Kg. The impact level of the PFI mill has been estimated by Walsh and Kerekes (12) to be in the range of 10^{-6} to 10^{-7} J/impact for 1000 roll revolutions. The Escher Wyss (EW) refiner operates in the range of 0.5 to 3.0 Ws/m, and at 31 and 206 impacts per fiber, the impact energy per fiber is 6×10^{-6} and 1×10^{-6} J/impact, respectively.

Just under one kilogram of pulp at 4% consistency was processed by the refiner for two conditions namely: a control (an untreated pulp), and a bulk HCl-treated pulp. For the bulk HCl-treated pulp the flow rate and temperature rise were measured for each pass through the refiner. The total number of passes through the refiner for each pulp was 13, and the fiber flow rate with the number of passes for the bulk HCl-treated pulp is shown in Figure 13, where the average fiber flow rate is 2.97 tons/day. Now assuming that the effective or net horse power in refining is 5 HP the total energy input to refining after 13 passes is **22.1 HPD/T** (396 KWh/T). This energy level is high however our temperature rise measurements confirmed that our estimate of 5 HP/pass was reasonable. The ΔT for 13 passes was 15°C , and 1°C at 4% consistency is equivalent to 1.481 HPD/T, therefore this yields a total energy of **22.2 HPD/T**.

The variation of never-dried zero-span strength to dry zero-span strength with number of passes is shown in Figure 14. In previous work with the PFI mill we had found that this ratio drops with refining; surprisingly, we did not see this effect with SW refiner. The variation of CSF with number of passes is shown in Figure 15, and we note that there is very little difference in freeness drop between the control and the bulk HCl-treated pulp. This would imply that the rate of fines (material passing a 200 mesh screen) production was not significantly affected by the HCl treatment. The fines content of the HCl-treated pulp was 6.01% and rose to 28.1% after 13 passes. However, the initial fines content of the control pulp was 3.3% and rose to 10.3% after 13 passes. It was also observed in determining the fines content of the HCl-treated pulp that the fines

appeared to be flocculated, and this may explain the why no CSF difference was observed.

It is great to report that in addition to the Kajaani FS-100, IPST now has a Fiber Quality Analyzer (FQA). The FQA can provide fiber length distributions as well as curl and kink data. The weighted fiber length variation with number of passes is shown in Figure 16. Initially, the fiber length of the control increases slightly; initially, this is attributed to curl removal, which will be substantiated shortly. However, there is an initial dramatic falloff in fiber length for the bulk HCl-treated pulp, which then remains fairly constant over the range of 3 to 13, passes through the refiner. This is attributed to the reduction in never-dried zero-span strength of the bulk HCl-treated pulp. The curl data in Figure 17 shows that refining reduces curl and more so for the HCl-treated pulp, i.e., greater curl reduction would be expected with a greater reduction in fiber length. The FQA weighted average "fines" fraction variation with passes through the refiner is shown in Figure 18. The control shows a slight decrease in "fines" in contrast to the large increase exhibited for the HCl-treated pulp.

The reduction in fiber length due to bulk HCl treatment may be similar to Irabane and Schroeder's superoxide treatment of their pulps. They claim that the short fiber fraction is more prone to weakening by chemical means than the long fiber fraction (see Figure 6). That this is so in the present situation is suggested by the differences in "fines" distribution shown in Figure 18. The large increase in fines of the HCl-treated pulp may be evidence of a preferentially weakened shorter fiber fraction. Fractionated zero-span measurements might be revealing in this situation. In spite of the increase in the "fines" fraction, there is no significant impact on CSF as shown in Figure 15. The levels of specific edge load and C-factor used in the current SW refiner experiments are clearly not sufficient to produce "cutting" of the untreated long fiber fraction.

Propensity to "Cutting" of Commercial Pulps

Concern was expressed at the last October PAC meeting about using bulk-HCl treatment to simulate the weakening of commercial pulps. Currently, we are in the process of looking at pulps from various sources. Measurements of wet, dry, and rewet zero-span, and fiber length distributions, fines, and FQA kink and curl data will be made. Some of these pulps have been obtained as a result of member company interest in this project.

One company together with viscosity data (TAPPI Test Method T230C) submitted pulp samples from various locations in a specific mill. The variation of zero-span strength with viscosity is shown in Figure 19. The correlation for dry zero-span with viscosity is virtually nonexistent for the dry case; however, the correlation is stronger for the never-dried samples, i.e., $r^2 = 0.54$. The variation of zero-span ratio with viscosity for the never-dried and rewet samples is shown in Figure 20

where the correlation's are $r^2 = 0.64$ and $r^2 = 0.73$ for the wet and rewet samples, respectively. The wet ratios are in the range of 0.5 to 0.6 and below the levels measured on our model pulps, i.e., and 0.93 to 0.61.

It should be emphasized that a reduction in wet zero-span strength not only has implications for refining, but the concomitant loss in dry zero-span strength, together with fiber length reduction, also has an impact on paper properties.

CONCLUSIONS

The main conclusions are summarized as follows:

1. Curl effects which can confound the interpretation of new pulping and bleaching techniques either need to be avoided or accounted for in making performance comparisons
2. The never-dried to dried zero-span ratio Z_{nd}/Z_{dried} is proposed as a measure of fibers propensity to cutting.
3. The varies from 0.931 to 0.612 over the kappa number range of 110 to 10.7
4. PFI refining further reduces the Z_{nd}/Z_{dried} ratio of DED and CED bleached pulps.
5. A pulp whose fiber strength was degraded using a bulk HCl treatment was found to undergo significant "cutting" when subjected to refining in a Sprout Waldron 12 in disk refiner and compared with an untreated control pulp.
6. Transmission Electron Microscopy of Iron colloid stained fiber has shown significant differences in the refining of earlywood and latewood fibers at different kappa numbers.

ACKNOWLEDGMENTS

The author would like to thank Miranda Bliss for her painstaking and careful work to date on this project and also to Barbara Lee Hing for her editorial revisions.

LITERATURE CITED

1. Page, D.H. "The beating of chemical pulps-the actions and its effects," in Trans. of the FRS, Cambridge, UK, 1989.
2. Kerekes, R.J. "Characterization of pulp refiners by a C-factor," Nordic Pulp and Paper Res. J. No. 1(5):3-8, 1990.
3. Kerekes, R.J., Clara, M., Dharni, S., and Martinez, D.M. "Application of the C-factor to characterize pulp refiners: JPPS 19(3):J125-J130, 1993.
4. Croney, C., Ouellet, D., and Kerekes, R.J. "Characterizing refining intensity for strength development," Proceedings 5th International Paper & Board Industry Conference, Scientific & Technical Advances in Refining, Vienna, Austria, April 1999.
5. Kerekes, R.J. and Ouellet, D. "Characterization of Pulp Refining," Annual Report Pulp and Paper Center, The University of British Columbia, pp. 30-31, July 1, 1998 - July 30, 1999.
6. Iribarne, J. and Schroeder, L. R. "The use of fiber cut probabilities to study fiber weak points," TAPPI International Paper Physics Conference, September 26-30, 1999, San Diego, CA.
7. Radoslavova, D., Roux, J.C. and Silvy, J. "Hydrodynamic modeling of the behavior of the pulp suspensions during beating and its application to optimizing the refining process." Vol. 1, 607-640, The Fundamentals of Papermaking Materials, Trans. 11th Fundamental Research Symposium, Cambridge: September 1997.
8. Gullichsen, J. and Harkonen, E. "Medium consistency technology. 1. Fundamental data," Tappi 64 (6): 69-72 (1981).
9. Waterhouse, J.F. "Characterizing pulps for paper machine runnability" Proceedings TAPPI Engineering/Process and Product Quality Conference. Vol. 3, September 12-16, 1999, Anaheim, CA.
10. Hurter, P. "A closer look at fiber characteristics and laboratory evaluation of pulp," Proceedings TAPPI Pulping Conference, Vol. 1, October 31- November 4, 1999, Orlando, FL.
11. Gurnagul, N. and Page, D.H. "The difference between dry and rewetted zero-span strength of paper," Tappi J. 72(12):164-167, December 1989.
12. Welch, L.V. and Kerekes, R.J. "Characterization of the PFI mill by the C-factor," Appita 47(5):387-390, September 1994.

TABLES

Table 1 Sprout Waldron Disk Refining Experiments - Pulp: Bl. Kraft Southern Pine Bulk Control 4% Consistency

Pass	Clearance	CSF	CSF-PTB	WP-ZST	std. dev.	% cons.	Dry ZST	std. dev.	Znd/Z dry	FQA								
										Kajaani			Length-weighted		% fines	Mean Curl		% fines
										Length-weighted	Weight-weighted	% fines	Length-weighted	Weight-weighted	arithmetic	Length-weighted	arithmetic	weighted
0		712		66.5	6.28	26.3	96.8	6.91	0.687	2.64	3.37	20.40	2.431	3.193	18.69	0.175	0.158	1.55
1	0.004"																	
2	0.001-0.0002																	
3	0.001-0.0002																	
4	0.001-0.0002																	
5	0.001-0.0002	630	576	82.5	8.19	39	111.2	8.76	0.742	2.69	3.44	21.73	2.497	3.335	20.28	0.200	0.113	1.66
6	0.001-0.0002																	
7	0.001-0.0002																	
8	0.001-0.0002	542	550	70.6	5.23	28	103.8	9.23	0.680	2.67	3.39	24.72	2.657	3.469	16.78	0.113	0.099	1.2
9	0.001-0.0002																	
10	0.001-0.0002																	
11	0.001-0.0002	408	407	85.2	3.77	26.3	109.4	9.98	0.779	2.50	3.19	21.66	2.465	3.237	16.90	0.124	0.106	1.27
12	0.001-0.0002																	
13	0.001-0.0002	378	353	74.8	5.23	26.2	102.4	5.76	0.730	2.60	3.35	20.00	2.495	3.298	17.05	0.117	0.099	1.3

152

Table 2 Sprout Waldron Disk Refining Experiments Pulp: Bleached Kraft Southern Pine Bulk HCl-treated 4% consistency

Pass	Clearance	CSF	Time sec.	Sample weight, g	Temp. °C	WP ZST	std. dev.	% cons	Dry ZST	std. dev.	Znd/Zdry	Kajaani			FQA			% fines weighted			
												Length-weighted	Weight-weighted	% fines	Length-weighted	Weight-weighted	% fines arithmetic		Length-weighted	Mean Curl arithmetic	
0		712		151.8	11	20.2	0.46	30.9	56.2	2.72	0.359	2.42	3.25	24.81	2.284	3.159	20.20	0.186	0.161	1.97	
1	0.002		32		14																
2	0.002		29		15																
3	0.002	692	29	116.2	16	26.7	2.97	31.4	68.6	7.73	0.389	1.90	3.09	41.62	1.596	2.944	28.10	0.116	0.097	5.94	
4	0.002		26		18																
5	0.002		28		19																
6	0.002	568	30	107.4	20	28.6	3.10	29.3	76.1	3.66	0.375	1.80	3.04	45.75	1.562	2.937	27.56	0.114	0.089	6.22	
7	0.002		27		22																
8	0.002		24		23																
9	0.002	503	19	76.9	24	29.2	2.12	27.8	75.9	3.31	0.385	1.89	3.09	46.27	1.586	3.157	30.00	0.103	0.086	7.19	
10	0.002		21		24																
11	0.002	443	25	80.6	25	30.6	2.37	27.2	81.8	4.70	0.374	1.80	3.06	46.03	1.586	3.157	30.00	0.103	0.086	7.14	
12	0.002		21		25																
13	0.002	356	20	87.6	26	30.8	2.68	24.8	64.2	5.78	0.480	1.64	2.83	44.73	1.423	2.850	28.26	0.105	0.085	7.26	

153

FIGURES

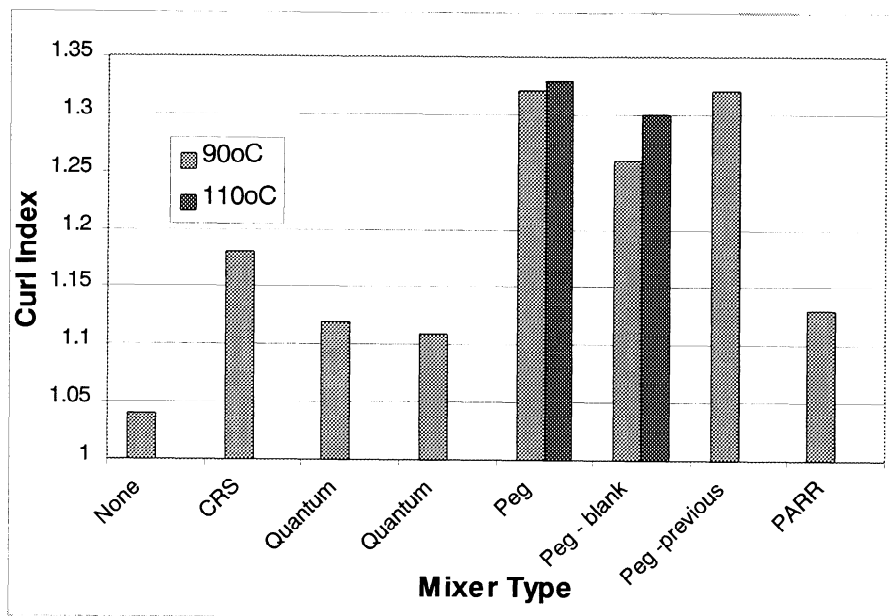


Figure 1. Curl Index for Different Types of Mixers

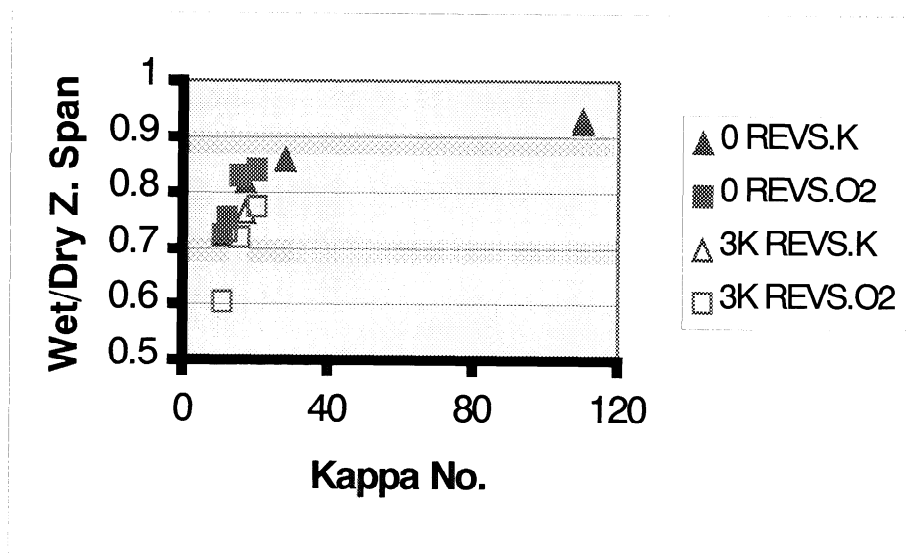


Figure 2. Variation of Wet/Dry Zero-span Ratio with Kappa Number

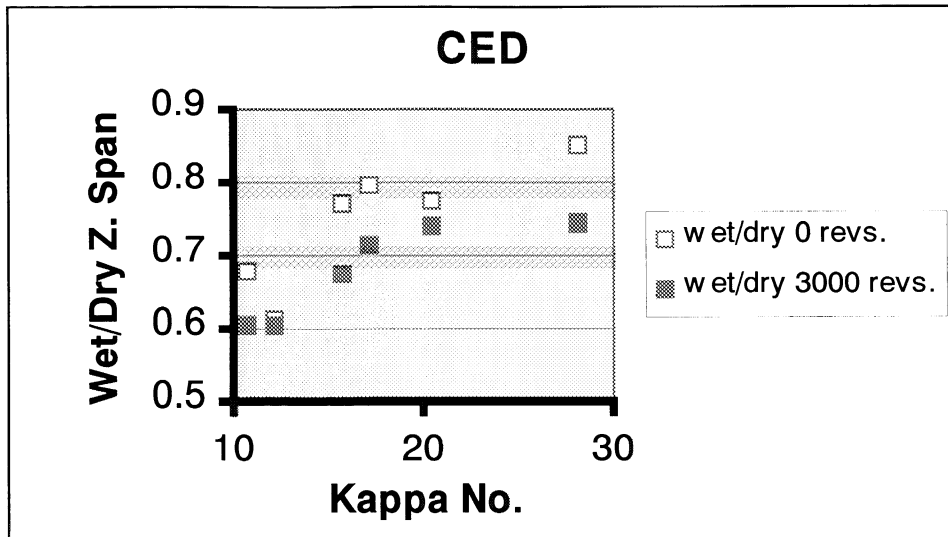


Figure 3. Variation of Wet/Dry Zero-span Ratio with Original Kappa Number for CED Bleach Sequence

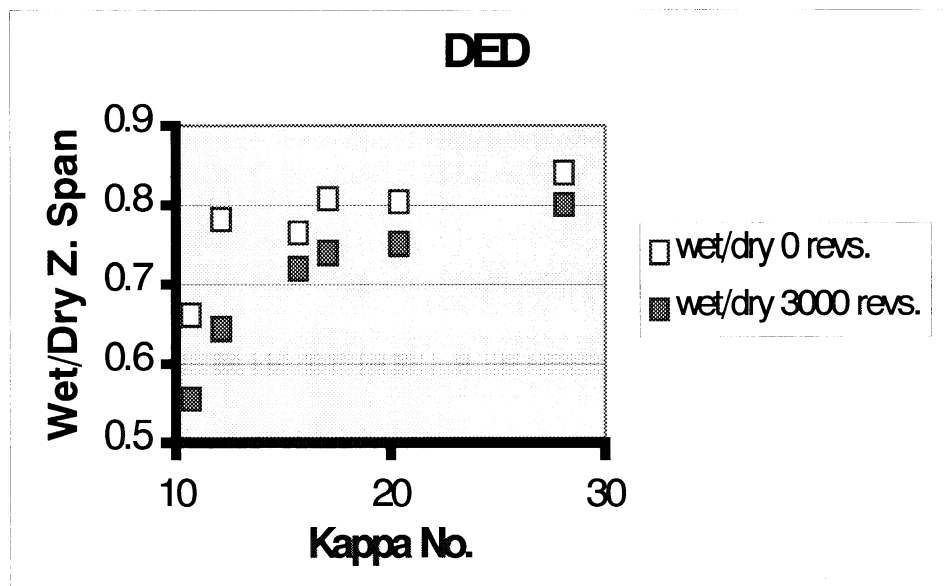


Figure 4. Variation of Wet/Dry Zero-span Ratio with Original Kappa Number for CED Bleach Sequence

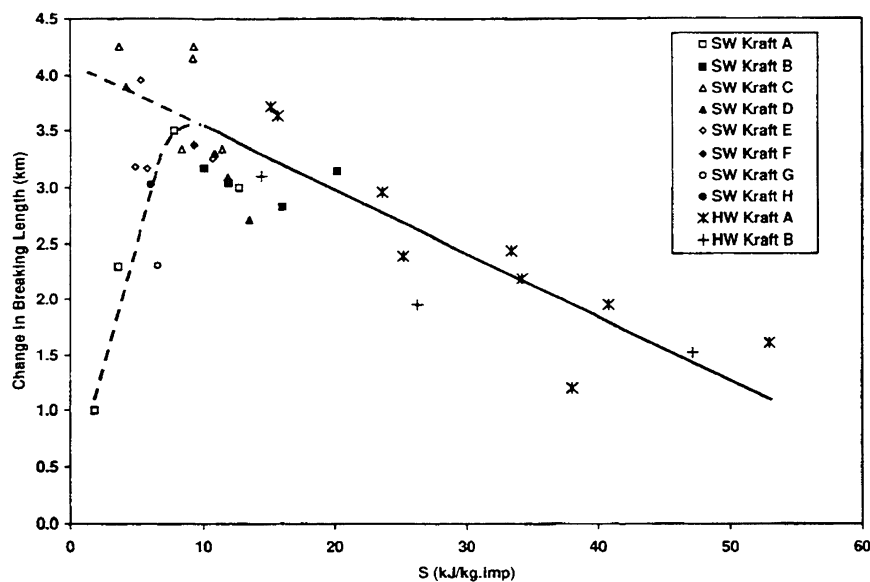


Figure 12: Change in breaking length as a function of Specific Energy per Impact (S) for hardwood and softwood pulps at E=120 kWh/t.

Figure 5. Taken from Croney, C. Ouellet, D., and Kerekes, R.J. (3)

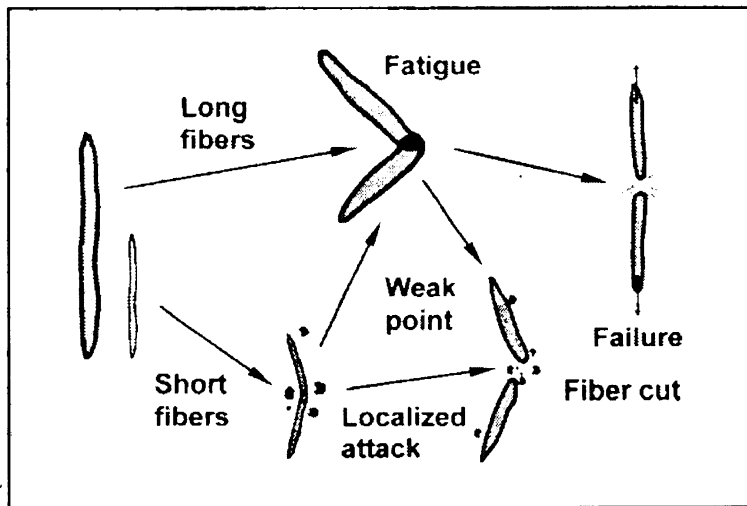


Figure 11. Proposed paths of weak-point formation and resulting effects.

Figure 6. Taken from Iribarne J. and Schroeder, L.R. (5)

Product Analysis
Functional Analysis
Function Model

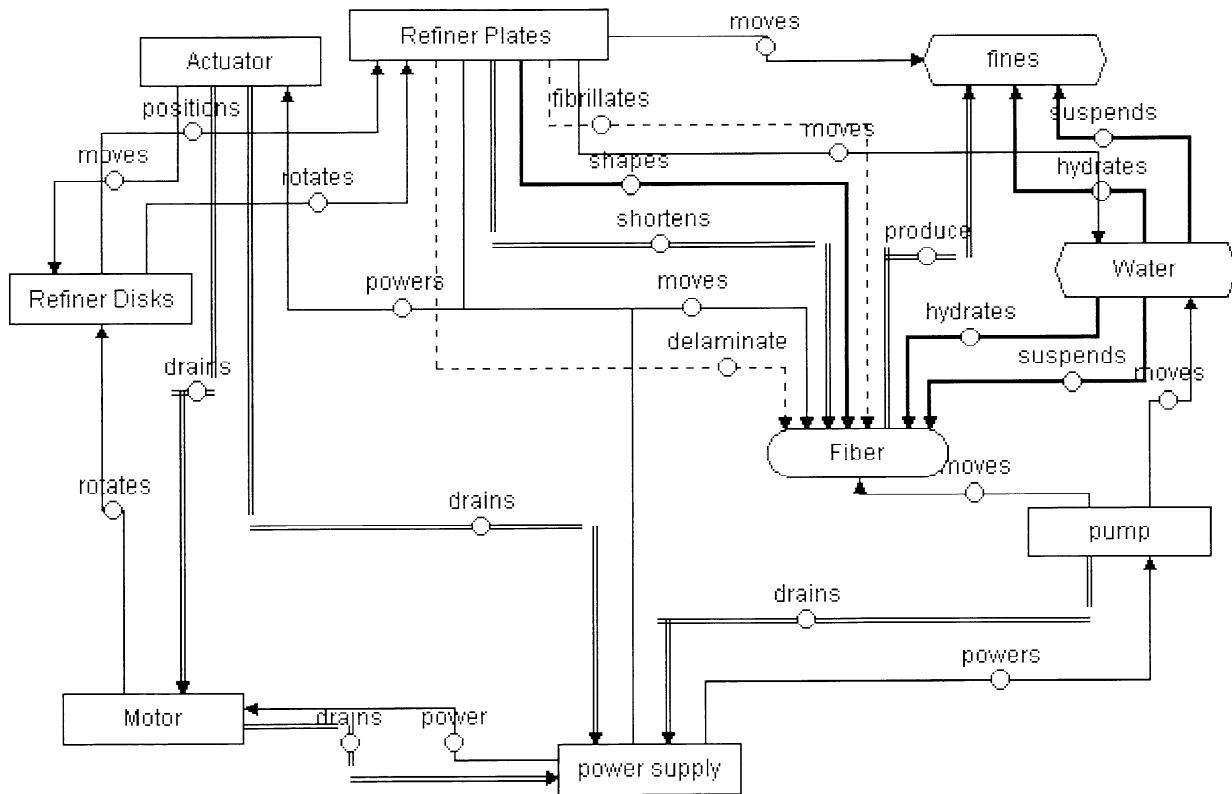
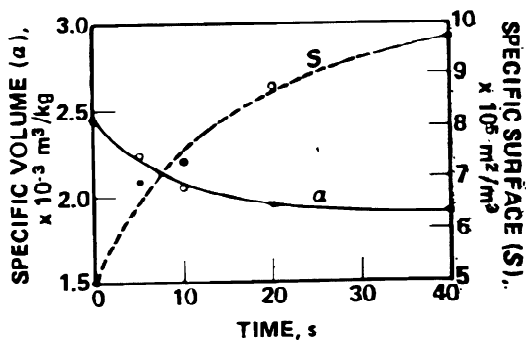


Figure 7. Disk Refiner Model - Tech Optimizer (Invention Machine)



8. Effect of time on fiber characteristics when maintaining turbulence in a 10% consistency suspension of softwood kraft pulp fibers.

Figure 8. Taken from Gullichsen, J. and Harkonen, E. (7)

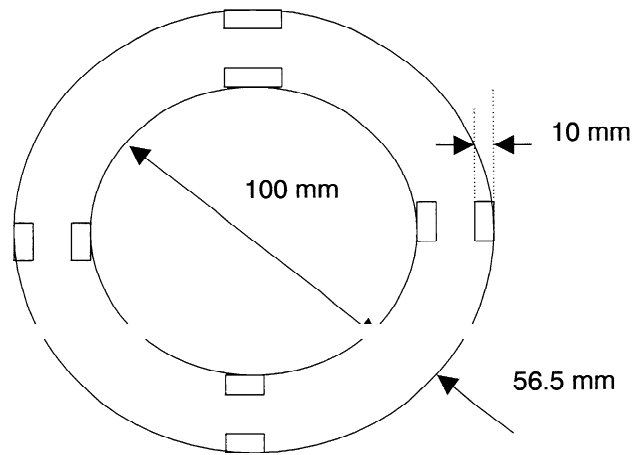


Figure 9. Cell Geometry for Producing Turbulent Flow at Medium Consistency

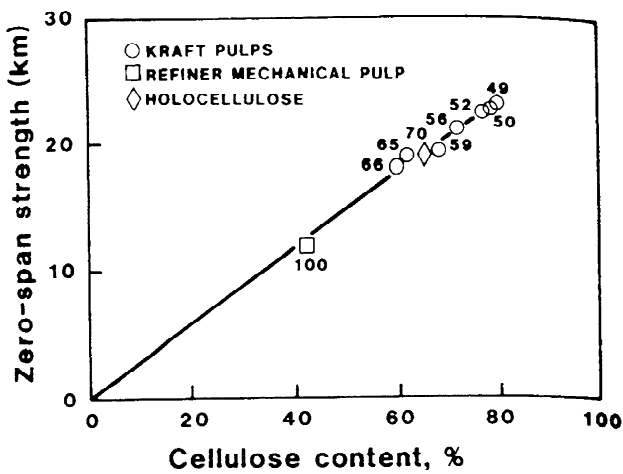


Fig. 1. Zero-span strength of well-bonded sheets of black spruce pulps plotted against cellulose content. The figures indicate % yield (Page et al. 1985).

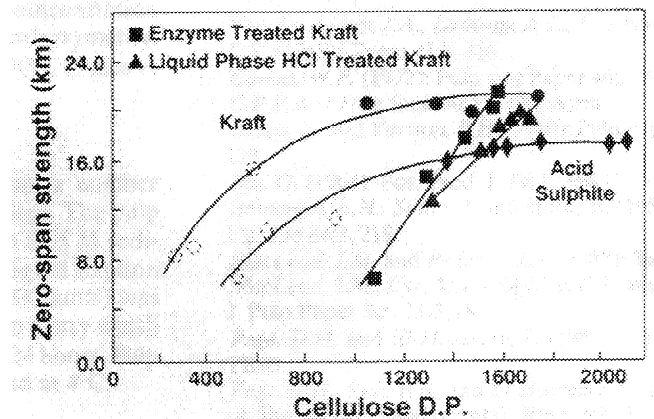


Fig. 4. Zero-span strength of handsheets of black spruce pulps as a function of D.P. of cellulose. The dotted symbols denote samples treated in the vapour-phase with hydrochloric acid.

Data of Gurnagul, N., Page, D.H., & Paice, M.G. in Nordic Pulp & Paper Research J. No. 3:152-154 (1992)

Figure 10

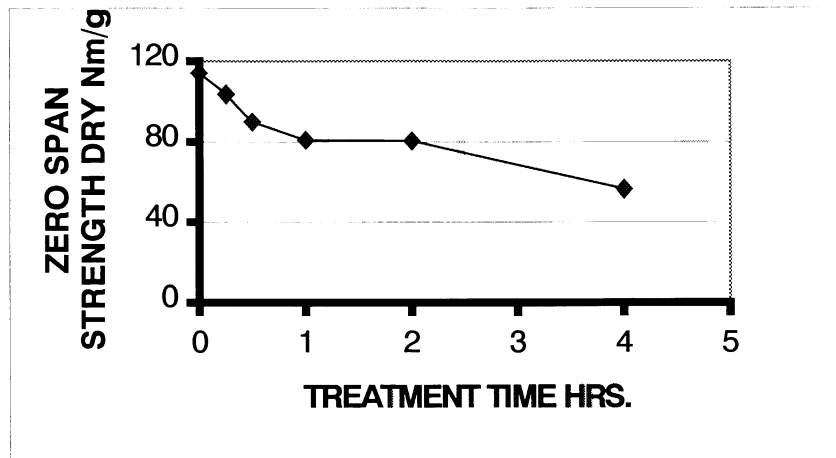


Figure 11. Variation of Zero-span Strength with Bulk-HCl Treatment Time

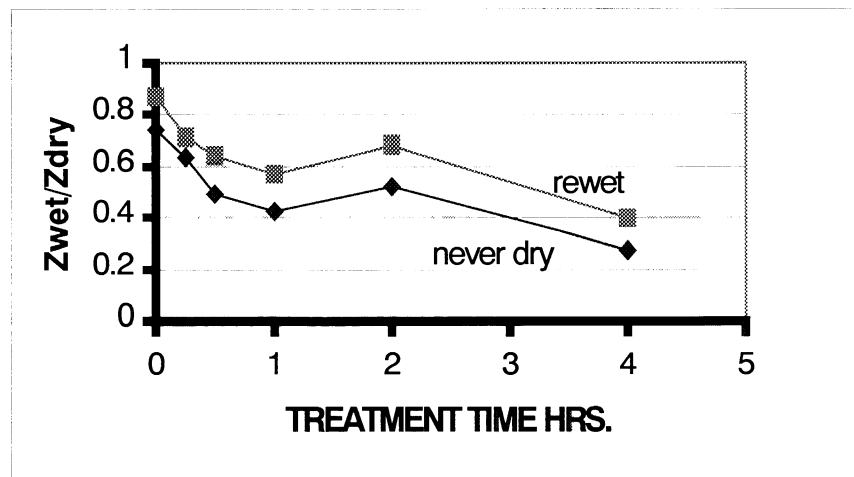


Figure 12. Variation of Wet/Dry Zero-span Ratio with Bulk-HCl Treatment Time

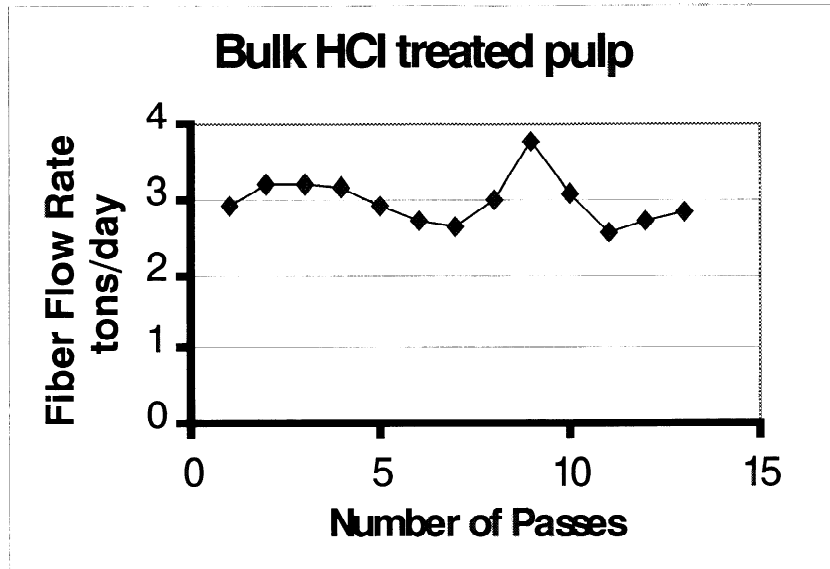


Figure 13. Variation of Fiber Flow Rate with Number of Passes Through 12"

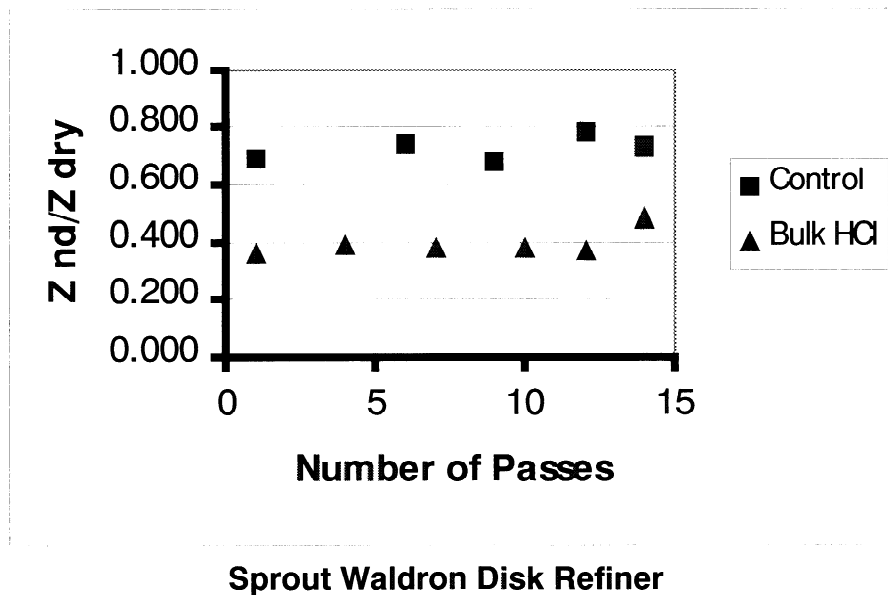


Figure 14. Variation of Wet/Dry Zero-span Ratio with Number of Passes Through 12" Sprout Waldron Disk Refiner

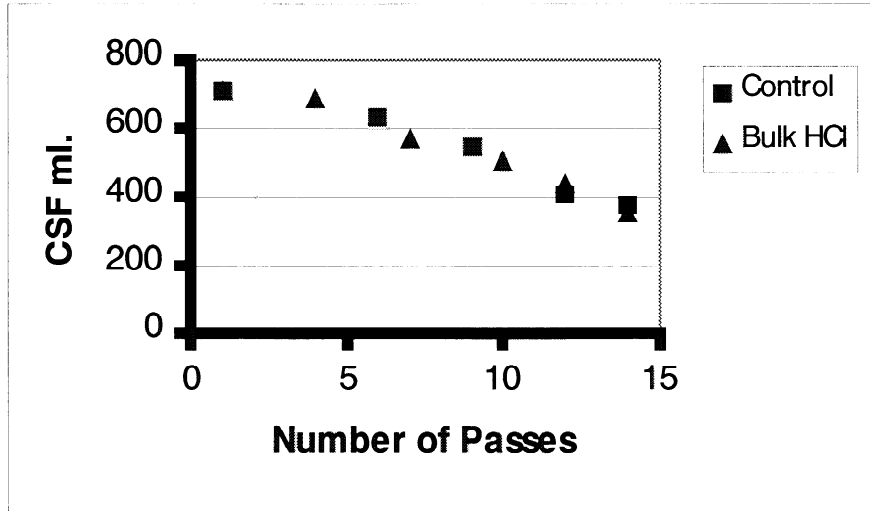


Figure 15. Variation of CSF with Number of Passes Through 12" Sprout Waldron Disk Refiner

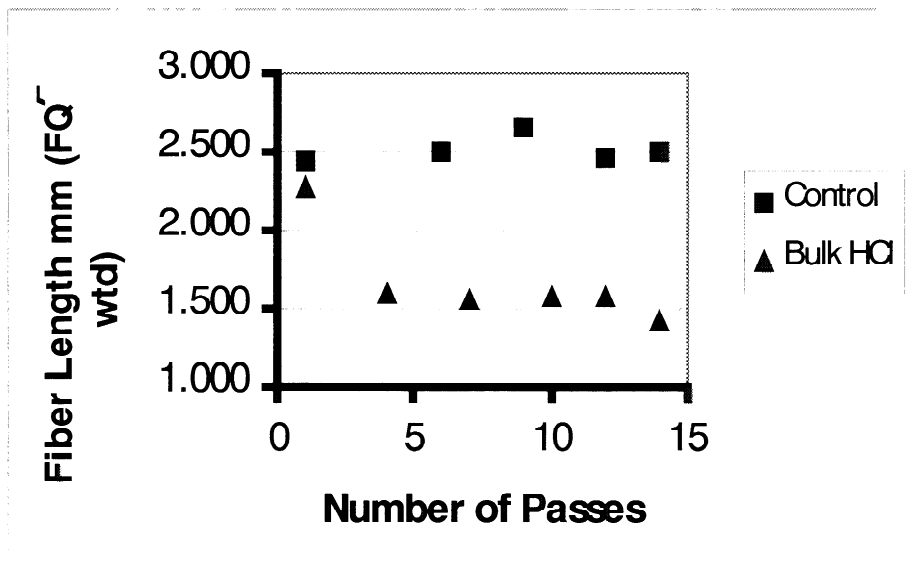


Figure 16. Variation of Fiber Length with Number of Passes Through 12" Sprout Waldron Disk Refiner

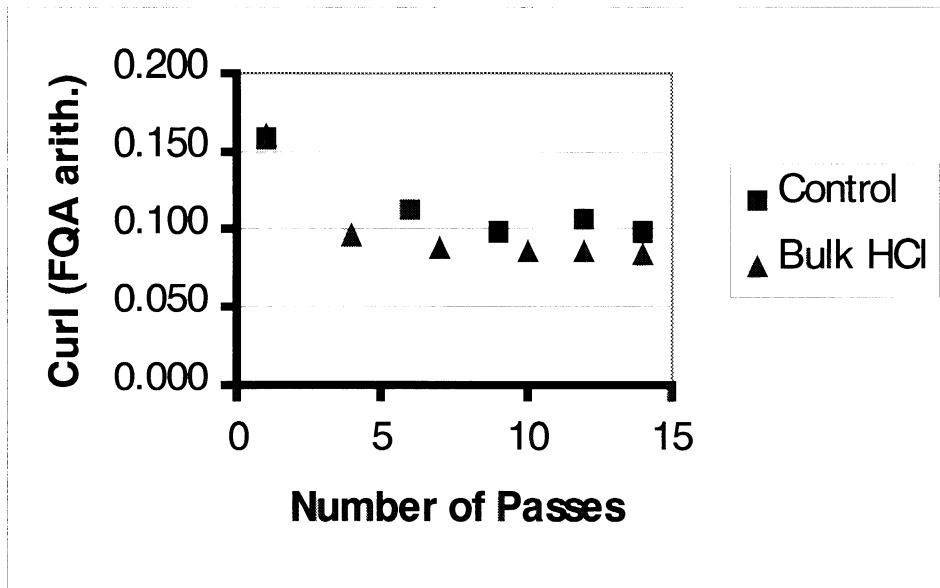


Figure 17. Variation of Curl with Number of Passes Through 12" Sprout Waldron Disk Refiner

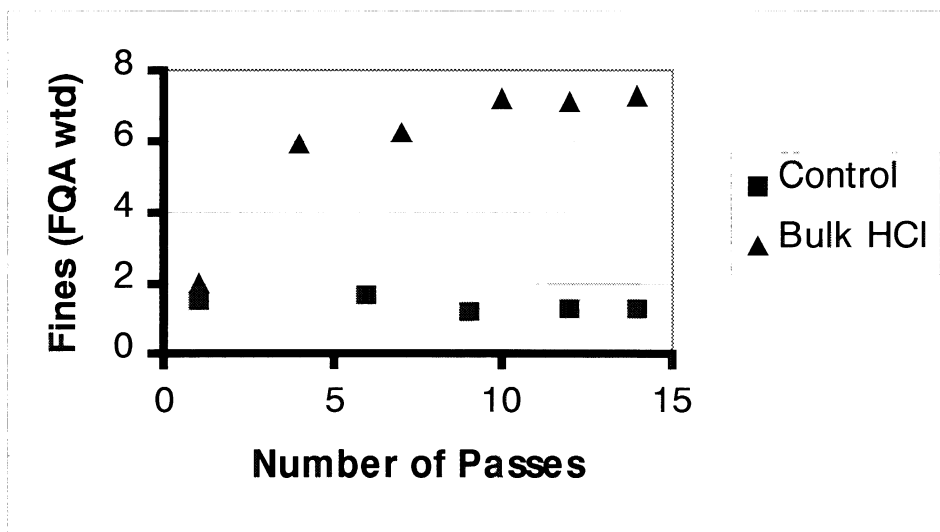


Figure 18. Variation of Fines Content with Number of Passes Through 12" Sprout Waldron Disk Refiner

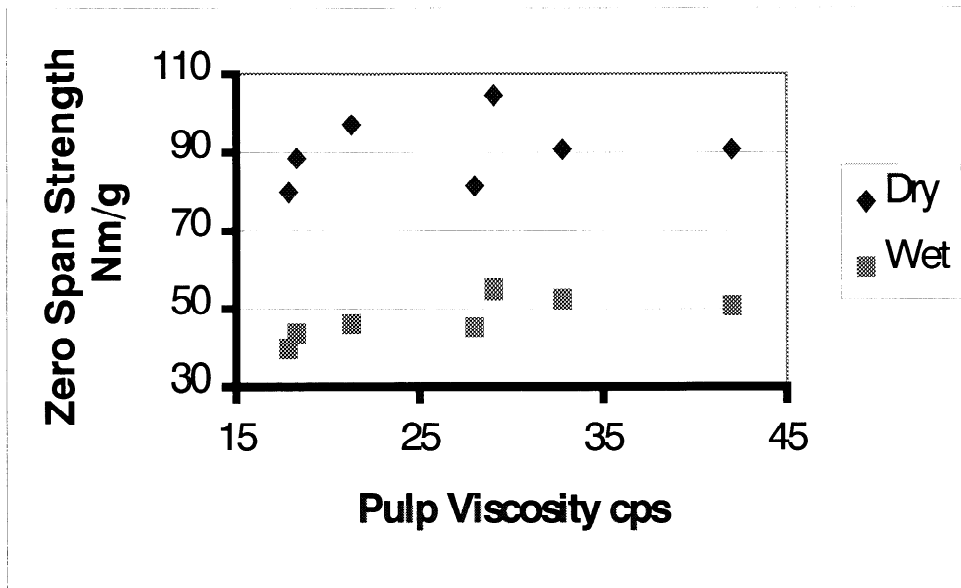


Figure 19. Variation of Zero-span Strength with Pulp Viscosity for Pulp Mill Samples

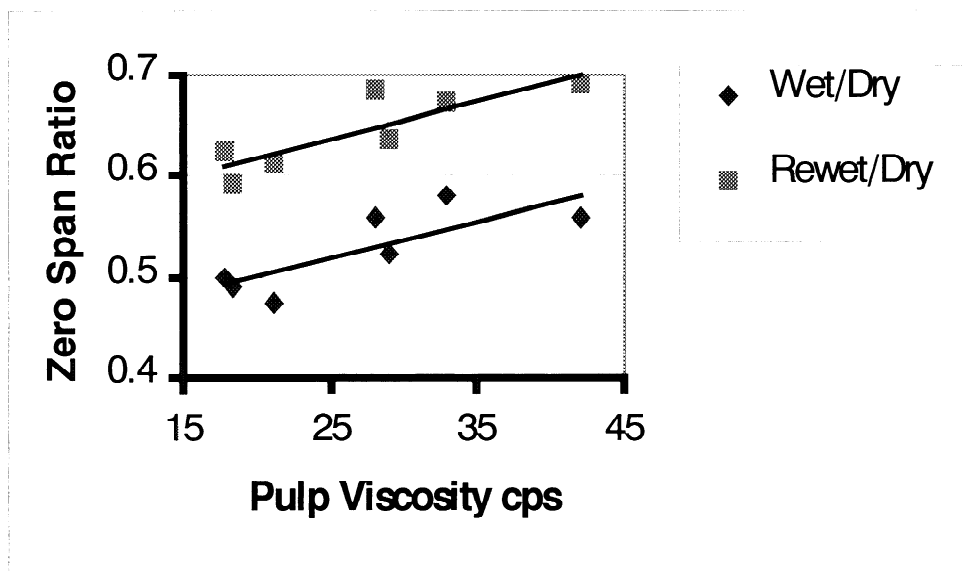


Figure 20. Variation of Wet/Dry Zero-span Strength Ratio with Pulp Viscosity for Pulp Mill Samples

FUNDAMENTALS OF INTERFIBER BONDING

STATUS REPORT

FOR

PROJECT F025

**Hiroki Nanko
Shaobo Pan**

**Institute of Paper Science and Technology
500 10th Street, N. W.
Atlanta, Georgia 30318**

DUES-FUNDED PROJECT SUMMARY

Project Title: Fundamentals of Fiber Bonding

Project Code: FBOND

Project Number: F025

PAC: Paper Physics

Project Staff

Principal Investigator: Hiroki Nanko

Co-Investigators: none

Research Support Staff: Shaobo Pan

PAC Subcommittee Anthony Colasurdo

FY 99-00 Budget: \$88,000

Allocated as Matching Funds: none

Time Allocation:

Principal Investigator: 38%

Research Support Staff: 50%

Supporting Research:

MS Students: Michelyn McNeal

External: none

RESEARCH LINE/ROADMAP:

Line 11 – Improve the ratio of product performance to cost for pulp and paper products by 25% by developing:

- Models, algorithms, and functional samples of fibrous structures and coatings that describe and demonstrate improved convertibility and end-use performance
- Break-through papermaking and coating processes that can produce innovative webs with greater uniformity than that achieved by current processes.

PROJECT OBJECTIVE:

Investigate the effects of dry strength additives on the structure and properties of interfiber bonding.

PROJECT BACKGROUND:

This project began in April of 1998. Its purpose is to give us a better understanding of how bonding agents work, including how bonding agents are adsorbed onto the fibers, where they are located in the paper, how they contribute to bond formation, how they enhance the bond strength, and how they improve sheet strength. In order to achieve this purpose, visualization techniques for bonding agents with transmission electron microscopy (TEM) are being developed. This project will provide new insights into interfiber bonding as enhanced by the bonding agents.

MILESTONES:

- Visualize cationic starch adsorption to the fibrils (Mar/00)
 - Cationic corn starch,
 - Cationic potato starch
- Visualize gum adsorption (Apr/00)
 - Guar gum (cationic, amphoteric, underivatized)
 - Locust bean gum

DELIVERABLES:

- Microscopy techniques for visualizing papermaking polymers.
- Strategy for improving the effectiveness of bonding agents.
- Insight for designing new bonding agents.

STATUS OF GOALS FOR FY 99-00:

Complete development of the visualization techniques for various bonding agents to include polyacrylamides, starches, and gums and clarify the way of adsorption for these bonding agents to the fibers under various wet-end conditions.

Start evaluation of bond quality by looking at the manner of bond failure.

Start developing visualization methods for bonding agents in paper.

SCHEDULE:

Task Descriptions	1999 Apr - Jun	1999 July - Sept	1999 Oct - Dec	2000 Jan - Mar	2000 Apr-Jun
Develop Microscopy Techniques	-----	-----	-----	-----	-----
Visualize PAMs	-----	-----	---x 10/20		
Visualize C-Starch				1/25-----	-----x5/30
Visualize Gums			10/10 -----	-----	-----x4/30
Examine Bond Failure					-----
Visualize Bonding Agents in Paper				-----	-----

SUMMARY OF RESULTS:

We have developed a technique with which bonding agents can be visualized using transmission electron microscopy. In order to validate this method, we applied it to the polyacrylamides (PAMs) under various wet-end conditions.

Cationic PAM molecules were adsorbed onto the fibers, and they formed strands stretching out into the solution. The shape of the strands (thickness, length, branching, and looping) varies with differences in the molecular structure of PAMs, as well as wet-end conditions. The strands become thicker at high molecular weight, high dosage, and high charge density. The transitions from single strands to large agglomerations of PAM parallel the increases in molecular weight, dosage, solution conductivity, pulp surface charge density, and mixing time.

This technique will provide new insights into the conformation of strength-enhancing polymers in aqueous solution as well as polymer/fiber interactions.

SUMMARY OF KEY CONCLUSIONS:

This visualization technique is sensitive enough to show the differences in adsorptive behavior of a variety of polyacrylamide derivatives. The obtained images were consistent with known facts. The influence of various wet-end conditions on the

molecular conformations can also be analyzed by this method. Visualization techniques can be useful in analyzing various wet-end conditions of paper mills. This approach can be applied to visualize the interactions of other chemicals in fiber slurries, such as retention and drainage systems, other dry strength agents, wet strength resins, and sizing agents.

DISCUSSION:

Introduction:

In the real world of papermaking, polyacrylamides (PAMs) are available in an assortment of charge densities with respect to cationic, anionic, and amphoteric derivatives. They also vary in molecular weight as well as molecular structures, such as linear and branched PAMs. For a given wet-end system, it is possible to select one of the PAMs based on factors such as pH, other chemical additives (such as sizing agents, fillers, and retention aids), electrokinetic conditions, and the presence of other potentially interfering substances. The addition point of the PAM into the wet-end system is also very important. Both the magnitudes of turbulence and mixing time allowed will affect the retention of the PAM. The adsorption of PAM onto the pulp fiber surfaces is a very complex phenomenon, especially when considering the effects of the various factors mentioned above.

We have developed a technique with which bonding agents can be visualized using transmission electron microscopy. This technique combines a negative staining method with a colloidal gold-marking method. With this procedure, we have determined that cationic starch and cationic polyacrylamide (C-PAM) are adsorbed onto the fibrils in different manners. Cationic starch molecules appear to be deposited onto fibril surfaces in an agglomerated condition (Fig. 1). Linear cationic PAM, however, forms strands. The strands are attached to the fibril at one end while the main body extends into the solution. The free ends are thin and branched, which indicates that the strands are bundles of individual C-PAM molecules that actually fray at the ends (Fig. 2). The linear cationic PAM molecules appear to be in this extended form rather than coiled in solution (Fig. 3).

The technique appears to provide new insights into the conformation of polymers in aqueous solution as well as polymer/fiber interactions. However, we must eliminate the possibility of artifacts in these images before we can rely on this technique as a tool for understanding the behavior of polymers during papermaking. The best way to validate this method is to apply it to the various wet-end conditions and determine if the results are consistent with known facts.

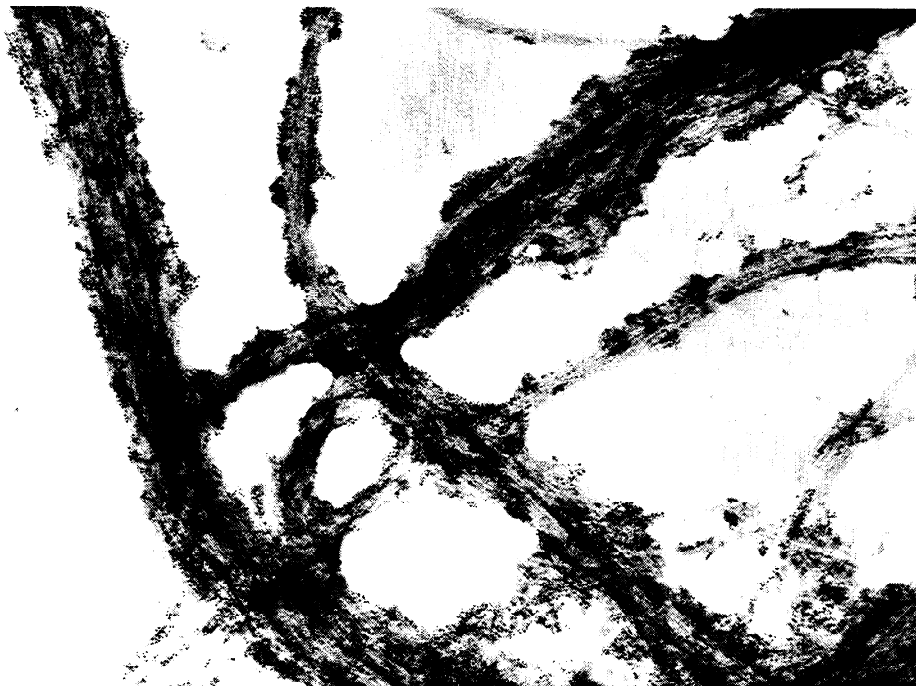


**Figure 1: Cationic starch (corn starch) adsorbed onto the fibrils.
Pulp: bleached kraft softwood; Dosage: 1.0%**

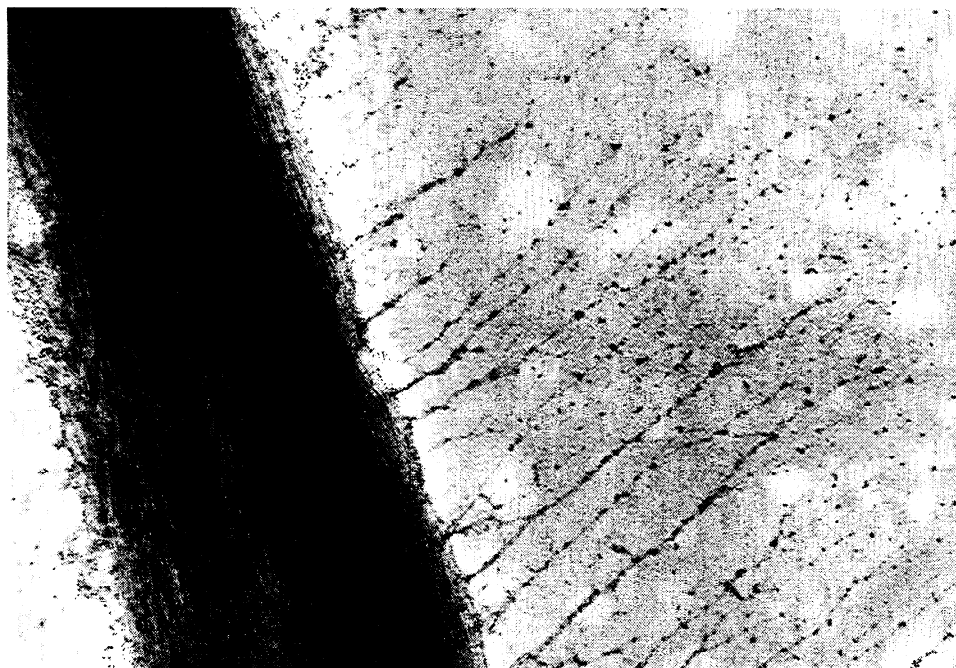


**Figure 2: Cationic linear PAM adsorbed onto the fibrils.
Pulp: softwood bleached kraft; Dosage: 0.5 %**

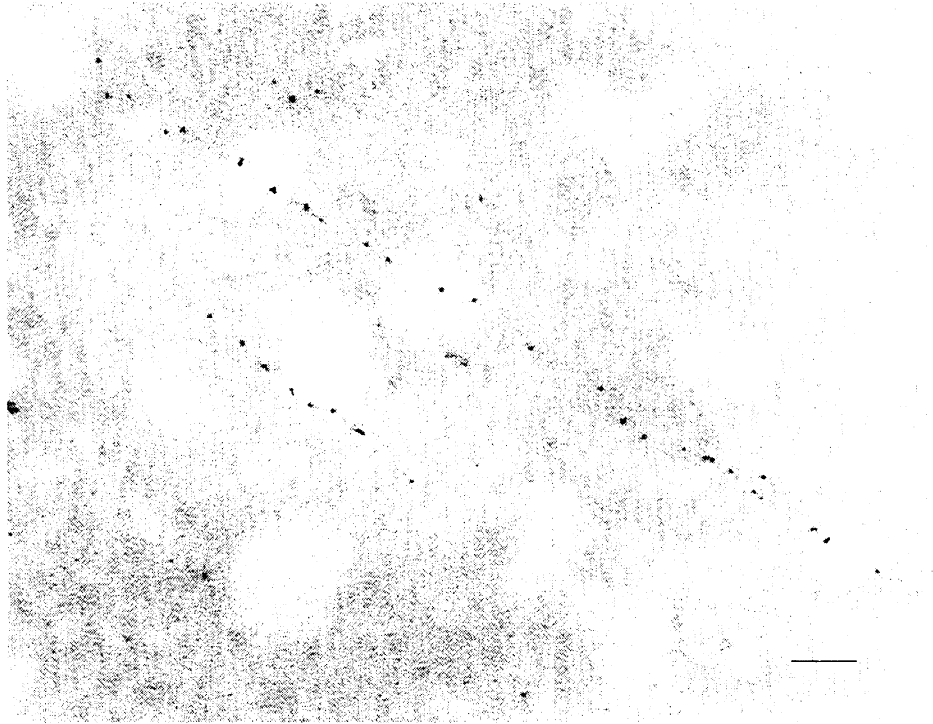


Figure 3: Cationic linear PAM in water solution.

Scale: 0.1 μm

Experimental:

In this report, we show the results of applying this visualization technique to several PAMs, under various wet-end conditions, and adsorbing onto different pulp furnishes. The standard conditions for PAM visualization follow. In each experiment, the dilution water was deionized (conductivity: 2 μ S).

PAM standard

Cationic Linear PAM

Charge density/0.46 meq/NV

Molecular weight/1,000,000

Dosage/0.5% on O.D. pulp

Pulp standard

Bleached kraft softwood (Southern Pine)

PFI mill beaten for 2500 revolutions

1. Effect of the molecular structure of polyacrylamide

We applied the visualization technique to linear cationic PAM, linear amphoteric PAM, and branched amphoteric PAM to see if the technique would show variations in PAM behavior based on the differences in the molecular structure and charge character.

Experiment:

The following PAMs were added to the standard pulp at a dosage of 0.5%.

- Linear cationic PAM

Molecular weight:	1,000,000
Charge density:	cationic 0.47 meq/NV

- Linear amphoteric PAM

Molecular weight:	1,500,000
Charge density:	cationic 1.25 meq/NV, anionic 0.94 meq/NV

- Branched amphoteric PAM

Molecular weight:	1,800,000
Charge density:	cationic 0.64 meq/NV anionic 0.77 meq/NV

Results:

We found obvious differences between strand conformations among the variations of PAM. Linear cationic PAM formed long strands of more than 1 micron in length extending from the fibril surfaces (Fig. 4). The linear amphoteric PAM formed shorter strands (Fig. 5). The strands of branched amphoteric PAM formed complex branched structures (Fig. 6).

The strands of linear cationic PAM appear to consist of entwined bundles of linear molecules that are aligned more or less parallel to each other. The wider strands are given a higher electron density by negative staining than the thinner strands. Many of the thin strands are linked with neighboring strands forming a fine, loose web. It is interesting to note that these polymer bundles are formed despite the repulsive forces of cationic sites. The strands are aligned extending out from the fibrils in a uniform direction (Fig. 2). We assume this is caused by the water flow created when suspended pulp fibers were placed on the grid and the excess water was removed with blotter paper. The conformation of linear PAM molecules in solution is unknown, and may be either coiled or linear. However, the strands are flexible enough to be easily extended to this linear form by the flow of water (Figs. 1 and 4).

The TEM visualization of linear amphoteric PAM showed shorter strands than the linear C-PAM (Fig. 5). However, some extremely long strands were seen that formed bridges between relatively distant fibrils (Fig. 7). The amphoteric nature of the polymer may aid in forming these long bridges, that is, the oppositely charged sites within and between molecules might initialize the entanglement of several separate strands.

Branched amphoteric PAM molecules form strands that are also very obviously branched. These strands are of non-uniform thickness. This is likely to be due to the branching of individual molecules within a strand. The molecular branching, in all probability, also causes this strand branching. As with the other PAMs, strands are formed from a buildup of individual molecules. In the case of branched strands, there is probably a branch at the molecular level that initializes the buildup of the strands in

two directions. The branches can then become linked to form visible networks. Such networks (Fig. 6) cover much of the area between fibrils.

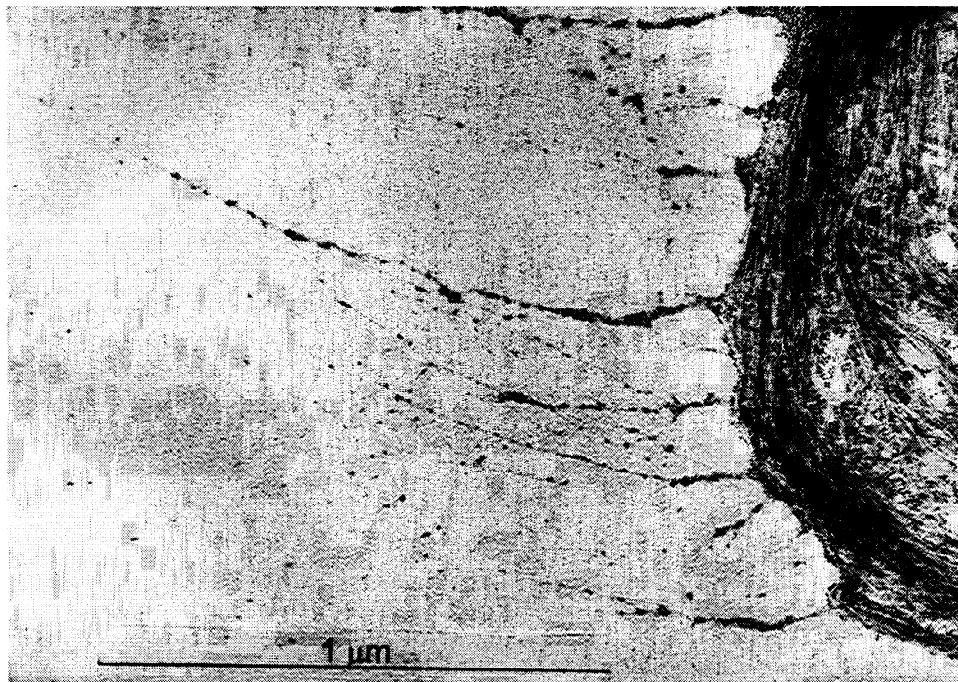


Figure 4: Linear cationic PAM (MW: 1,000,000)

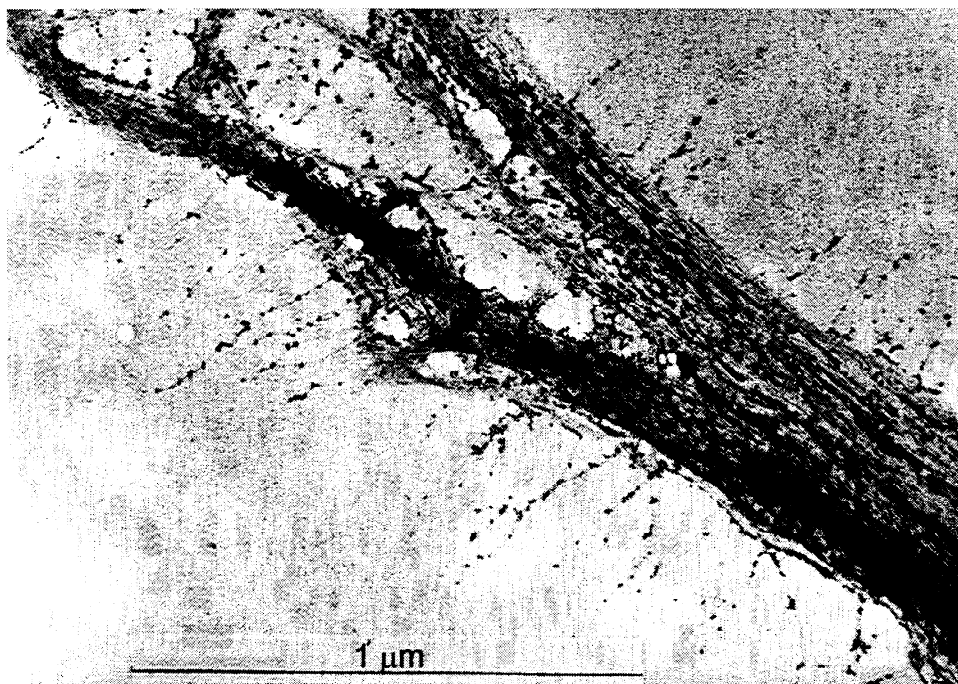


Figure 5: Linear amphoteric PAM (MW: 1,500,000)

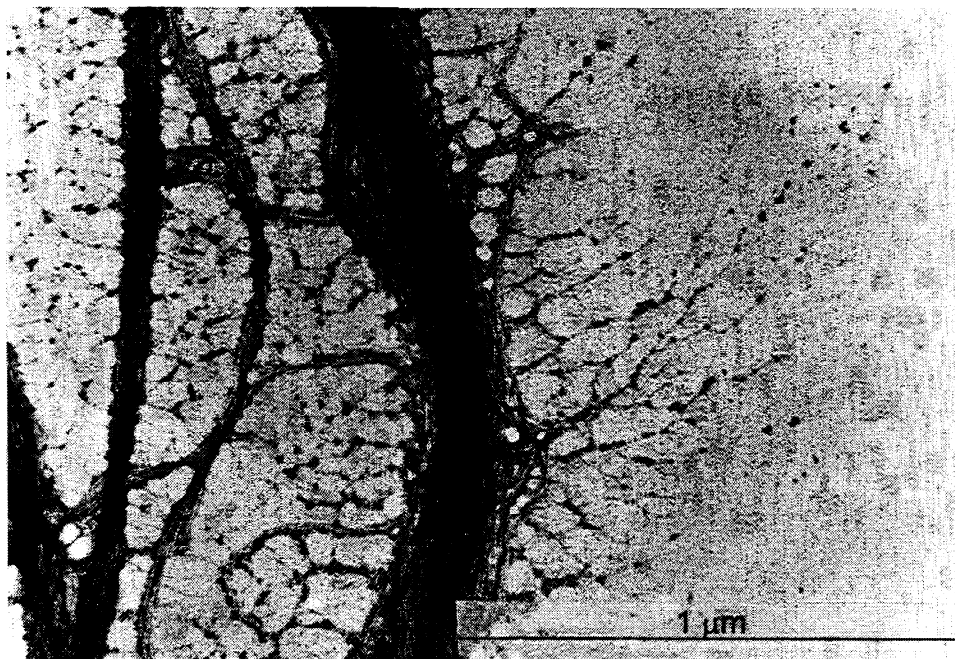


Figure 6: Branched amphoteric PAM (MW: 1,800,000)

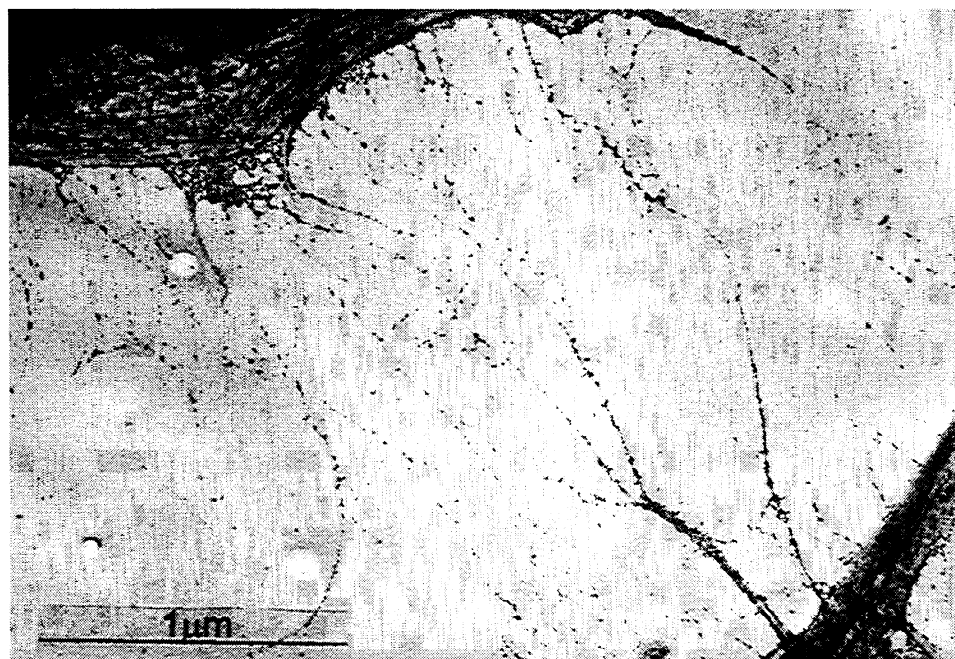


Figure 7: Linear amphoteric PAM (MW: 1,500,000)

2. Effect of the charge density of cationic polyacrylamide

Cationic polyacrylamides are commercially available at various charge densities. It is known that if the charge density of C-PAM is too low, the adsorption of C-PAM on the fibrils is insufficient to enhance the bond strength. If the charge density of the C-PAM is too high, the surface charge of the pulp is neutralized by the adsorption of fewer C-PAM molecules that fully adsorb to the fiber surface, rather than form “loops and tails”. Therefore, satisfactory bond strength cannot be achieved. There should be an optimum charge density of C-PAM for maximum bond strength; instead, the optimum is dependent on mill conditions. In order to discover why a particular charge density C-PAM is more effective for one mill’s wet-end conditions, it is necessary to see how the various C-PAMs perform in set conditions.

Experiment:

The following four linear C-PAMs were added to the standard pulp at a dosage of 0.5%.

- Standard charge density:
 - 0.46 meq/NV
 - Molecular weight: 3,500,000
 - 0.46 meq/NV
 - Molecular weight: 1,000,000

- Lower charge density:
 - 0.14 meq/NV
 - Molecular weight: 1,820,000

- Higher charge density:
 - 2.97 meq/NV
 - Molecular weight: 3,500,000

Results:

The standard charge density C-PAM shown in figure 8 has nearly twice the molecular weight as the low charge density PAM in figure 9, but is comparable to the high charge density PAM of figure 10. The high charge density PAM may be directly compared to this standard. However, to evaluate the different effects of charge density, the low charge density PAM should also be compared to the cationic PAM in Figure 2, though the molecular weight is approximately halved. The effects of molecular weight on C-PAM behavior, discussed elsewhere, must also be considered.

The standard charge density C-PAM formed strands of varying thicknesses. These strands show a tendency to link to one another as they extend away from the fibrils. A few large “loops” are visible in figure 8. At a lower molecular weight (Fig. 2), the strands are thinner and of a more uniform thickness. These strands do not appear to form the same links and are more uniformly spaced in a near parallel form. The sample of lower charge density C-PAM formed more delicate, thinner strands than either of the standard samples, and the gold colloid markers are sparse in comparison (Fig. 9).

The high charge density C-PAM was more fully adsorbed onto the fibrils. The C-PAM strands tend to be adsorbed to the fibrils onto both ends forming loops. The highly charged C-PAM formed agglomerations both on the fibril surface and among the extended loops (Fig. 10).

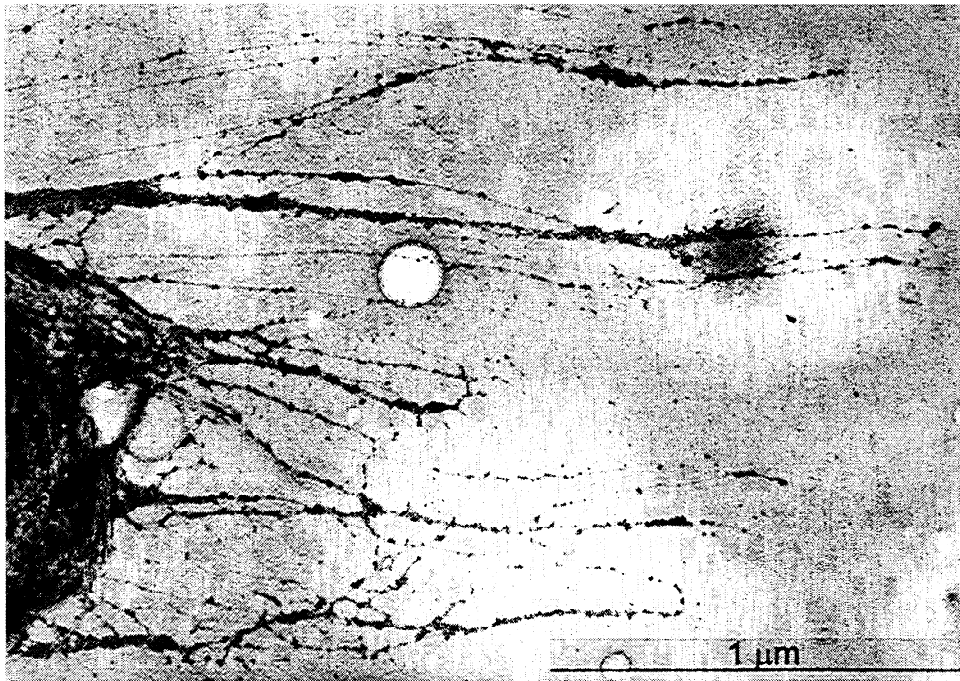


**Figure 8: Linear C-PAM with standard charge density
(0.46 meq/NV, MW=3,500,000)**

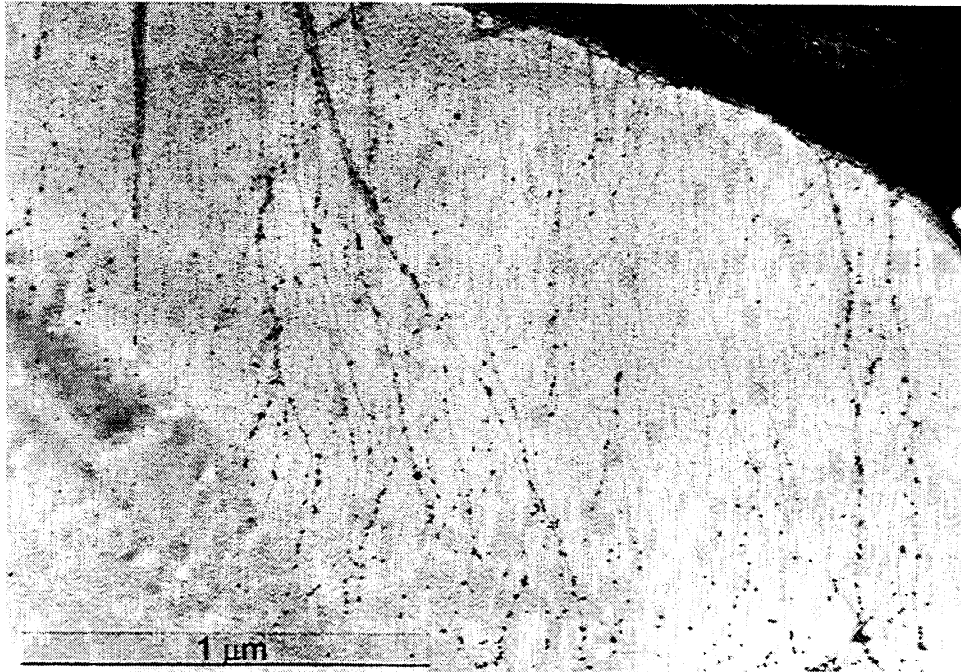


Figure 9: Linear C-PAM with low charge density
(0.14 meq/NV, MW=1,820,000)

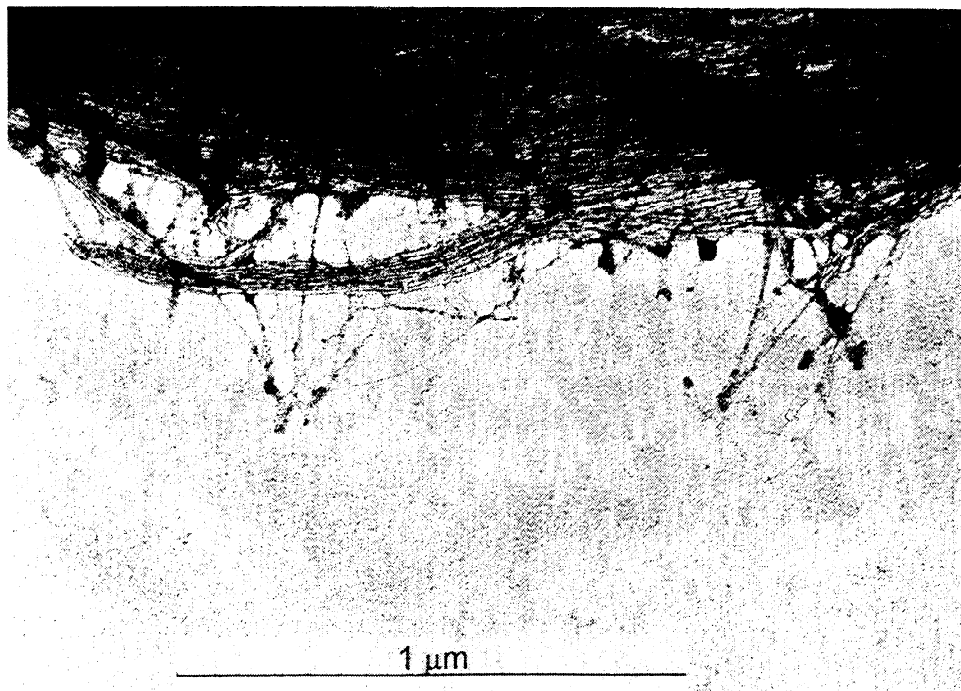


Figure 10: Linear C-PAM with high charge density
(2.97 meq/NV, MW=3,500,000)

3. Effect of increasing molecular weight

Excessively high molecular weight C-PAM causes large flocks, leading to poor formation. The definition of excessive is, of course, dependent on the wet-end conditions at the mill. In order to determine what constitutes “excessively high” molecular weight, we observed the effect of molecular weight of PAM on its manner of adsorption.

Experiment:

The following linear C-PAMs with the standard charge density (0.46 meq/NV) were added to the standard pulp at a dosage of 0.3%.

- Molecular weight: 1,000,000 (standard)
- Molecular weight: 2,360,000
- Molecular weight: 4,000,000

Results:

The extended strands of the mid-weight C-PAM were thicker and shorter than the strands of our standard. The C-PAM between fibrils was either adsorbed as agglomerations form or formed thick, networked strands (Fig. 11).

High molecular weight C-PAM (MW=4,000,000) extends into solution with a greater degree of networking. Several of the strands in the micrograph are extremely thick (Fig. 12). Long strands extend even farther from the network. Highly agglomerated PAM is adsorbed on the fibril surfaces.

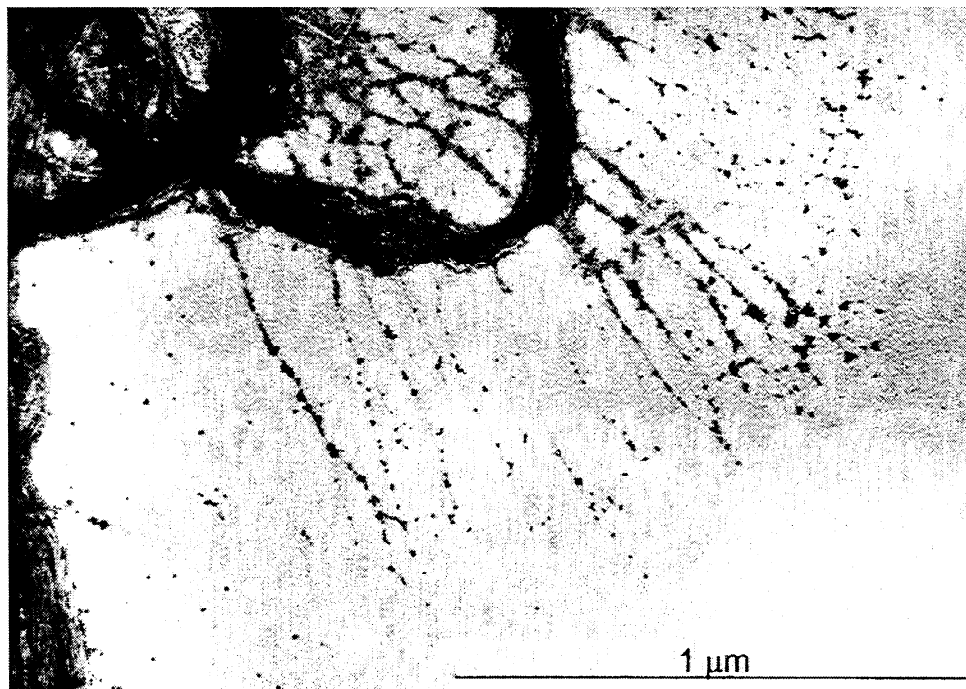


Figure 11: Linear C-PAM (MW: 2,360,000)

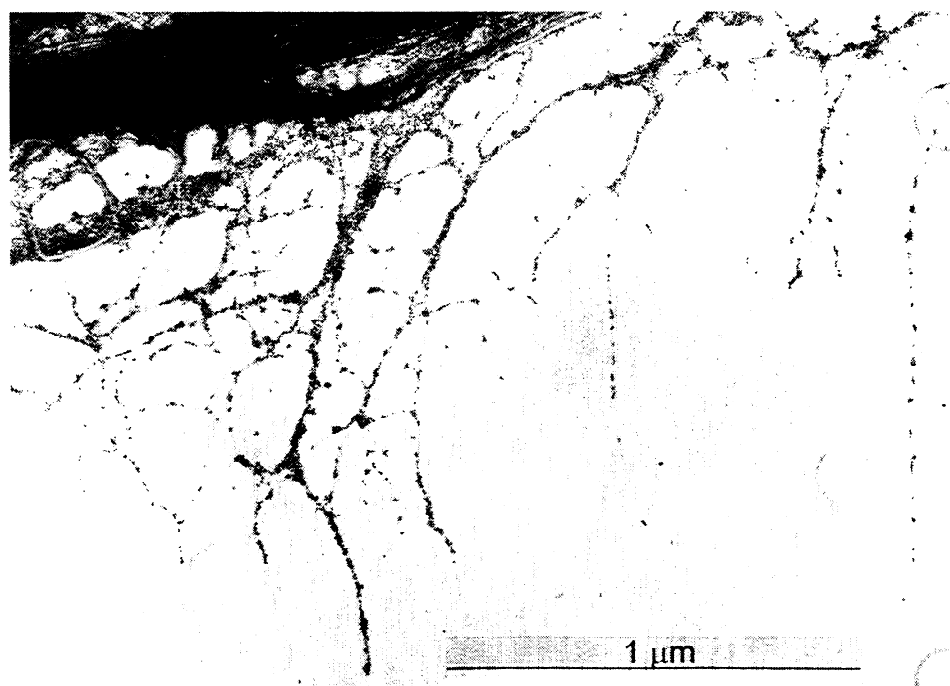


Figure 12: Linear C-PAM (MW=4,000,000)

4. Effect of increasing dosage

Dosage is an important factor in the performance of C-PAM. At lower dosage, the tensile strength of paper will increase proportionally with the dosage. However, at higher dosage the relationship is no longer linear, the rate of strength increase drops dramatically. It has been suggested that this reduction is due to the decrease of the adsorption ratio at higher dosage. We observed the effect of increasing PAM dosage on its adsorption to fibrils.

Experiment:

The standard PAM and conditions were applied at three dosage levels.

- 0.3% to O.D. pulp
- 0.5% to O.D. pulp (standard)
- 1.0% to O.D. pulp

Results:

The low-dosage C-PAM formed few strands (Fig. 13). These strands are thinner than the standard strands (Fig. 14). Agglomerations are seen on several strands, though none are adsorbed on the fibril. At a high dosage of 1.0%, surface adsorption of C-PAM is high; the fibril surface is nearly covered by the polymer (Fig. 15). The extended strands are short and thick, and fewer are noted at this level.

Agglomerated PAM is visible at all the dosage levels and increases in both size and quantity with increased dosage. Agglomerations also appear to move closer to the fibril surface as the dosage increases.

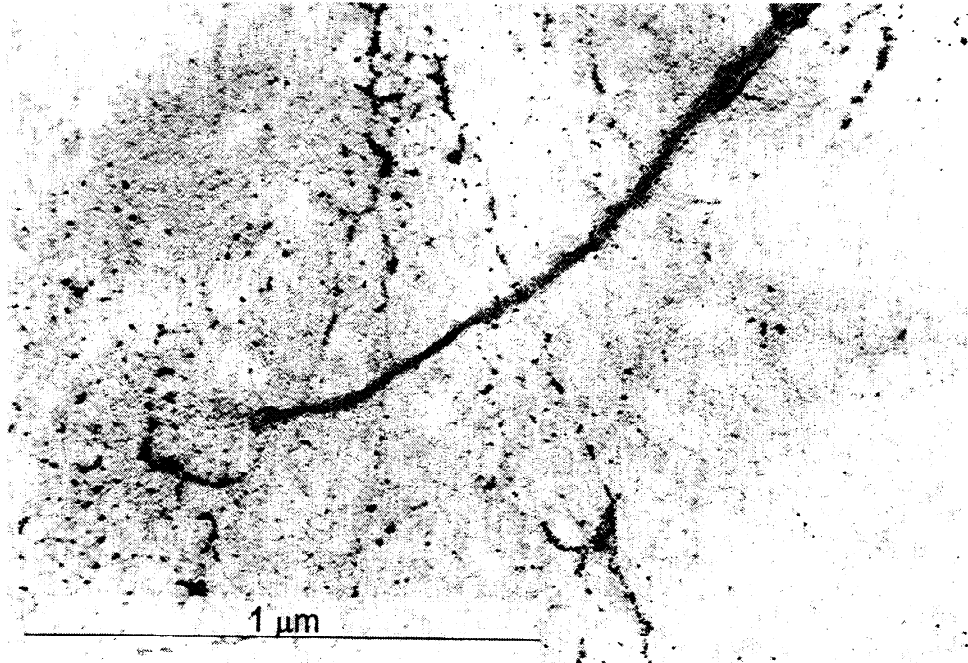


Figure 13: Linear C-PAM (MW:1,000,000 CD:0.47 meq/NV), Dosage=0.3%

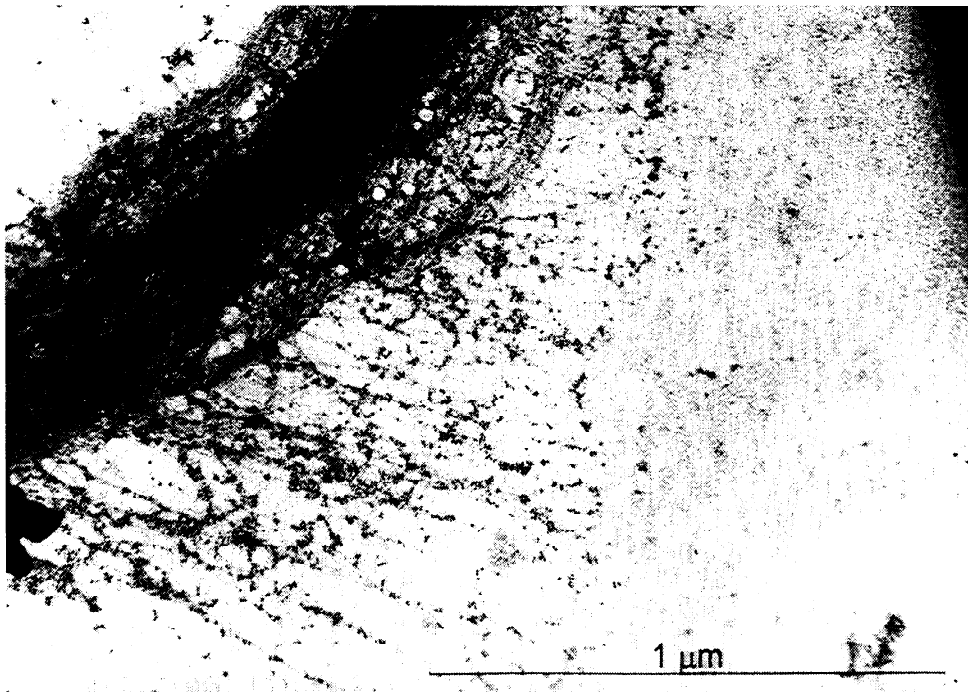


Fig. 14 Linear C-PAM (MW:1,000,000 CD:0.47 meq/NV), Dosage=0.5%

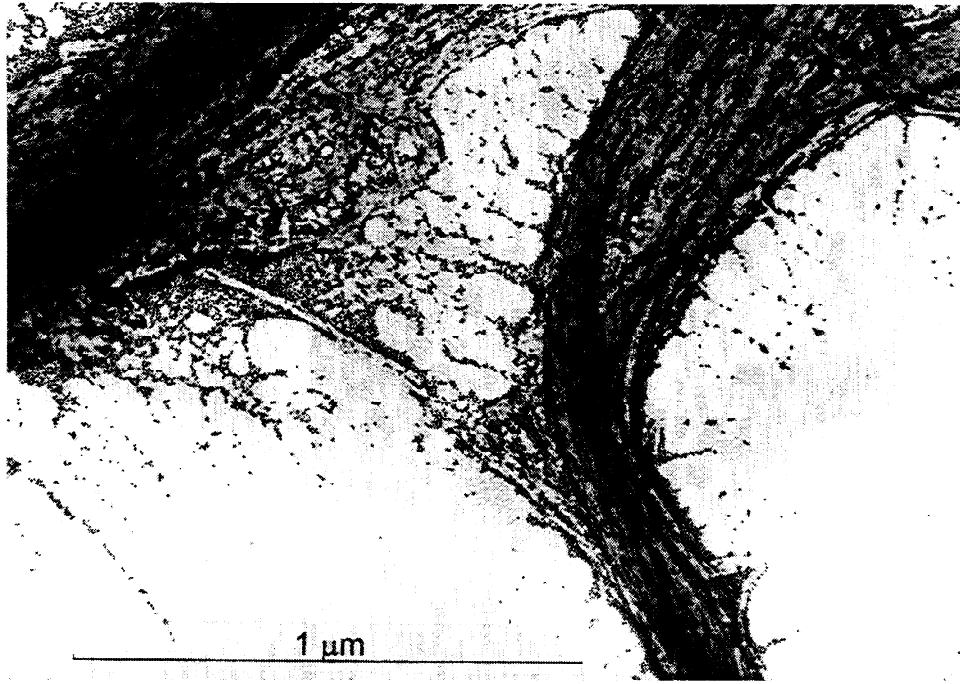


Figure 15: Linear C-PAM (MW:1,000,000 CD:0.47 meq/NV), Dosage=1.0%

5. Effect of mixing

The amount of time a polymer has for contact and adsorption onto the substrate surface will affect its final conformation. There are many sites along the wet-end process where additives may be introduced to the system. Although, in reality, the shear forces will vary throughout the process, there is always some amount of mixing occurring. The effects of mixing time at a constant shearing rate will give us some idea of how the point of addition will affect the polymer behavior.

Experiment:

The standard C-PAM and conditions were varied as follows:

- Dosage: 0.3%
- Propeller stirrer: 500 rpm
- 1 min mixing
- 60 min mixing

Results:

The low-molecular-weight C-PAM exhibited the characteristic long, thin-strand extensions after one minute of mixing. Several strand-to-strand entanglements were visible in the extended PAM (Fig. 16). With 60 minutes of mixing time, the majority of the PAM had been adsorbed onto the fibril surfaces in an agglomerated form. In a few areas, C-PAM appears to be adsorbed in a linear fashion; the gold colloid is lined up along the length of some microfibrils. The strand extensions on the free side of the fibrils are linked, and most of the ends have been adsorbed onto the fibril surface forming “loops and tails” (Fig. 17).

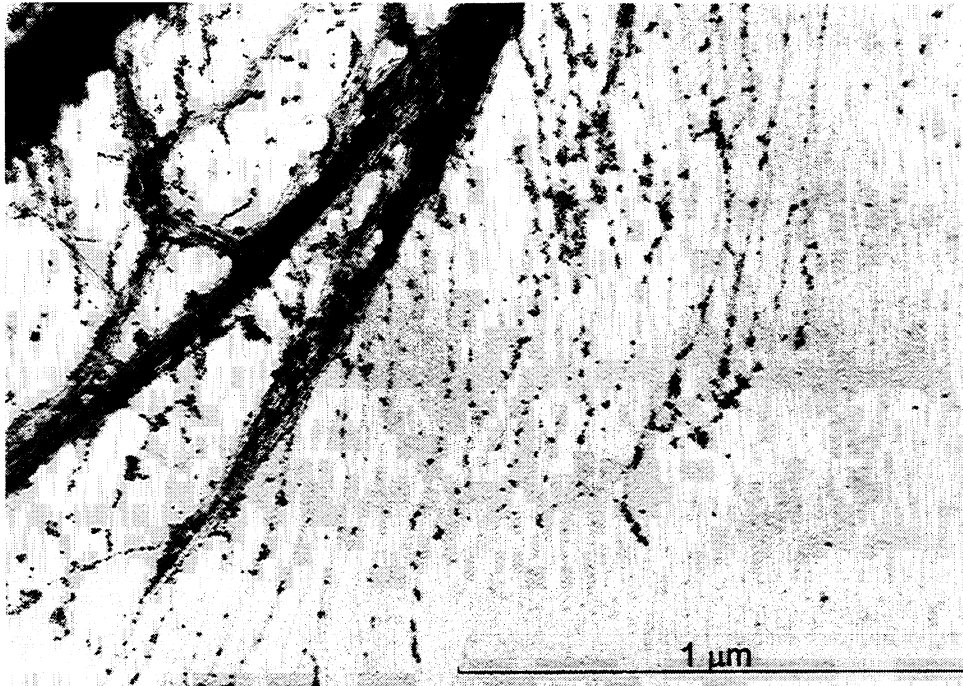


**Figure 16: Linear C-PAM (MW: 1,000,000, CD:0.46 meq/NV)
Mixing time: 1 min**

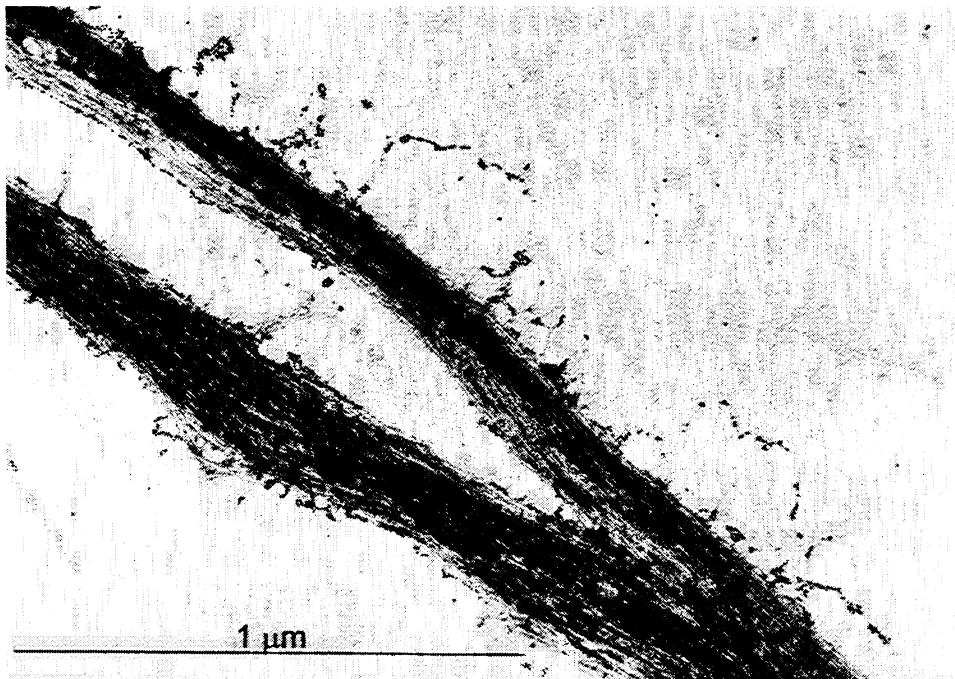


**Figure 17: Linear C-PAM (MW: 1,000,000, CD:0.46 meq/NV)
Mixing time: 60 min**

6. Effect of increasing conductivity

Electrolytic conditions of white water will vary with the use of fillers, additives, fresh water variations, and mill closure conditions. Sodium sulfate has been used here to investigate the effects of increasing conductivity on the behavior of C-PAM.

Experiment:

The standard conditions were implemented, and sodium sulfate was added to vary the conductivity.

- Conductivity: 2 μS (0 ppm Na_2SO_4 , control)
- Conductivity: 306 μS (600 ppm Na_2SO_4)
- Conductivity: 455 μS (1000 ppm Na_2SO_4)

Results:

The control case showed the long, thin strands with some apparent branching and entanglement extending into the solution (Fig. 18).

When the conductivity was increased to 306 μS , strand thickness increased.

Branching and entanglement of the strands were more prevalent (Fig. 19).

Agglomerated PAM on the strands makes those strands look thicker. Fibril surfaces are also heavily covered by agglomerated PAM.

The strands became fewer, thicker, and shorter at 455 μS . Large agglomerations grew on the strands, and the merging of these separate masses formed a network of larger agglomerations. Such agglomerations are both adsorbed onto the fibril surfaces and are seemingly free-floating in the solution (Fig. 20). This suggests that at such high conductivity, the linear C-PAM molecules are not in the stretched conformation but in coiled form.

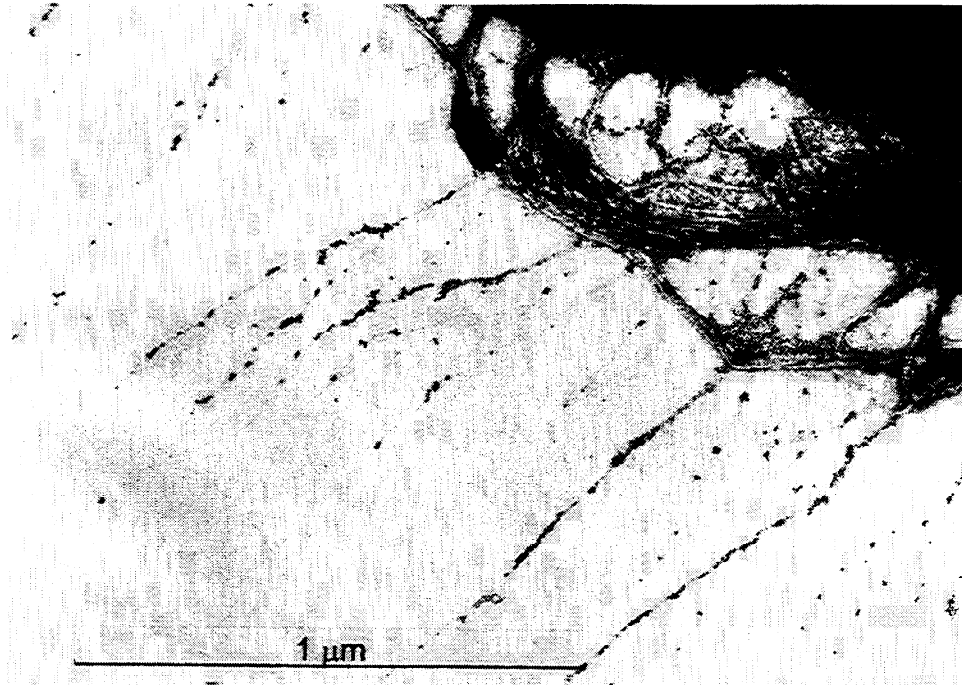


**Figure 18: Linear C-PAM (MW;1,000,000, CD:0.46 meq/NV)
Conductivity: 2 μ S (0 ppm Na₂SO₄)**

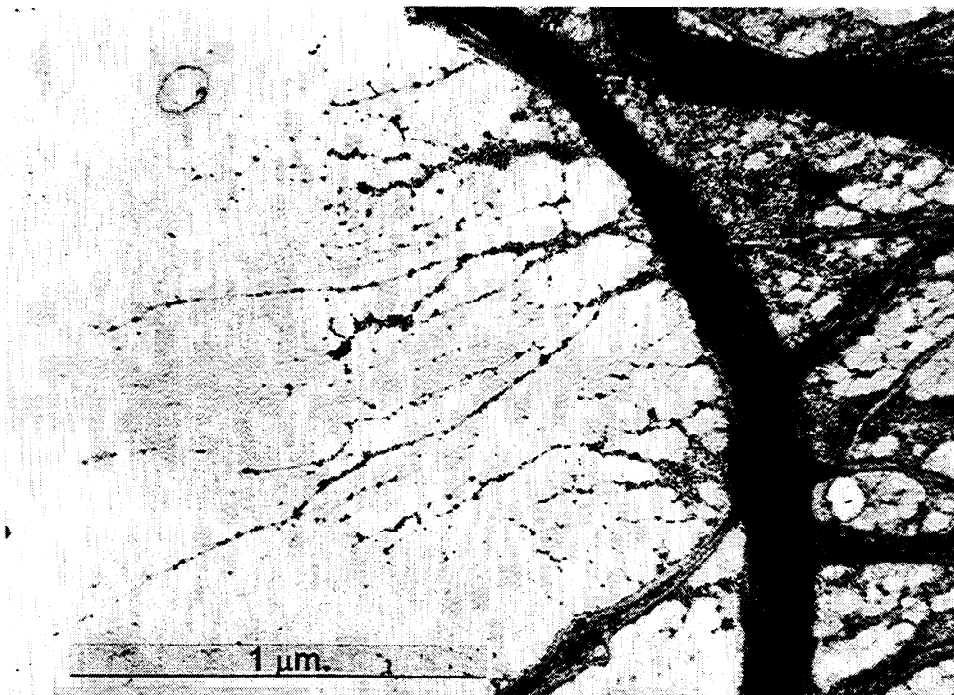


**Figure 19: Linear C-PAM (MW;1,000,000, CD:0.46 meq/NV)
Conductivity: 306 μ S (600 ppm Na₂SO₄)**

IPST Confidential Information – Not for Public Disclosure

(For IPST Member Company's Internal Use Only)



**Figure 20: Linear C-PAM (MW;1,000,000, CD:0.46 meq/NV)
Conductivity: 455 μ S (1000 ppm Na₂SO₄)**

7. Effect of charge density of pulps

The purpose of this experiment is to gain an understanding of how pulp charge density affects the C-PAM adsorption. We expect the higher charge density of the pulp surface to increase the adsorption ratio; therefore the polymer will be fully adsorbed to the surface. The negative charge of the pulp is more or less controlled by hemicellulose content. Hemicellulose content increases as follows:

Bleached Kraft < Unbleached Kraft < CTMP

Experiment:

The standard C-PAM was applied at a 0.3% dosage on the following pulp furnishes:

- Softwood bleached kraft pulp (standard)
- Softwood unbleached kraft pulp
- Softwood CTMP

The bleached and unbleached kraft pulp furnishes were beaten in the PFI mill for 2500 revolutions. The CTMP pulp was soaked in hot water to remove latency. All of the pulps were washed with deionized water to remove any trash ions before C-PAM was applied.

Results:

A thick layer of agglomerated C-PAM coated the fibril surfaces of unbleached kraft fibers (Fig. 21). Agglomerated C-PAM also filled the small spaces between fibrils. The majority of the strands extending from the fibril surface were thicker and much shorter than the strands on the fibrils of the standard bleached kraft pulp (Figs. 2 and 21). However, there were also a few long, thick strands that stretched out from the fibrils.

The coating of C-PAM on the fibril surfaces of CTMP was thicker than the agglomerated C-PAM on the surfaces of the unbleached kraft pulp fibrils. Long strands extended from, and possibly arose from, the adsorbed agglomerated layer (Fig. 22).

The biggest difference between the adsorptive behavior of C-PAM on bleached kraft pulp and the other furnishes is the lack of a thick agglomerated PAM layer on the fibril surface of the former. Such large agglomerations of C-PAM on the unbleached

kraft pulp and CTMP fibrils must be caused by the higher content of negatively charged hemicelluloses in these pulps.

Conclusions:

We have developed a technique with which bonding agents can be visualized using Transmission Electron Microscopy. In order to validate this method, we applied it to the polyacrylamides under various wet-end conditions. We obtained the following results:

- This visualization technique provided different images of PAM adsorption for various wet-end conditions.
- This visualization technique was sensitive enough to show the differences in adsorptive behavior of a variety of polyacrylamide derivatives.
- The obtained images are consistent with known facts.

These results support the validity of the technique. The probability of artifacts is very small.

This technique will provide new insights into the conformation of strength-enhancing polymers in aqueous solutions as well as polymer/fiber interactions. The influence of various wet-end conditions on the molecular conformations can also be analyzed by this method. Visualization techniques can be useful in analyzing various wet-end conditions of paper mills. This approach can be applied to visualize the interactions of other chemicals in fiber slurries, such as retention and drainage systems, other dry strength agents, wet strength resins, and sizing agents.

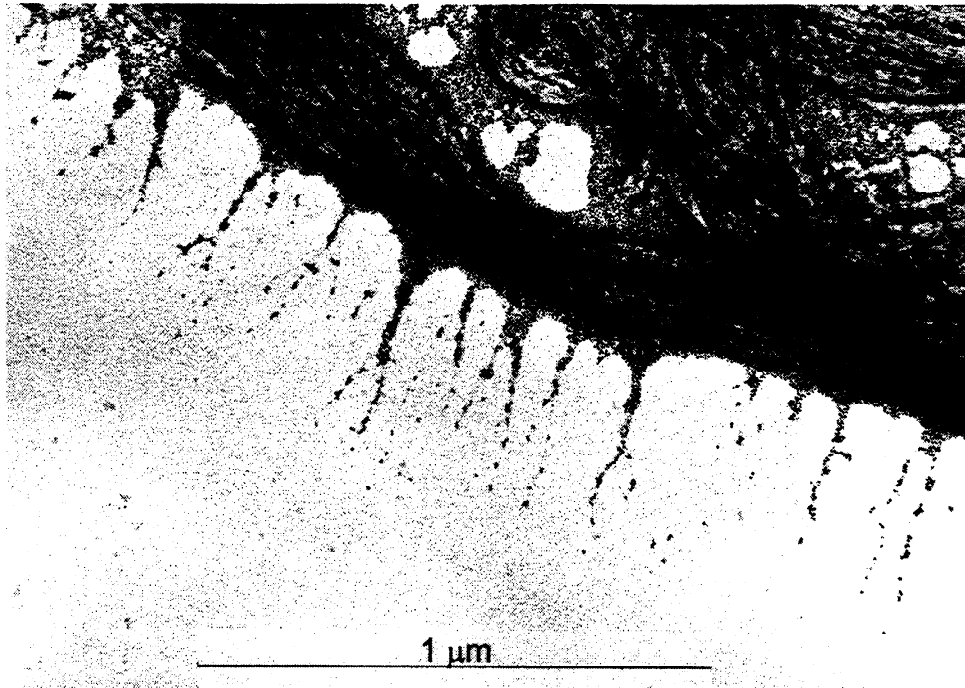


Figure 21: Linear C-PAM adsorbed to softwood unbleached KP

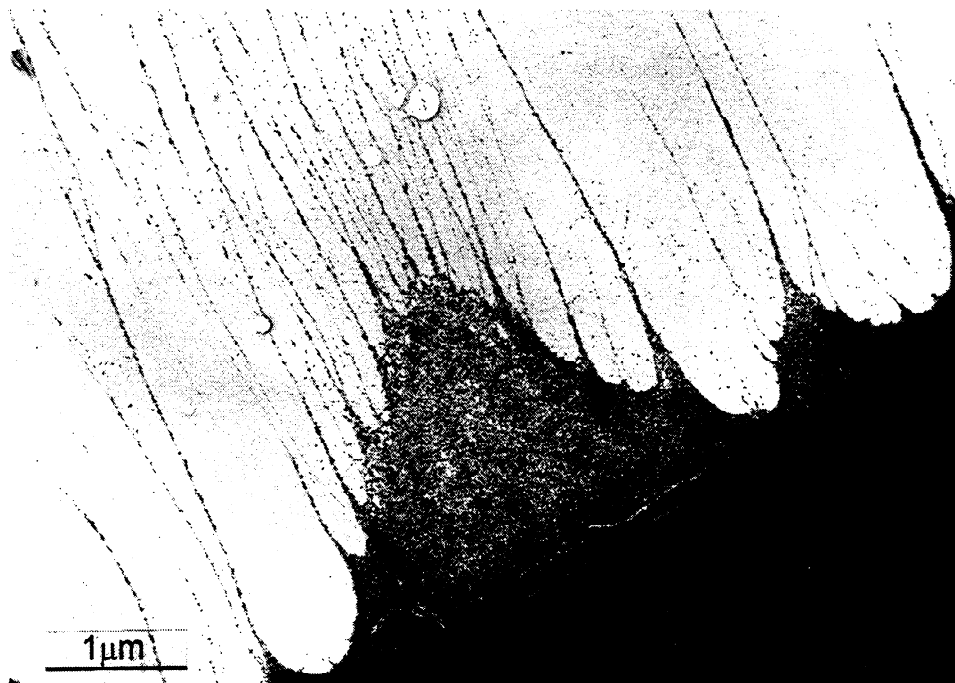


Figure 22: Linear C-PAM adsorbed to softwood CTMP

LIQUID/SUBSTRATE INTERACTIONS

STATUS REPORT

FOR

PROJECT F044

**Wayne Robbins
Tabitha Horton**

**Institute of Paper Science and Technology
500 10th Street, N. W.
Atlanta, Georgia 30318**

DUES-FUNDED PROJECT SUMMARY

Project Title: LIQUID/SUBSTRATE INTERACTIONS
Project Number: F044
PAC Paper Physics

Project Staff:

Principle Investigator: Wayne Robbins
Research Support Staff: Tabitha Horton

PAC Subcommittee: Not Yet Assigned

FY 99-00 Budget: \$ 86,000

Time Allocation:

Principle Investigator: 20%
Research Support Staff: 50%

Supporting Research: None

RESEARCH LINE/ROADMAP:

**11. Improve the ratio of product performance to cost for pulp and paper products
25% by developing:**

- + models, algorithms, and functional samples of fibrous structures and coatings which describe and demonstrate improved convertibility and end-use performance**
- + break-through papermaking and coating processes which can produce the innovative webs with greater uniformity than that achieved by current processes.**
 - Develop and implement relationships between materials & manufacturing variables AND paper structure, properties, & uniformity
 - Develop and implement relationships between paper structure, properties, & uniformity AND end use performance and convertibility
 - Improved papermaking processes
 - Improved converting processes

PROJECT OBJECTIVE:

The objective of this project is to describe the inter-relationship of surface roughness characteristics, pore size distribution, and the swelling characteristics (surface energy) of cellulose fibers, as they contribute to influence the interaction of liquids with dry paper and board substrates. The experimental program will be framed in such a way as to understand how each of these substrate characteristics influences the liquid/substrate interaction over a wide range of applied volume and viscosity of liquid that must be assimilated by a dry substrate within a finite time. A rigorous model of the relative effects can enable better paper and board manufacturing strategies to control such attributes as print quality (as liquid ink vehicle is absorbed into the substrate), size press effectiveness, and coating/base sheet interactions.

PROJECT BACKGROUND:

This project was proposed at the Spring 1999 PAC meeting, and accepted as a Dues Funded project at the subsequent RAC meeting. Goals proposed at that RAC meeting, exploration of theory and methods, were assumed acceptable, and were presented at the Fall 1999 PAC meeting. The project was funded beginning July 1999, and was staffed 30 September 1999.

MILESTONES:

Milestones proposed at the Fall 1999 PAC that were not formally acted upon include:

- 1) Identification of existing theories used to describe Liquid/Substrate interactions. (December 1999)
- 2) Identification of traceable methods to describe surface roughness, pore dimensions and surface energy. (June 2000)
- 3) Identification of methods to apply liquids to paper and board substrates that are comparable to commercial scale liquid application systems. (June 2000)
- 4) Perform designed experiments to understand the influence of surface roughness, pore structure and surface energy over a wide range of applied liquid volume and viscosity. (December 2001)
- 5) Integrate knowledge gained in Milestone # 4 into existing theories from Milestone #1 to create a predictive model that can be used in process and product development. (December 2001)
- 6) Test modified theories as described in Milestone #5 using commercial processes by testing commercially produced products produced during those trials. (June 2002)

DELIVERABLES:

Deliverables proposed at the Fall 1999 PAC that were not formally acted upon include:

- 1) Methods to establish surface roughness, pore dimensions and surface energy that are traceable and can be used in fundamental mathematical expressions. These methods will span multiple grades. This is not the case with most current methods. Therefore, knowledge gained by Member Companies using these methods in one grade line can be related to other grades produced by that Member Company.
- 2) Laboratory/pilot methods of liquid application that are relevant to industrial processes. By closing the loop among substrate testing methods and liquid application methods (comparable to industrial processes), Member Companies will be able to more productively perform product development and relate knowledge gained in one grade line application to other grades.
- 3) Fundamental mathematical expressions describing the assimilation of liquids over a broad range of applied volume and permitted period of assimilation, and the influence of substrate properties as they affect liquid assimilation. Predictive models improve the efficiency to any product or process development effort.

STATUS OF GOALS FOR FY 99-00:

FY 99-00 goals proposed at the Fall 1999 PAC that were not formally acted upon include:

- 1) Identification of existing theories used to describe Liquid/Substrate interactions. (December 1999) **Status: COMPLETE**
- 2) Identification of traceable methods to describe surface roughness, pore dimensions and surface energy. (June 2000) **Status: IN PROGRESS**
- 3) Determine the suitability of the JMP polynomial regression software for establishing the mathematical relationships among the independent variables. (March 2000) **Status: COMPLETE**
- 4) Identification of method(s) to apply liquids to paper and board substrates that are comparable to commercial scale liquid application systems. (June 2000) **Status: IN PROGRESS**

SCHEDULE:

PHASE	WORK ACTIVITY	99J-D	00J-J	00J-D	01J-J	01J-D	02J-J
Phase One	methods development	X	X				
Phase Two	designed experiment		X	X	X	X	
Phase Three	model development				X	X	
Phase Four	test of model					X	X

SUMMARY OF RESULTS:

- 1) Theory describing liquid/substrate interactions is abundant.
- 2) Structured application of theory to experimental design or data interpretation is not commonly employed in printing studies directed at uncoated or coated paper and board products. This appears to be a significant opportunity.
- 3) Profilometric and Interferometric methods of roughness are traceable using a roughness standard, but are useful at two different area of measurement scales.

SUMMARY OF KEY CONCLUSIONS:

- 1) Theories describing liquid/substrate interactions are well documented.
- 2) Application of theory to the practices of paper and board manufacture as related to the eventual application of liquids such as inks, sizing solutions and coatings, among others appears to be an opportunity for improved process and product development.

DISCUSSION:1. BASELINE LITERATURE SURVEY:

A. Significance:

A baseline literature survey is prudent for any newly funded project. It ensures that comparable work is not already in existence, and minimizes the potential for repeating specific tasks that may have already been performed by others. It also provides a foundation upon which to build.

B. Approach:

The approach in this literature review was to establish the current state of knowledge and application of that knowledge. It is recognized that the literature file is not exhaustive, and will become so only over time. Therefore, some references that readers may feel are key or important may not yet be included at this time.

It was believed necessary to establish the current state of knowledge by critically reviewing papers that had an application orientation. The reasoning was that if many papers, including those by the most prolific authors in the field, were found to be at a certain state of application of knowledge or theory, this would most likely be representative of the general industry.

Theory and methodology publications are listed in this review, but not critically reviewed at this time. As the experimental program proceeds, and model development evolves, data generated during the course of the project will be used to test the adequacy of the theories published in the open literature.

C. Results:

THEORY AND BASIC METHODOLOGY

The theory surrounding liquid/substrate interactions is published in three principle areas. One of these has been thoroughly explored by past workers at IPST under Project 3480, 'Fundamentals of Water Removal Processes'. The stated IPST Goal in this project was to "Develop novel processes for efficient water removal with enhanced control over paper properties" (1). The primary thrust of this project was to understand the fundamentals of water flow through wet webs in an effort to improve the overall efficiency of the press section of the paper machine. The experimental effort focused on displacement of water already in the web through pressure, and occasionally with the assistance of heat. Overlap of the knowledge gained during the course of this project was particularly valuable to an impulse drying related project that was ongoing during the same period. This particular aspect of liquid/substrate interactions is not the focus of this project, at this time. And, while most areas of liquid/substrate interactions share some common theoretical origins, it is inappropriate to assume that application of theory to practice is completely transferable since the experimental approach to displacement of liquids from wet webs is dissimilar to that application of liquid to dry webs (2-5).

This project is currently directed at the flow of liquids through dry porous paper and board substrates. Application of the models developed during the course of the project are initially expected in the area of ink/paper interactions, followed by size press and coating/base sheet applications. The open literature that addresses these principle areas of commercial interest can be generally grouped in two areas: those dealing with printing applications, and those dealing with coating applications. Both trace their theoretical origins to two early workers, Darcy (6) and Washburn (7). These early works were not directed specifically toward cellulose and porous structures composed of cellulose fibers, and therefore do not account for the hydrophilic nature of cellulose. However, a number of workers have studied the water/cellulose interactions specifically to describe the swelling of cellulose as it is exposed to water. These efforts are typified by Bristow (8), Scallon (9) and Hoyland (10). Lindstrom even reviewed the field (11).

There are structural properties associated with paper and board structures composed of cellulose fiber that are common to fibrous structures in general, and are primary factors affecting the way that liquids interact. These include pore dimensions and their distribution at the surface and throughout the sheet, and the surface topography, or roughness of the sheet.

The literature associated with pore structure can be categorized a number of different ways. For the purpose of this discussion, it will be organized into three sections. One of these is a description of measurement techniques, and attempts to describe the pore structure of paper and boards. There are several different methods that have been described to characterize the pore structure of papers and boards. These include Mercury porosimetry (12). The influence of surface roughness on the accuracy of this method was also described (13). Back described a technique using a variety of liquids, aqueous and non-aqueous (14). A method was described where an inert gas is passed through a sample immersed in a non-swelling liquid (15). Finally, Lyne described a spectral approach (16). The drawback of all of these methods is that none of the measurements were related to traceable reference substances.

A second area of concentration can be described as attempts to describe the pore structure of paper and boards in terms that can be more easily mathematically modeled. In this case, a number of workers have described paper and board structures as being analogous to capillary tubes (17-20). Still, Batton described coated paper and board in terms of a packed bed (21).

Another clearly identifiable area includes attempts to describe the actual flow of liquid as a function of pore structure (22-25).

Finally, a significant body of literature exists where paper coating structures are described, and the relationship of these structures as they affect the sorption of aqueous coatings or migration of coating components is discussed (26-34).

The surface topography and its influence on the permeability of liquids is also described in relationship to permeation of liquids. One section of literature describes methods, or a comparison of methods. Examples include discussions by Bichard (35), Wagberg (36) and Lloyd (37). Bristow described a method to derive a roughness index from a liquid sorption apparatus (38). Bristow and Mason also attempted to more completely describe the nature of the combined mechanical properties of pore structure and paper topography in extensive monographs (39, 40). In related studies, Aspler and Lepoutre discussed surface roughness as defined by "fibre rising", or simply as fiber swelling as aqueous liquids were applied (41, 42). And, although this will be discussed in detail in the section dealing with "Applications", several typical papers discussing the effect of roughness on printability (43-45) and coating/substrate interactions are included (46).

Another factor that is influenced by both the pulp yield and resulting chemical composition, contaminants such as extractives, and sizing additives is surface energy. The literature in this area can be organized into four categories. These include methods (47-50), the effect of wood and pulp components (51), the effects of sizing additives, the impact of sizing on contact angle (52-67), and the associated effect on print quality or the ink/paper interaction (68-73).

In another related area, a body of literature exists where the investigators simply describe various apparatus that are useful to apply liquids to paper and board substrates. Presumably, invention of these apparatus, is intended to accelerate the study and identification of substrate or liquid characteristics that affect the liquid/substrate interactions. This body of literature appears to be organized in two basic areas, printing (74-81) and coating (82-84).

As noted earlier, it is clear at this point in the discussion that none of the references cited or the accompanying theories are critically reviewed. Critical review of theory is most appropriate as experimental results are obtained to test theory. Simply stated, the objective of the project is intended to be application of theory to practice. It can be concluded that many of the concepts and methods developed above overlap, and provide different pathways for knowledge about liquid/substrate interactions to be applied in the manufacture of paper and board that enables better control of the application of liquids.

APPLICATION OF THEORY TO PRACTICE:

As with any scientific discipline, theory as an end to itself is interesting, but generally not a productive use of effort. Similarly, application that is not grounded in theory is typified by a very poor efficiency, since many experiments and trials are possible, but could amount to little more than a random search for primary factors. With this preamble, the next exercise that is appropriate, is to review "application" oriented literature in order to determine if, and the extent to which the theory that is outlined above was actually used in the experimental design and interpretation of data in liquid/substrate applications. Since the first task outlined in the project is to address liquid/substrate interactions as applied to ink/paper, or printing applications, this analysis is performed below for descriptions of printing.

As with the prior discussion, it is generally possible to organize the literature into basic sections. One of these includes descriptions of methods or apparatus intended to accelerate studies associated with print quality (85-87).

Another body exists that can be described as application of ink onto uncoated paper. This body of literature can be further subdivided and one of the principle areas can be termed as flexographic/linerboard applications (88-91). This particular group of publications is quite informative about the state of the application of theory to practice in the linerboard sector. It is important to note that most of these papers were published within the past 5 years, and should represent a common reference point.

McGratton's publication (88) is actually the result of discussions by the TAPPI Linerboard/Corrugated Subcommittee, and simply reports widely held views by the industry. A number of simple key characteristics are noted along with recommended test methods. Beliefs are stated about the influence of each characteristic, and potential problems if the characteristic is not controlled. Both sizing and roughness are among the characteristics noted, and beliefs are stated about how they might affect printability. No references or experimental results are given to support the stated views. The paper by Haglund (89), is another general publication, focusing solely on flexographic printing. No experimental data is presented, but several figures that are generally held beliefs are included in this publication. Again, no references are presented, and no supporting theory is presented to draw the conclusions, which represent conventional wisdom.

The paper by Zang and Aspler (90) is a review article. It attempts to discuss in general terms the flexographic printing process, and follows with some general definitions of criteria that are typically used to rate the resulting printed image. A discussion follows about the general linerboard properties that have been traditionally attributed to influence linerboard printability. Specific test methods are even mentioned. The Lucas-Washburn

equation is shown in this publication, and is even discussed as being applicable in very general terms. However, the equation is dismissed with the comment that “it is unsuitable to quantitatively predict the transfer and setting of water based inks on linerboard.” The remainder of this publication is little more than a general discussion of factors such as water absorbancy, formation and several other properties. The paper contains a number of references, but really never engages in the process of critical review.

The final publication in this area is also co-authored by Aspler and Zang (91), and appears to be the result of a consortia funded experimental effort to establish the primary variables of both linerboard and the printing process that affect linerboard print quality. Printability, for the purpose of this study, was defined as, but not limited to, half tone images and bar code readability. General conclusions were also drawn about solid print density and hold out. The general experimental description is quite detailed, but the experimental design did not appear to be statistically designed, nor did it take advantage of any specific theories in an effort to more effectively evaluate specific variables. Data are presented both graphically, and with regression analysis. The conclusions eventually drawn tend to support the conventional practices of the industry. In any event, since there was no statistical design of the experiment, and no theory was used to narrow the possible variables, the conclusions could hardly be termed as “definitive”. It might be concluded that the conclusions are limited by the nature of the experimental design. Thus, in the area of linerboard printability, the current state of the art of the open literature does not appear to have taken advantage of the wealth of available theory and methods listed above.

Another group of the uncoated paper and board publications includes uncoated free sheet applications (92, 93, 95-98). Again, while this group of articles is not considered exhaustive, it does represent a body of literature that can be considered to be the state of current application of theory to practice. Lu (92) studied the permeation of liquid developer into a variety of different papers, most of which were uncoated. In this study, the subject was introduced with a discussion of the Lucas-Washburn equation. This equation was carried to the point where they predicted the $t^{1/2}$ relationship with penetration rate, and their data is interpreted using this argument. However, the author never reaches a fundamental conclusion with respect to the base paper properties, choosing only a “permeability” discussion represented primarily by caliper measurements. It is difficult to understand how to apply the knowledge gained in the experiment.

Walker (93) chose to employ the empirical relationship originally derived by Fetsko (94) that describes the transfer of ink to paper. In this relationship, paper smoothness is the only potentially traceable variable used to describe the paper. Although he generally confirmed the empirical model, it is again difficult to understand how this information is directly useful to manufacturers of paper and board products.

Lyne and Aspler discuss the effect of various silica coatings on dot gain of ink jet printed papers (95), and even recommend in very general terms the desired paper properties, but not in any measurable context. Again, no application of theory was given. Yamazaki (96) effectively reproduces the work by Walker, with the Fetsko equation, and evaluated many of the same base stock types; however, no useful information is gained in application of this work to base paper properties. Zang (97) effectively repeats the same ink transfer modeling exercise in an effort to develop a new algorithm, and does not relate that algorithm to base paper properties. Finally, Busche (98) chose a very specific parameter, surface chemistry, to understand its impact on rotogravure printability. In doing so, he varied the pH of the base stock, and the level of AKD sizing. With this single variable approach, the reader does not have the opportunity to compare the relative effect of the surface chemistry effects with others, such as roughness or pore dimensions.

Another area of uncoated paper printing literature includes newsprint (99-101). Again, Aspler dominates the open literature in this area. In the first of these studies (99), Aspler attempts to use the Lucas-Washburn equation to establish the relative effects of pore structure, roughness and surface chemistry. In this paper, they conclude that the principle mechanism of ink transfer to newsprint is hydraulic impression into surface pores, although he discounts this conclusion later in the paper without benefit of data. In a subsequent paper dealing with ink ruboff (100), the study was limited to a random empirical analysis, and no justification was given for the physical properties of the paper he chose to analyze and perform regression analysis on the data. This is especially confusing in light of the earlier study. In the last of the studies cited (101), it is even more surprising that another empirical study was performed where physical properties such as air permeability, and fiber length were evaluated as a plausible explanation for observed printing properties. Again, no benefit of theory was used in this approach.

The last body of literature that will be discussed relates to the printability of coated papers. This particular body of literature is difficult to organize. There are a number of representative publications that consider the composition of the coating. The influence of pigment content, type, and/or the associated properties is a common subject (102-106). It is interesting that this set of articles represents a more direct attempt at an experimental design. Both Zang (106) and Desjumaux (103) have chosen specific variables, such as content and size, and examined variables such as pore volume or roughness that resulted, and expressed these effects on printing properties. The remaining papers by Ahlroos (102) and Donigan (104) fall back to efforts that seem random. Drage (105) falls into a similar category as this study simply collected some commercial samples, and attempted to attribute print performance to the variables analyzed. It appears that in the area of coating pigments, that samples of a designed nature seem easier to produce on a lab or pilot scale, and therefore lend themselves more directly to a designed experiment.

In an attempt to segregate effects, Zang (109) used the same papers produced in his study of pigments, and attempted to examine the effect of binder content. Although the experiment has elements of experimental design such as the latex content of the coating, which is varied over an extended range, no attempt is made to compare the relative effects of binder content to the effect of mineral content from the earlier work. Therefore, an opportunity is lost. It is interesting that neither pieces of work take advantage of any of the more fundamental theory in the experimental design or interpretation of their data. In contrast to this study, Huang and Lepoutre (107) initiated their study of base stock surface structure with a discussion of the Lucas-Washburn equation, and attempted to vary important variables, such as pore size, roughness and contact angle. Although the study was performed on hand sheets, the design and interpretation of the data actually employed an application of theory to practice, something that does not appear common in the open literature. However, in another study by Kim and coworkers (108), an effort was made to affect the coating structure through a designed trial of the coating dryer section. Unfortunately, this study is entirely empirical, and does not employ any theoretical concepts in either the planning of the trial or interpretation of the data.

A number of workers have examined paper properties as they affect Gravure print quality. Both Bristow (110) and Kunz (111) discussed the effect of base stock properties. Kunz discusses the properties in a random fashion with little regard to theory. His paper can be best described as a collection of interesting observations that support his personal beliefs. Bristow, while performing an empirical study to support his conclusions about roughness, simply does not take into account the other potential variables that might affect gravure print quality. By severely limiting the variables included in their experimental design, the reader is unable to conclude if the authors are studying a major or minor factor in base paper properties. Sprycha and Hruzewicz co-authored two publications in the area of gravure printing as they relate to base paper properties (12, 13). Although one can not clearly determine the relative effects of surface chemistry, pore structure and roughness from these publications, the authors initiate the discussion in one of the papers (12), with the Lucas-Washburn equation, and interpret the results using Darcy's Law. Again, these studies, where theory is applied to practice, are unusual.

Three relatively recent reviews of ink/paper interactions were examined (114-116). In the most recent review by Aspler (114), the discussion is initiated using the Lucas-Washburn equation to ground their arguments. The review seems well balanced, and seems to have selected most of the credible application oriented publications that have considered theory in the design or interpretation of the results. The author also includes a number of single variable experiments, or those studies that have not been statistically designed, or are purely empirical in nature, and has given them equal weighting in his analysis. The final conclusions speak of the influence of surface chemistry as being dominate, but admit that much is unknown. Given the number of poorly designed or interpreted studies included in this review, the conclusions are difficult to justify.

In an earlier review by Lyne and Aspler(115), a more fundamental approach is used, combining both theory, such as the Lucas-Washburn equation and Darcy's Law, with more empirical models for ink transfer, such as that derived by Fetsko. These theories were used to develop a more conceptual understanding of various printing processes as they are applied to base papers. The conclusion of the review points out where experimental data can be used to prove some theories, such as a Poiseuille model to estimate hydraulic impression of ink into inter-fiber capillaries. This review, unlike the later one by Aspler does not attempt to rank the influence of various substrate properties as they affect various printing processes. The review is lacking in that it does not allow the reader to easily apply the concepts developed to the manufacture of paper and board, or the printing of these substrates.

The review by Kadoya and Usuda (116) mirrors the 1993 Lyne and Aspler review, only it focuses on the penetration of non-aqueous liquids. It employs well grounded theoretical models in developing a conceptual understanding of non-aqueous liquid penetration. Some laboratory methods and procedures are included that describe substrate characterization or liquid application methods. The same conclusion can be drawn about this paper as was drawn for the Lyne and Aspler publication. That is, the paper is written at a level so that application of the conclusions drawn therein would be difficult in a manufacturing environment or a press room.

D. Conclusions:

- 1) Theory of liquid penetration and methods to characterize paper and board substrates are plentiful.
- 2) The open literature in two potential areas of application, printing of uncoated and coated substrates appears dominated by single variable experiments, empirical designed experiments that are not grounded in theory in the initial design or in the ultimate interpretation of the data.
- 3) The opportunity that appears to exist is structured application of theory to practice.

E. References:

- 1) Lindsay, J.D., Status Report for Project 3480, dated 23 February 1990.
- 2) Lindsay, J.D., "Displacement dewatering to maintain bulk", *Paperi ja Puu*, Vol. 74, No. 3, p. 232 (1992).
- 3) Lindsey, J.D. and Brady, P.H., "studies of anisotropic permeability with applications to water removal in fibrous webs", *TAPPI J.*, Vol. 76, No. 9, p. 119 (1993).
- 4) Jonsson, K. A-S. and Jonsson, B.T.L., "Fluid Flow in Compressible Porous Media: I: Steady-State Conditions", *AIChE*, Vol. 38, No. 9, p. 1340 (1992).
- 5) Jonsson, K. A-S. and Jonsson, B.T.L., "Fluid Flow in Compressible Porous Media: II: Dynamic Behavior", *AIChE*, Vol. 38, No. 9, p. 1349 (1992).
- 6) Darcy, H., *Les Fontaines Publiques de la Ville de Dijon* (Dalmont, Paris) 1856.
- 7) Washburn, E.W., *Phys. Rev.* 17: 273 (1921).
- 8) Bristow, J.A., "The swelling of paper during the sorption of aqueous liquids", *Svensk Papperstidning*, Vol. 74, No. 20, p. 645 (1971).
- 9) Scallon, A.M. "The accommodation of water within pulp fibres", *Fibre-Water Interact. Pap.- Making, Trans. Symp. 1977, Br. Pap. Board Ind. Fed., London* (1978), pp.9-27.
- 10) Hoyland, R.W., *ibid.*, pp. 557-577.
- 11) Linstrom, T., *Paper: Structure and Properties* (Bristow and Kolseth eds.) Ch. 4: 75-97 (c 1986, Marcel Dekker).
- 12) Johnson, R.W., Abrams, L., Maynard, R.B., and Amick, T.J., "Use of Mercury porosimetry to characterize pore structure and model end-use properties of coated papers - Part 1: Strength and Optical Properties.", *TAPPI J.*, Vol. 82, No. 1, p. 239 (1999).
- 13) Kadoya, T. and Usuda, M., "The Penetration of Non-aqueous Liquids", *Handbook of Physical and Mechanical Testing of Paper and Paperboard*, Vol. 2, edited by R.E. Mark, Marcel Dekker, Inc., NY (1984).

- 14) Back, E.L., "The pore anisotropy of paper products and fibre building boards", Svensk Papperstidning, No. 7, April 1966.
- 15) Leekley, R.M. and Tyler, R.F., "The measurement of pore size distribution by the bubble stream counting method", TAPPI J., Vol. 59, No. 11, p. 131 (1976).
- 16) Lyne, B., "Measurement of the distribution of surface void sizes in paper", TAPPI J., Vol. 59, No. 7, p. 102 (1976).
- 17) Guin, J.A., Kessler, D.P. and Greenkorn, R.A., "The permeability tensor for anisotropic nonuniform porous media", Chem. Eng. Sci., Vol. 26, p. 1475 (1971).
- 18) Youngs, E.G., "Fundamental aspects of fluid flow through porous materials", Trans. BPBIF Symp. Fund. Props.: Paper Related to Uses (Cambridge): 452-460, disc.: 461-463, 511-516 (Sept. 1973; pub. 1976).
- 19) Salminen, P.J., "water transport into paper - the effect of some liquid and paper variables", TAPPI J., Vol. 71 (1988).
- 20) Horstmann, D.H., Lindsay, J.D. and Stratton, R.A., "Using edge-flow tests to examine the in-plane anisotropic permeability of paper", TAPPI J., Vol. 74 (1991).
- 21) Batton, G.L., "Paper as a packed bed", TAPPI Proceedings: International Paper Physics Conference, p. 67 (1991).
- 22) Tollenaar, D., "Capillarity and wetting in paper structures: properties of porous systems", Surfaces and Coatings Related to paper and Wood, R.H. Marchessault and C. Skaar (eds.), Syracuse Univ. Press, pp. 195-219 (1967).
- 23) Bliesner, W.C., "A study of the porous structure of fibrous sheets using permeability techniques", TAPPI J., Vol. 47, No. 7, p. 392 (1964).
- 24) Van den Akker, J.A. and Wink, W.A., "Mechanisms of liquid-phase movement of water through paper", TAPPI J., Vol. 52, No. 12, p. 2406 (1969).
- 25) Winspear, S., "The characterization of liquid acceptance by paper", Appita, Vol. 33, No. 1, p. 25 (1979).
- 26) Beazley, K.M. and Climpson, M., "Liquid migration from coating colors; I: correlation between electrical and optical measurements", TAPPI J., Vol. 53, No. 12, p. 2227 (1970).

- 27) Windle, W., Beazley, K.M. and Climpson, M., "Liquid migration from coating colors; II: the mechanism of migration", TAPPI J., Vol 53, No. 12, p. 2232 (1970).
- 28) Hoyland, R.W., Howarth, P. and Field, R., "Fundamental parameters relating to performance of paper as a base for aqueous coatings" in: The fundamental properties of paper related to its uses; Tech. Div. BPBIF, London, p. 464 (1976).
- 29) Lepoutre, P., "Liquid absorption and coating porosity", Paper Technology Industry, Vol. 19, No. 9, p. 299 (1978).
- 30) Eklund, D. E. and Salminen, P. J., "Water transport in the blade coating process", TAPPI J., Vol. 69, p. 116 (1986).
- 31) Leskinen, A.M., "Latex structure in model coatings", TAPPI Proceedings, Coating Conference, p. 71 (1987).
- 32) Arai, Y. and Nojima, K., "Coating structure for obtaining high print gloss", TAPPI J., Vol. 81, No. 5, p. 213 (1998).
- 33) Young, T.S., Pivonka, D.E., Weyer, L.G. and Ching, B., "A study of coating water loss and immobilization under dynamic conditions", TAPPI J., Vol. 76, No. 10, p. 71 (1993).
- 34) Chen, K.S.A. and Scriven, L.E., "Liquid penetration into a deformable porous substrate", TAPPI J., Vol. 73, No. 1, p. 151 (1990).
- 35) Bichard, W., "The inter-relationship among air-leak roughness/smoothness methods: a canadian newsprint study", Pulp and Paper Canada, Vol. 93, No. 6, p. 43 (1992).
- 36) Wagberg, P., "A correlation between results achieved with an optical profile tester, conventional paper evaluation and printability", TAPPI Proceedings, International Printing and Graphic Arts Conference, p. 187 (1992).
- 37) Lloyd, M.D., Ashburn, M. J. and Chalmers, I.R., "Use of a laser sensor to characterize roughness of linerboard and other paper grades", Appita, Vol. 48, No. 3, p. 218 (1994).
- 38) Bristow, J.A., "Liquid absorption into paper during short time intervals", Svensk Papperstidning, Vol. 70, No. 19, p. 623 (1967).

- 39) Bristow, J.A., "The paper surface in relation to the network", Paper: Structure and Properties, Bristow and Kolseth (eds.), Ch. 8, pp. 169-182, Marcel Dekker, c. 1986.
- 40) Oliver, J.F. and Mason, S.G., "Scanning electron microscope studies of spreading of liquids on paper", The Fundamental Properties Paper Related to its Uses, Tech. Div. BPBIF, London, p. 428 (1976).
- 41) Aspler, J.S. and Beland, M.-C., "A review of fibre rising and surface roughening effects in paper", JPPS, Vol. 20, No. 1, p. J27 (1994).
- 42) Enomae, T and Lepoutre, P., "Observation of the swelling behavior of kraft fibers and sheets in the environmental scanning electron microscope", Nordic Pulp and Paper J., Vol. 13, No. 4, p. 281 (1998).
- 43) Hansuebsai, A. and Morantz, D.J., "Smoothness - assessing various paper-surface characteristics can be helpful in predicting ink transfer and rintability", American Ink Maker, p. 28, November (1988).
- 44) Bristow, J.A. and Ekman, H., "Paper properties affecting gravure print quality", TAPPI J., Vol. 64, No. 10, p. 115 (1981).
- 45) Aspler, J.S. and Lyne, M.B., "How important is water absorbancy in newsprint?", TAGA Proc. 39th Conference, San Diego, pp. 340-351 (1987).
- 46) Huang, T. and LePoutre, P., "Effect of basestock surface structure and chemistry on coating holdout and coated paper properties", TAPPI J., Vol. 81, No. 8, p. 145 (1998).
- 47) Miller, B.M. and Young, R.A., "Methodology for studying the wettability of filaments" Textile Research Journal, p. 359, May (1975).
- 48) Bristow, J.A., "The reproducibility of contact angle measurements", Papper och Tra, Vol. 4a, p. 171 (1968).
- 49) Uyama, Y., Inoue, H., Ito, K., Kishida, A. and Ikada, Y., "Comparison of different methods for contact angle measurement", J. of Coll. And Surf. Sci., Vol. 141, No. 1, p. 275 (1991).
- 50) Liukkonen, A., "Contact angle of water on paper components: sessile drops versus electron scanning electron microscope measurements", Scanning, Vol. 19, p. 411 (1997).

- 51) Sheng, Y.J., Shen, W. and Parker, I.H., "the influences of pulping method and pH on the surface energy of eucalypt fibres", Proceedings of the 52nd Annual Appita Conference, part 1 of 2, p. 91 (1998).
- 52) Bristow, J.A., "The absorption of water by sized papers", Svensk Papperstidning, Vol. 71, p. 33 (1978).
- 53) Garrett, P.D. and Lee, K.I., "Characterization of polymers for paper surface sizing using contact angle measurements", TAPPI J., Vol. 81, No. 4, p. 95 (1998).
- 54) Aspler, J.S., Davis, S. and Lyne, M.B., "The dynamic wettability of - effect of surfactants, alum, and pH on self sizing", TAPPI Proceedings; Int. Paper Phys. Conf., p. 229, Sept. 1983.
- 55) Wasser, R.B. and Brinen, J.S., "Effect of hydrolyzed ASA on sizing in calcium carbonate filled paper", Vol. 81, No. 7, p. 139 (1998).
- 56) Lindstrom, T., "Alum and starch - their use and abuse", Paper, p. 18, September (1984).
- 57) Aspler, J.S., Davis, S. and Lyne, M.B., "The dynamic wettability of paper: the effects of surfactants, alum and pH on self sizing", TAPPI J., Vol. 67, No. 9, p. 128 (1984).
- 58) Jing, Q., Chen, M., and Biermann, C.J., "Octadecylamine as an internal sizing agent", TAPPI J., Vol. 81, No. 4, p. 193 (1998).
- 59) Aspler, J.S., Davis, S. and Lyne, M.B., "The surface chemistry of paper in relation to dynamic wetting and sorption of water and lithographic fountain solutions", JPPS, Vol. 13, No. 2, p. J55 (1987).
- 60) Bazaj, R.K., dePierne, O.S., Proverb, R.J., Barker, L.j. and Errigo, L.E., TAPPI Proceedings, Papermakers Conference, p. 401 (1995).
- 61) Luukkonen, K., Malmstrom and Zetter, C., "New and innovative sizing strategies for the sizing of PC containing fine paper", TAPPI Proceedings Conference, p. 435 (1995).
- 62) Tsai, Y-G, Colasurdo, A.R. and Cordoba, C., "An alternative chemistry for paper: surface size with high performance and a large window of operation", TAPPI Proceedings Conference, p. 427 (1995).

- 63) Truong, Y.B., Kuys, K. and Parker, I., "Adsorption of alkyl ketene dimer on eucalypt kraft fibers in relation to single fiber contact angles", Conference Proceedings, 9th Int. Symp. On Wood and Pulp. Chem.", p. 115-1 (1997).
- 64) Lyne, M.B. and Huang, Y.C., "Measuring acid-base and dispersive interactions with paper surfaces under dynamic surfaces", Nordic Pulp and Paper Research J., No., 8, p. 120 (1993).
- 65) Tsai, Y-G, Inoue, M. and Colasurdo, A.R., "The effect of sizing materials on the ink absorption of paper" TAPPI 1999 Proceedings, p. 111 (1999).
- 66) Isogai, A., "Mechanism of paper sizing by alkylketene dimers", JPPS, Vol. 27, No. 7, p. 251 (1999).
- 67) Isogai, A., "Mechanism of paper sizing by cationic emulsion of fatty acid anhydrides", JPPS, Vol. 25, No. 6, p. 211 (1999).
- 68) Lyne, M.B. and Aspler, J.S., "Paper for ink jet printing", TAPPI J., Vol. 68, No. 5, p.106 (1985).
- 69) Krueger, J.J. and Hodgson, K.T., "Single fiber wettability of highly sized pulp fibers", TAPPI J., Vol. 77, No. 7, p. 83 (1994).
- 70) Krueger, J.J. and Hodgson, K.T., "The relationship between single fiber contact angle and sizing performance", TAPPI Proceedings: Paper Makers Conference, p. 143 (1994).
- 71) Etzler, F.M. Buche, M., Bobalek, J.F. and Weiss, M.A., "Surface free energy of paper and inks: printability issues", TAPPI Proceedings: Paper Makers Conference, p. 383 (1995).
- 72) Borch, J., "The effect of paper sizing on print quality in business and office non-impact printing", TAPPI Proceedings: Paper Makers Conference, p. 395 (1995).
- 73) Krueger, J.J. and Hodgson, K.T., "The relationship between single fiber contact angle and sizing performance", TAPPI J., Vol. 78, No. 2, p. 154 (1995).
- 74) Bristow, J.A., "Liquid Absorption into paper during short time intervals", Svensk Papperstidning, Vol. 70, No. 19, p. 623 (1967).

- 75) Chatterjee, P.K., "The sonic velocity response during the absorption of water in paper", *Svensk Papperstidning*, Vol. 74, No. 17, p. 503 (1971).
- 76) Okagawa, A. and Mason, S.G., "Capillarography: a new surface probe", *Fibre-Water Interactions in Papermaking*, BPBIF, pp. 581-586, London (1978).
- 77) Lyne, M.B. and Aspler, J.S., "Wetting and the sorption of water by paper under dynamic conditions", *TAPPI J.*, Vol. 65, No. 12, p. 98 (1982).
- 78) Anderson, B.L. and Higgins, B.G., "Apparatus for measuring wetting delays and sorption rates for paper/liquid systems", *TAPPI Proceedings, Coating Conference*, p. 47 (1985).
- 79) Pan, Y-L., Kuga, S. and Usuda, M., "An ultrasonic technique to study wetting and liquid penetration of paper", *TAPPI J.*, Vol. 71, No. 5, p. 119 (1988).
- 80) Banerjee, S., Reed, K.R., Hooper, R.C., Van Eperen, R.H., Crouse, B. and Moynihan, J.T., "Radiochemical study of z-directional mobility of varnish in paper", *TAPPI J.*, Vol. 76, No. 10, p. 107 (1993).
- 81) Rosenberger, R., "A method for measuring ink-jet wicking using a document scanner and a personal computer", *TAPPI J.*, Vol. 81, No. 3, p. 71 (1998).
- 82) Mark, W.R., "Measurement of the water retention of coatings: the static terminal ring cell", *TAPPI J.*, Vol. 52, No. 1, p. 70 (1969).
- 83) Kiiha, T., Linnonmaa, J and Paulapuro, H., "Comparing coating heads on a pilot coater: a call for reliable results", *TAPPI J.*, Vol. 81, No. 5, p. 185 (1998).
- 84) Willenbacher, N., Hanciogullari, H. and Radle, M., "New laboratory test to characterize immobilization and dewatering of paper coating colors", *TAPPI J.*, Vol. 82, No. 8, p. 167 (1999).
- 85) Oliver, J.F. and Forsyth, R.C., "A dynamic liquid sorption apparatus for studying interactions of microscopic drops in situ on porous substrates", *Colloids and Surfaces*, Vol. 43, P. 295 (1989).
- 86) Kowalczyk, G.E. and Trksak, R.M., "Image analysis of ink-jet quality for multi use office paper", *TAPPI J.*, Vol. 81, No. 10, p. 181 (1998).

- 87) Trepanier, R.J., Jordan, B.D. and Nguyen, N.G., "Specific perimeter: a statistic for assessing formation and print quality by image analysis", TAPPI J., Vol. 81, No. 10, p. 191 (1998).
- 88) McGratton, W., "Key characteristics of linerboard, corrugating medium, and roll stock mechanical condition and their influence on the manufacture of corrugated products, part 1", TAPPI J., Vol. 73, No. 11, p. 99 (1990).
- 89) Haglund, N., "Improving the printability of kraftliner", Paper Technol. Ind., Vol. 29, No. 8, p. 265 (1988).
- 90) Zang, Y.H. and Aspler, J.S., "Factors that affect the flexographic printability of linerboards", TAPPI J., Vol. 78, No. 10, p. 240-23 (1995).
- 91) Aspler, J., Jordan, B. and Nguyen, N., "TAGA Conference Proceedings, p. 749 (1998).
- 92) Lu, C.H., "The relevance of paper characteristics in the liquid electrostatic imaging process", TAPPI J., Vol. 60, No. 10, p. 130 (1977).
- 93) Walker, W.C., "Determination of ink transfer parameters", TAPPI J., Vol. 64, No. 5, p. 71 (1981).
- 94) Walker, W.C. and Fetsko, J.M., American Ink Maker, p. 99, December (1955).
- 95) Lyne, M.B. and Aspler, J.S., "Paper for ink jet printing", TAPPI J., Vol. 68, No. 5, p. 106 (1985).
- 96) Yamazaki, H., "Modified methods for the determination of the ink transfer parameters by non-linear regression", TAPPI Proceedings, International Paper Physics Conference, p. 685 (1991).
- 97) Zang, Y.H., "Asymmetric splitting and ink transfer: a new ink transfer model", TAPPI Proceedings, International Printing and Graphic Arts Conference, p. 103 (1992).
- 98) Busche, M., Triantafillopoulos, N. and Serafano, J., "Papermaking for water based gravure printability", TAPPI Proceedings, Papermakers Conference, p. 409 (1995).
- 99) Aspler, J.S. and Lyne, M.B., "How important is water absorbancy in newsprint", TAGA Proceedings, 39th Conference, p. 340 (1987).

- 100) Aspler, J.S., De Grace, J.H. and Dalphond, J.E., "Newsprint contributions to ruboff of oil based inks", JPPS, Vol. 17, No. 5, p. J149 (1991).
- 101) Aspler, J.S., Beland, M.C., Piquard, L., DeGrace, J.H. and Maine, C., "Transfer and setting of water-based ink, part II: pH, water absorbancy and uncoated paper structure", TAPPI Proceedings, International Printing and Graphic Arts Conference, p. 251 (1992).
- 102) Ahlroos, J., Alexandersson, M. and Gron, J., "Influence of base-paper filler content and precalleddering on metered film press coating - paper and print quality", TAPPI J., Vol. 82, No. 5, p. 94 (1999).
- 103) Desjumaux, D., Bousfield, D.W., Glatter, T.P., Donigan, D.W., Ishley, J.N. and Wise, K.J., "Influence of pigment size on wet ink gloss development", JPPS, Vol. 24, No. 5, p. 150 (1998).
- 104) Donigian, D.W., Wernett, P.C., McFadden, M.G. and McKay, J.J., "Ink-jet fixation and coating pigments", TAPPI J., Vol. 82, No. 8, p. 175 (1999).
- 105) Drage, P.G., Hiorns, A.G., Parsons, D.J. and Coggon, L., "Factors governing print performance in offset printing of matte papers", TAPPI J., Vol. 81, No. 11, p. 175 (1998).
- 106) Zang, Y.H. and Aspler, J.S., "The influence of coating structure an the ink receptivity and print gloss of model clay coatings", TAPPI J., Vol. 78, No. 1, p. 147 (1995).
- 107) Huang, T. and Lepoutre, P., "Effect of basestock surface structure and chemistry on coating holdout and coated paper properties", TAPPI J., Vol. 81, No. 8, p. 145 (1998).
- 108) Kim, L.H., Pollock, M.J., Wittbrodt, E.L., Roper, J.A., Smith, D.A. Stolarz, J.W., Rolf, M.J., Green T.J. and Langolf, B.J., "Reduction of back trap mottle through optimization of the drying process for paper coatings, part I", TAPPI J., Vol. 81, No. 8, p. 153 (1998).
- 109) Zang, Y.H. and Aspler, J.S., "The effect of surface binder content on print density and ink receptivity of coated paper", JPPS, Vol. 24, No. 5, p. 141 (1998).
- 110) Bristow, J. A. and Ekman, H., "Paper preproperties affecting gravure print quality", TAPPI J., Vol. 64, No. 10, p. 115 (1981).

- 111) Kunz, W., "Influence of paper on quality of gravure printing", Wochenbl. Papierfabr., Vol. 114, No. 17, p. 675 (1986).
- 112) Hruzewicz, J.N., Auerbach, R. and Sprycha, R., "Impact of ink/paper interactions on printability of aqueous publication gravure inks, Part II: sorption of liquids by paper during ink setting and drying", Gravure, p. 28, Fall (1997).
- 113) Hruzewicz, J.N., Auerbach, R. and Sprycha, R., "Impact of ink/paper interactions on printability of aqueous publication gravure inks, Part III: acid/base interactions at the paper/ink interface", Gravure, p. 38, Winter (1998).
- 114) Aspler, J.S., "Interactions of ink and water with the paper surface in printing", Nordic Pulp and Paper Research J., No. 1, p. 68 (1993).
- 115) Lyne, M.B. and Aspler, J.S., "Ink-paper interactions in printing: a review", ACS Symp. Ser. 200 (Colloids Surfaces Reprographic Technol.) pp. 385-420 (Aug. 1981) c. 1982.
- 116) Kadoya, T. and Usuada, M., "The penetration of nonaqueous liquids", Handbook of physical and mechanical testing of paper and paperboard, Vol. 2, Ch. 19, p. 124, Marcel Dekker Inc., NY (1984).

2. METHODS DEVELOPMENT

A. Significance:

There are several key parameters of both fibrous substrates and liquids that are useful in relating their fundamental properties to accepted theory. There are an abundance of measurement techniques used by the pulp and paper industry to characterize paper and board. Many of these measurement techniques, such as “air leak” smoothness methods, or the Hercules Size Test method to evaluate sizing, are indirect, and are not traceable. It is also important to identify traceable methods that are capable of producing data over several grade ranges to improve the potential breadth of application and to decrease the experimental complexity of generating data for a model that is broad in scope. This need can be extended to include liquid characterization, liquid application methods and measurement techniques to trace the location of the liquids once they have been applied.

B. Approach:

Substrate parameters of interest that evolve from the Lucas-Washburn equation include, pore radius, surface roughness, and surface energy. The initial desire is that methods be identified that can be traced to primary standards, or reference materials, or synthetic materials for which values have been established by more than one laboratory.

Liquid parameters of interest include liquid surface tension and viscosity of the liquid. While these test methods are inherently more fundamental in nature, it will be necessary to either confirm that the capability to measure these parameters exists at IPST, or to identify and qualify another laboratory to eventually perform these measurements.

Liquid application parameters of interest in this project include the ability to measure and control the equilibrium pressure of the penetrating liquid over a range of industrial applications, the ability to accurately control the line speed, and replicate immobilization of any applied liquids to imitate industrial application.

Quantitative depth and/or radius measurements of penetration of applied liquids is the principal dependent variable in the experimental program. It will be necessary to identify methods to both visualize and quantify the location and amount of applied liquids in the x, y and z planes.

C. Results:

As indicated above in the Approach section, identification of traceable methods that span several grade ranges is an important aspect to this project. Surface topography, or roughness was considered to be an important variable. Many methods used by the industry are indirect methods involving air leakage. Examples include Parker Print Surface (PPS), Sheffield Smoothness and Bendtsen Roughness.

Recently, EMVECO has aggressively marketed a stylus type profilometer, that typically measures five hundred points over a 5 inch length. Values are reported as “micro average” and “microdeviation”. The calculation of “microdeviation” closely resembles that of a traditional “ R_z ” definition (1). That is: R_z , the *average maximum height of the profile*, is the average of the successive values of R_{i_i} calculated over the evaluation length. R_{i_i} is the vertical distance between the highest and lowest points of the profile within a sampling length. It is the average of the greatest peak-to-valley separations. Note that the points used for determining R_z are profile peak and valleys (must cross the mean line), not local peaks and valleys.

An R_z value can also be determined using an optical interferometry method. Although IPST does not have this capability, measurements of this type can be performed at the Tribology Laboratory at Western Michigan University.

A roughness standard was purchased from the Mahr Corporation, Cincinnati, OH, whose values are traceable to the BAM Laboratories in Germany. The assigned R_z value approximates the general roughness of an uncoated free sheet. Subsequently, the standard was measured using both the EMVECO profilometric and interferometric methods. The results are shown in Table A. It is important to note that the measuring area for the interferometer is 0.5 mm^2 , while the EMVECO measurement, while programmable to different sampling rates and distances, typically collects 500 data points over a distance of five inches. Also, it should be noted that due to the thickness of the standard, it was not possible to re-zero the EMVECO profilometer immediately prior to evaluation of the standard. The values shown in Table A suggest that both methods are capable of accurate analysis. Actual raw data scans of the standard for both interferometric and EMVECO profilometer methods are included in Figures A and B, respectively.

In an effort to determine the applicability of the methods over several grade ranges, two samples of linerboard were equilibrated at 12% and 50% RH. The samples were then evaluated using both the EMVECO profilometric and interferometric techniques. This data is shown in Table B. It can be seen that the EMVECO and interferometric results diverge, with the EMVECO results being much greater. Realizing that the EMVECO instrument was programmed to acquire 500 data points over a 5 inch line, while the interferometer measure only 0.5 mm², it is appropriate to conclude that the sampling area for the interferometric method is not representative of the bulk surface. Therefore, the EMVECO profilometer was chosen for subsequent roughness evaluations.

Another finding during the evaluation of the data shown in Table B is that the EMVECO results showed an increase in roughness with increasing moisture, while the interferometry method demonstrated little divergence as a function of moisture. Raw data for the interferometry results for a linerboard samples designated F-2 and B-2 at low and high moisture are shown in Figures C and D, respectively. Subsequently, a number of commercially produced linerboard samples, with wide ranging physical properties and composition were evaluated similarly. That is, the samples were initially equilibrated at varying humidity levels ranging from 8% to 75%. After equilibration, the moisture content was determined, and EMVECO roughness and contact angle (water) were established. Data for three samples is included in Figures E, F and G. It can be seen that the roughness for all of the samples increases with increasing moisture, and then drops at the highest moisture content. This is attributed to gradual swelling of the fibers to a point at the highest moisture, where void space between fibers begins to fill, resulting in a decline in roughness.

An even more interesting phenomenon is the trend in contact angle (water). The data collected for these specimens appears to fall into three trends, increasing, decreasing and random, as a function of moisture content. There appears to be no correlation with either fiber composition or sizing content, as measured using HST and Cobb sizing evaluations. Clearly, this suggests that roughness and contact angle (water) measurements are confounded, and vary significantly as a function of moisture content.

In an effort to perform a more controlled evaluation, a set of uncoated free sheet papers were evaluated similarly. These papers were produced on a pilot scale paper machine. The design of this trial was a 3 x 3 factorial where HWD/SWD ratio was maintained as a constant, and the independent variables included % ash and level of sizing. The design and sample designations are detailed in Table C. Examples of the EMVECO Roughness and Contact Angle (water), as a function of equilibrated moisture content are shown in Figures H, I and J. In this set of samples, both the EMVECO roughness and Contact Angle (water) fall into three categories, increasing, decreasing and random, as a function of moisture content. Furthermore, the changes as a function of moisture content are not predictable, based upon either ash content or degree of sizing, as measured using water drop penetration or Cobb sizing evaluations.

Based upon both linerboard and uncoated free sheet EMVECO roughness and Contact Angle (water) measurements as a function of moisture, it appears that roughness and Contact Angle (water) are confounded. This suggests that a technique should be developed to separate fibers from the web in order to evaluate single fiber contact angle.

D. Conclusions:

- 1) Both the EMVECO profilometric and interferometric methods of surface roughness profiling are accurate, as both can be confirmed using the same traceable standard.
- 2) As the surface topography increases in variation, results from the two methods diverge. This is due to the fact that the field of view available for the interferometric method is 0.5 mm^2 . The sampling area for the EMVECO profilometric method is much more representative as it is typically programmed to collect 500 data points over a length of specimen of 5 inches or more. Therefore, the EMVECO method is more representative of the bulk surface.
- 3) The EMVECO profilometer measurements are sensitive to moisture and composition changes for both uncoated free sheet and linerboard grades, suggesting the potential for use of this method over several grade ranges.
- 4) Contact angle (water), measurements appear confounded with roughness, as moisture of the sheets increases for both linerboard and uncoated free sheet. A designed experiment will be required where both single fiber contact angle and that of the sheet surface will be measured to more clearly understand this relationship.

E. References

- 1) EMVECO, Inc., Model 210-R, Computerized Smoothness Measuring System, Operating Manual, Newberg, OR.

TABLE A
STANDARD REFERENCE MATERIAL
ASSIGNED AND MEASURED VALUES

<u>Method I.D.</u>	<u>R_z, μm</u>
Assigned Standard Value	10.9
EMVECO Method	11.7
Interferometric Method	11.8

TABLE B
COMPARISON OF EMVECO AND INTERFEROMETRY
ROUGHNESS OF LINERBOARD AS A FUNCTION
OF MOISTURE CONTENT

Sample I.D.	Equilibrated RH	R_z Value, μm
F-2 (EMVECO)	12%	125.7
F-2 (interferometer)	12%	42.34
B-2 (EMVECO)	12%	119.6
B-2 (interferometer)	12%	41.26
F-2 (EMVECO)	50%	150.4
F-2 (interferometer)	50%	39.04
B-2 (EMVECO)	50%	134.3
B-2 (interferometer)	50%	46.92

TABLE C
UNCOATED FREESHEET
COMPOSITION AND SIZING DESIGN

<u>Sample I.D.</u>	<u>HWD Content</u>	<u>SWD Content</u>	<u>% CaCO₃</u>	<u>Sizing Level</u>
A	80%	20%	5	Low
B	80%	20%	5	Medium
C	80%	20%	5	High
D	80%	20%	15	Low
E	80%	20%	15	Medium
F	80%	20%	15	High
G	80%	20%	25	Low
H	80%	20%	25	Medium
I	80%	20%	25	High

Figure A

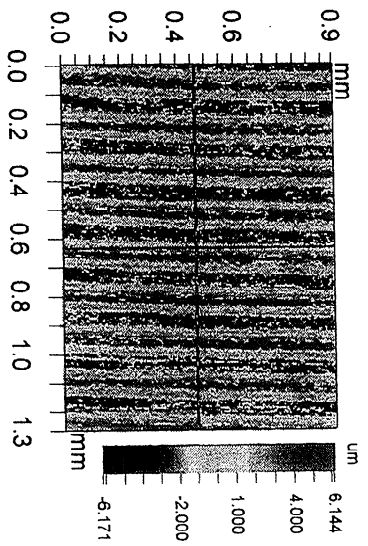
Title: 4.9 X

Note:

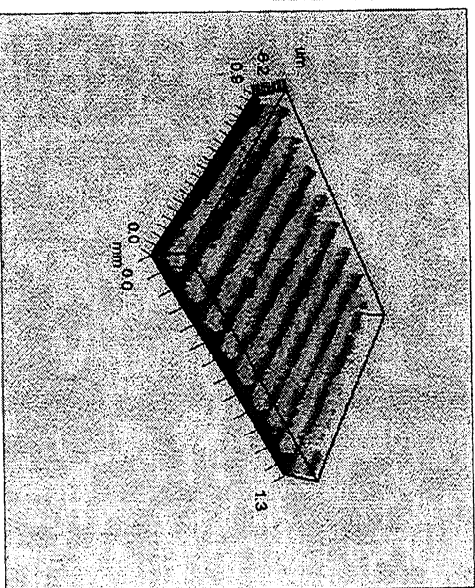
Date: 12/15/99
Time: 12:02:48
Mag: 4.9X
Size: 368 X 236 pixels
Pixel Size: 3.45 μm
Restore: No
Ra: 2.92 μm
Rq: 3.30 μm
Rt: 12.315 μm
Rsk: 0.10
Rku: 1.70
Rz: 11.79 μm
Terms Removed:
Tilt



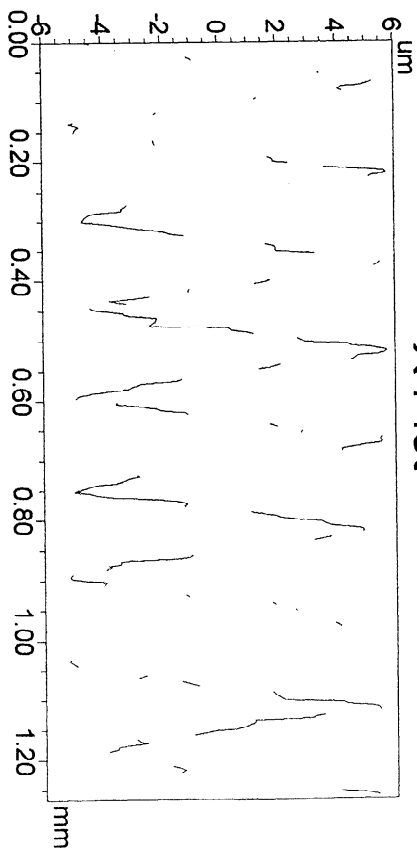
Contour



3D Plot



X Plot



Y Plot

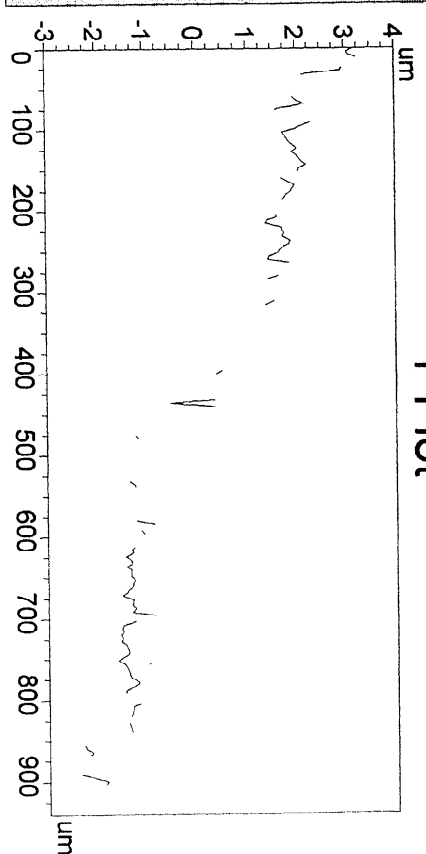
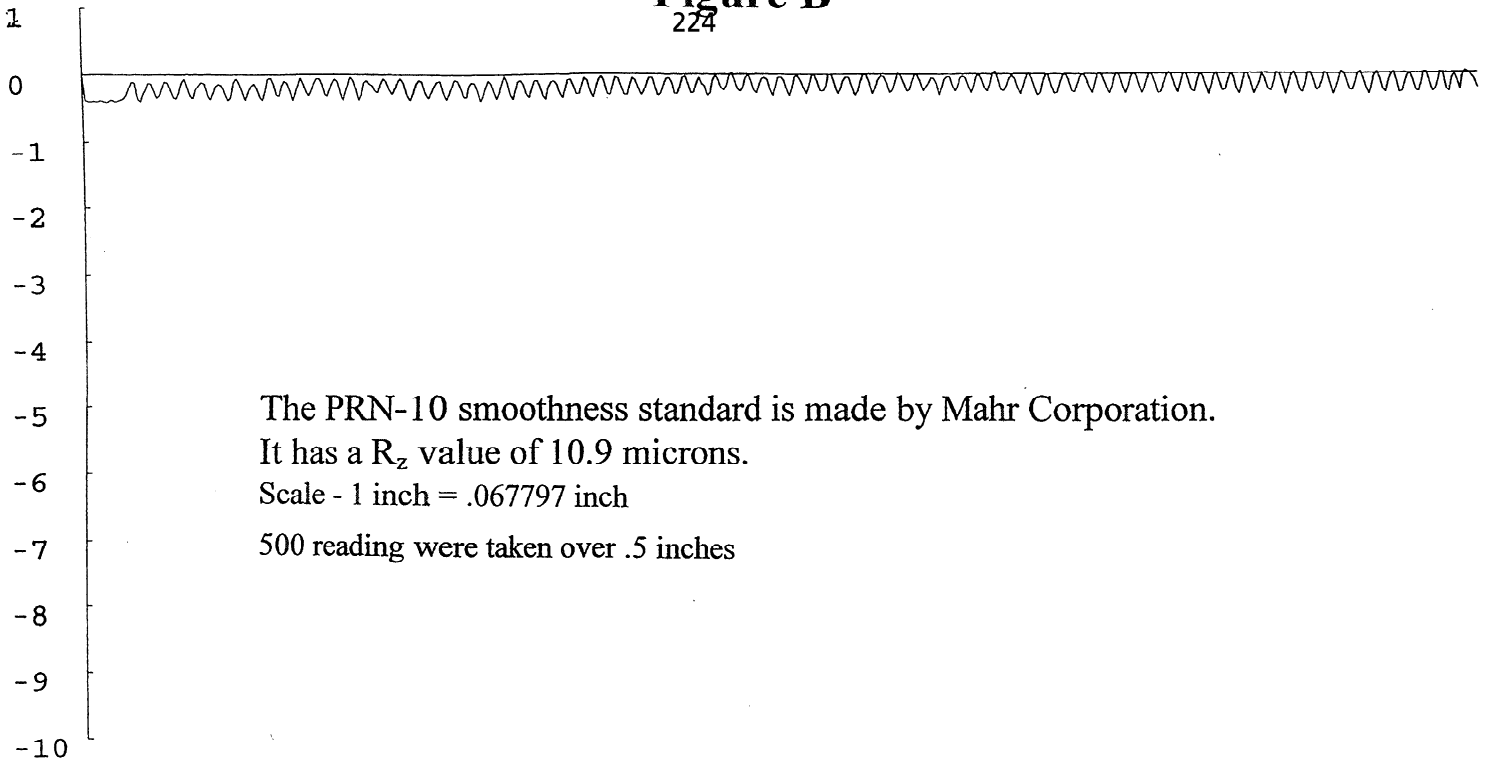


Figure B

224



The PRN-10 smoothness standard is made by Mahr Corporation.

It has a R_z value of 10.9 microns.

Scale - 1 inch = .067797 inch

500 readings were taken over .5 inches

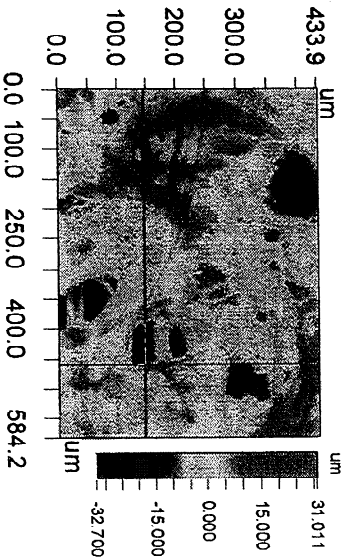
TEST NAME:

Group#	Micro Dev	Micro Avg
1	11.65	.0947

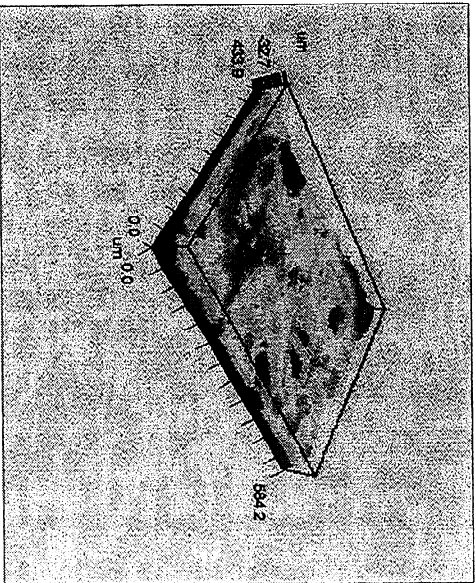
Figure C

Title: 12% r.h. F2
Note: #4

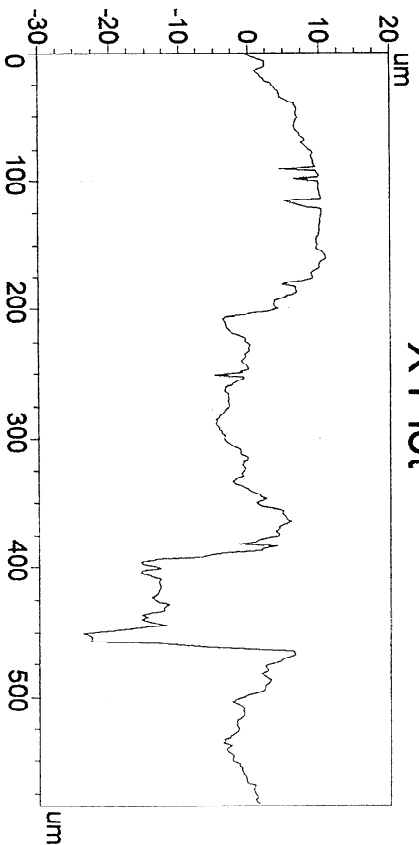
Contour



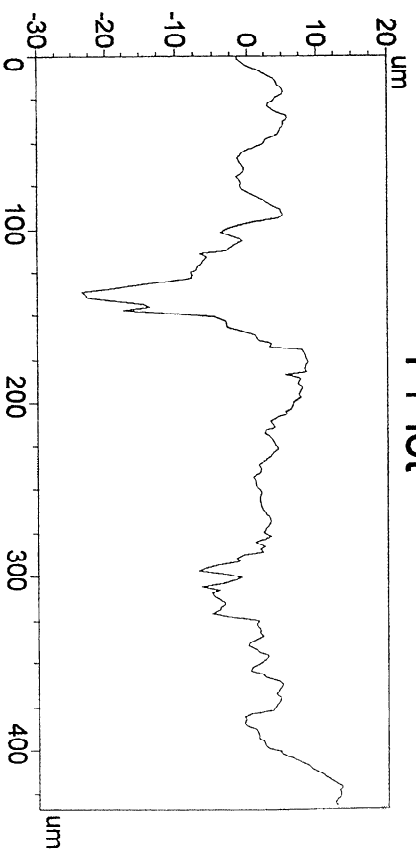
3D Plot



X Plot



Y Plot



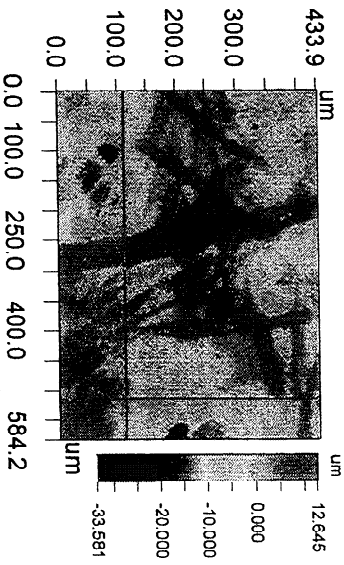
Date: 12/15/99
Time: 14:26:20
Mag: 10.7X
Size: 368 X 236 pixels
Pixel Size: 1.59 um
Restore: Yes
Ra: 4.78 um
Rq: 5.99 um
Rt: 63.711 um
Rsk: -0.34
Rku: 3.02
Rz: 42.34 um
Terms Removed:
Tilt



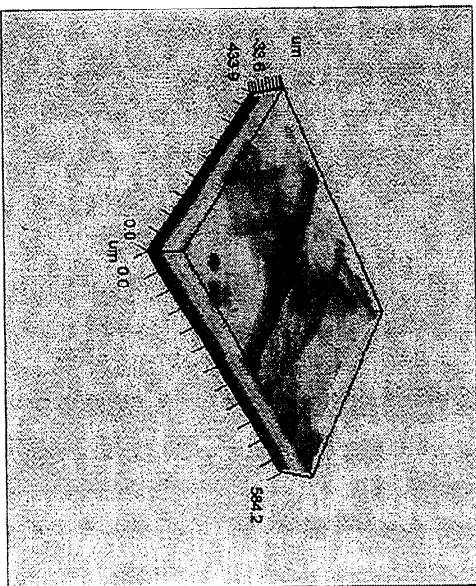
Figure D

Title: 50% r.h. F2
Note: #1

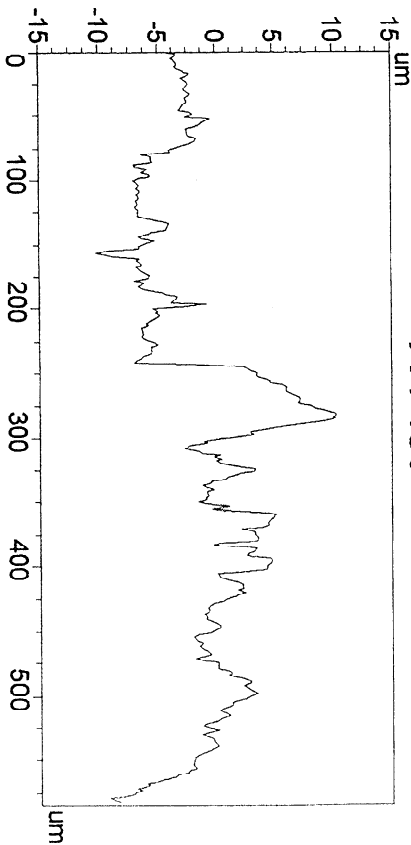
Contour



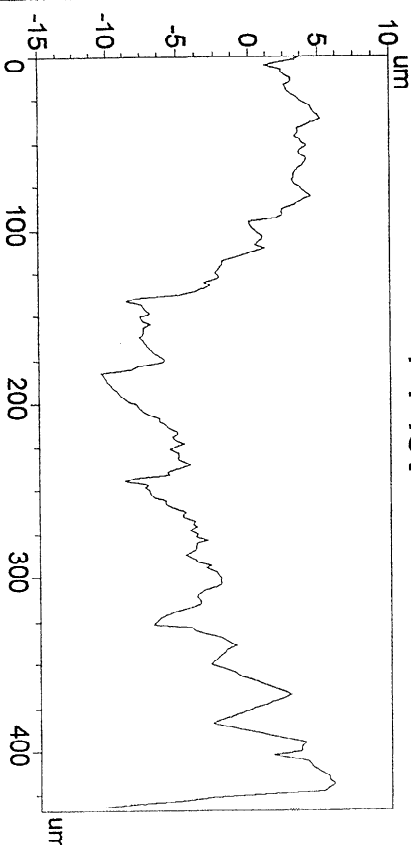
3D Plot



X Plot



Y Plot



Date: 12/15/99
Time: 14:00:22
Mag: 10.7X
Size: 368 X 236 pixels
Pixel Size: 1.59 um
Restore: Yes
Ra: 4.80 um
Rq: 5.99 um
Rt: 46.225 um
Rsk: -0.48
Rku: 3.61
Rz: 39.04 um
Terms Removed:
TIH

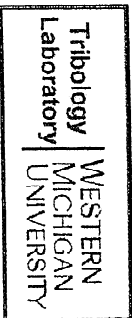
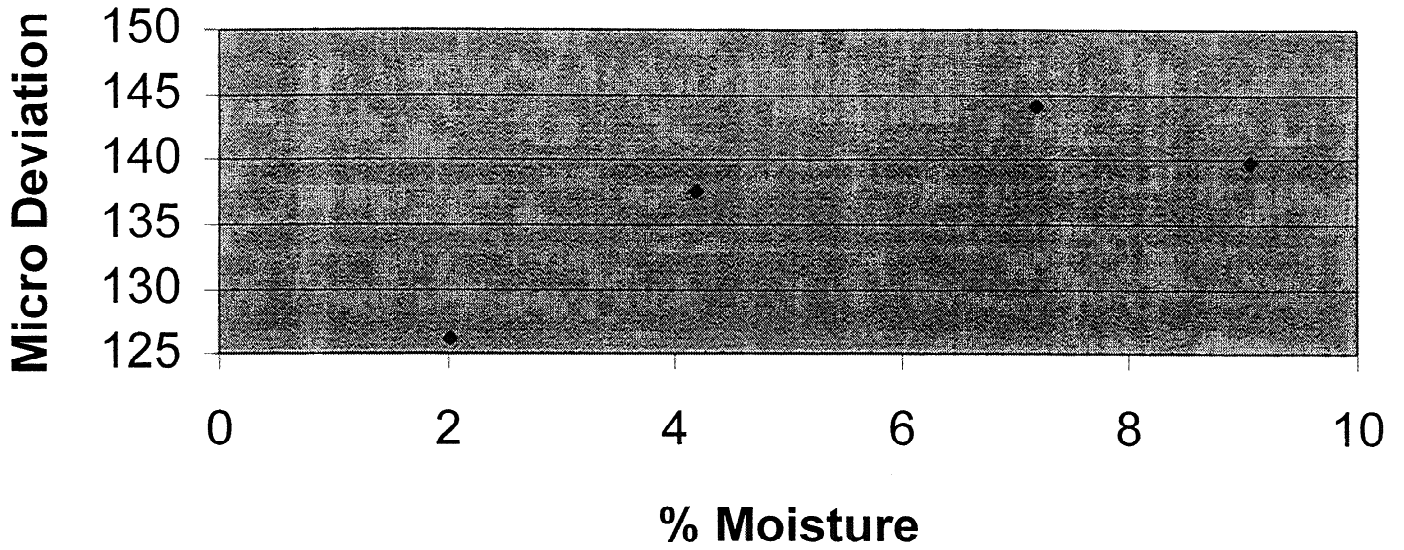


Figure E
Sample A



Sample A

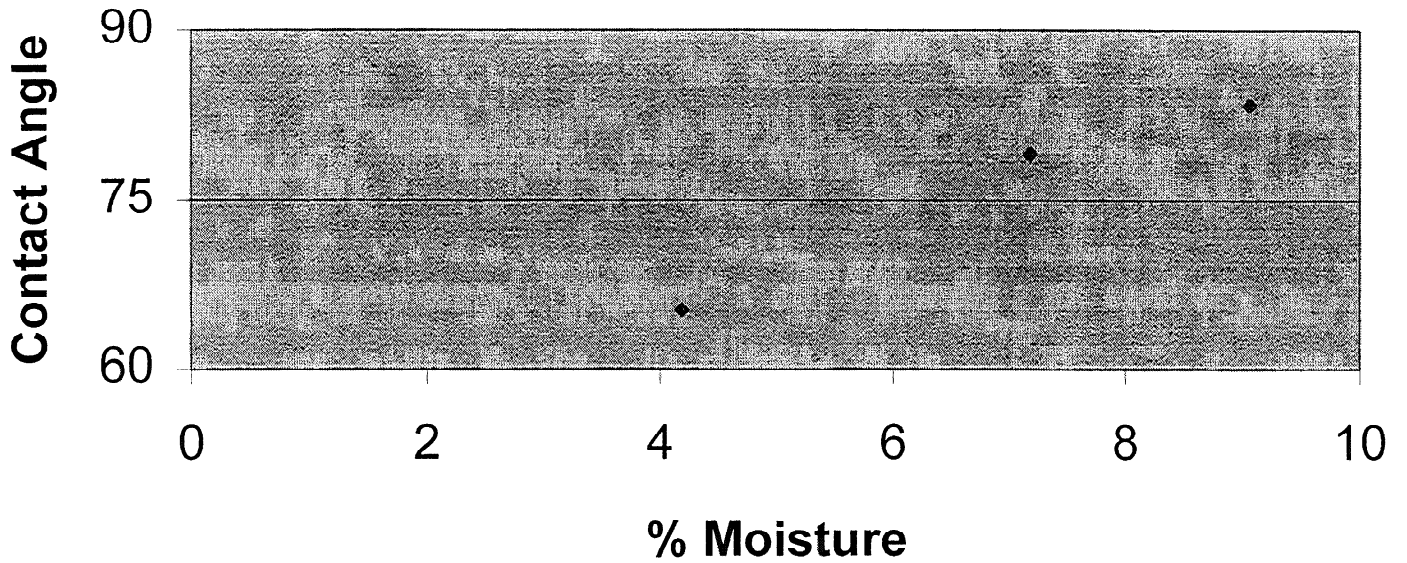
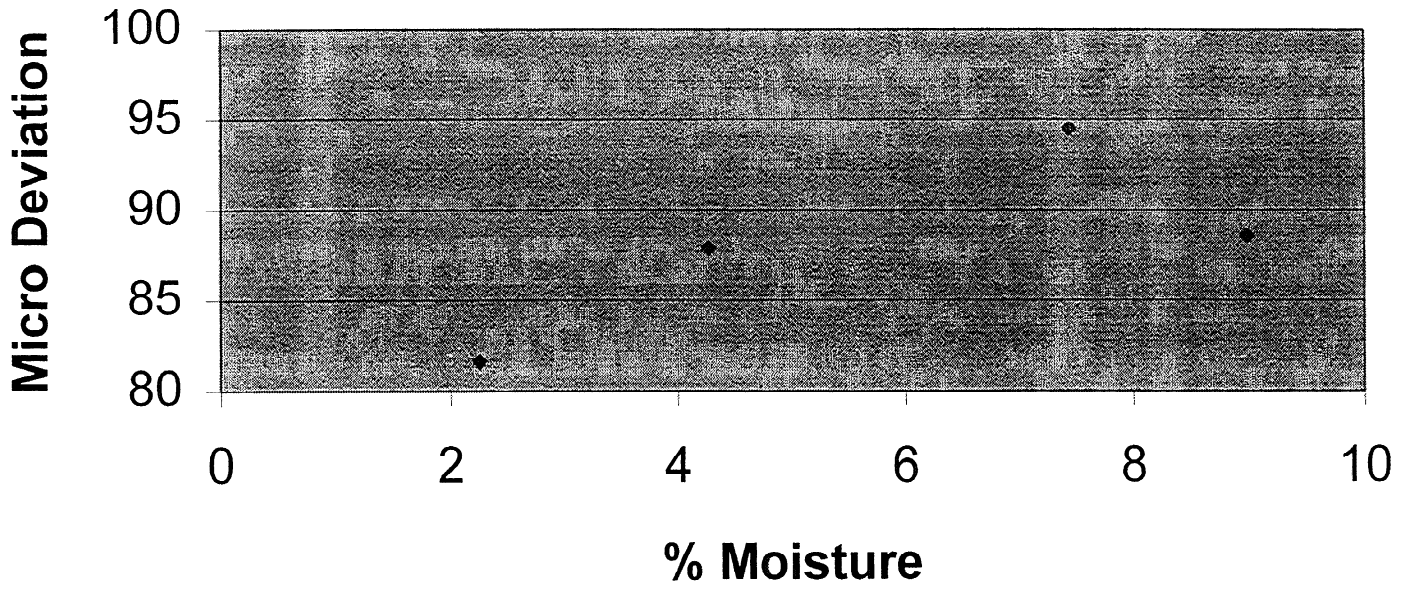


Figure F
Sample H



Sample H

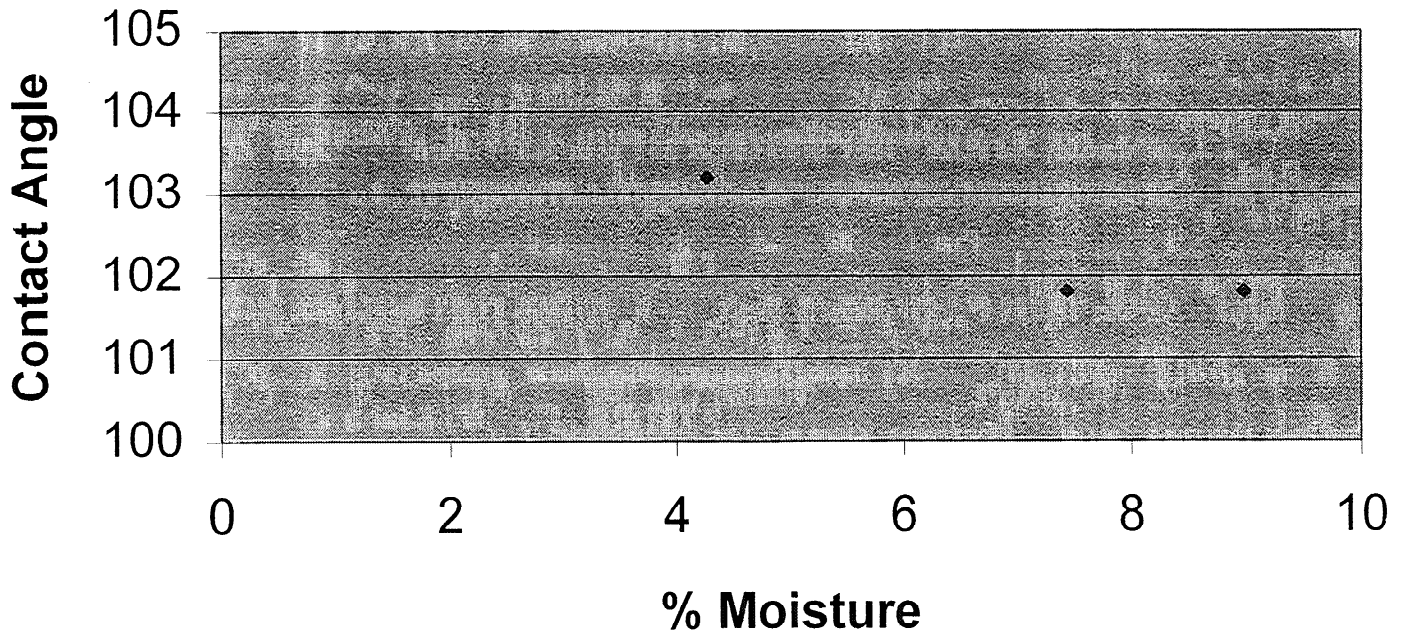
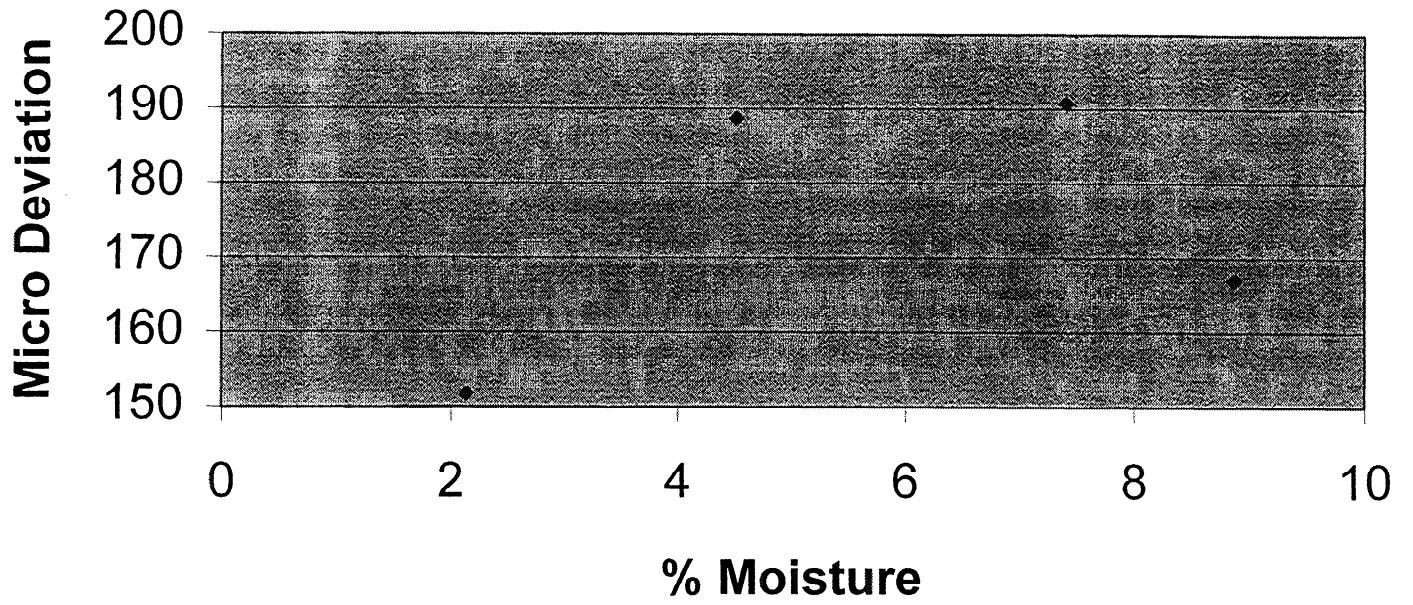
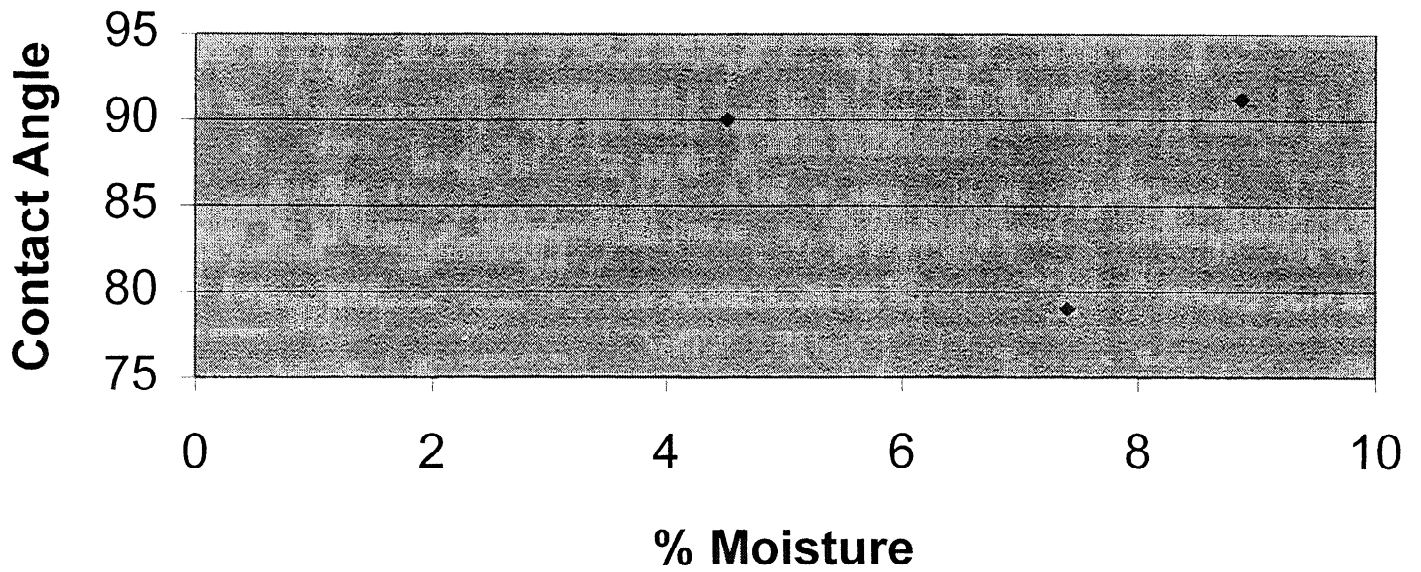


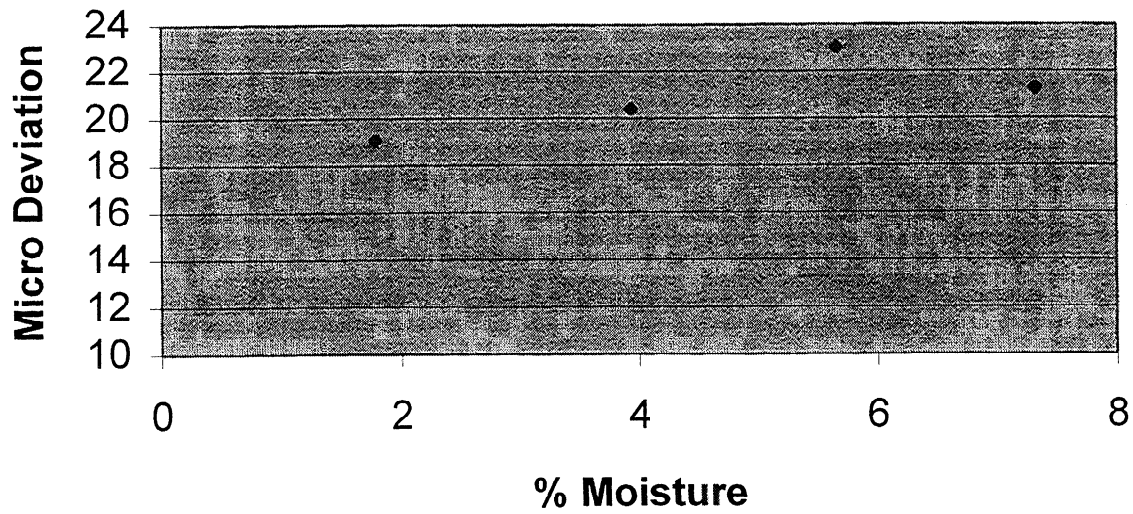
Figure G
Sample E



Sample E



**Figure H
Sample A**



Sample A

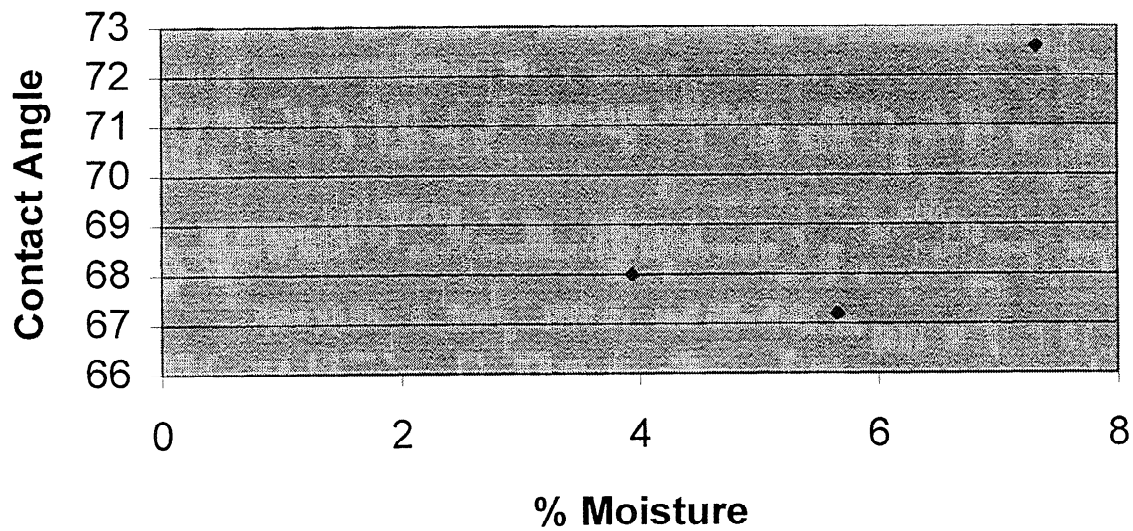
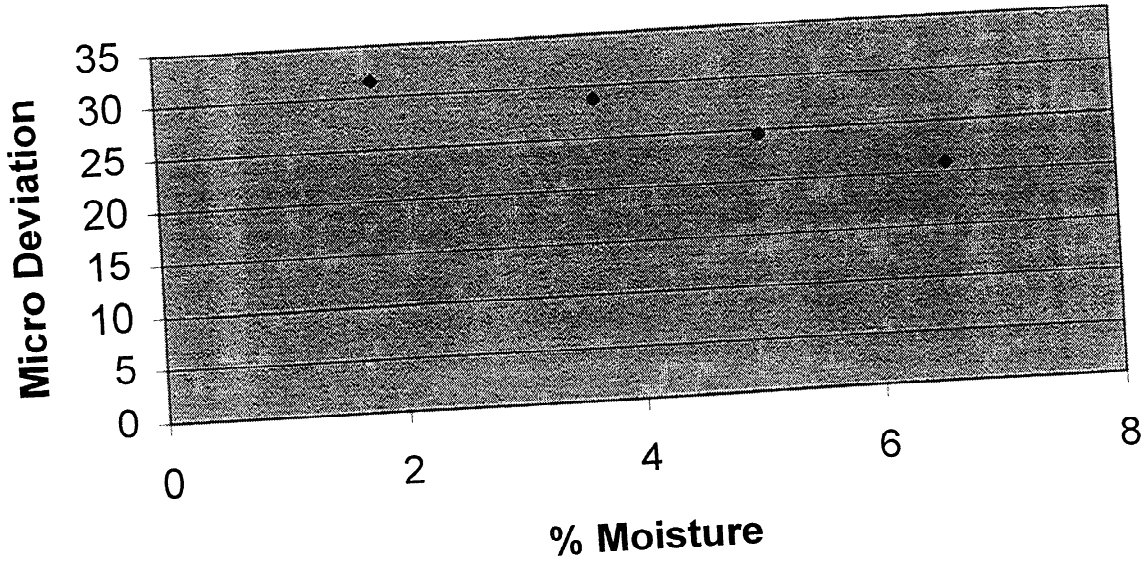


**Figure I
Sample F**



Sample F

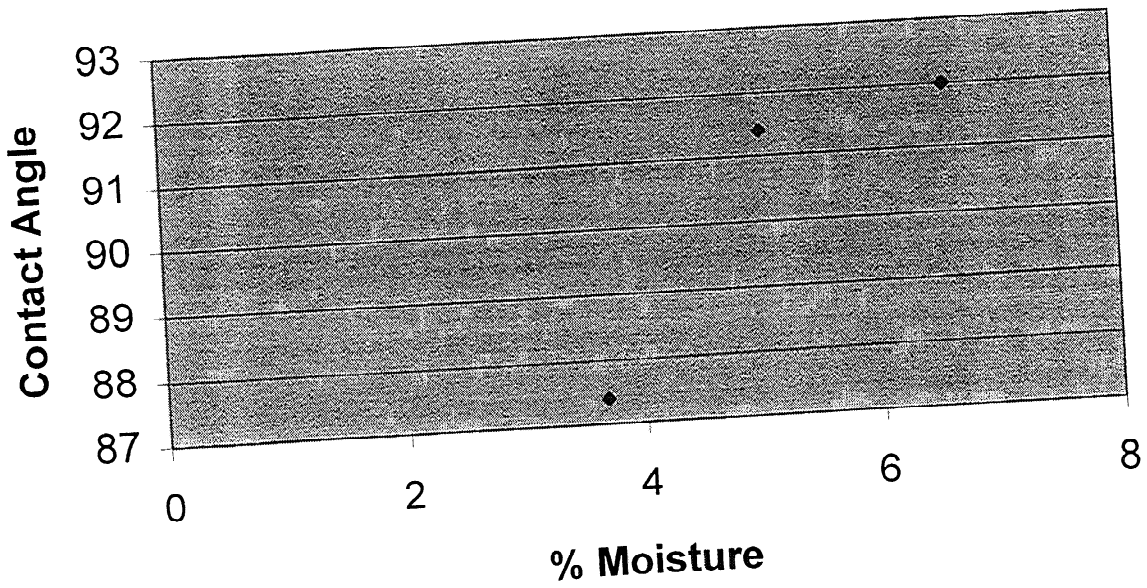
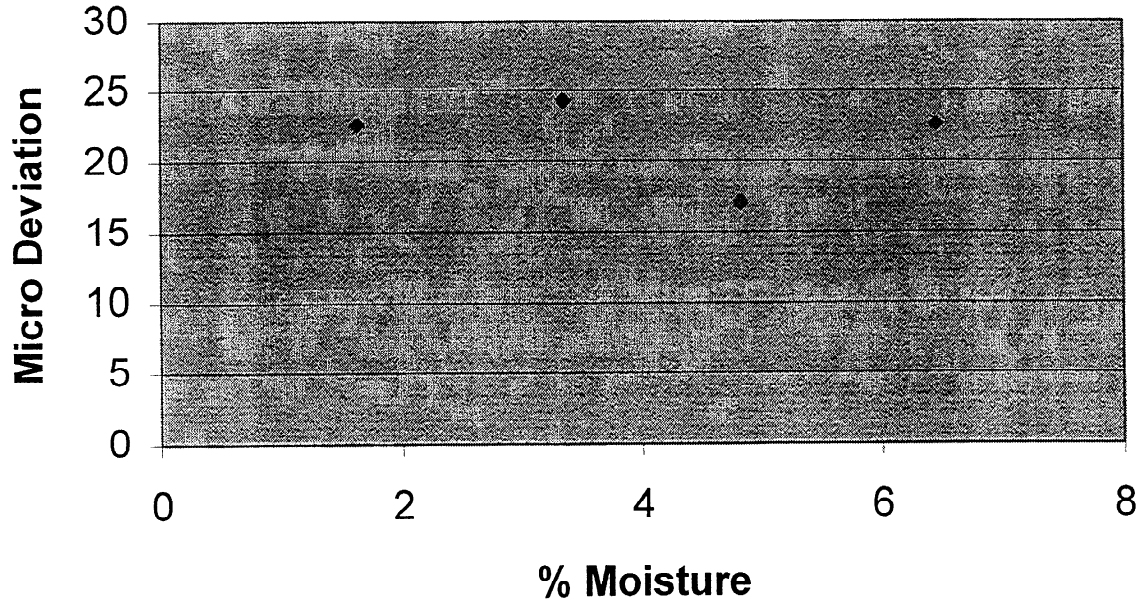


Figure J
Sample I



Sample I

